DIPLOMARBEIT | DIPLOMA THESIS

Titel | Title

Metal alloying anodes for Li-ion batteries: Phase relations in the intermetallic system In-Li

verfasst von | submitted by

Tobias Feichtinger BSc

angestrebter akademischer Grad | in partial fulfilment of the requirements for the degree of

Diplom-Ingenieur (Dipl.-Ing.)

Wien | Vienna, 2024

Studienkennzahl lt. Studienblatt | Degree programme code as it appears on the student record sheet:	UA 066 658
Studienrichtung lt. Studienblatt | Degree programme as it appears on the student record sheet:	Masterstudium Chemie und Technologie der Materialien
Betreut von | Supervisor:	ao. Univ.-Prof. Mag. Dr. Hans Flandorfer

Acknowledgements

I would like to thank ao. Univ.-Prof. Mag. Dr. Hans Flandorfer of the Department of Functional Materials and Catalysis for his supervision on my diploma thesis.
I also would like to thank Mag. Dr. Franz Jirsa of the Department of Inorganic Chemistry and ao. Univ.-Prof. i.R. Dr. Herta Silvia Effenberger of the Department of Mineralogy and Crystallography for their assistance at elemental analysis techniques and crystallographic measurements.
I especially appreciated the advice, assistance and training during the work on my thesis of Lukas Fischer BSc MSc of the Department of Functional Materials and Catalysis.
Last but not least, I thank my family, which is and was always there for me.

Table of Contents

1. Introduction

1.1 Energy storage

Energy storage is one of the most important measures to satisfy the up-coming technical demands on the increasing electrification of mobility and better energy storage possibilities for the power sector, mandatory to reduce the global CO_2-emissions as planned by the UN in 2015 in the Paris agreement. This legally binding international treaty agreed on limiting the global warming, resulting from anthropogenic greenhouse gas emissions to 1.5 to 2 °C above the pre-industrial level. Because the global temperature of the pre-industrial level let humankind (Homo sapiens) thrive during the Neolithic Revolution resulting in the achievement of civilization. However, an increase above 2 °C would enhance the risk of crossing “tipping points” leading to irreversible changes in the climate system, which would threaten many species with the extinction. Thus, more research on energy storage systems like lithium-ion batteries LIBs is urgently needed to contribute to the Paris agreement. [1][2]

1.2 Lithium-Ion Batteries

Batteries in general and nowadays especially LIBs are one of the most important techniques to store and release energy in form of electricity in a fast and convenient way. They were for the first time commercialized in the 1990s by Sony. The major advantages of LIB are the high energy density, long cycling life, no memory effect and low self-discharge.

Today they are everywhere to find from portable devices like smart phones or notebooks to electric cars. “Second life” applications of LIBs in the near future like stationary energy storage for photovoltaic power plants etc. could also become of interest. [3][4]

Basically, they are made of an anode, e.g. of graphite, which is separated from the cathode, e.g. made of $LiFePO_4$ by a membrane soaked with electrolyte like $LiPF_6$ solved in ethylene carbonate/dimethyl carbonate (see Fig.1).

Li^+ acts as ionic charge transfer agent, migrating by the rocking-chair principle during discharge from the anode through the electrolyte to the cathode and vice versa during charging. So, at discharging will the anode be oxidized and the electrons flow through a Cu-collector to an electrical device and further to an Al-

current collector and at last to the cathode reducing it. The lithiation/delithiation reaction of the cathode/anode during charging/discharging can lead to an intercalation reaction or to a phase transition depending on the electrode material.
During the first charging, reacts a significant part of the contained Li^+ irreversible with a part of the thermodynamically instable electrolyte to form a metastable interface, called solid-electrolyte interphase, SEI. The on the surface of the anode[a] deposited SEI works as a protective layer between the electrodes and the electrolyte inhibiting further loss of Li^+ and electrolyte. However, the solid-state diffusion of Li^+ through the SEI remains possible. The SEI consist of a complicated phase system of different compounds like $(CH_2OCO_2Li)_2$, Li_2CO_3, LiF, Li_2O etc. [5]

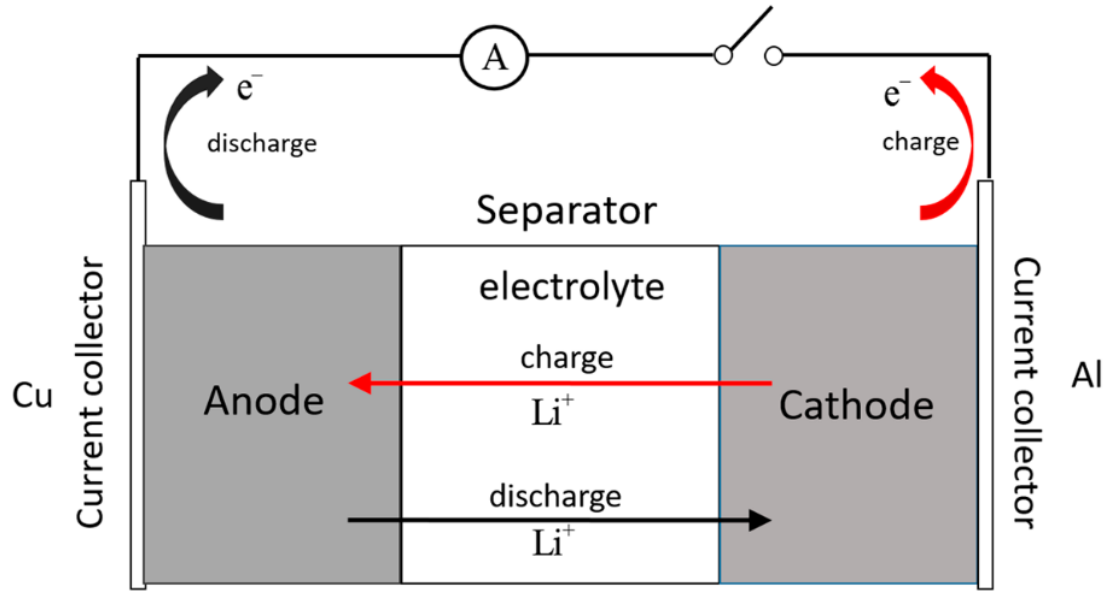

Figure 1 Schematic of a common LIB. [6]

A big disadvantage concerning the cyclability of LIB are the loss of contact to the current collectors and partially destruction of the SEI caused for example by mechanical stress through volume changes of electrode materials, resulting in capacity degradation.
Methods to counteract these issues are the utilization of self-healing electrodes. One technique to acquire self-healing effects is the use of metal alloy anodes, which are (partially) liquid at room temperature. Such liquid metal alloys can be

[a] The term anode refers to discharge, on charge it is the cathode where the SEI is formed on reduction.

found in the systems Ga- In-Sn with a melting point of ~9 °C at a mass composition 7:2:1 = Ga:In:Sn), Ga-In-Sn-Zn with a melting point of ~3 °C at 79.02 at.% Ga, 10.66 at.% In, 8.94 at.% Sn and 1.38 at.% Zn or In-Ga with a melting point of ~15 °C (21.8 wt.% In and 78.2 wt.% Ga). [2][4][7][8][9]

The latter alloy can be used for example to produce nano-droplets/particles NPs which can be 3D-assembled with a binder like polyvinylidene fluoride PVDF combined with a contacting agent like carbon black to form a self-healing composite anode for LIB and Sodium-ion batteries. During charging Li^+ or Na^+ respectively diffuses to the surface of the anode reacting there after reduction with the liquid alloy to form solid $InLi_2$ and $GaLi_2$ with a voluminous crystal structure when fully discharged. This expansion damages the SEI until a certain point where the SEI growth slows down, because the SEI has reached enough volume to compensate the volume changes of the alloy. In addition, shrinking of the anode during discharging can result in contact loss to the current collector producing dead Li-species. However, the latter sort of damage can be repaired by the reliquefied alloy, restoring the interface contact to the current collector due to its enhanced wettability (see Fig. 2).

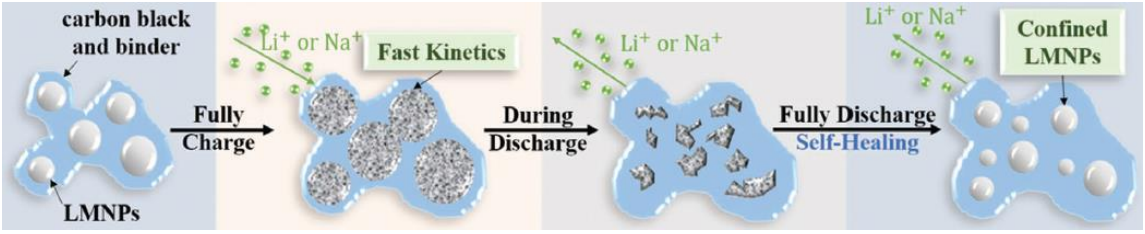

Figure 2 Process of Lithiation/Delithiation of eutectic melting, liquid metal nano particles LMNPs within a carbon black + binder matrix (Ga–In NPs@C + binder). [7]

Bulk liquid Ga-In alloys can also be applied as anode materials lowering the issue of contact loss. However, some parts of dead Li-species do still appear due to faster bulk diffusion compared to surface diffusion of Li-species. This leads to mechanical stress between surface and bulk of the anode material during discharging, which results in fracturing of the anode and thereby to the partial contact loss. This drawback gets intensely decreased when In-Ga nano-particles are in use, because their increased surface to volume ratio improves the rate of the solid-state surface diffusion. [7]

Pure metallic Li is a promising anode material for LIB due to its very low redox potential of -3.04 V vs. SHE (standard hydrogen electrode) and its very high theoretical capacity of 3860 mAh/g. However, Li electrodes have some big issues like their reactivity at ambient conditions with, H_2O, O_2, N_2, CO_2 or commonly used liquid electrolytes. Latter results in the formation of a SEI. Another issue is the growth of dendrites on charge, of which the mechanism is not fully understood yet. As far as known is it caused by an inhomogeneous electrode surface leading to sites with different local polarization, promoting dendrite growth. These dendrites can eventually lead to an internal short circuit when reaching the cathode after several times of deposition and dissolution during charging/discharging. Hence, a thermal runaway would occur, becoming a serious safety risk if a typical liquid, flammable electrolyte for LIB is in use. Dendrite proliferation causes also mechanical stress on the SEI resulting in metallic Li sites exposed to the liquid electrolyte. This leads to a higher consumption of Li and electrolyte for the regeneration of the damaged SEI. In addition, also partially contact loss to current collectors can occur. [5][4][10][11]

Liquid metal alloys can also be effectively used as artificial SEI for metal anodes in LIBs, suppressing Li dendrite growth. An example for such an application is the already mentioned liquid system Ga-In-Sn-Zn, which can cover a current collector like a Cu foil under formation of $CuGa_2$. This system reacts with Li to solid compounds during charging like $GaLi_2$, In_3Li_{13}, $Li_{4.25}Sn$ and LiZn showing improved lithiophilicity and fast electronic and ionic conductivity, which prevents the build-up of defect sites which would lead to Li-dendrite growth. Hence, the nucleation overpotential decreases enhancing dendrite-free Li-platting on the whole surface (see Fig. 3). [4][12]

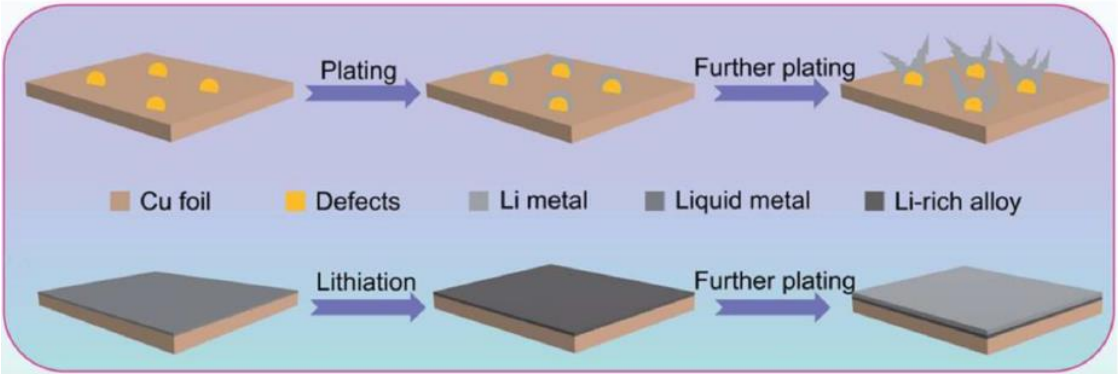

Figure 3 Comparison of the reaction behavior of Li with a Cu-current collector with and without liquid metal alloy coating. [12]

Solid In-Li alloys are also of interest for anode applications with improved electrochemical properties in comparison to pure Li-metal anodes. In the literature are assembled batteries described like a LIB: $Li(Ni_{0.6}Co_{0.2}Mn_{0.2})O_2$//In-Li/Cu with a liquid electrolyte and an anode made of In-Li alloy@Cu by casting of In-Li melt on a Cu-foil or a LIB: Li/In/$80Li_2S \cdot 20P_2S_5$/$Li_4Ti_5O_{12}$ with the solid-state electrolyte Li_2S-P_2S_5 separated from a Li-metal anode by a thin foil of In which reacts in situ during battery cycling to a layer of In-Li alloy, consisting of (Li) and In_3Li_{13}. Another LIB with a liquid electrolyte and an In-Li alloy anode would be In- Li//$Li_{1.2}Ni_{0.2}Mn_{0.6}O_2$. A In-Li alloy can also be used as anode for Li-S batteries e.g. In-Li//S. The anode can be described as composition of the phases (In), (Li), In_2Li_3 and In_3Li_{13} made by mechanical alloying (cold-welding) through rolling.

In-Li systems do have excellent properties, wanted for batteries like no significantly volume change during cycling, a good lithiophilicity, a lower interfacial resistance and thereby a lower overpotential as well as a similar redox potential and a inhibited dendrite growth compared to pure Li. [10][5][11][13]

The mechanism behind the dendrite growth inhibition of In-Li alloys can be explained by the fast diffusion of Li-species mostly through a large amount of grain boundaries into the bulk, leading to a homogeneous distribution of incoming Li^+ which prevents local surface polarization. Such a local polarization would promote Li-dendrite growth during plating. A uniform distribution of the In-species like a 3D-network in a (Li)-matrix, helps also to prevent dendrite growth, due to uniform Li deposition (see Fig. 4). [10][5][13][16]

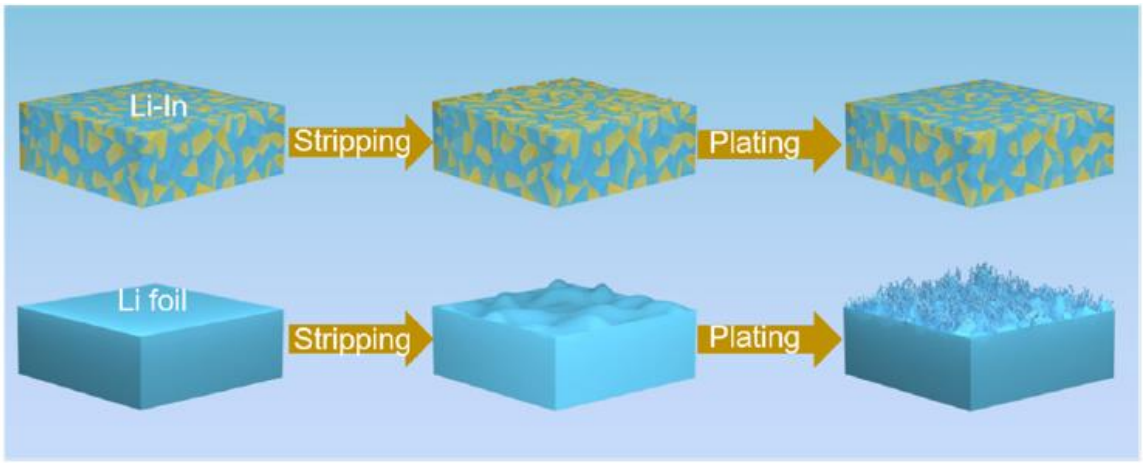

Figure 4 Comparison of the reaction of Li with a Li-anode (Li-foil) and with a Li-anode protected by an Li-In layer. [10]

A fast solid-state diffusion of Li in In-Li compounds during charging/discharging occurs not only at the grain boundaries, but also within crystallites. This fast diffusion can be explained by the occurrence of high-rate transportation channels for interstitial and vacancy diffusion mechanisms. At first diffuses a Li-atom, after reduction during charging to an interstitial site of the In-Li compound leading in the case of In_2Li_3 and $InLi_2$ to a structural rearrangement of the crystal surface or in the case of InLi and In_3Li_{13} to the formation of a local cluster region. Next occurs solid-state diffusion in the case of In_3Li_{13} and In_2Li_3 mostly through the coordinate mechanism (= knock-off or kick-out mechanism), which is an interstitial diffusion mechanism. In the case of InLi and $InLi_2$ occurs mostly the direct-hopping mechanism, which is vacancy diffusion mechanisms. What mechanism takes place depends on the activation energy E_A of the respective point defects. For example, the high symmetry of the InLi vacancy structure enables diffusion by vacancy diffusion mode duo to a lower E_A barrier. However, one should mention that the diffusion mechanism depends not only on the sort of compound, but also on other parameters like the Li concentration etc. [5]

In conclusion, the non-equilibrium state during charging/discharging at room temperature of In-Li anodes, result in fast solid-state kinetics implementing a continuous change of the Li-activity of the surface, which can be used for example to get dendrite-free electrodes. [14][15]

The probably biggest disadvantage of In-Li alloys as electrode materials are the high cost of In due to its classification as endangered and critical element. This makes the large-scale use of In-Li alloys not be feasible at the moment (see section 2.1.3 “Occurrence and production (of Indium)”).

However, In-Li alloys as counter electrodes are convenient for the preparation of model solid-state LIBs due to the high ductility of metallic In and Li, which enables easy assembling of such batteries. Furthermore facilitates such an electrode electrochemical investigations, when it serves as an anode at a constant redox potential of ~0.6 V vs. Li^+/Li over a range ~2.5 to 45 at.% Li at room temperature. [16][17]

It is crucial to have as much information as possible on the In-Li system to fundamentally understand the (electro)chemical properties of In-Li alloys in terms of mechanisms, kinetics and thermodynamics. Thus, the binary In-Li phase diagram is a useful information for battery research. It can be used for example to explain

on thermodynamic basis, the behavior of the open circuit voltage OCV as a function of Li in at % or to construct and improve ternary phase diagrams of systems like Ga-In-Li, Sn-In-Li and Zn-In-Li or quaternary systems like Ga-In-Sn-Li as well as more complex systems like Ga-In-Sn-Zn-Li. [2][16]

Hence, investigations on the In-Li system were made in this diploma thesis by experimental methods to enhance the current information on this phase diagram (see section 3. “Experimental methods”).

2. Literature review

2.1 Indium

2.1.1 Discovery

The element Indium In was discovered by Ferdinand Reich and Hieronymus Theodor Richter in 1863 at the German Freiberg School of Mines. It was named after the characteristic indigo blue lines observed during flame spectroscopy of a sphalerite ore sample. [9][18][19]

2.1.2 Properties

The element of the third main group of the periodic table is a shiny, silver colored, soft and ductile metal. It makes during bending the same high frequency cracking sound as Sn called “tin cry”. In has a density of 7.31 g/cm^3 at 20 °C, a molar mass of 114.82 g/mol a melting point of 156.2 °C and a boiling point of 2080.15 °C.
The element crystalizes at standard conditions in the tetragonal body centered crystal structure (In), according to X-ray diffraction XRD results of Hull et al. [20] (see Fig. 5 and Table 1). It has to be mentioned that in old literature, e.g., Graham et al. [21], the crystal structure of In can be described as face centered tetragonal, with a = 4.5891 Å and c = 4.9370 Å. However, the tetragonal face-centered Bravais lattice does not correspond to the standard set-up, as these lattices can always be described by a body centered lattice with a unit cell half the size with $a_{fc} = \sqrt{2}.a_{bc}$, and $c_{fc} = c_{bc}$, leading to lattice parameters given in Table 1.
The tetragonal (In) transforms into the orthorhombic high-pressure phase (In) hp under pressure of 93(5) GPa at room temperature. This was discovered by synchrotron angle-dispersive powder XRD using a gasketed diamond anvil cell and published by Takemura et al. [22] (see Fig. 6 and Table 2).

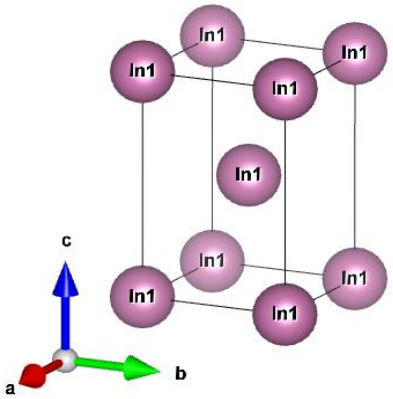

Figure 5 Crystal structure of (In). [23][20]

Table 1 Standardized crystal structure information on (In).

Phase	Structure class	Phase (proto)type	Person symbol	Space group	Ref.
(In)	tetrago-nal	In	tI2	*I4/mmm* (139)	[23]
a (Å)	b (Å)	c (Å)	α (°)	ß (°)	γ (°)
3.252 (1)	3.252 (1)	4.941 (4)	90	90	90
Site	x	y	z	Occ.	Wyckoff
In	0	0	0	1	2a

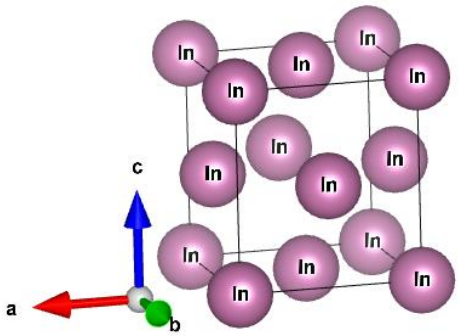

Figure 6 Crystal structure of (In) hp at 93(5) GPa. [24][22]

Table 2 Standardized crystal structure information on (In) hp at 93(5) GPa.

Phase	Structure class	Phase (proto)type	Person symbol	Space group	Ref.
(In) hp	orthorhom-bic	In	oF4	*Fmmm* (69)	[24]
a (Å)	b (Å)	c (Å)	α (°)	ß (°)	γ (°)
3.7690 (0)	3.8460 (0)	4.1400 (0)	90	90	90
Site	x	y	z	Occ.	Wyckoff
In	0	0	0	1	4a

2.1.3 Occurrence and production

The main feedstock for In-production is the Zn ore sphalerite ZnS. Other minerals like the Pb ore galena PbS, or the Sn ore cassiterite SnO_2, as well as Cu ores like chalcopyrite $CuFeS_2$, bornite Cu_5FeS_4 etc. do also contain traces of about 10 to 20 ppm In, feasible to recover in industrial scale. Hence, the industrial Zn-production is the most important supplier for the economic demand of In. Thus, is only produced as a byproduct, which results in the high costs for In. In addition is In like Zn an endangered and critical element and the recycling rates of In are small, while the demand is high and will probably increase in the future, especially electronic applications. This increases the costs further. The main production countries in 2019 were China with 40 %, Korea with 31 % and Japan and Canada with 9 % each. China does also hold the largest reserves according to the year 2015. [9][17][18][19]

In is commonly recovered hydrometallurgical from residues, slags, metallic intermediates or flue dust by different leaching methods followed by selective precipitation or liquid-liquid extraction steps. The last steps are the cementation and the purification by electrorefining. A typical example for the In-production from Zn based resources of the Anaconda Copper Mining Company is described in Fig. 7 and 8. [9][18][19]

First is Zn removed by solving at a moderate pH through addition of $H_2SO_{4(aq.)}$ to the educt (ZnO-fume or roasted Zn-blende also called Zn-calcine). Then is In leached out of the left residue via $H_2SO_{4(aq.)}$ with a concentration of 20 to 25 g/l, followed by precipitation of In through the addition of ZnO and $NaHSO_3$. Eventually will the impure In precipitate be purified in 3 steps. First, by adding concentrated $NaOH_{(aq.)}$ followed by washing steps with H_2O and diluted $H_2SO_{4(aq.)}$ to remove left Zn. Next gets the cleaned residue solved in $H_2SO_{4(aq.)}$ followed by precipitation of left impurities like Cu, As. Sb, Ge etc. as sulfides by adding H_2S. At last is In sponge gained by cementation with Zn (see Fig. 7). [9][18][19]

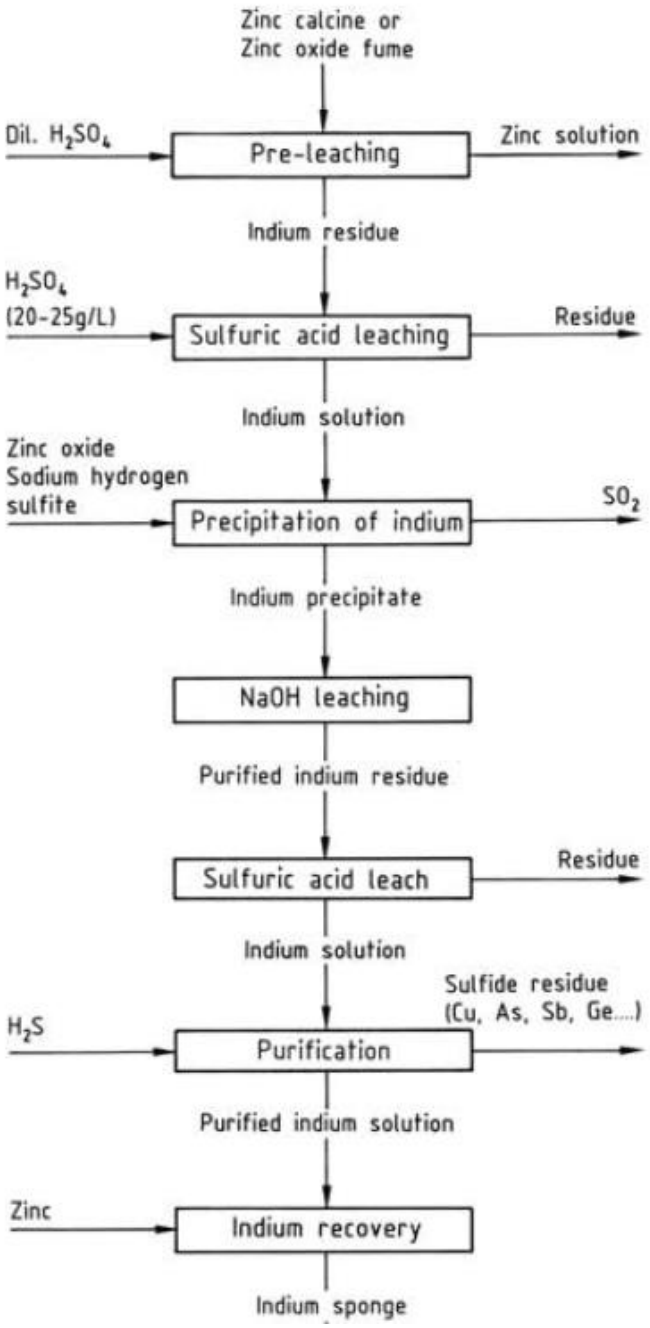

Figure 7 Flow chart of a representative In production process from Zinc calcine or Zn oxide fume by Anaconda Copper Mining Company. [19]

In sponge can be melted with $NaOH_{(s)}$ for casting. Further refining is necessary to obtain high purity In. Thus, In sponge gets solved in $HCl_{(aq.)}$ followed removing SO_4^{2-} as $BaSO_{4(s)}$ with $BaCl_2$, followed by precipitation of heavy metals by addition of H_2S and NaOH. Finally, will traces of impurities be removed by (pre)-electrorefining (see Fig. 8). [9][18][19]

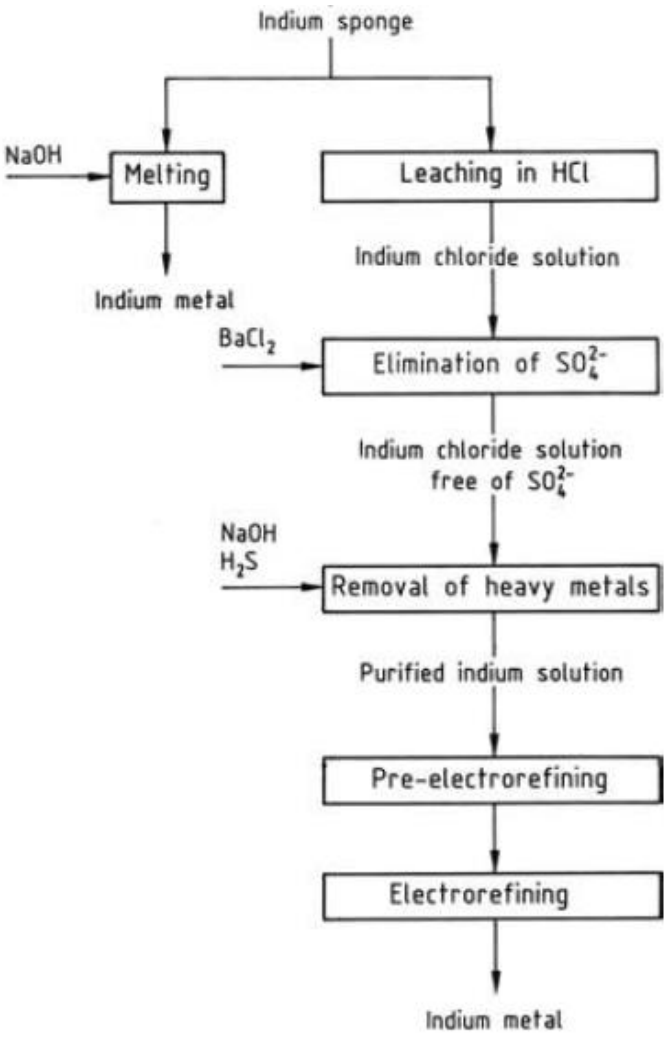

Figure 8 Flow chart of the casting and refining process of In by Anaconda Copper Mining Company. [19]

2.1.4 Application

The element is in industrial-scale in use, whereas 45 % of the produced In is used as indium-tin oxide ITO, where In_2O_3, acts with a concentration of 80 % as doping agent for SnO_2. ITO is transparent for visible light but not for infrared radiation, it is polycrystalline and an electron conductor. All these properties are crucial for applications in photovoltaic panels, LCDs and touch screens as well as micro-chips and semiconductors. Intermetallic compounds of indium are also in use for semiconductors. Some examples worth mentioning, are In-Ga-As-P compounds in laser diodes or In-Ga-As compounds for photodetectors as well as InSb in CCDs for infrared radiation detection. Further applications for In are low melting alloys, which can be used in combination with Sn etc. for solders in electronics as well as for bearings, which can resist harsh conditions leading to seizure and

fatigue or corrosion. Such conditions exist for example at piston-type aircraft engines or in formula 1 cars. Possible future applications for low-melting In alloys are also self-healing materials for batteries described above. Other areas of applications are phosphors, nuclear reactor control rods and dental alloys. [9][17][18][19]

2.2 Lithium

2.2.1 Discovery

The element Lithium Li was discovered by J. A. Arfwedson 1817, who was working at this time at the Berzelius laboratory. It is named after the Greek meaning “from stone” due to its discover in the mineral petalite $Li[AlSi_4O_{10}]$. [25]

2.2.2 Properties

Li is a very soft, ductile, shiny and silver colored metal with the lowest density of all metals with 0.53 g/cm^3 at 20 °C. The alkali metal has a molar mass of 6.9 g/mol, a melting point of 180.5 °C and a boiling point of 1342 °C. Li reacts spontaneous with O_2, N_2 and CO_2 and violently with water at standard conditions like the other alkali metals. [25][26]

Li crystallizes at standard conditions in body centered cubic bcc structure as published by Hull et al. [27] and by Levinson et al. [28] (see Fig. 9 and Table 3).

Investigations of metallic Li with XRD and neutron diffraction by Berliner et al. [29] led to the discovery of the (αLi) crystal structure at low temperatures. (Li) undergoes a martensitic transformation from the bcc structure to a hexagonal close packed hcp structure of Sm-type at a temperature of ~77 K. This structure has a stacking sequence of ABCBCACAB and cold work affects the density of stacking faults as well as other properties like the transformation temperature and the reverse-transformation temperature etc. (see Fig. 10 and Table 4).

Three high-pressure Li phases (see Fig. 11, 12 and 13 as well as Table 5, 6 and 7) are experimentally verified, the face centered cubic fcc phase (Li) hp1 described by Smith et al. [30] via high resolution neutron diffraction, the hcp phase (Li) hp2 and a low symmetry cubic phase (Li) hp3, which has “paired-atoms” leading to near-insulating electronic properties. The latter two phases were investigated by Hanfland et al. [31] through synchrotron X-ray diffraction. At a

temperature of 180 to 200 or 300 K respectively, leads a pressure increase from atmospheric pressure to ~44.5 GPa to the following phase transition:

$$\text{(Li)} \overset{300\ \text{K, 7.5 GPa}}{\rightleftharpoons} \text{(Li) hp1} \overset{180\ \text{K, 39.8 GPa}}{\rightleftharpoons} \text{(Li) hp2} \overset{180\ \text{K, 44.5 GPa}}{\rightleftharpoons} \text{(Li) hp3.}$$

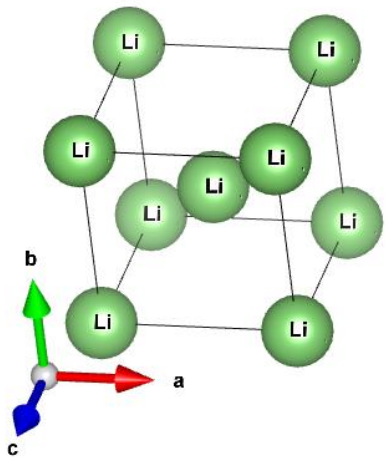

Figure 9 Crystal structure of (Li). [28]

Table 3 Crystal structure information on (Li).

Phase	Structure class	Phase (proto)type	Person symbol	Space group	Ref.
(Li)	bcc	W	cI2	$Im\bar{3}m$ (229)	[27]
a (Å)	b (Å)	c (Å)	α (°)	ß (°)	γ (°)
3.500 (0)	3.500 (0)	3.500 (0)	90	90	90
Site	x	y	z	Occ.	Wyckoff
Li	0	0	0	1	2a

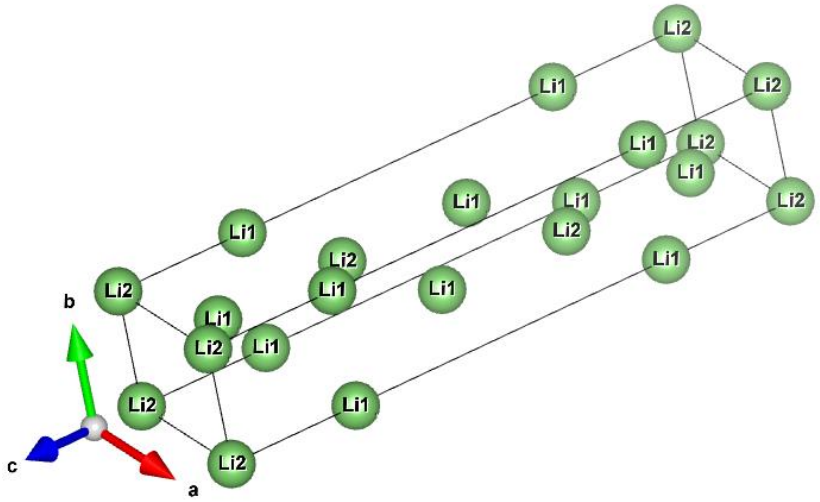

Figure 10 Crystal structure of (αLi) lt at 20 K. [32][29]

Table 4 Crystal structure information on (αLi) lt at 20 K.

Phase	Structure class	Phase (proto)type	Person symbol	Space group	Ref.
(αLi) lt	hcp	Sm	hR9	$R\bar{3}m$(166)	[32]
a (Å)	b (Å)	c (Å)	α (°)	ß (°)	γ (°)
3.10 (1)	3.10 (1)	22.764 (9)	90	90	120
Site	x	y	z	Occ.	Wyckoff
Li1	0	0	0.22222	1	6c
Li2	0	0	0	1	3a

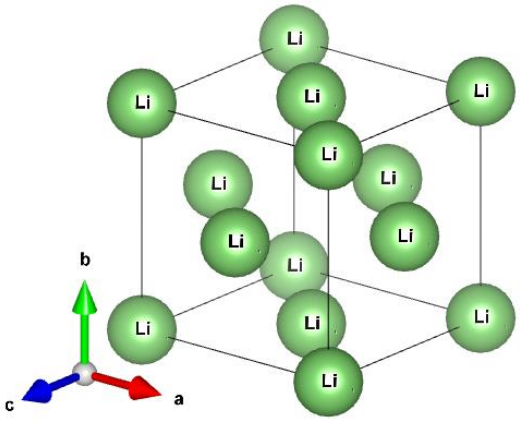

Figure 11 Crystal structure of (Li) hp1 at 140 K and 0.65 GPa. [33][30]

Table 5 Crystal structure information on (Li) hp1 at 140 K and 0.65 GPa.

Phase	Structure class	Phase (proto)type	Person symbol	Space group	Ref.
(Li) hp1	fcc	Cu	cF4	$Fm\bar{3}m$ (225)	[33]
a (Å)	b (Å)	c (Å)	α (°)	ß (°)	γ (°)
4.327 (1)	4.327 (1)	4.327 (1)	90	90	90
Site	x	y	z	Occ.	Wyckoff
Li	0	0	0	1	4a

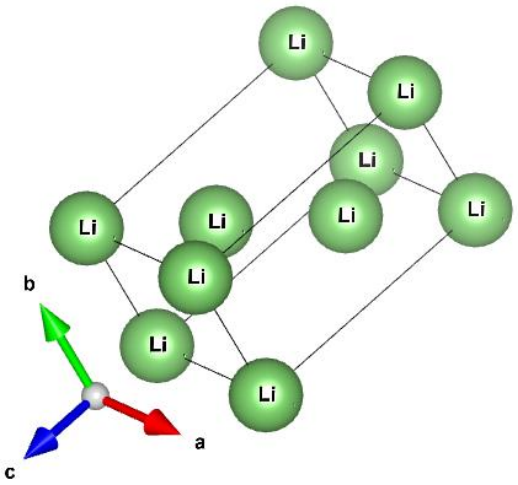

Figure 12 Crystal structure of (Li) hp2 at 180 K and 39.8 GPa. [34][31]

Table 6 Crystal structure information on (Li) hp2 at 180 K and 39.8 GPa.

Phase	Structure class	Phase (proto)type	Person symbol	Space group	Ref.
(Li) hp2	hcp	Hg	hR3 (or hR1)	$R\bar{3}m$ (166)	[34]
a (Å)	b (Å)	c (Å)	α (°)	ß (°)	γ (°)
2.402 (3)	2.402 (3)	5.515 (9)	90	90	120
Site	x	y	z	Occ.	Wyckoff
Li	0	0	0	1	3a

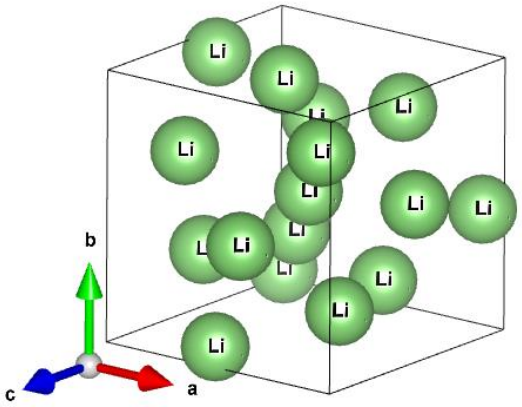

Figure 13 Crystal structure of (Li) hp3 at 180 K and 44.5 GPa. [35][31]

Table 7 Crystal structure information on (Li) hp3 at 180 K and 44.5 GPa.

Phase	Structure class	Phase (proto)type	Person symbol	Space group	Ref.
(Li) hp3	cubic	Na	cI16	$I\bar{4}3d$ (220)	[35]
a (Å)	b (Å)	c (Å)	α (°)	ß (°)	γ (°)
5.13 (8)	5.13 (8)	5.13 (8)	90	90	90
Site	x	y	z	Occ.	Wyckoff
Li	0.055	0.055	0.055	1	16c

2.2.3 Occurrence and production

The main feedstock for the Li-production is the brine from Chile, China and Argentina as most source. In 2017 were 65 % obtained by the lime soda evaporation process, which is the main production process of Li_2CO_3 (see Fig. 14). The rest of the Li-supply with approximately 35 %, originates from clays and ores like petalite $LiAlSi_4O_{10}$, zinnwaldite $KLiFeAl(AlSi_3)O_{10}(OH,F)_2$, amblygonite $(Li,Na)Al[(F,OH)PO_4]$, lepidolite $KLi_2Al(Al,Si)_3O_{10}(F,OH)_2$ and the most important Li ore α-spodumene $LiAlSi_2O_6$. However, more energy intensive steps are necessary to recover Li from ore compared to the lime soda evaporation process. [25][26][36]

In the lime soda evaporation process are shallow ponds filled with brine for water evaporation through sun irradiation for about 1 to 2 years. This leads to precipitation of $NaCl_{(s)}$ at the beginning, followed by $KCl_{(s)}$ and $NaCl{\bullet}KCl_{(s)}$ and at last of Mg- and other alkali salts. Each salt precipitates in a certain pond similar to NaCl winning from sea water. Next will the solved B^{III}-species be removed by solvent extraction from the to 6 % concentrated Li solution, leading to in $B(OH)_3$ as

byproduct. The precipitation of Mg^{2+} via lime milk $Ca(OH)_{2(aq)}$ as $Mg(OH)_{2(s)}$ is the next step. The resulting byproduct $CaCl_{2(aq)}$ gets precipitated by addition of $Li_2CO_{3(s)}$ or soda $Na_2CO_{3(s)}$. The produced $CaCO_{3(s)}$ will be calcined and hydrated to get lime milk needed for the Mg removal step. If necessary, can residually traces of impurities be removed by ion-exchange chromatography. Eventually will a evaporation step be applied followed by precipitation through addition of soda and the filtration of $Li_2CO_{3(s)}$. [25][26]

The feedstock for the production of metallic Li is LiCl, which can be synthesized in the reaction of Li_2CO_3 with $HCl_{(aq.)}$. Fused-salt electrolysis of a mixture of 45 to 55 % LiCl and 55 to 45 % KCl at 400 to 460 °C under Ar atmosphere leads to metallic Li. The salt mixture reduces the melting point (eutectic point at 352 °C with 44.3 % LiCl and 55.7 % KCl). As reactor is a Downs-cell in use with a steel cathode and a graphite anode at a cell voltage of 6.0 to 6.8 V and a current of 41 kA. [37][36]

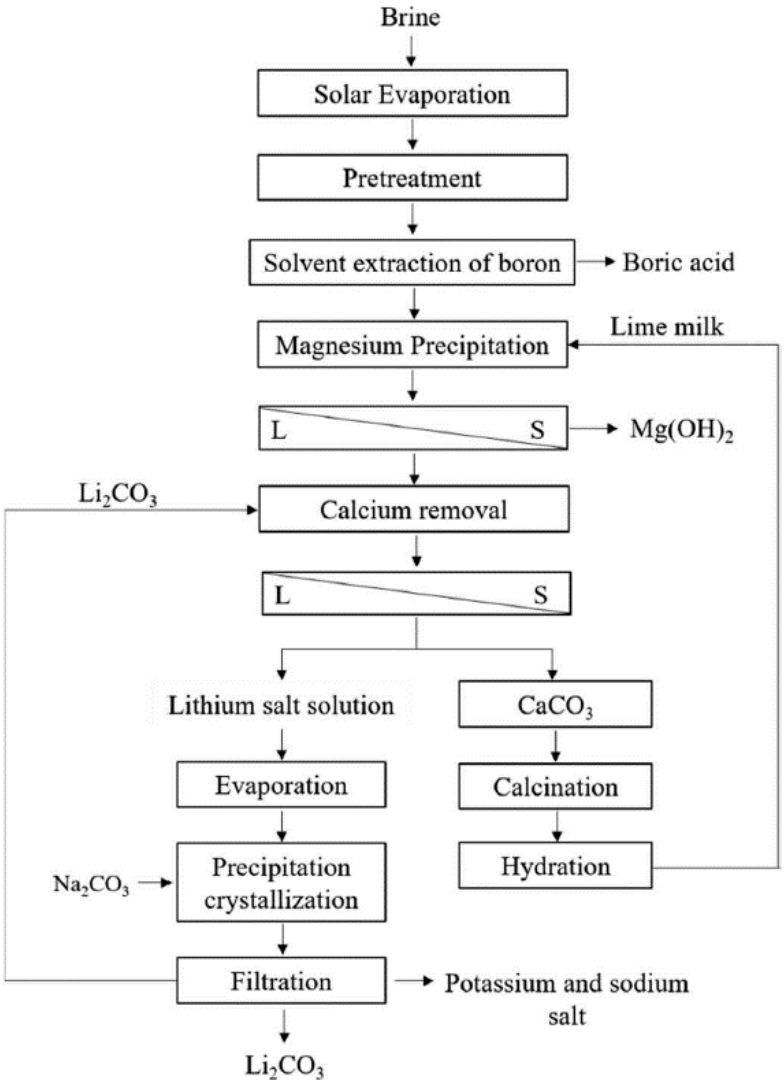

Figure 14 Flow chart of the industrial production of Li_2CO_3 from brine. [26]

2.2.4 Application

Nowadays more than half of the Li-based products goes into the LIB production. In 2017 reached this part already 59 % and the demand is still growing. Other consumers are the glass and ceramic industry and the production of lubricating grease as well as the metallurgical industry, especially the primary Al-production where Li_2CO_3 is used to improve the fused-salt electrolysis. Al-Li alloys are also of interest for the aviation industry. Other areas of application are the fine chemical and pharmaceutical industry and the nuclear industry. In 2017 was Li_2CO_3 with 60 %, followed by LiOH with 23 % the most important Li product. Metallic Li had only a share of 5 % on the market, while the rest was n-butyllithium, LiCl and other derivatives. [26][25]

2.3 The binary system In-Li

One can find in the current literature 5 different binary phase diagram versions of the system In-Li. However, lots of phase boundaries (marked with dashed lines) are not confirmed entirely yet and there are distinctive differences between these versions.

Zintl et al. [38] were the first who investigated the In-Li system in 1933. They searched for the occurrence of NaTl-type (and β-brass-type) compounds at 50 at.% Li via XRD measurements in Debye-Scherrer geometry and discovered the NaTl-type, non-stoichiometric compound InLi (see Fig. 15, Table 8). Kuriyama[39] did grow large InLi single crystals by the Bridgman method and characterized them through powder XRD in Debye-Scherrer geometry and single crystal X-ray diffraction SCXRD with X-ray back reflection and Polaroid Laue camera.

According to Huang et al. [40] can the composition of the non-stoichiometric compound vary (see Fig. 16), mainly by the formation of vacancies on Li-sites v_{Li} in the In-rich range (< 50 at.% Li) and Li-antisites Li_{In} in the Li-rich range (> 50 at.% Li). They came to these results via the lattice parameters determined by powder XRD in Debye-Scherrer geometry and density measurements by weighing in CCl_4 as well as in air at 26 °C. The mechanical behavior of polycrystalline InLi in respect to temperature and composition was also investigated by compression testing and microhardness testing according to Vickers.

InLi is the most stable phase in the In-Li system in terms of its melting point of ~630 °C and is quite brittle. The reason for these properties is the NaTl-structure, which belongs to the Zintl-phases which typically show an ionic character. In the host fcc-sublattice of In all octahedral sites and 4 tetrahedral sites are occupied by Li, where the other 4 tetrahedral sites are occupied by In. Each In-atom is surrounded by 4 other In-atoms forming a In_4^--polyanion. Li-atoms in the tetrahedral sites are coordinated by 4 In-atoms, those in the octahedral sites in turn are surrounded by 6 in-atoms. One can also describe the structure with a diamond-like sublattice of each element, where every atom has 8 nearest neighbor atoms. [41]

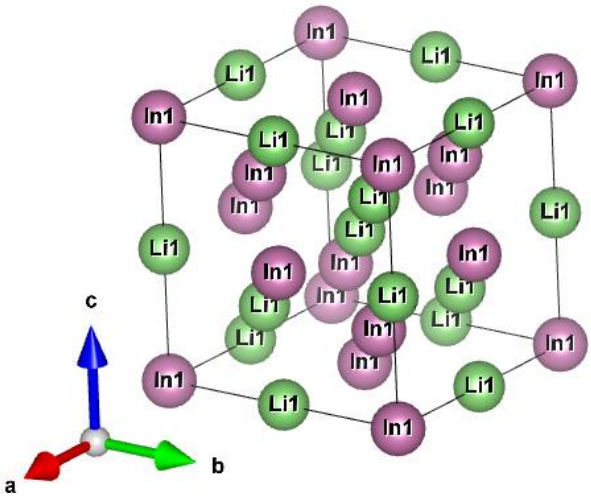

Figure 15 Non-standardized crystal structure of InLi. [38]

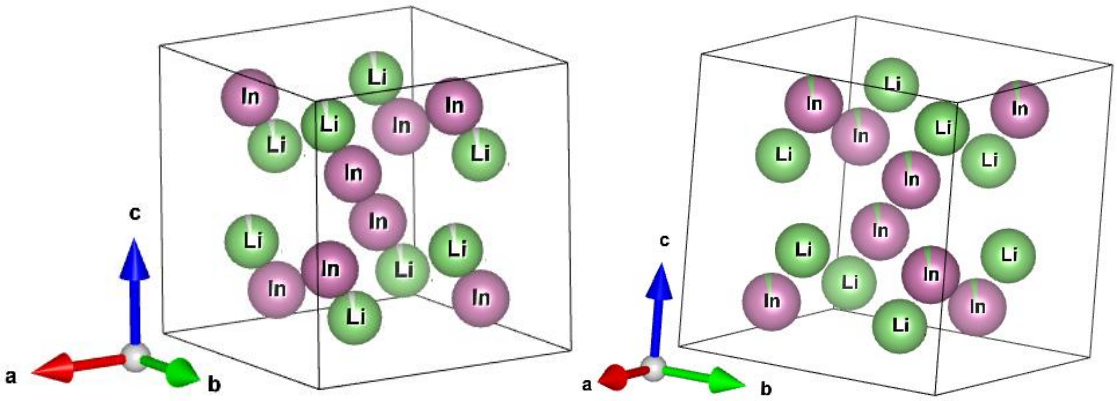

Figure 16 Non-stoichiometric compound InLi with standardized crystal structure. Described as $InLi_{0.97}$ at 300 K (left) and described as $InLi_{1.03}$ at 300 K (right). [39][42][43][44][45]

Table 8 Crystal structure information on InLi.

Phase	Structure class	Phase (proto)type	Person symbol	Space group	Ref.
InLi	cubic	Zintl#NaTl	cF16	*Fd$\bar{3}$m* (227)	[46]
a (Å)	b (Å)	c (Å)	α (°)	ß (°)	γ (°)
6.799 (0)	6.799 (0)	6.799 (0)	90	90	90
Site	x	y	z	Occ.	Wyckoff
In	3/8	3/8	3/8	1	8b
Li	1/8	1/8	1/8	1	8a

Grube et al. [47], determined for the first time in 1935 the liquidus line of the system as well as the congruent melting temperature of InLi at 625 °C through thermal analysis. They also postulated a solubility of ~10 at.% Li in (In). In addition the In-Li system was investigated by Klemm et al. [48] and Lamprecht et al. [49] as well.

Eventually was the first phase diagram published in 1970 by Thümmel et al. [50] (see Fig. 17). Experimental data were used for its construction, mostly from thermal analysis but also from pycnometry and Debye-Scherrer XRD measurements. They postulated the existence of 8 intermetallic compounds. InLi, In_2Li_3, In_2Li_9, $InLi_9$, $InLi_{20}$, $InLi_3$, $InLi_4$ and In_4Li_9.

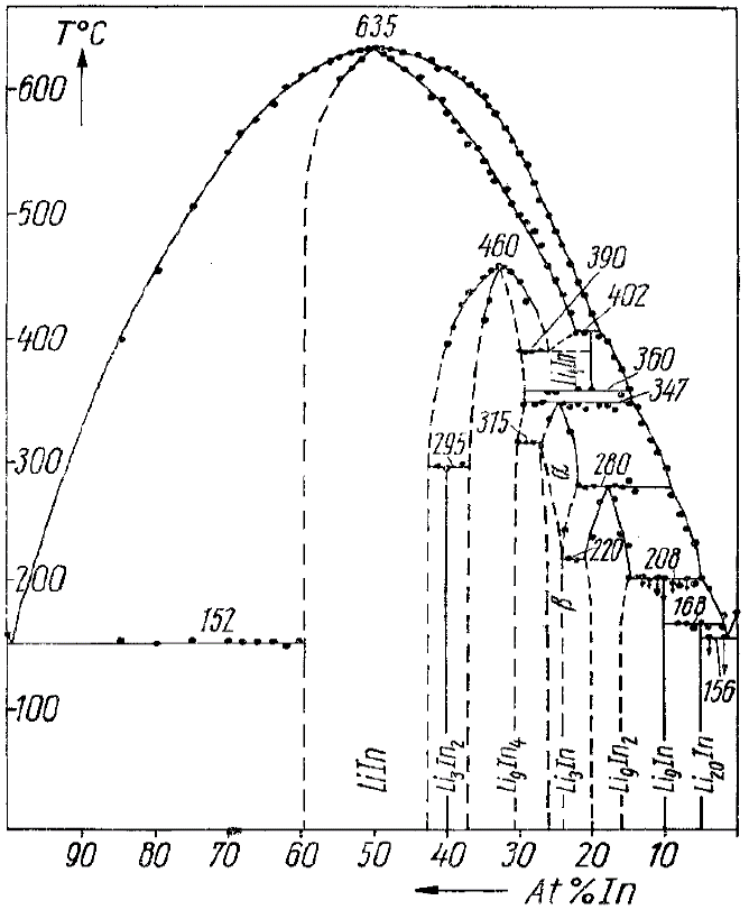

Figure 17 In-Li phase diagram of Thümmel et al. [50]

Alexander et al. [51] published in 1975 a phase diagram based on the information of the liquidus data of Grube et al. [47] and their own results from thermal analysis and Debye-Scherrer XRD measurements. It was also tried to do metallographic examination, but the high reactivity of the samples on humid air inhibited the polishing process. They postulated 12 intermetallic compounds. InLi, In_4Li_7, $InLi_2$, In_3Li_8, $In_{27}Li_{73}$ and $InLi_3$ all stable at room temperature and In_2Li_5, In_4Li_{11}, $InLi_4$, $InLi_6$ and $InLi_{12}$ as well as $In_{28}Li_{72}$, which are only stable at elevated temperatures. However, the assumed phases In_4Li_{11} and $In_{28}Li_{72}$ on the complex Li-rich side at higher temperatures of the phase diagram could not be verified. (In) was described as solid solution with maximum of 1.5 at.% Li. However, this result is only estimated based on XRD measurements showing the presence of InLi in samples with > 1.7 at.% Li and on the assumption of a linear relation between the atomic volume of (Li) and (In). Graham et al. [21] proposed a maximum solubility of ~14 at.% Li in (In) based on XRD measurements in Debye-Scherrer geometry. This solubility was described through a substitutional solid solution, where Li-

atoms partially occupy an In-site Li_{In} (see Fig. 18,). Thus, the discrepancy to the description of Graham et al. [21] was explained by the high background of the XRD results overlapping InLi reflections.

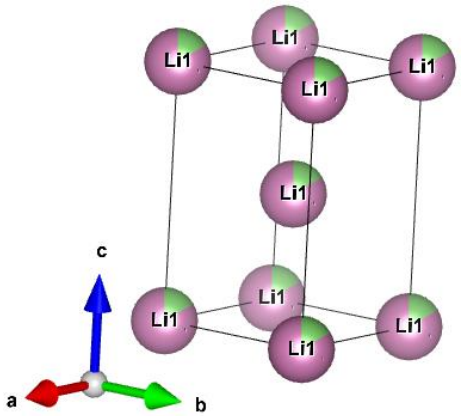

Figure 18 Substitutional solid solution $In_{1.7}Li_{0.3}$. The green part symbolizes the Li fraction at In1 sites (cf. Fig. 5). [21]

The liquidus line of Grube et al. [47] was also verified and extended (see Fig. 19).

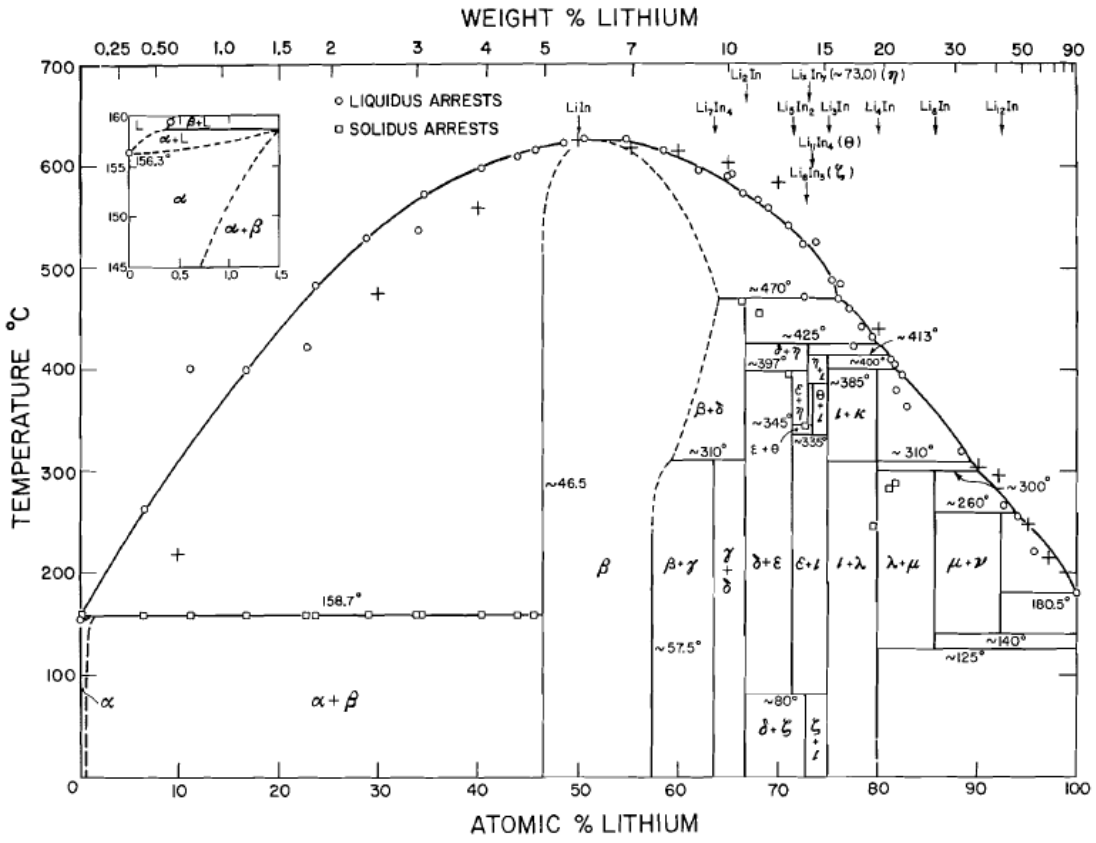

Figure 19 In-Li phase diagram of Alexander et al. [51]

The first assessment of the In-Li system in 1991 from Sangster et al. [52] resulted in a third phase diagram. They used the thermal analysis data from Grube et al. [47], Lamprecht et al. [49], Thümmel et al. [50] and Alexander et al. [51] to construct the liquidus line. The solubility of 1.5 at.% Li in (In) was based on data of Alexander et al. [51] and Graham et al. [21] The solubility of In in (Li) is described as very small. 7 intermetallic compounds are postulated: InLi, In_4Li_5, In_2Li_3, $InLi_2$, In_3Li_{13}, $InLi_3$ and $InLi_7$. Whereas only InLi, In_4Li_5, In_2Li_3, $InLi_2$ and In_3Li_{13} are experimentally verified via SCXRD in 2-circle geometry by Stöhr et al. [53][54][55] and Kuriyama[39], but also via XRD in Debye-Scherrer geometry by Alexander et al. [51]

Stöhr et al. [53][54] were the first who described the crystal structures of $InLi_2$, In_3Li_{13} and In_2Li_3,by SCXRD in the years 1978/79 (see Fig. 20, 21 and 22 as well as Table 9, 10 and 11). The line compound In_4Li_5 was crystallographic determined by Stöhr et al. [55] (see Fig. 23 and Table 12), but others could not reproduce this crystallographic result to confirm the existents of In_4Li_5.

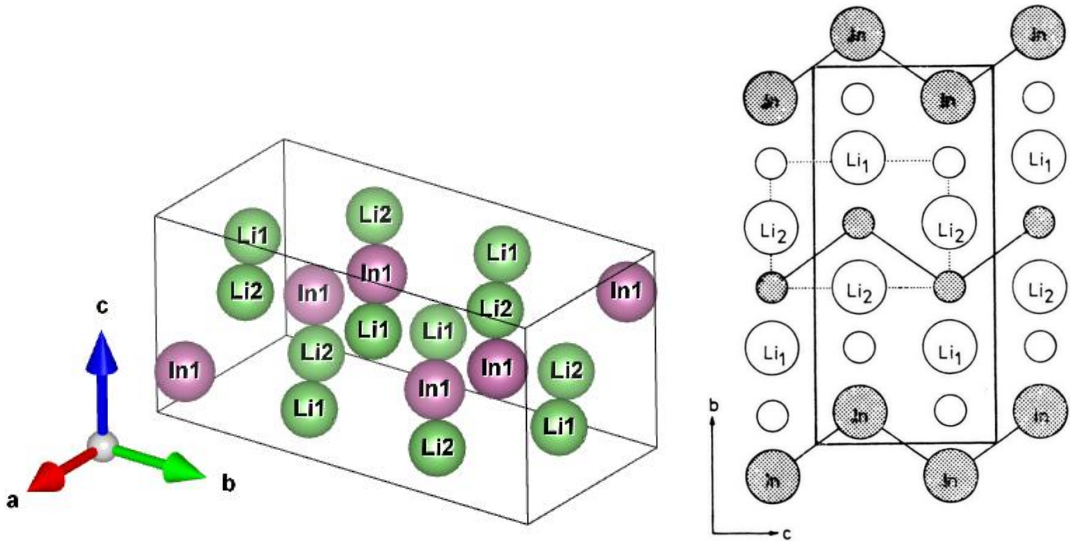

Figure 20 Crystal structure of $InLi_2$. Left: in 3D. Right: in 2D.[56][54]

Table 9 Crystal structure information on $InLi_2$.

Phase	Structure class	Phase (proto)type	Person symbol	Space group	Ref.
$InLi_2$	orthorombic	$GaLi_2$	oS12	*Cmcm* (63)	[56]
a (Å)	b (Å)	c (Å)	α (°)	ß (°)	γ (°)
4.763 (0)	10.017 (0)	4.735 (0)	90	90	90
Site	x	y	z	Occ.	Wyckoff
In1	0	0.0763	1/4	1	4c
Li1	0	0.412	1/4	1	4c
Li2	0	0.757	1/4	1	4c

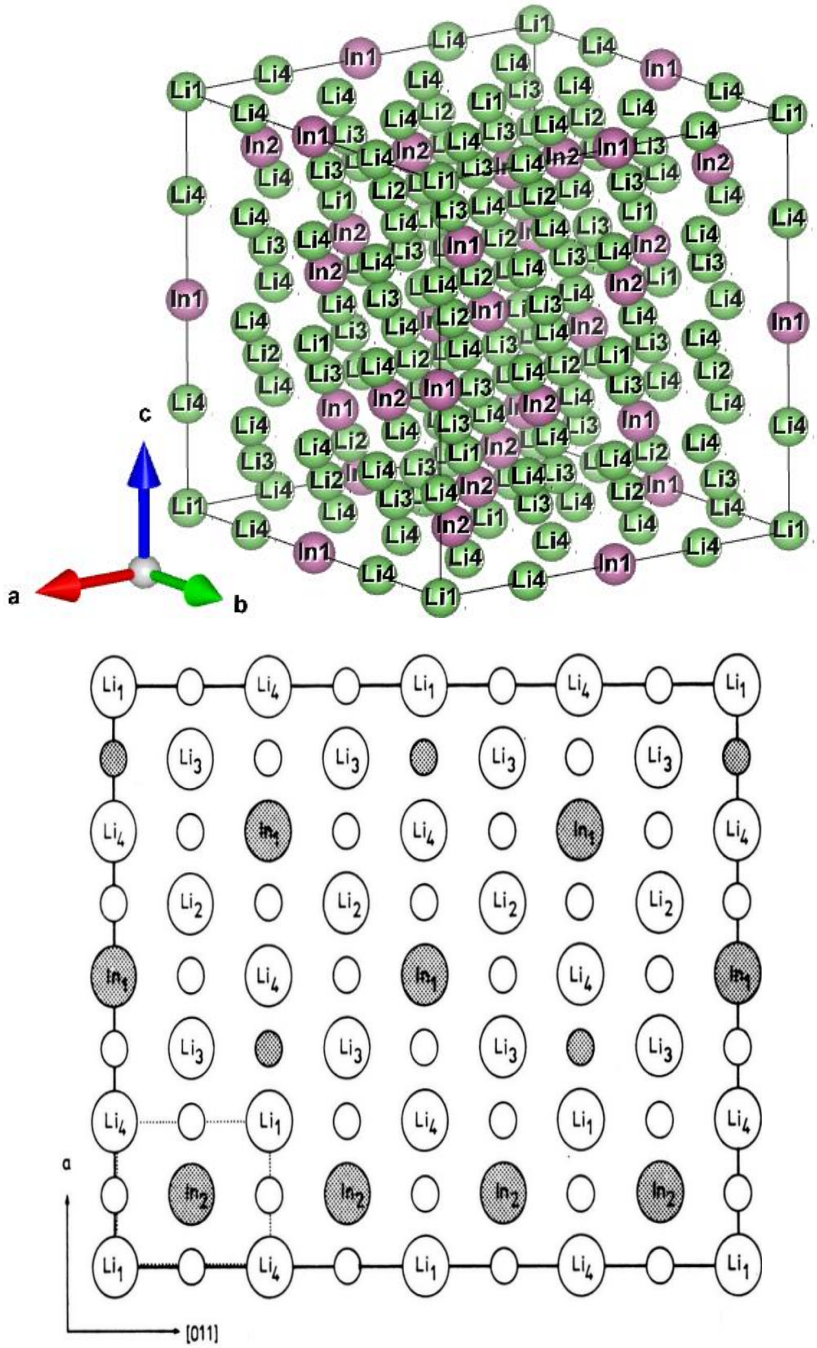

Figure 21 Crystal structure of In_3Li_{13} in 3D (top) and in 2D (bottom).[46][54]

Table 10 Crystal structure information on In_3Li_{13}.

Phase	Structure class	Phase (proto)type	Person symbol	Space group	Ref.
In_3Li_{13}	cubic	In_3Li_{13}	cF128	$Fd\bar{3}m$ (227)	[54]
a (Å)	b (Å)	c (Å)	α (°)	ß (°)	γ (°)
13.556 (0)	13.556 (0)	13.556 (0)	90	90	90
Site	x	y	z	Occ.	Wyckoff
Li1	0	0	0	1	8a
In1	1/2	1/2	1/2	1	8b
In2	1/2	1/8	1/8	1/8	16c
Li2	0.625	0.625	0.625	1	16d
Li3	0.365	0.365	0.365	1	32e
In4	1/4	0	0	1	48f

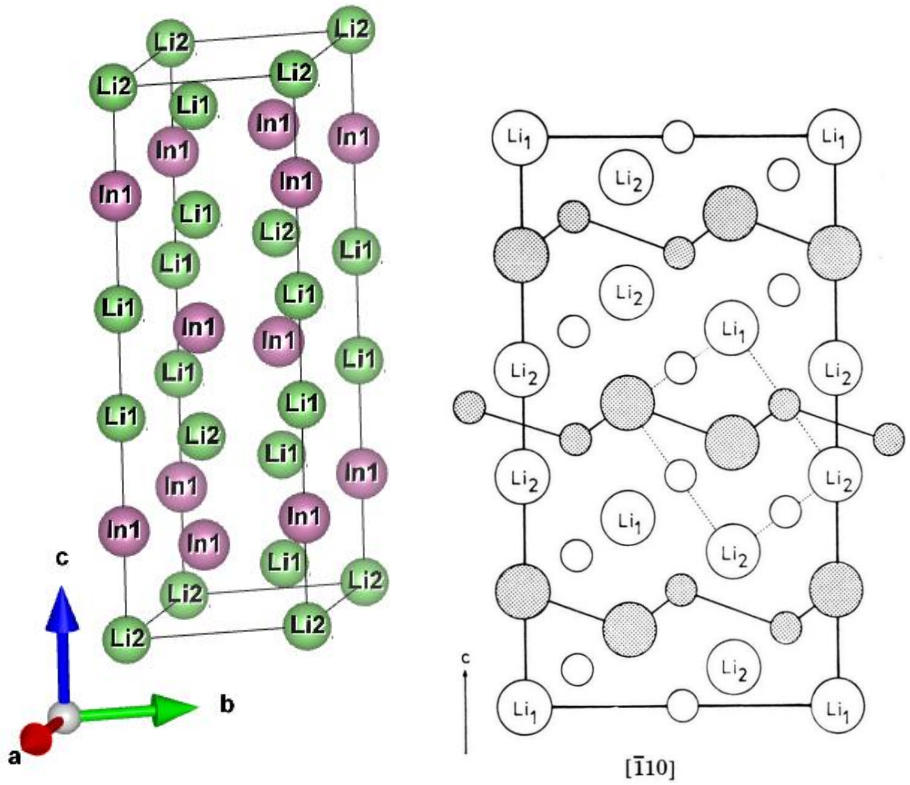

Figure 22 Crystal structure of In_2Li_3 in 3D (left) and in 2D (right).[57][53]

Table 11 Standardized crystal structure information on In_2Li_3.

Phase	Structure class	Phase (proto)type	Person symbol	Space group	Ref.
In_2Li_3	hexago-nal	Al_2Li_3	hR15	$R\bar{3}m$ (166)	[53]
a (Å)	b (Å)	c (Å)	α (°)	ß (°)	γ (°)
4.74 (8)	4.74 (8)	14.7 (4)	90	90	120
Site	x	y	z	Occ.	Wyckoff
In1	0	0	0.2054	1	6c
Li1	0	0	0.3990	1	6c
Li2	0	0	0	1	3a

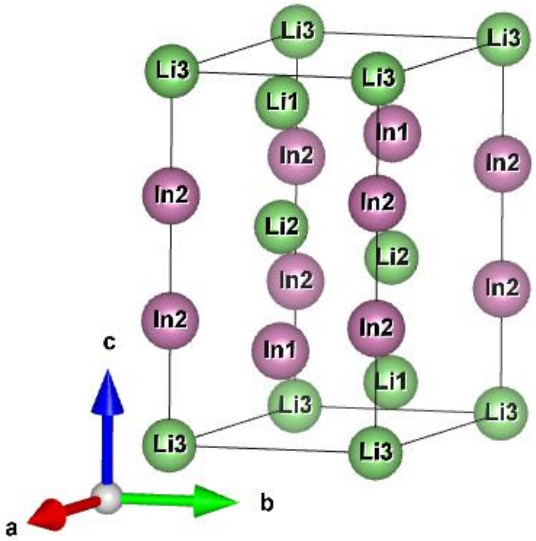

Figure 23 Crystal structure of In_4Li_5. [58][55]

Table 12 Standardized crystal structure information on In_4Li_5.

Phase	Structure class	Phase (proto)type	Person symbol	Space group	Ref.
In_4Li_5	hexago-nal	Ga_4Li_5	hP9	$P\bar{3}m1$ (164)	[58]
a (Å)	b (Å)	c (Å)	α (°)	ß (°)	γ (°)
4.7 (8)	4.7 (8)	8.8 (8)	90	90	120
Site	x	y	z	Occ.	Wyckoff
Li1	1/3	2/3	0.112	1	2d
Li2	1/3	2/3	0.445	1	2d
Li3	0	0	0	1	1a
In1	1/3	2/3	0.7765	1	2d
In2	0	0	0.3329	1	2c

The earlier postulated phase In_4Li_7 was described as In_2Li_3, In_4Li_9 as $InLi_2$ and $InLi_4$ or In_2Li_9 respectively corresponds actually to In_3Li_{13}, but the possible existence of a high temperature modification of In_3Li_{13} similar to $InLi_4$ could not be excluded.

Thermodynamic data was also assessed. Hence, the enthalpy of formation for InLi at a temperature of 527 °C with Δ_fH = -24.5 kJ/mol of atoms was gained through solution calorimetry by Sommer et al. [59]

The enthalpy of fusion of InLi at 630 °C obtained via differential scanning calorimetry DSC by Bushmanov et al. [60] and via drop calorimetry measured by Schneider et al. [61] with values of $\Delta_{fus}H$ = 13.5 and 12.8 kJ/mol of atoms was used for the phase diagram as well as the standard free enthalpy of formation for InLi with Δ_fG^0 = -24.0 kJ/mol of atoms and for $InLi_2$ with Δ_fG^0 = -34.1 kJ/mol of atoms. Latter two were calculated via the free enthalpies of formation of $Li_{(l)}$ and of $In_{(l)}$ at 415 °C determined coulometric titration by Wen et al. [62]

The excess free enthalpy of the liquid In-Li mixture ΔG_E(L) determined by electromotive force measurement EMF at 120 to 150 °C above the liquidus line was measured by Yatsenko et al. [63] and for diluted solutions of Li in In at 510 to 560 °C by Morachevskii et al. [64], were also taken into account. In addition, the extreme value of the Knight shift of ^{7}Li obtained by NMR and a maximum of the electrical resistivity at ~75 to 100 at.% Li investigated by Marel et al. [65], were included in the assessment. These results indicated the formation of an $InLi_3$ associate in the liquid phase, while the molar excess enthalpy of Li in the liquid, measured by calorimetry at 650 °C from Bushmanov et al. [60] and at 712 °C from Predel et al. [66] showed a minimum at ~60 at.% (In_2Li_3) with Li $\Delta_{mix}H_m$(L) ≈ -21 kJ/mol. This would in any case describe some kind of order in the liquid (see also Morachevskii et al. [64][65]). The pressure induced phase transformation InLi → InLi hp at 2.1 x 10^9 Pa and 800 K (see Fig. 24 and Table 13) calculated via local density approximations of the total energy by Christensen [67] was also taken into consideration (see Fig. 25).

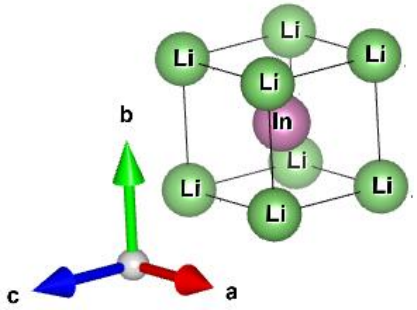

Figure 24 Crystal structure of InLi at 15 GPa.[68][69]

Table 13 Crystal structure information on InLi at 15 GPa.

Phase	Structure class	Phase (proto)type	Person symbol	Space group	Ref.
InLi hp (15 Gpa)	cubic	CsCl	cP2	$Pm\bar{3}m$ (221)	[68]
a (Å)	b (Å)	c (Å)	α (°)	ß (°)	γ (°)
3.1 (3)	3.1 (3)	3.1 (3)	90	90	90
Site	x	y	z	Occ.	Wyckoff
In	1/2	1/2	1/2	1	1
Li	0	0	0	1	1

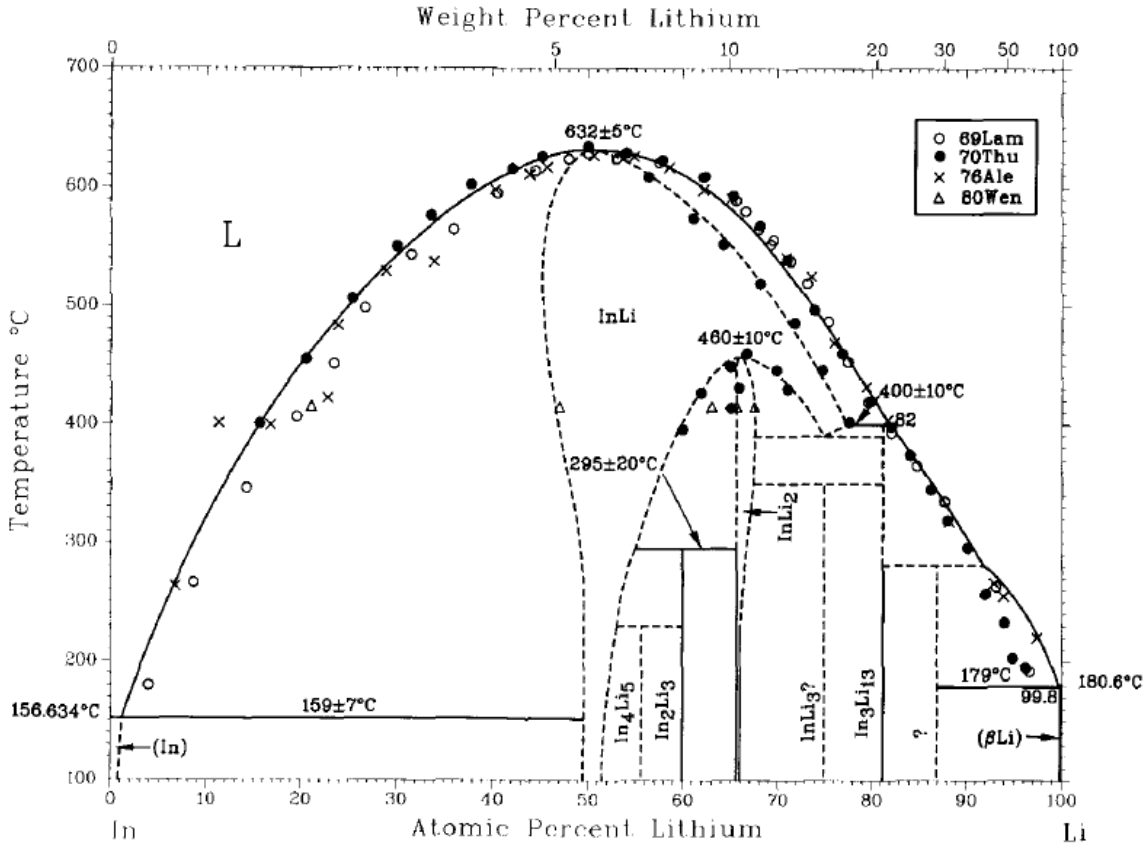

Figure 25 In-Li phase diagram of Sangster et al. [52]

Zhou et al. [70] modeled a phase diagram in 2020 (see Fig. 26) and hence, an assessment of experimental and simulated data from own work and literature was accomplished. The data from Sangster et al. [52] mentioned before were supplemented by thermodynamic data like the diffusion coefficient D of Li in InLi, measured via EMF by Wen et al. [62][63] and the electromotive force, the activity of Li and In as well as the partial enthalpy of Li for liquid and solid solutions from EMF measurements done by Gasior et al. [71]. In addition, the integral molar mixing enthalpy of the liquid phase, $\Delta_{mix}H_m$, at 380, 667, 671 and 803 °C investigated by calorimetric studies from Debski et al. [72] and the entropy of fusion of InLi at 630 °C $\Delta_{fus}S$, determined via drop calorimetry by Schneider et al. [61], were utilized. The temperature for the peritectic reaction L + InLi → (In) was measured by DSC and the enthalpy of formation, Δ_fH, for stable phases at 0 K was calculated via first-principles methods e.g. density functional theory DFT calculations, implemented in the Vienna ab initio simulation package. The results were compared with the first principal data from the literature.[73]

The In-Li system was modeled Via Thermo-Calc software by iterative optimization of parameters describing the Gibbs energies of the phases. In addition, XRD measurements as well as metallographic investigation of a polished sample in the 2-phase region (In) + InLi via scanning electron microscopy SEM and quantitative elemental analysis by EPMA were included in the results. The latter method could only be used to measure the In content due to the low number of electrons of Li. Zhou et al. [70] postulated the existents of 5 intermetallic compounds: InLi, $InLi_2$, In_2Li_3, $InLi_3$ and In_3Li_{13}.

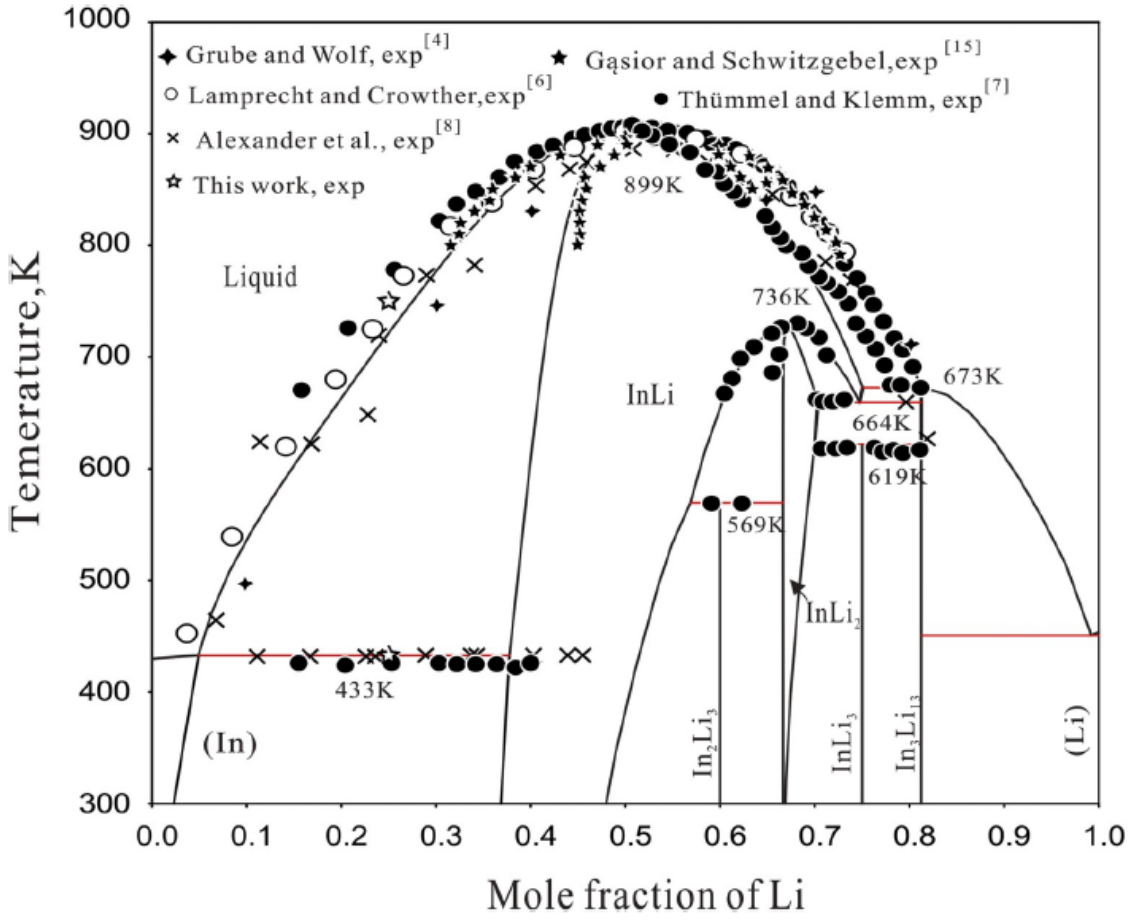

Figure 26 In-Li phase diagram of Zhou et al. [70]

The latest version of an In-Li phase diagram was published by Gierlotka et al. [74] in 2022 (see Fig. 27). They also modeled it via the CALPHAD approach using the Thermo-Calc software. It was based on the same data which Sangster et al. [52] already used, with additional experimental data of their own group (see Debski et al. [103]). They described the existents of 5 stable intermetallic line compounds at room temperature: InLi, In_2Li_3, $InLi_2$, In_3Li_{13} and $InLi_6$. However, $InLi_6$ was not verified yet by crystal structure investigation. It is also the only compound used to model the phase diagram which is not stable at 0 K according to the ab initio calculation listed in the Materials Project database [73].

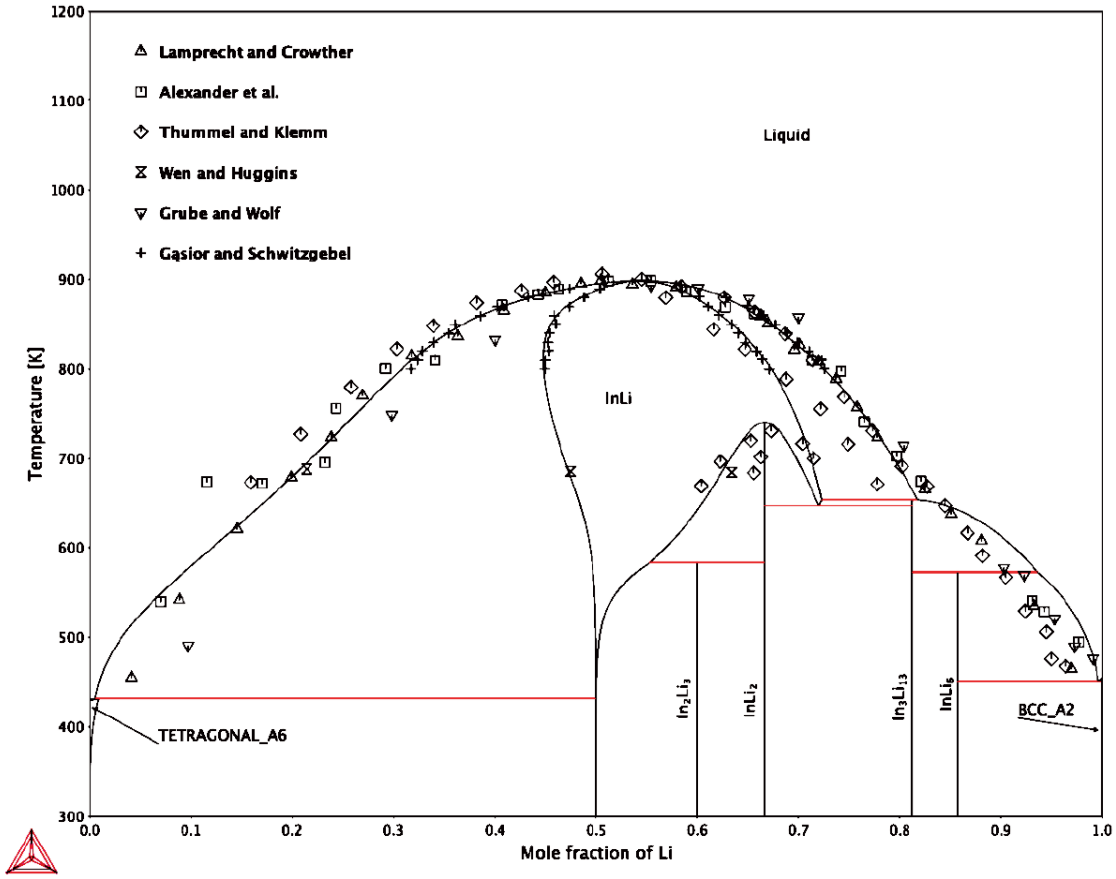

Figure 27 In-Li phase diagram of Gierlotka et al. [74]

It is noteworthy that some phases described in literature were not taken into account in any of the published phase diagrams like the intermetallic compounds $In_{4+x}Li_{11-x}$ (x=1.05), $In_{2+x}Li_{10-x}$ (x=1.59) and $In_{8+x}Li_{22-x}$ (x=0.1), which were experimentally discovered by Chumak et al. [75] (see Fig. , 28, 29, 30, 31, 32, 33 34 and 35 as well as Table 14, 15,16, 17 and 18).

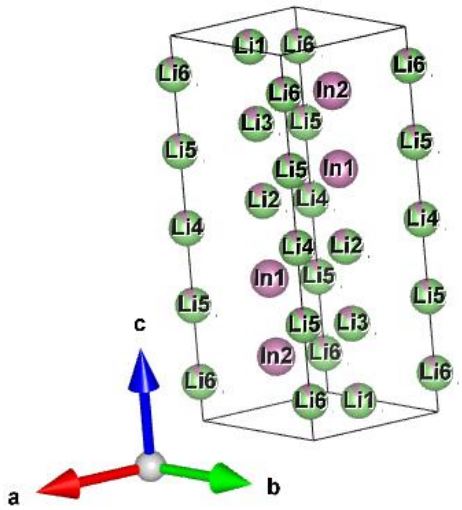

Figure 28 Crystal structure of $In_{4+x}Li_{11-x}$ (x=1.05) (=$In_{5.05}Li_{9.95}$). [75]

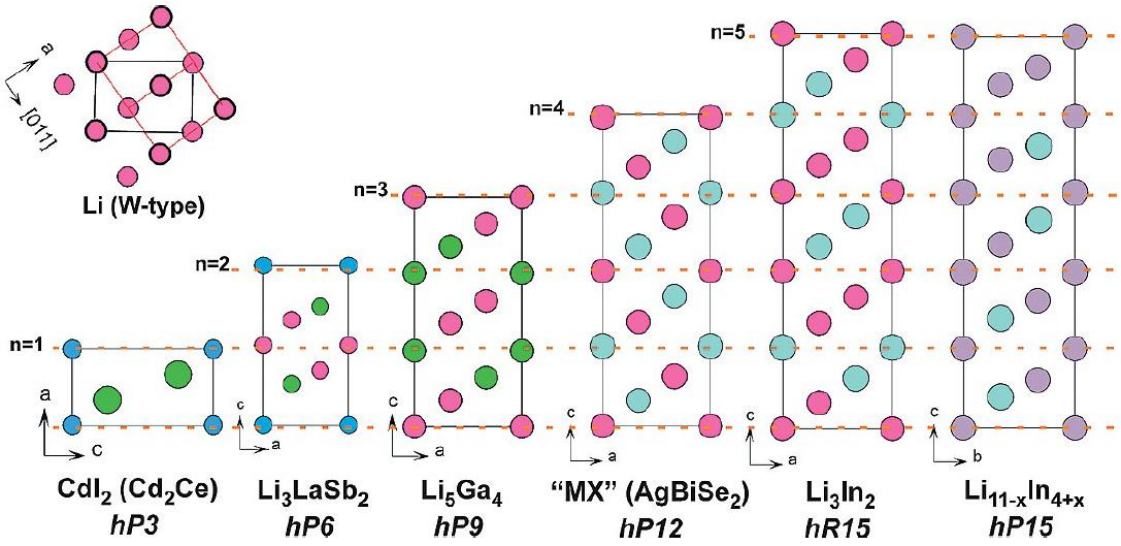

Figure 29 Structural relationship between the phases Li, CdI_2, Li_3LaSb_2, Li_5Ga_4, $AgBiSe_2$ and In_2Li_3 to $In_{4+x}Li_{11-x}$. [75]

Table 14 Crystal structure information on $In_{4+x}Li_{11-x}$ (x=1.05) (=$In_{5.05}Li_{9.95}$).

Phase	Structure class	Phase (proto)type	Person symbol	Space group	Ref.
$In_{4+x}Li_{11-x}$ (x=1.05)	trigonal	$(Li_{0.90}In_{0.10})_{11}In_4$ related to CdI_2	hP15	$P\bar{3}m1$ (164)	[75]
a (Å)	b (Å)	c (Å)	α (°)	ß (°)	γ (°)
4.74 (8)	4.74 (8)	14.28 (3)	90	90	120
Site	x	y	z	Occ.	Wyckoff
In2	1/3	2/3	0.84103(6)	1	2d
In1	1/3	2/3	0.63849(6)	1	2d
Li1	1/3	2/3	0.0365(6)	0.90	2d
In3	1/3	2/3	0.0365(6)	0.10	2d
Li2	1/3	2/3	0.4368(6)	0.889	2d
In4	1/3	2/3	0.4368(6)	0.111	2d
Li3	1/3	2/3	0.7629(6)	0.887	2d
In5	1/3	2/3	0.7629(6)	0.113	2d
Li4	0	0	0.5	0.917	1b
In6	0	0	0.5	0.083	1b
Li5	0	0	0.7001(9)	0.93	2c
In7	0	0	0.7001(9)	0.07	2c
Li6	0	0	0.8990(8)	0.912	2c
In8	0	0	0.8990(8)	0.088	2c

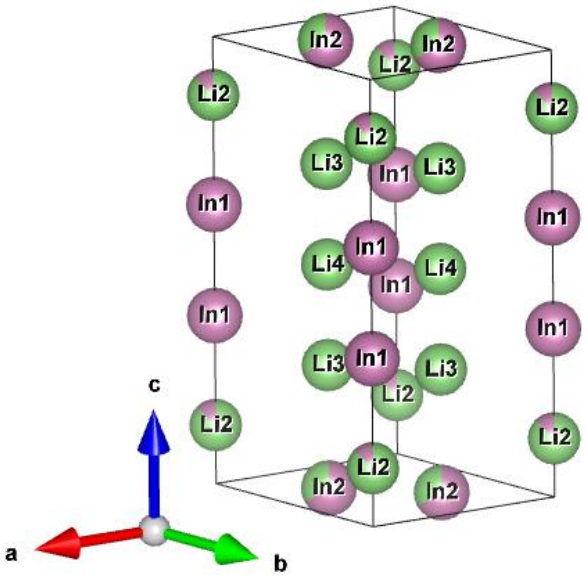

Figure 30 Crystal structure of $In_{2+x}Li_{10-x}$, (x=1.59) (=$In_{1.80}$ $Li_{4.20}$).[75]

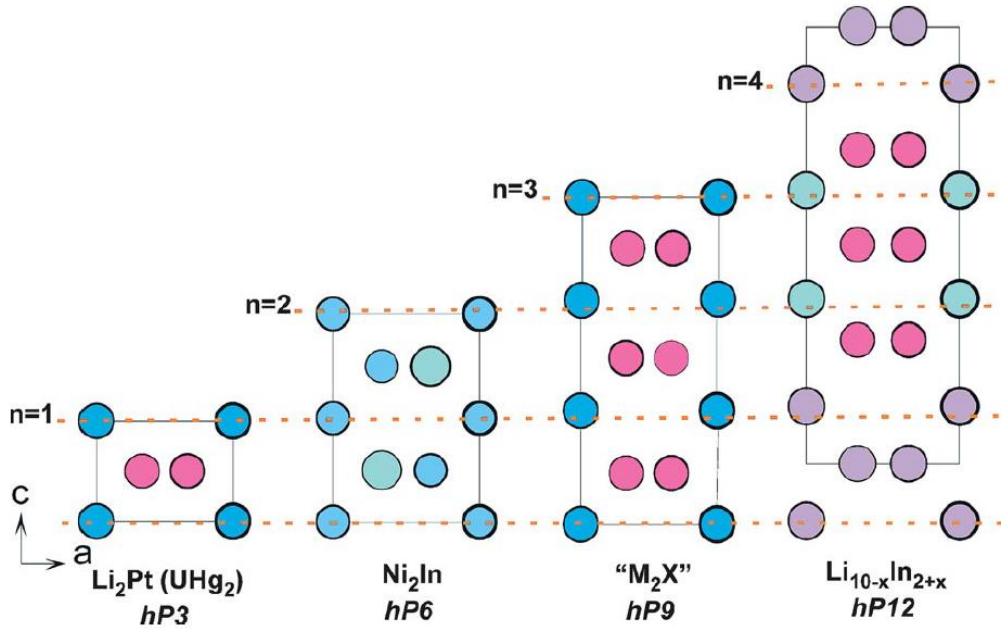

Figure 31 Structural relationship between the phases Li_2Pt, Ni_2In and "M_2X" to $In_{2+x}Li_{10-x}$. [75]

Table 15 Crystal structure information on $In_{2+x}Li_{10-x}$ (x=1.59) (=$In_{1.80}Li_{4.20}$).

Phase	Structure class	Phase (proto)type	Person symbol	Space group	Ref.
$In_{2+x}Li_{10-x}$ (x=1.59)	hexago-nal	$Li_3(Li_{0.60}In_{0.40})_2In$ re-lated to Li_2Pt	hP12	*P6/mmm* (191)	[75]
a (Å)	b (Å)	c (Å)	α (°)	ß (°)	γ (°)
4.697 (5)	4.697 (5)	11.52 (6)	90	90	120
Site	x	y	z	Occ.	Wyckoff
Li3	1/3	2/3	0.275(4)	1	4h
In1	0	0	0.3758(2)	1	2e
Li2	0	0	0.1310(12)	0.881	2e
In3	0	0	0.1310(12)	0.119	2e
Li1	1/3	2/3	0	0.326	2c
In2	1/3	2/3	0	0.674	2c
Li4	1/3	2/3	1/2	1	2d

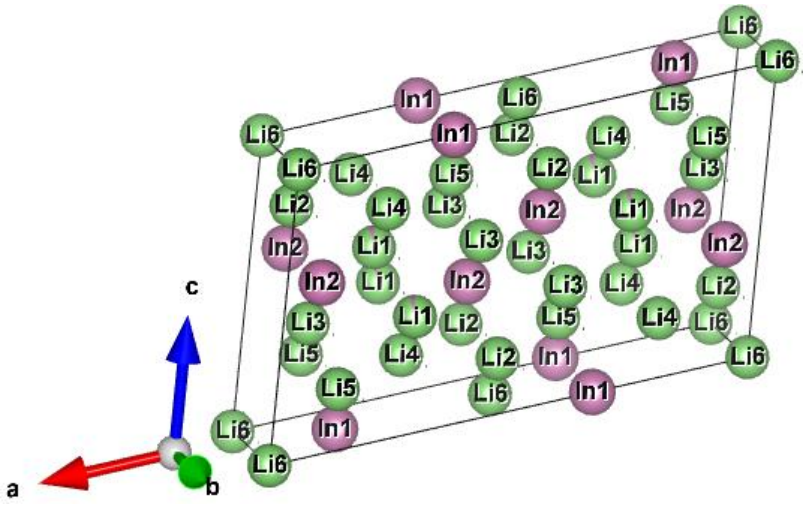

Figure 32 Crystal structure of $In_{8+x}Li_{22-x}$, (x=0.1) (=$In_{4.05}$ $Li_{10.95}$). [75]

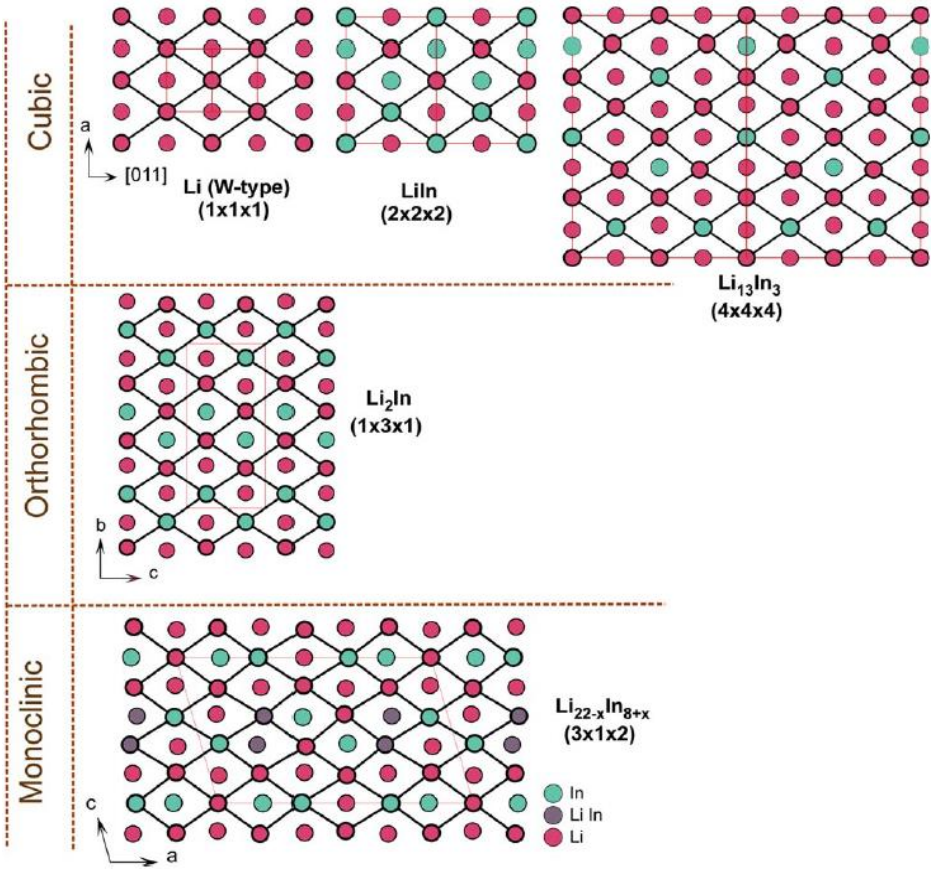

Figure 33 Structural relationship between the phases Li, InLi, In_3Li_{13} and $InLi_2$ to $In_{8+x}Li_{22-x}$. [75]

Table 16 Crystal structure information on $In_{8+x}Li_{22-x}$ (x=0.1) (=$In_{4.05}Li_{10.95}$).

Phase	Structure class	Phase (proto)type	Person symbol	Space group	Ref.
$In_{8+x}Li_{22-x}$ (x=0.1)	mono-clinic	$Li_9(Li_{0.975}In_{0.025})_2In_4$ related to W	mS30	*C2/m* (12)	[75]
a (Å)	b (Å)	c (Å)	α (°)	ß (°)	γ (°)
14.15 (6)	4.72 (9)	8.61 (7)	90	105.8(9)	90
Site	x	y	z	Occ.	Wyckoff
In1	0.32442	0	0.00126	1	4i
In2	0.07316	0	0.4083	1	4i
Li1	0.2796	0	0.5992	0.97	4i
In3	0.2796	0	0.5992	0.03	4i
Li4	0.1986	0	0.2047	1	4i
Li3	0.4052	0	0.3881	1	4i
Li2	0.5345	0	0.1917	1	4i
Li5	0.1298	0	0.7889	1	4i
Li6	0	0	0	1	2a

The low temperature and high-pressure phases InLi-lt, In_3Li-hp and InLi-hp were also not included into any In-Li phase diagram modeling. Ehrenberg et al. [45] discovered via cryo-powder XRD and cryo-powder neutron diffraction a phase transition of $In_{53}Li_{47}$, $In_{50}Li_{50}$, and $In_{47}Li_{53}$ into tetragonal InLi lt structure at ~170 K (see Fig. 34). Schwarz et al. [69] published in 1997 the partial decomposition of InLi into a phase mixture containing the cubic In_3Li-hp phase showing Cu_3Au-type structure. In_3Li-hp was identified via high pressure XRD at above 5.5(5) GPa or after compression to 15 GPa followed by fast decompression to 3.3 GPa. After annealing at 450 K for 6 h at a pressure above 11(1) GPa InLi started to transform into InLi-hp with CsCl-structure, detected by high pressure XRD.

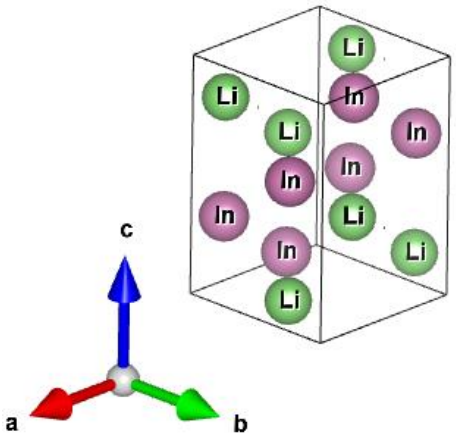

Figure 34 Crystal structure of InLi at 2 K. [76][45]

Table 17 Crystal structure information on InLi at 2 K.

Phase	Structure class	Phase (proto)type	Person sym-bol	Space group	Ref.
InLi lt (2 K)	tetragonal	InLi	tl8	$I4_1/amd$ (141)	[76]
a (Å)	b (Å)	c (Å)	α (°)	ß (°)	γ (°)
4.773 (7)	4.773 (7)	6.788 (4)	90	90	90
Site	x	y	z	Occ.	Wyckoff
In	0	1/4	3/8	1	4b
Li	0	3/4	1/8	1	4a

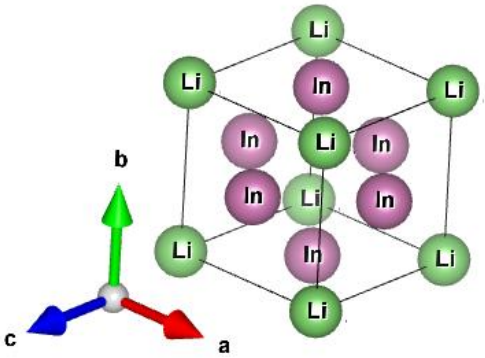

Figure 35 Crystal structure of In_3Li at 3.3 GPa. [77][69]

Table 18 Crystal structure information on In_3Li at 3.3 GPa.

Phase	Structure class	Phase (proto)type	Person symbol	Space group	Ref.
In_3Li hp (3.3 GPa)	cubic	Cu_3Au	cP4	*Pm*$\bar{3}$*m* (221)	[77]
a (Å)	b (Å)	c (Å)	α (°)	ß (°)	γ (°)
4.40 (4)	4.40 (4)	4.40 (4)	90	90	90
Site	x	y	z	Occ.	Wyckoff
In	0	1/2	1/2	1	3
Li	0	0	0	1	1

Overall, the existence of 34 intermetallic compounds was postulated in literature, they are summarized in the Table 19. After merging phases that differed only in terms of stoichiometry, their number was reduced to 27.

Table 19 Postulated phases of the system In-Li from the literatures (see Thümmel et al. [50], Alexander et al. [51], Sangster et al. [52], Zhou et al. [70], Gierlotka et al. [74], Takemura et al. [22], Stöhr et al. [53] [54] [55], Graham et al. [21], Schwarz et al. [69], Ehrenberg et al. [45] and Chumak et al. [75]). x_{Li}…mole fraction of Li.

Phase	**Measured**[b]	**Identical phase**	**x_{Li} (at.%)**	**Ref.**
(In)-hp	yes	-	-	[22]
(In)	yes	-	0-(1) at 156 °C	[50][52][74]
			0-1.5 at 156 °C	[51][70]
			0-14 at 156 °C	[21]
In_3Li-hp(3.3 GPa)	yes	-	-	[69]
InLi	yes	-	49.5-51.5 at 156 °C	[52]
			50 at 156 °C	[74]
			40-57.1 at 156 °C	[50]
			46.5-57.5 at 156 °C	[51]
			49.2-50.7 at 27 °C	[45]
			37-48 at 27 °C	[70]
InLi hp (15 GPa)	yes	-	-	[69]
InLi lt (2 K)	yes		-	[45]
In_4Li_5	yes	-	55.6 at 156 °C	[52][55]
In_2Li_3	yes	-	60 at 156 °C	[52][70][74][53][50][55]
In_4Li_7	no	In_2Li_3	63.6 at 156 °C	[54][51]

[b] Crystal structure experimentally verified e.g. by SCXRD etc.

$In_{4+x}Li_{11-x}$ (x=1.05)	yes	-	~66.3	[75]
$InLi_2$	yes	-	65.5-66 at 156 °C	[52]
			67 at 156 °C	[74]
			62.9-69.1	[50]
			67-68 at 156 °C	[70]
			~66.8	[51]
			-	[55]
In_4Li_9	no	$InLi_2$	~69.2	[50]
$In_{2+x}Li_{10-x}$ (x=1.59)	yes	-	~70.1	[75]
In_2Li_5 ht	no	In_3Li_8	~71.8	[51]
In_3Li_8	no	-	~71.9	[51]
$In_{8+x}Li_{22-x}$ (x=0.1)	yes	-	~72.9	[75]
In_4Li_{11} ht	no	-	~73.4	[51]
$InLi_3$	no	-	75 at 156 °C	[52][70]
			73.9-75.9	[50]
			~75.8	[51]
$InLi_3$ ht	no	-	74-78 at 280 °C	[50]
$InLi_4$ rt	no	In_3Li_{13}	~80.7	[51]
$InLi_4$ ht	no	In_3Li_{13}	80 at 360 °C	[50]
			80.7 at 400 °C	[51]
In_3Li_{13}	yes	-	81.3 at 156 °C	[52][70][74]
			79.8-83.5 at 156 °C	[50]
			-	[55]
In_2Li_9	no	In_3L_{13}	~81.8	[52][54][50]
$InLi_6$ ht	no	-	~85.5	[51]
$InLi_6$	no	-	~85.5	[74]
$InLi_7$	no	$InLi_6$	~87.5	[52]
$InLi_9$	no	-	~90	[50]
$InLi_{12}$ ht	no	-	~92.6	[51]
$InLi_{20}$	no	-	~95.2	[50]

(αLi) (< -193 °C)	yes	-	100 at 156 °C	[52]
(Li)	yes	-	100 at 156 °C	[52][74][50]
(Li) hp1	yes	-	-	[30]
(Li) hp2	yes	-	-	[31]
(Li) hp3	yes	-	-	[31]

The invariant reactions occurring in literature are characterized as eutectic, peritectic, eutectoid, peritectoid, metatectic and as congruent transformation. However, not every sort of the mentioned invariant reactions occurs in all In-Li phase diagram versions. All 34 transformation reactions, the associated temperature T and the literature references are summarized in Table 20.

Table 20 Postulated reaction occurring in the system In-Li according to literature (see Grube et al. [47], Lamprecht et al. [49], Schneider et al. [61], Thümmel et al. [50], Alexander et al. [51], Sangster et al. [52], Zhou et al. [70] and Gierlotka et al. [74]).

Reaction	Type of reaction	T (°C)	Alternative reaction	Ref.
L + InLi ⇄ (In)	peritectic	159±10	-	[52]
		160	-	[70] ex[c]
		159.8	-	[70] cal[d]
		158	-	[51]
	eutectic[e]	159	-	[74]
L ⇄ (In) + InLi	eutectic	152	-	[50]
L ⇄ InLi	Congruent melting	634	-	[52]
		626	-	[70] cal
		625	-	[47]
		629	-	[49]
		630	-	[61]
		630	-	[50]

[c] Experimentally determined.

[d] Determined by calculation.

[e] Designated as eutectic but formulated as peritectic reaction by Gierlotka et. al.[74]

		625	-	[74]
$InLi + InLi_2 \rightleftarrows In_2Li_3$	peritectoid	295	-	[52]
		296	-	[70] cal
		310	$InLi + InLi_2 \rightleftarrows In_4Li_7$	[51]
		295	$InLi + In_4Li_9 \rightleftarrows In_2Li_3$	[50]
		300	-	[74]
$InLi \rightleftarrows InLi_2$	congruent transformation	460	-	[52]
		463	-	[70] cal
		460	$InLi \rightleftarrows In_4Li_9$	[50]
		459	-	[74]
$InLi \rightleftarrows InLi_2 + In_3Li_{13}$	eutectoid	374		[74]
		390	-	[52]
		391	-	[70] cal
		390	$InLi \rightleftarrows In_4Li_9 + InLi_4$ ht	[50]
$L + InLi \rightleftarrows In_3Li_{13}$	peritectic	400	-	[52]
		395	-	[74]
		400	-	[70] cal
		402	$L + InLi \rightleftarrows InLi_4$ ht	[50]
$L + In_3Li_{13} \rightleftarrows InLi_6$	peritectic	307	-	[74]
		300	$L + InLi_4$ rt $\rightleftarrows InLi_6$ ht	[51]
		280	$L + In_3Li_{13} \rightleftarrows InLi_7$	[52]
$L \rightleftarrows InLi_6 + (Li)$	eutectic	179	-	[52]
		180	-	[74]
$L \rightleftarrows InLi_{20} + (Li)$	eutectic	156	-	[50]
$L \rightleftarrows InLi_{12}$ ht+ (Li)	eutectic	180.5	-	[51]
$In_3Li_{13} + InL_2 \rightleftarrows InLi_3$ rt	peritectoid	346	-	[70] cal
		350	-	[52]
$InLi + In_2Li_3 \rightleftarrows In_4Li_5$	peritectoid	230	-	[52]
$L + In_4Li_9 \rightleftarrows InLi_3$ ht	peritectic	347	$InLi_2 + L \rightleftarrows InLi_3$ ht	[50]

$InLi_4$ ht ⇄ L + In_4Li_9	metatectic	360	In_3Li_{13} ⇄ L + $InLi_2$	[50]
L + $InLi_3$ ht ⇄ In_2Li_9	peritectic	280	$InLi_3$ ht + L ⇄ In_3Li_{13}	[50]
L + In_2Li_9 ⇄ $InLi_9$	peritectic	208	In_3Li_{13} + L ⇄ $InLi_9$	[50]
L + $InLi_9$ ⇄ $InLi_{20}$	peritectic	168	-	[50]
In_4Li_9 + InL_3 ht ⇄ $InLi_3$ rt	peritectoid	315	$InLi_2$ + $InLi_3$ ht ⇄ $InLi_3$ rt	[50]
$InLi_3$ ht ⇄ $InLi_3$ rt + In_2Li_9	eutectoid	220	-	[50]
L + InLi ⇄ $InLi_2$	peritectic	470	-	[51]
L + $InLi_2$ ⇄ In_3Li_8	peritectic	425	-	[51]
$In_{28}Li_{72}$ + $InLi_2$ ⇄ In_2Li_5 ht	peritectoid	397	-	[51]
$InLi_3$ + $InLi_4$ ht ⇄ $InLi_4$ rt	peritectoid	310	-	[51]
$In_{28}Li_{72}$ ⇄ In_2Li_5 ht + In_4Li_{11} ht	eutectoid	345	$In_{28}Li_{72}$ ⇄ In_3Li_8 + $In_{8+x}Li_{22-x}$ (x=0.1)	[51]
In_4Li_{11} ht ⇄ In_2Li_5 ht + $InLi_3$	eutectoid	335	$In_{8+x}Li_{22-x}$ (x=0.1) ⇄ In_3Li_8 + $InLi_3$	[51]
In_2Li_5 ht ⇄ $InLi_2$ + In_3Li_8	eutectoid	80	-	[51]
$In_{28}Li_{72}$ + $InLi_3$ ht ⇄ In_4Li_{11} ht	peritectoid	385	$In_{28}Li_{72}$ + $InLi_3$ ⇄ $In_{8+x}Li_{22-x}$ (x=0.1)	[51]
L + $InLi_3$ rt ⇄ $InLi_4$ ht	peritectic	400	L + $InLi_3$ rt ⇄ In_3Li_{13}	[51]
L + $In_{28}Li_{72}$ ⇄ $InLi_3$ ht	peritectic	413	-	[51]
L + $InLi_6$ ht ⇄ $InLi_{12}$ ht	peritectic	260	-	[51]
$InLi_{12}$ ht ⇄ (Li) + $InLi_6$ ht	eutectoid	140	-	[51]
$InLi_6$ ht ⇄ (Li) + $InLi_4$ rt	eutectoid	125	$InLi_6$ ⇄ (Li) + In_3Li_{13}	[51]

$InLi_4$ ht ⇄ $InLi_4$ rt + L	metatectic	310	-	[51]

In conclusion there is a common agreement on the course of the liquidus line in the range of ~20 to 95 at.% Li and on the low solubility of In in (Li) as well as on the existence of the intermetallic compounds InLi, In_2Li_3, $InLi_2$ and In_3Li_{13}, but described with different homogeneity range. InLi melts congruently at an average temperature of ~629 °C. At the other side, there are many contradictions between the In-Li phase diagrams versions in terms of the position of phase boundaries, the occurring phases or the sort of invariant reactions taking place. For example, the formation of the 2-phase field (In) + InLi is on the one hand described as peritectic reaction and on the other as eutectic reaction. Also, the maximum solubility of Li in (In) given in literature varies from 1 to 15 at.%.

All these contradictions and inconsistencies in the description of the phase relations in In-Li makes new investigations necessary.

3. Experimental methods

3.1 Thermoanalytical methods

Thermoanalytical methods were used for the investigation of the temperature-dependent phase transformations. This was done with samples under their own vapor pressure (pseudo-constant pressure) at selected compositions (see Fig. 36). [78]

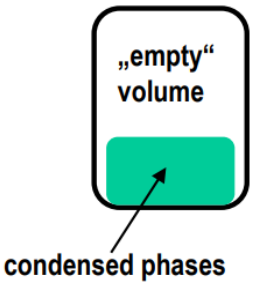

Figure 36 Sample conditions during measurements of thermoanalytical methods. [78]

3.1.1 Differential Thermal Analysis

A Differential Thermal Analysis DTA device of heat flow Boersma-type is constructed from a resistance furnace for example with SiC-heating elements, surrounding two separated sample holder rods made from a suitable material like sintered α-Al_2O_3 with embedded thermocouples e.g. of S-type (Pt-Pt10%Rh). The separation of the sample holder rods enables a better differentiation of the measured thermal effects, because under idealized conditions occurs only a direct heat flow via thermal conduction from the furnace to sample $\dot{Q}_{FS}$ and from furnace to reference $\dot{Q}_{FR}$, but not directly between sample and reference $\dot{Q}_{SR}$ (see Fig. 37and 38). The DTA investigation results in a plot of the temperature difference between sample and the reference ΔT_{SR} vs. time t or the temperature of the sample T_S. Another option is a plot of the heat flow $\dot{Q}$ or the electrical voltage per sample mass, which is proportional to $\dot{Q}$, vs. t or T_S. The phase transition temperatures as well as their exo/endothermic nature can be identified through the shape of the curve of the thermal effect and its maximum/minimum in respect to $\dot{Q}_{SR}$. [79][80][81][82][83]

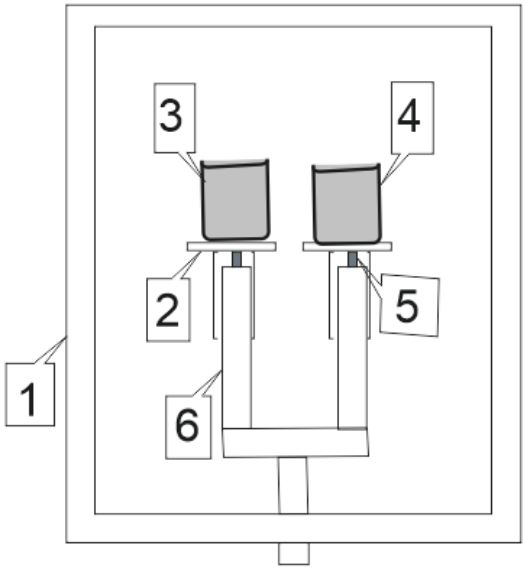

Figure 37 Schematics of a DTA instrument of the Boersma-type. 1…Surroundings (furnace), 2…plate mounted on the sample/reference holder rods, 3…sealed Ta-crucible containing the sample, 4…sealed Ta-crucible containing the reference, 5…thermocouples, 6…heat conduction path (sample/reference holder rods). Modeled with CorelDraw 2018. [79]

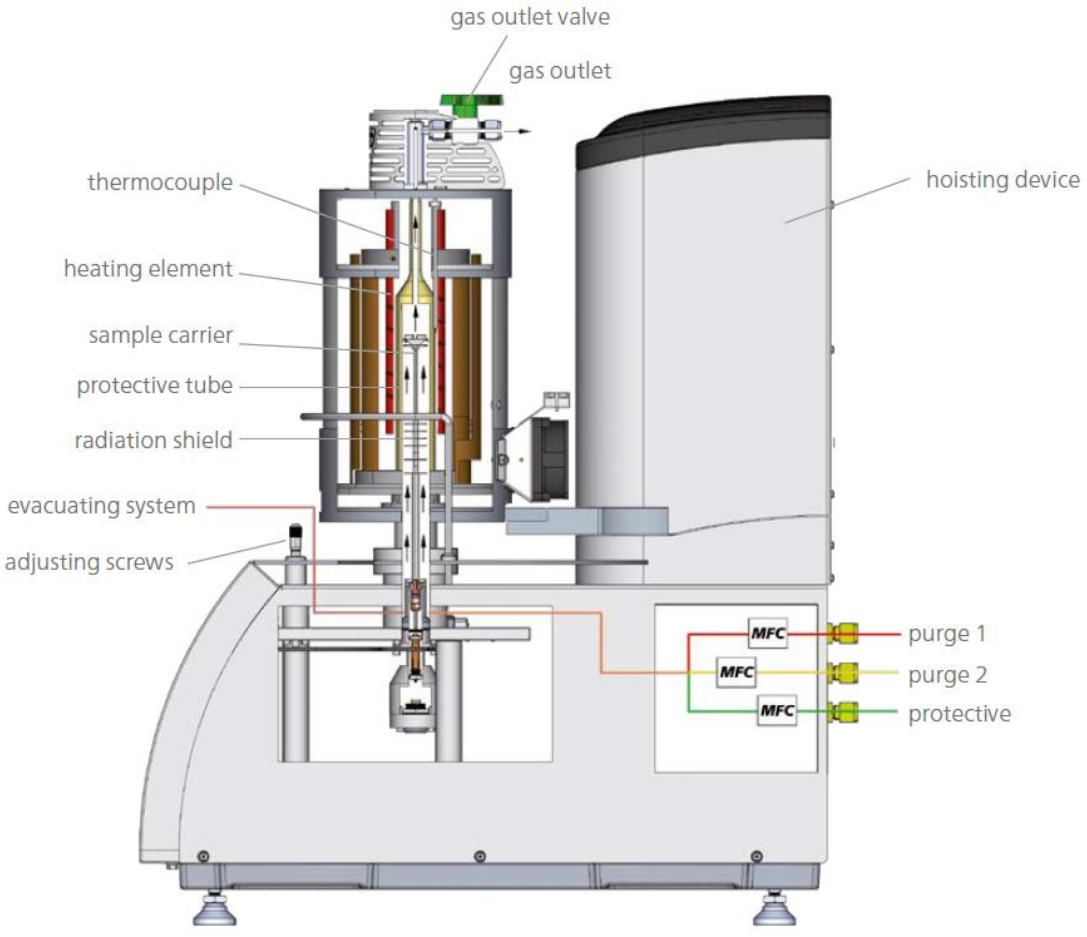

Figure 38 DSC 404 F1 of NETZSCH used for DTA measurements (Boersma-type). [80]

3.1.2 3D-heat flow calorimetry

A Calvet-type 3D-heat flow calorimeter 3D-DSC consist of a massive calorimetric block with a resistance furnace surrounding two measuring cells containing the crucibles with the sample or the reference respectively. Each is surrounded by a thermopile (Calvet sensor, multiple thermocouples) used on one hand for the temperature measurement and on the other hand for a defined direct heat flow $\dot{Q}_{FS}$, $\dot{Q}_{FR}$ and $\dot{Q}_{SR}$, enabling a high reproducibility. In addition will be a high sensitivity reached due to the stable temperature of the surrounding and the use of thermopiles (see Fig. 39 and 40).

In principle can any calorimeter be described as a system composed of a surrounding (furnace) separating the environment from the measurement system (sample/reference, sample container etc.). The surrounding is connected via a defined thermal resistance R_{th} with the measuring system. In case of a DTA measurement are scanning conditions present, thus the temperature of the furnace T_F is continuously and linearly changed in respect to time t through a certain heating/cooling rate β:

$$\beta = \frac{dT_F}{dt} => T_F = T_F(t) = T_0 + \beta \cdot t$$

T_0 is the initial furnace temperature. These conditions result in a large defined steady-state heat flow (small R_{th}) between furnace and sample $\dot{Q}_{FS}$ and furnace and reference $\dot{Q}_{FR}$. If a reaction of the sample takes place, appears a small change in the heat flow $\dot{Q}_{SR}$, which results in a directly proportional local temperature difference ΔT_{SR} between sample and the reference in respect to the device and its calibration described by the calibration constant $C_{cal}(T)$.

ΔT_{SR} is detected by the thermocouples via the thermoelectric effect (Seebeck effect) leading to a proportional voltage:

$$\dot{Q}_{SR} \ll \dot{Q}_{FS}, \dot{Q}_{FR} => \dot{Q}_{SR} \propto \Delta T_{SR}$$

$$\dot{Q}_{SR} = \frac{dQ_{SR}}{dt} = -C_{cal}(T) \cdot \Delta T_{SR}(t)$$

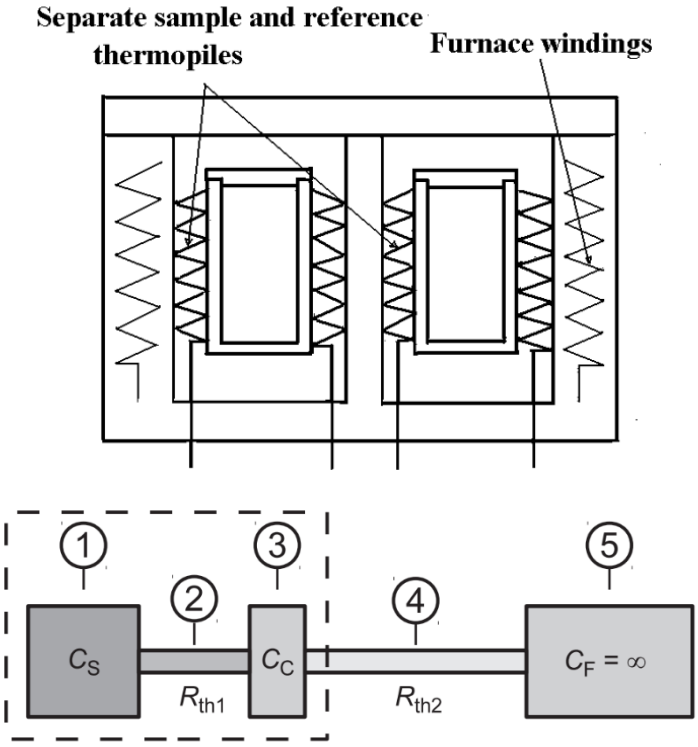

Figure 39 Top: Schematics of a Calvet-type heat flow 3D-DSC. Bottom: Thermal equivalent diagram for one measuring cell. 1…sample/reference with certain heat capacity c_s, 2…crucible containing the sample/reference with certain thermal resistance R_{th1}, 3…measuring cell with certain heat capacity c_c, 4 thermopile with certain thermal resistance R_{th2} and 5…furnace with its heat capacity c_F. [79][81]

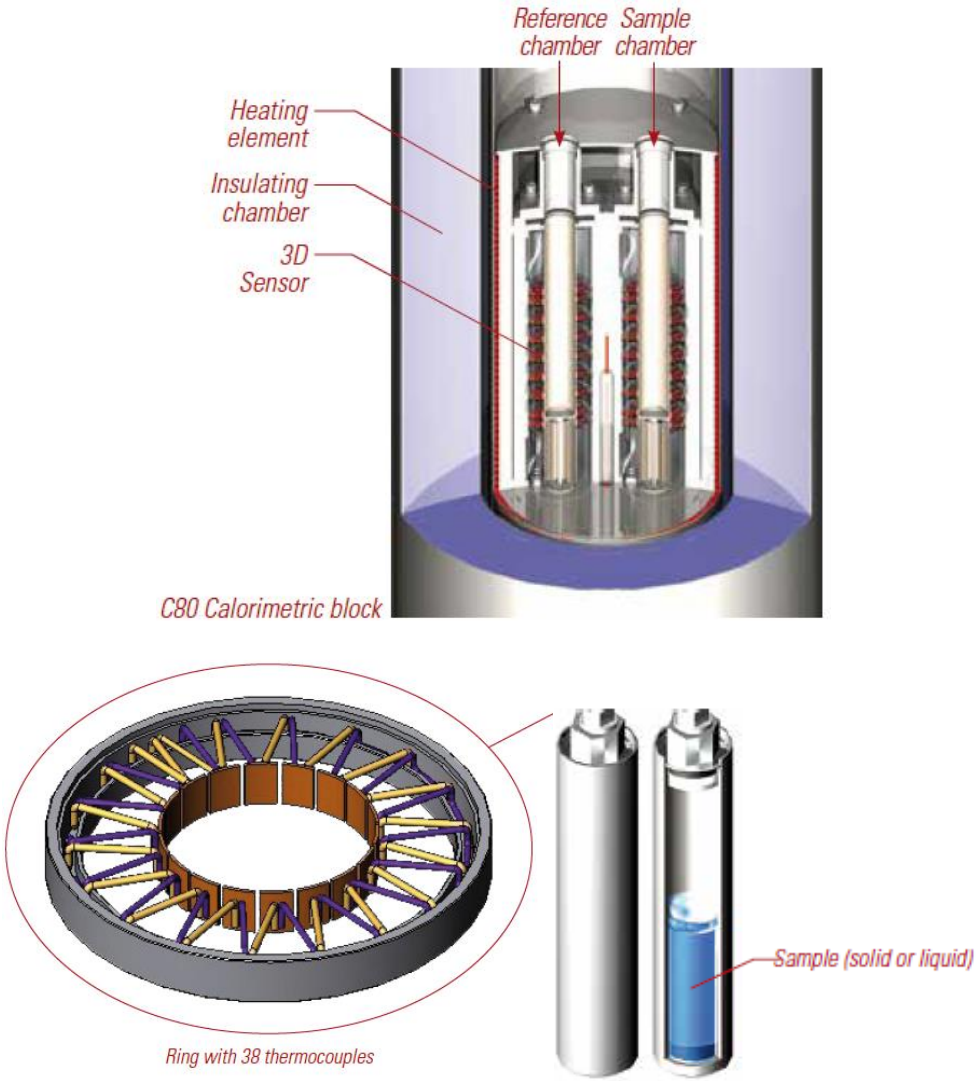

Figure 40 Top: Interior of the Calvet-type heat flow 3D-DSC C80 - Seteram Instrumentation of KEP Technologies group used for DTA measurements. Bottom: Sample cell and 3D-Calvet sensor consisting of multiple rings with 38 thermocouples. [83]

3.2 X-ray diffraction techniques

X-ray diffraction techniques at room temperature was used to investigate the quenched isothermal phase equilibria of alloy samples. This was done at selected compositions and after annealing and quenching at certain temperatures.

3.2.1 X-rays

The necessary radiation for X-ray diffraction and X-ray fluorescence spectroscopy techniques in the laboratory is mostly produced by an X-ray tube, which consists of an evacuated cathode e.g. a W-coil and an anode (target) e.g. a water-cooled Cu- or Mo-stripe (see Fig. 41). Electric current flows through the

cathode heating it to excite electrons. If a high voltage electric field is now applied between cathode and anode, then will primary electrons be accelerated towards the anode (thermionic emission). The resulting collision generates heat, Bremsstrahlung (“white X-rays”) and characteristic radiation depending on the anode material e.g. Cu$K_{\alpha 1}$, $K_{\alpha 2}$ and K_{β} would result from a Cu-anode. The produced X-ray beam can leave the tube through X-ray-transparent Be-windows.

Bremsstrahlung occurs, when a fast electron gets deflected by the electrostatic field of an atom core. This leads to a deacceleration of the electron under energy loss as heat and polychromatic X-ray radiation.

However, if a primary electron interacts with the electron shell of an atom, a core-near secondary electron is emitted. The resulting ion with an empty core-near shell gets occupied by an electron of the outer shell (higher energy level) of the atom. This relaxation process leads to the emission of a monochromatic X-ray photon. The characteristic wavelength of this photon corresponds to the energy difference of the electron shells (energy levels of the orbitals). Hence, the possible energy levels for relaxation depend on the element.

X-ray fluorescence is based on a similar process, but instead of a primary electron, X-rays excite electrons, which then emit part of their energy as X-rays which lower photon energy (higher wavelength). The emitted spectrum is characteristic for the respective elements, quantitative analysis is possible after calibration.

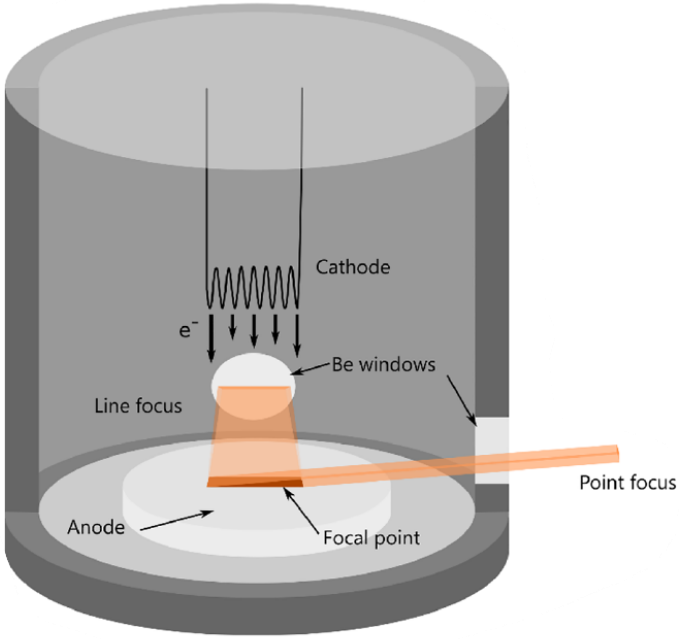

Figure 41 Schematic of an X-ray tube with W-coil, stripe anode and Be-windows for point or line focusing of the beam. [84]

3.2.2 X-ray diffraction

A crystal structure is a periodic arrangement of lattice points in the space. The lattice points can be occupied by atoms, ions or molecules. It can be described by the unit cell, a parallel epipedon described by lattice parameters (distances a, b, c and angles α, β, γ) and the atomic coordinates (fractional coordinates) (xyz) of an element j on a lattice site (group of lattice points). The unit cell is the smallest unit which comprises all symmetry elements of a crystal lattice. All lattice points are generated by the application of the symmetry elements to the lattice sites. The symmetry elements are summarized in space groups. All these data (lattice parameters, atomic coordinates and space group), can be determined from information collected by X-ray diffraction.

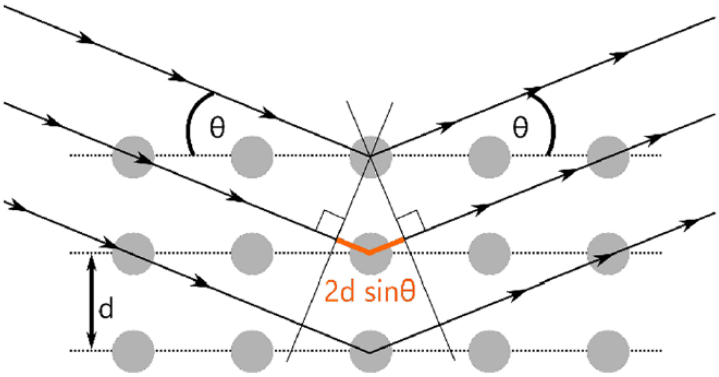

Figure 42 Representation of the Bragg-diffraction occurring by 3 lattice planes stacked under each other with the lattice plane spacing d at the Bragg-angle θ. [84]

The basis for X-ray diffraction is the occurrence of an interference pattern (reflections) resulting from phase shift of X-ray quants, which got elastically scattered by interactions with the electron shells of periodic arranged atoms/ion in a crystal. Constructive interference takes place when the Bragg-law is fulfilled:

$$n \cdot \lambda = 2d_{hkl} \cdot \sin(\theta)$$

This is the case if the wavelength λ, (X-rays have the same order of magnitude as the interatomic distance) and an integer of the order of the diffraction maxima n (in most cases n = 1) is proportional to the product of twice the lattice plane spacing d_{hkl} and the sinus of the incident angle of the X-ray (Bragg-angle) θ. Lattice planes are described by Miller indices (hkl), which correspond to a certain point in the reciprocal lattice. So, the lattice parameters can be determined via the Bragg-law. For example, reads d_{hkl} of a cubic lattice:

$$d_{hkl} = \frac{a}{\sqrt{h^2+k^2+l^2}}$$

The structure factor F_{hkl} of a Bragg reflection (hkl) can be described as the Fourier transformation of the coherent X-ray beam which gets diffracted by the periodically distributed electron density ρ(xyz) of the crystal. Thus, F_{hkl} contains information on atoms/ions j which do cause a superposition of X-ray waves via interference. This information contains the atomic coordinates (xyz) within the phase Φ_{hkl} and the elemental specific scattering factor (atomic form factor) f_j, as well as information on thermal displacement factor t_j:

$$F_{hkl} = \iiint_0^1 \rho(x,y,z) \cdot e^{i \cdot \Phi_{hkl,j}} \, dxdydz$$

$$= \sum_{j=1}^{N} (f_j \cdot t_j) \cdot e^{i \cdot \Phi_{hkl,j}}$$

$$= |F_{hkl}| \cdot e^{-i \cdot \Phi_{hkl,j}}$$

One can only measure the intensity I_{hkl} of the reflex (hkl) which is directly proportional to the absolute value of the structure factor squared $|F_{hkl}|^2$:

$$I_{hkl} = |F_{hkl}|^2 \cdot \left(I_0 \cdot L_\theta \cdot P_\theta \cdot \lambda^3 \cdot \frac{V_{crystal}}{V_{unit\ cell}^2} \cdot \left(\frac{\mathbf{e}^2}{m \cdot c^2} \right)^2 \cdot G_\theta \cdot A \cdot E \cdot p \right)$$

However, as already described the information on the atomic coordinates is contained in the phase Φ_{hkl} of the complex number F_{hkl}:

$$\Phi_{hkl,j} = 2\pi \cdot (h \cdot x_j + k \cdot y_j + l \cdot z_j)$$

Hence, the phase information is lost, only the amplitude $|F_{hkl}|$ can be determined directly. This is called the phase problem.

Further depends I_{hkl} on other parameters, which will not be discussed in detail in this diploma thesis. Such parameters are the intensity I_0 of the non-diffracted X-ray beam, the Lorentz factor L_θ, describing the ratio of the angular velocity of the rotating crystal to the velocity of the reflex (hkl) penetrating the Ewald-sphere (see “3.2.4 Single-Crystal X-ray Diffractometry”). It depends also on the polarization factor P_θ, considering the X-ray polarization, the X-ray wave length λ, the volumina of the measured crystal $V_{crystal}$ and of the unit cell $V_{unit\ cell}$, the coefficient from the Thomson scattering (elastic scattering of electromagnetic radiation) consisting of the elementary charge **e,** the mass of an electron m and the speed of light in the vacuum c. Last but not least depends I_{hkl} on the factor G_θ describing

certain beam geometries, the absorption A, the factor E, correcting the primary and secondary extinction and in case of diffraction of a polycrystalline sample, the (reflection) multiplicity factor p. [78][84][85][86][87][88][89]

3.2.3 Powder X-Ray Diffractometry

An powder X-ray diffractometer XRD with Bragg-Brentano pseudo-focusing geometry consists of an X-ray tube e.g. as line source and incident optics like an axial soller-collimator with fixed divergent slit or with variable automatic divergent slit (variable incident slit), as well as the sample holder, receiving optics like a K_β-filter and an X-ray detector e.g. a 1D-Si-strip detector (see Fig. 43).

In principle targets a divergent X-ray beam, originating from the incident optics the sample (specimen) on the sample holder which is spinning around the z-axis. The X-rays are diffracted by the polycrystalline sample with randomly oriented crystallites and powder particles leading to several reflections at certain 2Θ angles, if the Bragg-law is fulfilled. These reflections are commonly scanned in Θ/Θ- or Θ/2Θ-goniometer-mode. At the first goniometer mode moves the X-ray source and the incident optics as well as the receiving optics with the detector, while the sample holder is fixed. At Θ/2Θ-goniometer-mode the sample holder is moving, instead of the X-ray source and the incident optics, which is fixed.

The reflections are detected after filtering out white and K_β radiation. In case of a 1D-Si-stripe detector the photoelectric effect is used to generate an electrical signal proportional to the intensity I_{hkl}. Its big advantage is the possibility to detected along a wider 2θ-range simultaneously, resulting in a faster scan rate.

In Bragg-Brentano pseudo-focusing geometry is the sample holder positioned in the center of the diffraction circle while X-ray source, detector and optics are positioned on the diffraction circle. Due to the divergent beam geometry is a simultaneous movement in Θ/Θ- or Θ/2Θ-goniometer-mode within the x-z-plane crucial for a focused beam received by the detector along the focusing circle (see Fig. 44).

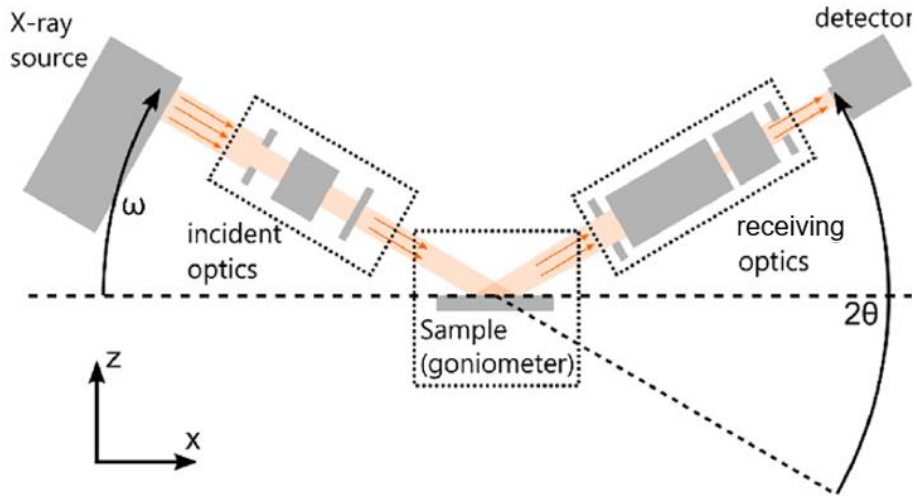

Figure 43 Schematics of an XRD instrument. [83]

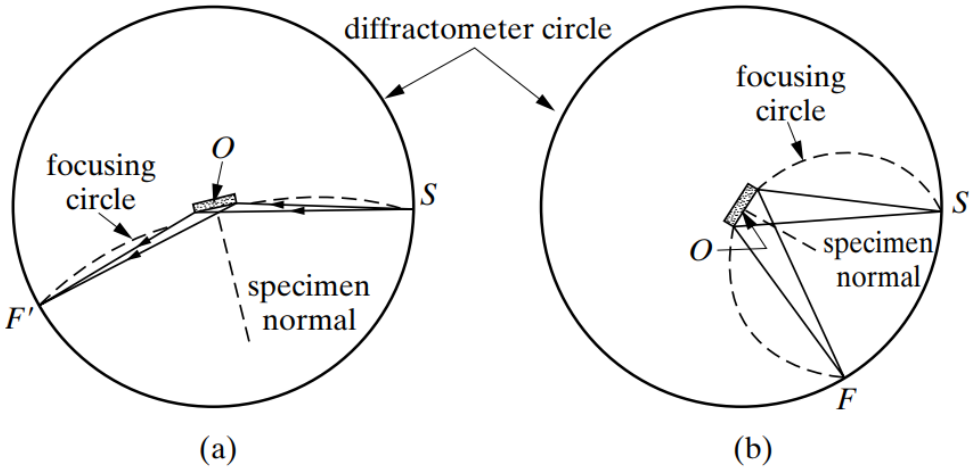

Figure 44 Bragg-Brentano pseudo-focusing at Θ/2Θ-goniometer-mode. (a) shows a larger focusing circle than (b). S…X-ray source, O sample holder, F…detector. [89]

The result is a diffractogram plotting the detected intensity I_{hkl} of diffracted X-ray beams against the known 2Θ-steps of the scanned range. By comparison of models of already known crystal structures e.g. literature or data base, with the measured data in terms of position 2Θ and I_{hkl}-distribution of the reflections, is the identification of the phases present in the sample possible. In addition, full profile Rietveld refinement enables quantitative phase analysis, deconvolution of overlapping peaks, identification of non-stoichiometric phase and determination of its lattice parameters.

Rietveld refinement is a least square method for a “full pattern refinement”. An iterative improvement leads to the best possible fit of the measured pattern with

the calculated one based on models of known crystal structures, instrumental and sample parameters, e.g. related to the background correction $y_{back,i}$, the peak position i, the peak profile $\phi_{hkl,p,i}$ and to the intensity. Hence, the goal is to reach a minimum between all observed intensities $y_{obs,i}$ and all calculated intensities $y_{calc,I}$, while using a certain weighting of every peak position w_i:

$$\sum_{i} \left(w_i \cdot \left(y_{obs,i} - y_{calc,i} \right)^2 \right) \rightarrow \min.$$

$$y_{calc,i} = y_{back,i} \cdot \sum_{p} \left(S_p \cdot \sum_{hkl(p)} \left| F_{calc,hkl,p} \right|^2 \cdot \phi_{hkl,p,i} \cdot C_{hkl,p,i} \right)$$

$y_{calc,i}$ is affected by lots of parameters of mathematical models which describe the crystalline phases present, the instrument and the sample characteristics, e.g. crystallite size. Parameters related to the peak shape are for example the crystal domain size, the emission profile, microstrain parameters and parameters to determine the instrumental peak broadening. While parameters related to the peak position are e.g. the lattice parameters, the sample displacement parameter. Parameters related to intensity are: the scaling factor S_p, parameters influencing the calculated absolute structure factor $|F_{calc,hkl,p}|$ like the thermal displacement parameters, the occupancy, the atomic coordinates, or factors correcting the intensity $C_{hkl,p,I}$, like the multiplicity factor, the Lorentz-Polarization factor, the absorption correction, the extinction factor, the surface roughness function and the preferred orientation etc. [84][85][86][87][89][90]

3.2.4 Single-Crystal X-Ray Diffractometry

A 4-cycle single crystal X-ray diffractometer SCXRD was used for tis work. It consists of an X-ray tube with a Mo-target, equipped with monochromator made from graphite and a collimator. Next part is the 4-cycle goniometer with e.g. a κ- geometry with 4 possible rotation axes around a ϕ-, κ-, ω- and 2θ-angle. The single crystal is mounted e.g. on a glass fiber, on top of the goniometer head. The crystal can be rotated by 360° around the ϕ-, κ- and ω-angle. The detector is able to rotate around the 2θ-angle and its distance to the crystal can be changed too. Mostly is a 2D-detector like a charge coupled device CCD equipped with a scintillator and fiber optics in use. A beam stopper prevents damaging the detector through non-scattered intense X-ray beams (see Fig. 45).

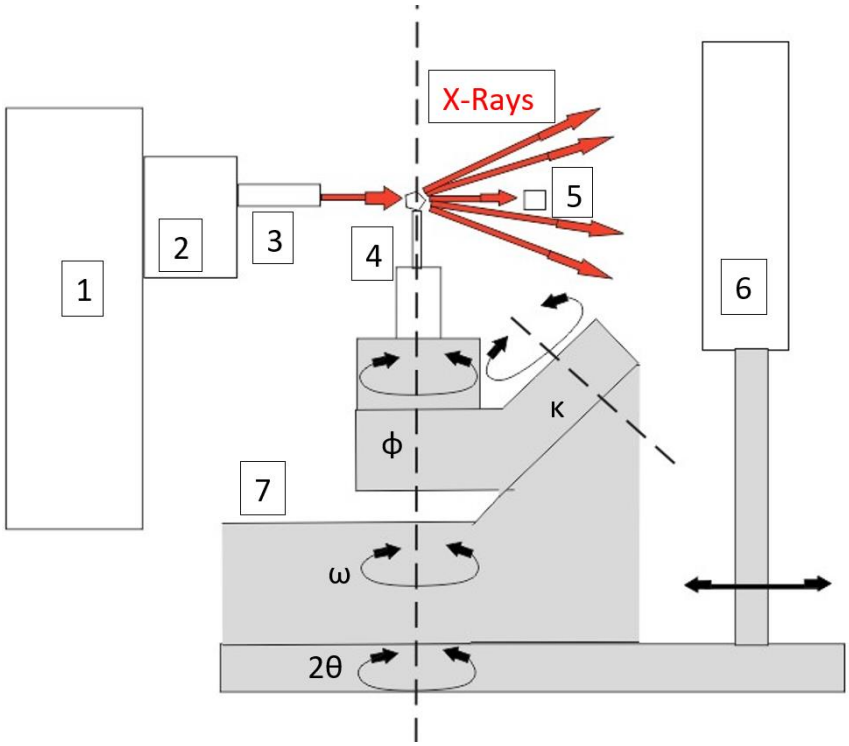

Figure 45 Schematics of a 4-circle SCXRD with κ-goniometer. 1…X-Ray tube, 2…monochromator, 3…collimator, 4…sample holder with mounted single crystal, 5…beam stopper, 6…2D-detector, 7…4-circle κ-goniometer. Modeled with CorelDraw 2018 after Enraf Nonius FR590 device.

Basically, can a SCXRD measurement be described by the steps: Data collection, data integration, data scaling, phasing and refinement.

Data collection was accomplished by measuring the intensity I_{hkl} of as many as possible reflections coming from different known angles. The reflections result from the diffraction of the monochromatic and well aligned X-ray beam targeting the centered single crystal, while moving. A 2D-detector uses for example a scintillator to convert the X-ray photons by photoluminescence into photons in the UV/vis range. These photons with lower energy can be used by a CCD to generate an electric signal proportional to the I_{hkl} through the photoelectric effect.

Next follows data integration, thus extracting the intensity data from the reflections. This is done by indexing and background correction. Indexing means basically calculating the Ewald-sphere backwards (see Fig. 46), hence determining all (hkl) of the reflections in the reciprocal space from the measured θ at different goniometer positions and calculating on basis of the Bragg-law via the known λ, all d_{hkl} in the real space. This makes it possible to determine the crystal orientation

via (hkl) and the lattice parameters via all d_{hkl} by cell refinement. These data in combination with the evaluated systematic extinctions, leads to the Bravais lattice, the space group, the point group and the Laue group.

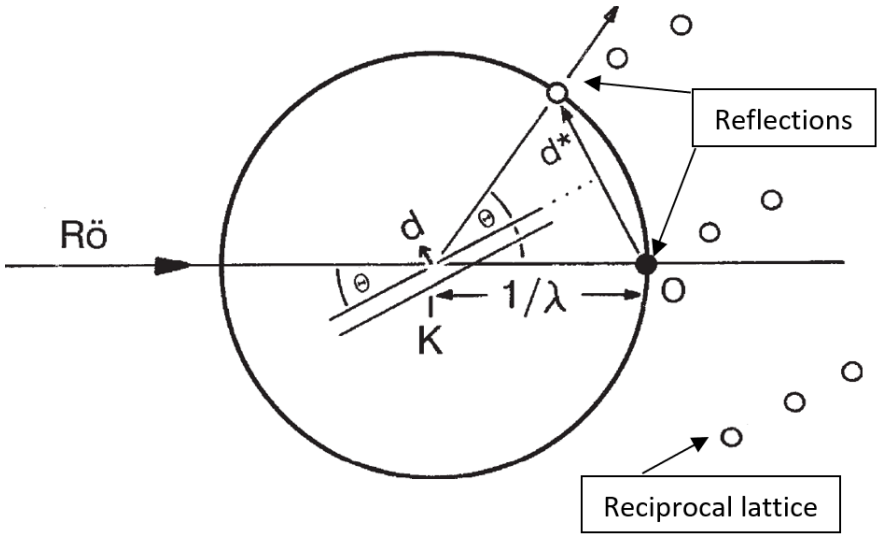

Figure 46 The 2D-Ewald-sphere. Reflections occur at a certain angle θ, if a circle of the reciprocal lattice intersects the 2D-Ewald-sphere. Rö…incident X-ray beam, d… lattice plane spacing, d*…reciprocal lattice plane spacing, K…Crystal, θ…Bragg-angle, λ…wavelength of the X-ray beam. [86]

Next step is data scaling, which means data reduction. So, the measured data gets idealized by determining the mean intensity of symmetry equivalent and several times measured reflections as well as applying Lorentz, polarization and absorption correction.

Afterwards is phasing accomplished, thus solving the phase problem (see section 3.2.2 “X-ray diffraction”). There are different algorithms for the phasing of inorganic materials, but most use the Patterson summation (Patterson method, Patterson map) or the direct methods or a combination of both like dual space recycling, which uses the direct methods with random atoms/ions from the Patterson summation etc.

The Patterson summation can be used for phasing, if the crystal structure contains a mixture of elements with a large difference between their number of electron and if not too many “heavy” atoms/ions are present. While direct methods are preferred for phasing when the elements present in the crystal structure have a similar number of electrons and the electron density is statistically distributed within the unit cell, which is sometimes not the case for hexagonal or trigonal unit

cells. However, both methods have in common that the unit cell should not contain “too many” atoms/ions, which would be the case if used for a protein crystal. The Patterson summation is based on a Fourier synthesis of the determined $|F_{hkl}|^2$ without the phase information, leading to the interatomic distance vectors of all atoms/ions present in the unit cell and further to the Patterson map, which enables the calculation of the atomic coordinates.

The direct methods are based on the condition that the electron density cannot be negative and that its maxima are located in points in the unit cell. This results in a relationship of the phase to the normalized structure factor. Simplified, it is possible to determine the unknown phase Φ_{hkl} of the investigated crystal structure through combination of the measured amplitude $|F_{hkl}|$ with a known phase.

The last step is the refinement, hence improving the model of the electron density map resulting from phasing, in respect to a crystal chemically sensible structure or unit cell respectively. This is done by least square methods and model building methods. Least square methods are iterative methods which improve parameters like the atomic coordinates, the thermal displacement factor and the occupancy etc., until a good fit of the measured data with the refined model is reached. Model building methods do add, remove or change elements. However, both methods apply the difference Fourier summation to identify and reduce differences between measured and modeled data influencing the electron density map. [85][86][88][91]

3.3 Verification of the composition of the samples by elemental analysis

3.3.1 Total Reflection X-Ray Fluorescence Spectrometry

A total reflection X-ray fluorescence spectrometer TXRF (see Fig. 47) consist of an X-ray tube, mostly with Mo-target as excitation source for the sample, a modifier like a single crystal Ge-monochromator to get the wanted wavelength of the X-ray beam as well as a reflector with the sample holder e.g. made from quartz glass, holding a solid sample and an energy dispersive detector e.g. a solid-state Si(Li) detector (PIN diodes) .

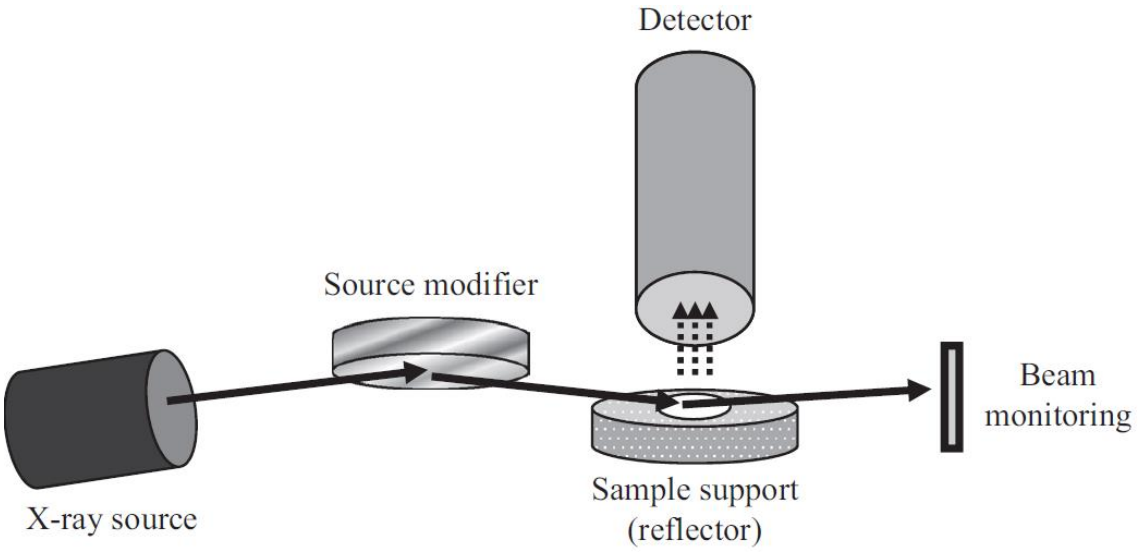

Figure 47 Schematics of a TXRF instrument. [92]

At first separates the source modifier a polychromatic X-ray beam coming from the X-ray tube. The resulting monochromatic beam targets a flat sample at an angle of < 0.1 °. This leads to X-ray fluorescence which is detected at an angle perpendicular to the incident beam. These photons are transformed by the detector via the photoelectric effect into an electronic signal, where the photon energy (wavelength) is proportional to the voltage of the detected pulse and the beam intensity is proportional to the number of pulses. A multi-channel analyzer is necessary to count the produced voltage pulses, due to the lack of a monochromator separating photons by their wavelength.

The analysis is performed qualitatively through the identification of the characteristic fluorescence emission spectrum of the investigated element and quantitatively through internal calibration by the equation:

$$c_A = \frac{(c_s \cdot N_A \cdot S_s)}{(N_s \cdot S_A)}$$

Hence, the concentration of the analyte (investigated element) c_A is equal to the product of the concentration of the internal standard element c_s, the net signal of the analyte N_A and the relative sensitivity of the internal standard element S_s divided by the product of the net signal of the internal standard element N_s and the relative sensitivity of the analyte S_A. Thus, N_A and N_s are measured while c_s and the correction term S_s/S_A must be known. Latter can for example be experimentally determined. [92]

3.3.2 Flame Atomic absorption spectroscopy

A typical flame atomic absorption spectroscope F-AAS (see Fig. 48) consists of a light source e.g. a hollow cathode lamp HCL, emitting an UV/Vis spectrum characteristic for the element of interest, an optical system sometimes with a chopper as modulator and deuterium lamp for background correction. A burner system (atomization system) is also necessary, consisting of a peristaltic pump for sample feeding, a nebulizer to generate a sample/oxidant/fuel-aerosol, a spray chamber to separate bigger drops from the aerosol and a slot burner for the atomization. Then follows a monochromator like an echelle optic with echelle grating and the last part of the instruments, the detector e.g. a segmented solid-state strip detector.

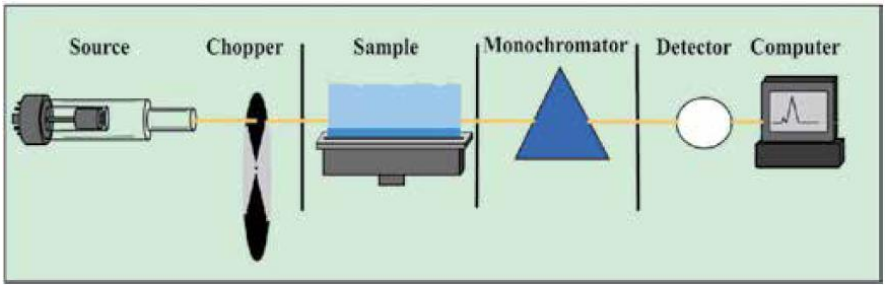

Figure 48 Schematics of a F-AAS instrument.[94]

In a HCL occurs a process similar to sputtering, which leads to the excitation of electrons in the outer shell of the element of interest in the lamp. Eventually starts relaxation of the exited electrons under emission of photons characteristic for this element of interest. These photons get absorbed by the analyte, which was atomized by the flame, leading to an attenuated intensity of the beam. This beam gets separated by the wavelength with a monochromator and transformed according to the photo electric effect into an electronic signal by the detector, proportional to its intensity.

The analysis is performed qualitatively through the characteristic absorption spectrum of the investigated element and quantitatively mostly by external calibration on basis of the Lambert-Beer law:

$$A = \log_{10} \frac{I_0}{I} = \varepsilon \cdot d \cdot c$$

The absorbance A is equal to decadal logarithm of the incident intensity I_0 divided by the attenuated intensity I, which is also equal to the product of the molar absorption coefficient ε, the optical path length d and the molar concertation c. [93][94]

4. Experimental Section

4.1 Weighing and sealing of the samples

Due to the high reactivity of Li the samples were prepared in a Glovebox and sealed in Ta-crucibles for heat treatments. Ta is inert to Li and In in opposite to quartz glass. These crucibles and their lids were made from 99.95 % pure Ta-sheets from Alfa Aesar via deep drawing followed by multiple cleaning steps to remove grease and other contaminations. Latter was done by a washing step with water and soap followed by ethanol and acetone. Next was pickling via a solution of 65 % H_2SO_4, 30 % HNO_3 and 5 % HF and sonication in distilled water for several minutes. In the last cleaning step was again ethanol and acetone in use. The bottoms of the clean and dry crucibles were flattened by a uniaxial press for about 1 min at 25 kN, to ensure better contact with the sample holder of the DTA.

However, Ta has the tendency to oxidize at temperatures above 300 °C in the presents of oxygen. So, annealing of the samples in a muffle furnace on air required the encapsulation of the crucibles under vacuum in quartz glass ampules. For the preparation of the samples 99.9 % pure Li-rods with diameter 12.7 mm from Sigma-Aldrich, 99.999 % pure In-rods from Asarco and 99.9999 % pure In-shots with diameter 3 to 5 mm from Smart Element GmbH were used.

First Li was weighed by an analytical balance (Satorius) in a glovebox (MBRAUN Labmaster pro ECO) with a dry Ar-atmosphere (0.6 ppm H_2O, > 0.1 ppm O_2), after a thin oxide layer was mechanically removed. The Li-rod was cut by a small pair of scissors and placed as single bead in the weighted Ta crucible. Then In was scaled in the correct nominal stoichiometry, through another analytical balance (Satorius) outside the glovebox. The formed oxide-layer on the surface of the In-rods was removed by a steel file. Then was the rod cut in suitable pieces with a side cutter for scaling. The newly bought In-shots did not have an oxide-layer. The scaled In was transferred into the mentioned glovebox and carefully combined with Li. It was crucial to fill the crucible not more than half way up (< 40 mg Li) to prevent the loss of components (mostly Li) during welding and to enable air-tight sealing.

The closed and weighted Ta-crucibles were placed for sealing by TIG-welding in a direct current arc furnace (Focus TIG 161 DC HP PFC) inside the glovebox.

The arc furnace was equipped with a water-cooled W-cathode and Cu-anode (see Fig. 49 and 50).

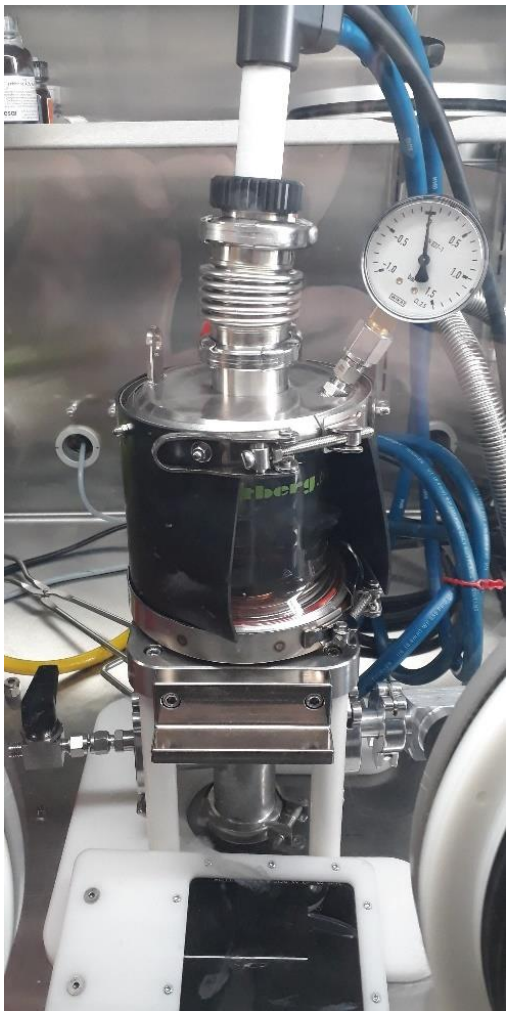

Figure 49 Arc furnace inside the glovebox used for Ta-crucible sealing.

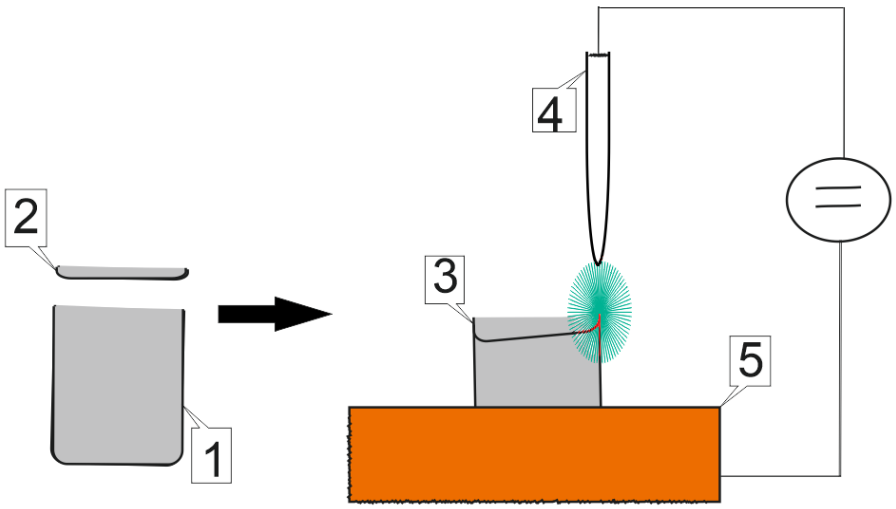

Figure 50 Schematic of the sealing process of Ta-crucibles by TIG-welding through an arc furnace. 1…Ta-crucible, 2…Ta-lid, 3…sealed Ta-crucible, 4…W-cathode, 5…Cu-anode. Modeled with CorelDraw 2018.

An optimal welding joint was accomplished by a distance of around 1 to 2 mm between cathode and the border of the lid, while applying a current of 46 to 48 A. Sometimes it was necessary to do the welding several times until no leak was visible for the naked eye. It was crucial to let the crucible cool down for about 10 to 20 min before welding and to weld only for a very short time to prevent sample evaporation and heat damage of the Ta-crucible or of the arc furnace, caused by the high temperature of the produced Ar-plasma.

The air-cooled crucibles were again weighed to check for any loss of sample caused by evaporation.

The welding joints of the crucibles were checked outside the glovebox by a reflected light stereomicroscope with zoom function (Stemi 2000-C of Carl Zeiss AG) (see Fig. 51) to ensure the absence of any leaks, verifying a gas tight welding joint (see Fig. 52).

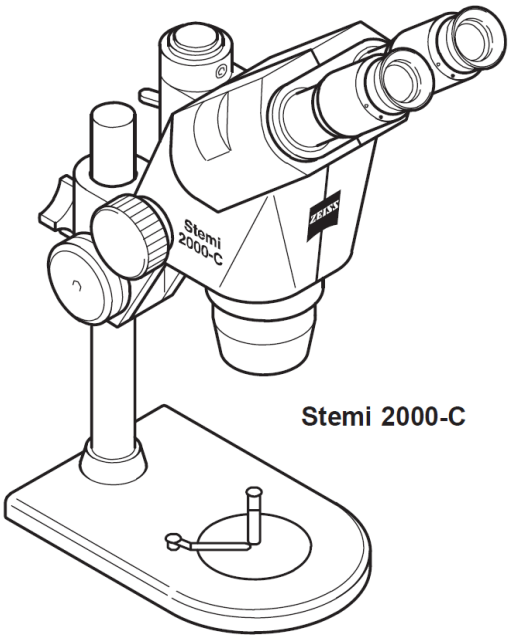

Figure 51 Stemi 2000-C Stereomicroscope of Carl Zeiss AG used to control the welding joints of the Ta-crucibles.[95]

Figure 52 Left: Birdseye view of the closed Ta-crucible before TIG-welding. Right: Birdseye view of the closed Ta-crucible after TIG-welding.

The next step was the encapsulation of the welded crucibles in quartz glass ampules. Quartz glass tubes with a diameter of 14 or 16 mm, which were closed at one end were cleaned with distilled water and ethanol. These washed tubes were dried in a drying chamber over night at ~140 °C. On the next day was a spacer made from folded and cleaned Ta-sheets, placed at the closed bottom of the tube. 1 to 4 sealed crucibles were vertically stacked on top of the spacer. The spacer counteracted possible mechanical stress on the quartz glass coming from the weight of the crucibles, similar a spring. When necessary, was a second spacer placed on top of a crucible. The filled tube was assembled on the vacuum line to

generate a dynamic vacuum. This was done with the help of a cooling trap filled with $N_{2(l)}$ connected to a rotary vane pump (Oerlikon Leybold vacuum PT 361TRI-VAC) (see Fig. 53). Several concavities towards the inside of the tube were melted in a circular arrangement ~2 cm above the crucibles. Accomplished was this with an oxyhydrogen torch and the force of the vacuum (see Fig. 54, step A). Next step was placing a quartz glass inlay with a diameter of 8, 10 or 12 mm inside the with Ar refilled tube. The inlay itself was closed at the bottom. The concavities stopped the inlay from touching the crucibles to ensure no mechanical stress (see Fig. 54, step B and bottom, left). This inlay enabled a proper sealing, because it prevents the molten wall to burst. The filled tube was again assembled to the vacuum line, evacuated and flushed 3-times with Ar to remove air from the tube. After reaching a vacuum of ~$1.13 \cdot 10^{-2}$ to ~$9.87 \cdot 10^{-3}$ mbar was the tube sealed under dynamic vacuum with the mentioned torch. Thus, the walls of the tube were fused with the inlay. At this step it was very important that the distance around the inlay to the tube wall was evenly distributed to achieve a homogeneous thickness of the molten glass (see Fig. 54, step C). Then closing the tube was accomplished by melting several concavities towards the inside of the inlay in a circular arrangement until they touched each other (see Fig. 54, step D). Last step was separating the quartz glass ampule from the rest of the evacuated tube by heating the thickest part at the closed inlay until it was completely molten, while pulling it off (see Fig. 54, step E).

The hermetically sealing of the ampules was tested by applying voltage with a “Tesla-gun” (small Tesla coil). The sealing was successful if a purple glow did appear. The glow resulted from a plasma coming from a low amount of O_2 (air) left in the ampule which got partially ionize by the applied voltage. When the ionized species fell back from the exited energy state to a lower state, was purple light emitted. However, if the ampule was not hermetically sealed no glow was visible due to the higher content of molecules in the ampule resulting in more collisions between the molecules and smaller mean free path distributing the energy evenly. Hence not enough energy would be present to generate a glow. Finally, were the ampules engraved for labeling (see Fig. 54, bottom, right).

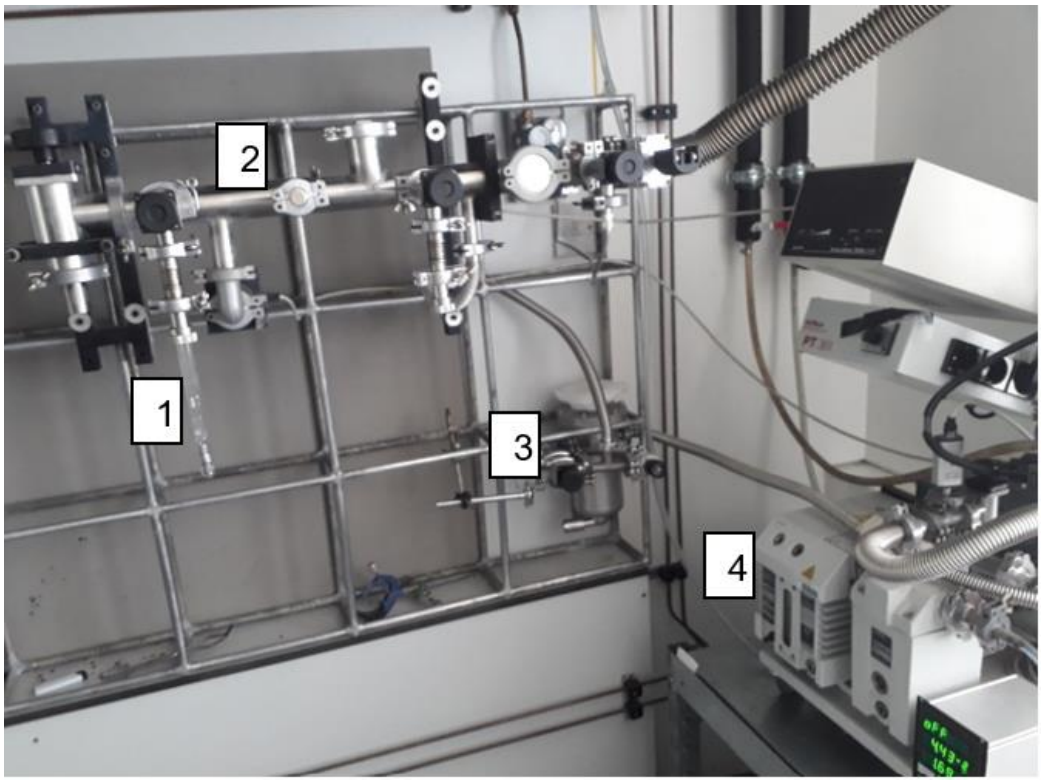

Figure 53 Vacuum system with assembled quartz glass tube…1 (vacuum line…2, connected through cooling trap…3, to the rotary vane pump…4).

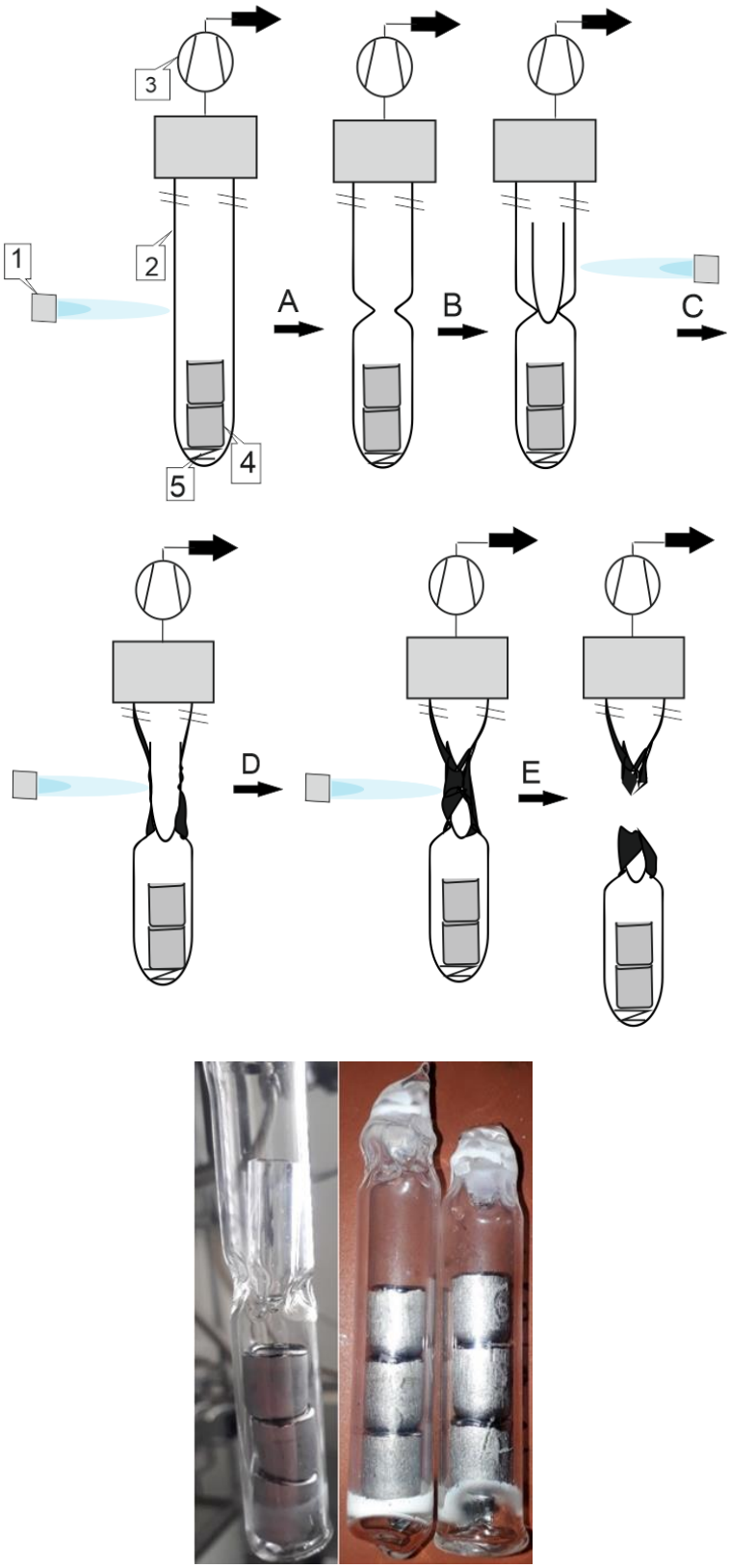

Figure 54 Top: Schematic of the encapsulation process. 1…H_2/O_2-torch, 2…quartz glass tube, 3…vacuum rotary vane pump, 4…sealed Ta-crucibles, 5…Ta-spacer. Modeled with CorelDraw 2018. Bottom, left: quartz glass tube filled with 3 closed Ta- crucibles before sealing of the tube. Bottom, right: 2 sealed quartz glass ampules filled with samples in closed Ta-crucibles.

4.2 Alloy preparation (alloying)

9 different methods for the preparation of the alloys were tested to ensure homogeneity of the molten phase:

1. The ampules were placed in a muffle furnace (Nabertherm), see Fig. 55, and heated slowly from room temperature to 700 °C within ~2 h. This temperature was chosen because it was well above the liquidus of the In-Li systemaccording to the literature. Additional 30 min under isothermal conditions ensured fully molten samples. They were homogenized by turning the ampules up-side down and heating them again for 30 min at 700 °C. This was done 2- to 6-times. Next were the ampules quenched by putting them vertically into a water bath to cool the melt fast down to room temperature. That facilitates a good contact to the bottom of the crucible improving DTA measurements.
2. The 2nd method was identical to the 1st, however a temperature of 900 °C instead of 700 °C was applied.
3. The ampules were placed in a muffle furnace and heated slowly from room temperature to 700 °C within 2 h. After additional 30 min were the ampules turned up-side down and heated again for 30 min at 700 °C. This was done twice identical to the 1st method. Then were the ampules left for further 24 h at 700 °C. At last were the ampules quenched with water to room temperature as described before.
4. The sample was sealed in a Ta-crucible and heated to 1100 °C for 15 min under dynamic ultrahigh vacuum of ~$5.00 \cdot 10^{-4}$ to ~$1.50 \cdot 10^{-4}$ mbar by an induction furnace (see Fig. 55). Eventually was the crucible cooled down to room temperature by shutting the furnace off. The vacuum system was a combination of a turbomolecular pump and a rotary fane pump (Pfeiffer DCU). The temperature was measured by a pyrometer connected through an optical fiber to the bottom of the crucible. The water-cooled induction coil was powered alternating current (TIG 5/300 of Hüttinger Elektronik).

Figure 55 Left: Induction furnace. The display in the left corner shows the pressure in mbar, the display in the right corner shows the temperature of the crucible. Right: Muffle furnace of Nabertherm.

5. The ampules were placed in a muffle furnace and heated from room temperature to 160 °C within 2 h. This temperature was chosen because it was above the melting point of In but beneath the melting point of Li, probably enabling a better covering of the solid Li with molten In. This should improve the homogenization and prevent $Li_{(l)}$ from wetting the crucible walls too much, which could counteract the mixing. After additional 24 h under isothermal conditions were the ampules heated to 700 °C as fast as possible. Fast heating should reduce the risk of separation. Additional 30 min under isothermal conditions ensured fully molten samples. They were mixed by shaking and turning the ampules up-side down and heating them again for 30 min at 700 °C. This was done 8-times. At last were the ampules cooled down to room temperature by quenching with water or by cooling overnight in the turned off furnace.
6. The ampule was placed in a muffle furnace and heated from room temperature to 160 °C within 1 to 2 h. After additional 30 to 48 min under isothermal conditions was the ampule heated to 700 °C as fast as possible. Additional 30 min under isothermal conditions ensured fully molten sample. The sample was mixed by turning the ampules up-side down and heating it again for 30 min at 700 °C. This was accomplished 6- to 10-

times. Then was the temperature reduced to 650 °C within 1 h and held there for another hour. Eventually was the sample furnace-cooled to 610 °C within 48 h to counter any non-equilibrium crystallization products (Scheil-solidification) and held there for 1 to 16 h. Then was the sample cooled down to 550 °C within 24 h and annealed at this temperature for 1 day. Finally, was the ampule quenched by putting it vertically into a water bath to cool the melt fast down to room temperature.

7. The 7th method was identical to the 6th, however after quenching was the ampule and the crucible opened inside the glovebox for powdering and homogenization by a WC-mortar. After removing a representative part of the sample for XRD measurement, was the rest sealed in a crucible and an ampule. Next was the ampule fast heated from room temperature to 700 °C and held there for 30 min. After shaking was the ampule furnace-cooled to 610 °C within 48 h and held there for 1 h. Further cooling to 550 °C within 24 h and annealing at this temperature for 3 days was carried out. The last step was quenching by putting the ampule into a water bath for cooling to room temperature.
8. The ampule was placed in a muffle furnace and heated from room temperature to 700 °C within 2 h. After additional 30 min at this temperature was the ampule mixed by shaking. Next was the ampule quenched with water to room temperature, turned up-side down and heated again for 30 min at 700 °C. This was repeated 6-times. Then was the temperature reduced to 650 °C within 1h and held there for another hour. Eventually was the sample furnace-cooled to 610 °C within 48 h and held there for 1 h. Next was it cooled down to 550 °C within 24 h and annealed at this temperature for 1 day. Finally, was the ampule quenched again with water to room temperature.
9. A sealed Ta-crucible containing the sample was encapsulated in a quartz glass ampule with 14 mm in diameter. This was done as described before, but with the difference that the inlay with 10 mm in diameter had direct contact to the top of the crucible. At the bottom was a larger Ta-spacer placed (see Fig. 56). This ensured a fixation of the crucible during strong shaking, which should prevent the fracturing of the evacuated ampule. This sample was heated in the muffle furnace within 2 h to 650 °C and

held at this temperature overnight (~14 h). On the next day was the sample heated to 800 °C within 1 h. After additional 30 min was the ampule placed inside a with fireclay and rock wool thermally isolated steel tube. Thoroughly shaking up and down by hand and mixing with a vortexer was accomplished. Then was the sample turned upside-down and heated again for 30 min at 800 °C. This procedure was done 3- to 6-times. At last was the ampule slowly cooled down to room temperature by turning the furnace off or fast cooled down by quenching in water to room temperature.

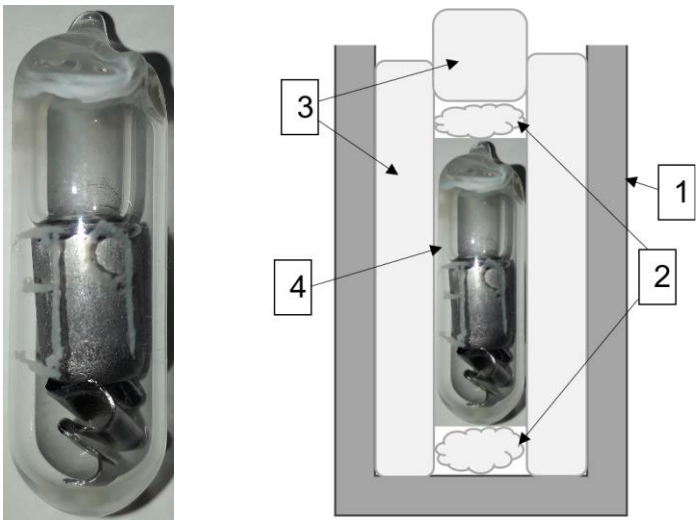

Figure 56 Left: Ampule containing sample In-Li 39 for alloy preparation method 9. Right: Schematics of the assembly for shaking by method 9 (1…steel tube, 2…rock wool, 3…fireclay cylinder with plug, 4…ampule with sample), Modeled with Microsoft Word.

4.3 DTA measurement

First the α-Al_2O_3 sample holder rod, equipped with a specimen plate to carry the Ta-crucibles inside of the electric resistive heating SiC-furnace of the heat flow DTA (Netzsch DSC 404 F1, software: Netzsch software Proteus® 6.1.0., see Fig. 57) was cleaned. This was done by heating it under vacuum from 30 to 1200 °C and eventually to 1300 °C while flushing it with dry, O_2-filtered Ar until it cooled down to 30 °C. That procedure resulted in an almost “sputtering-like” effect removing residual contaminations especially from the thermocouples. Next was the calibration of the thermocouples (S-type) via a linear fit of measured melting points of multiple elements, plotted against their melting points from

literature.[97] These elements were Cd (320.9 °C), In (156.2 °C), Ag (961.9 °C) and Sn (323 °C). Measured was at 20 ml/min Ar flow and a heating rate of 5 K/min.

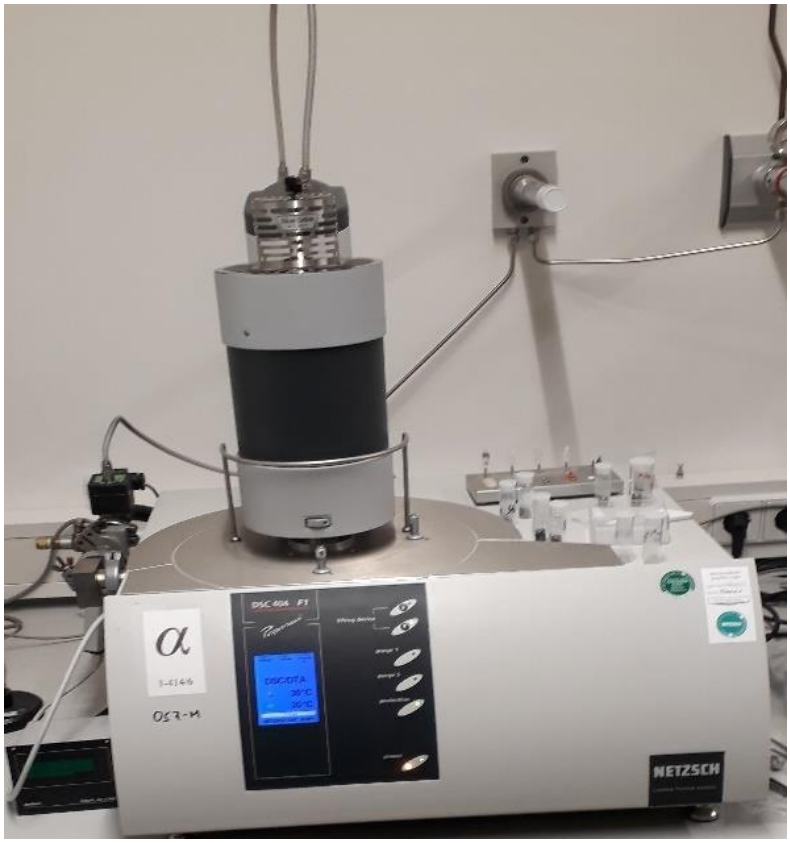

Figure 57 DSC 404 F1 of Netzsch with SiC-furnace used for DTA measurements.

Eventually was a sealed Ta-crucible filled with a NIST (National Institute of Standards and Technology) SRM 720 standard α-Al_2O_3 single crystal as reference material, placed on the back of the DTA sample holder. The reference material with a mass of ~50 mg was sealed under Ar in the glovebox by the arc furnace mentioned before. The quenched quartz glass ampules containing the samples sealed in a Ta-crucibles were opened by crushing. The Ta-crucible with the sample was placed on the front of the sample holder. Then was the system purged to remove all O_2 by evacuation to ~$2.4 \cdot 10^{-1}$ mbar and flushing 4-times with Ar.
Measured was under 20 ml/min Ar flow with following temperature program: 1st step was heating from room temperature to 30 °C with 15 K/min. After 2 h of thermal equilibration followed a heating step to the programed maximum temperature with a ramp of 5 K/min. Then followed cooling to 30 °C with a cooling rate of 5 K/min. This heating/cooling cycle was repeated. The maximum temperature

was adapted depending on the liquidus lines from the literature [50][52] (see Fig. 58 and 59).

Num	Mode	°C	K/min	pts/min	hh:mm	STC	PG:Ar	Vac
---	Initial	25,0		4x E+F		1	20,0	0
1	Dynamic	30,0	15,000	600,00	00:00	1	20,0	0
2	Isothermal	30,0		20,00	02:00	1	20,0	0
3	Dynamic	400,0	5,000	75,00	01:14	1	20,0	0
4	Dynamic	30,0	5,000	75,00	01:14	1	20,0	0
5	Isothermal	30,0		20,00	02:00	1	20,0	0
6	Dynamic	400,0	5,000	75,00	01:14	1	20,0	0
7	Dynamic	30,0	5,000	75,00	01:14	1	20,0	0
8	Emergency	430,0					20,0	0
---	StdBy Heat.	20,0	40,000		00:00	1	20,0	0
---	StdBy Iso	20,0			01:00	1	0,0	0

Figure 58 Temperature program table of the measurement of sample In-Li 6, programed with the Netzsch software Proteus® 6.1.0.

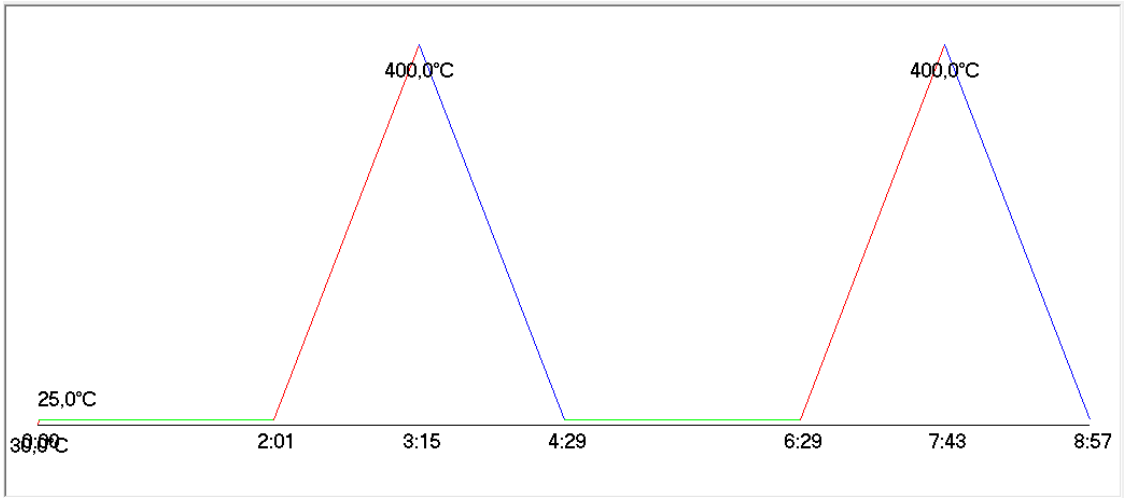

Figure 59 Plot of the temperature program (time (°C) vs. time (h:min)) of the measurement of sample In-Li 6, programed with the Netzsch software Proteus® 6.1.0.

Afterwards the resulting characteristic transition temperatures from the detected peaks of the thermal analysis were evaluated. Depending whether it was heating or cooling and on the transition type (invariant or not) the extrapolated onset (the intersection of the extrapolated baseline and the tangent of the signal peak) or the peak maximum was calculated.

4.4 3D-heat flow calorimetry measurement

After DTA measurement Calvet-type heat flow 3D-DSC (C80 - Seteram Instrumentation KEP Technologies group, software: CALISTO Evaluation and Processing) was used to get further, more precise thermal data on samples, which were slow cooled by DTA, within a temperatur range of 30 to 300 °C (see Fig. 60).

Figure 60 Heat flow 3D-DSC - C80 Clavet calorimeter of Seteram.

Therefore a sealed Ta-crucible with a NIST SRM 720 standard α-Al_2O_3 single crystal as reference material as well as a Ta-crucible with the sample were placed in a standard stainless steel measuring cell with cylindrical shape and cap. The cell with the reference material was transfered into the back and the cell with the sample was transferred into the front sample tube inside the furnace. A heating rate of 1 K/min was applied. The calibration was accomplished with measured melting points of the elements In, Li and Sn, plotted against the melting points from the literature [97] and a least square fit to a polynomial of 2nd order.

The samples were measured under air with following temperature program: 1st step was heating from room temperature to 30 °C with 10 K/min. After 3 h of

thermal equilibration followed a 2nd heating step to 300 °C within 1 K/min. Then was again thermally equilibrated at this temperature for 3 h. Next was cooling to 30 °C with a cooling rate of 1 K/min. This heating/cooling cycle was repeated (see Fig. 61 and 62).

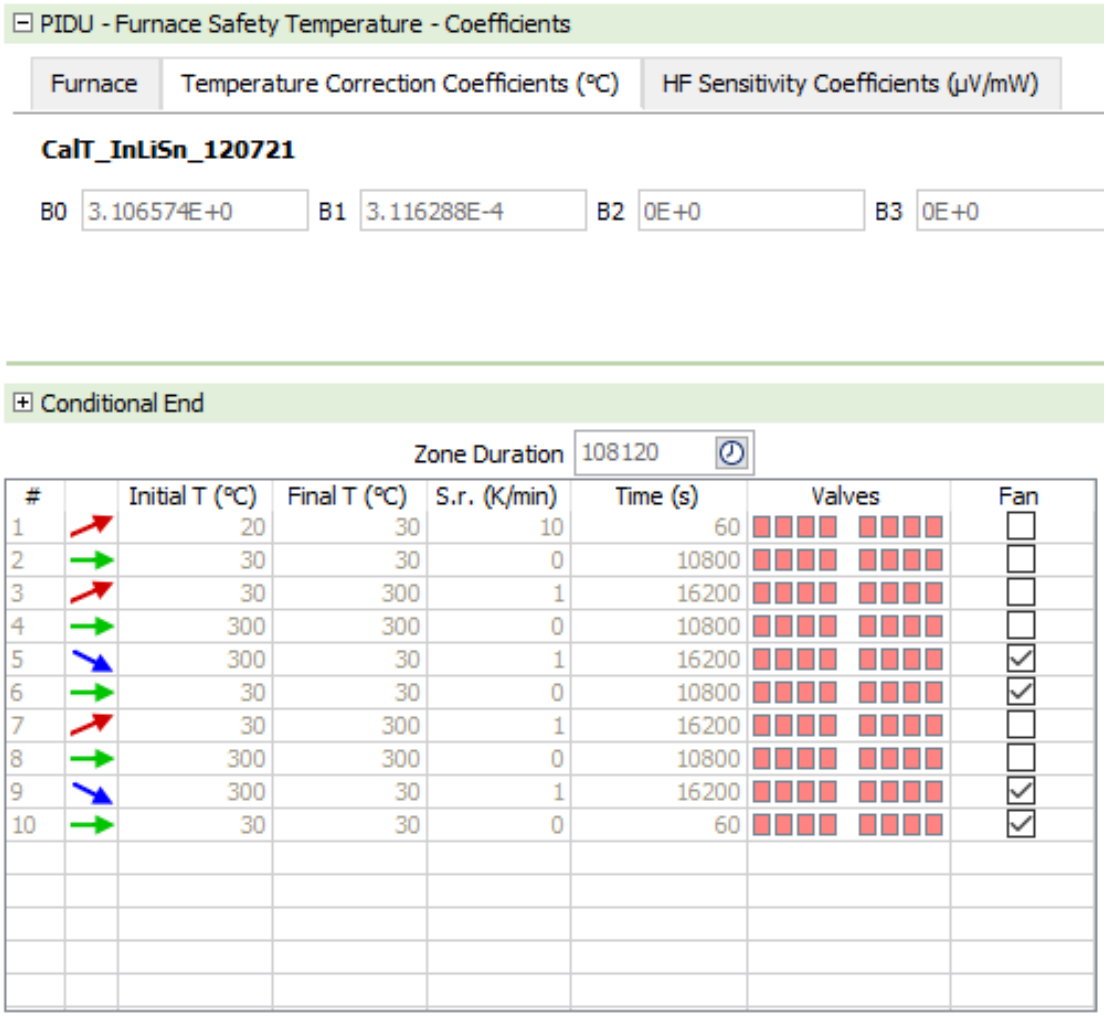

#		Initial T (°C)	Final T (°C)	S.r. (K/min)	Time (s)	Valves	Fan
1	↗	20	30	10	60		☐
2	→	30	30	0	10800		☐
3	↗	30	300	1	16200		☐
4	→	300	300	0	10800		☐
5	↘	300	30	1	16200		☑
6	→	30	30	0	10800		☑
7	↗	30	300	1	16200		☐
8	→	300	300	0	10800		☐
9	↘	300	30	1	16200		☑
10	→	30	30	0	60		☑

Figure 61 Top: Used temperature correction coefficients for Calvet sensor calibration. Bottom: Temperature program table used for all sample measurements, programed with SETSYS Evaluation.

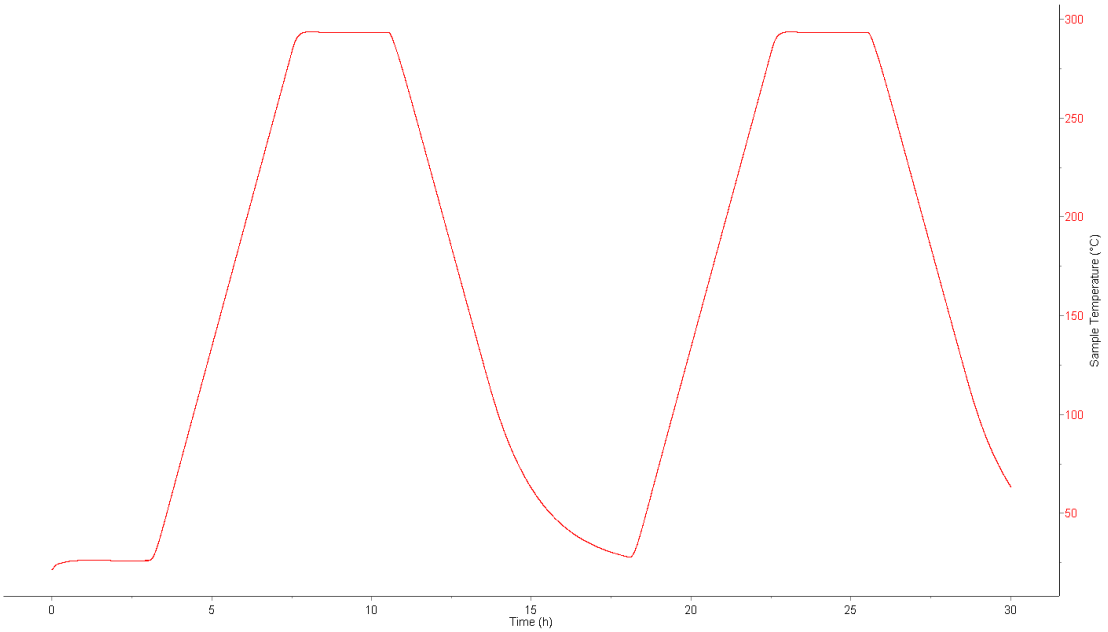

Figure 62 Plot of the temperature program (Time (h) vs. Sample Temperature (°C)) used for all sample measurements, programed with SETSYS Evaluation.

Afterwards the characteristic temperatures from the detected reactions of two heating/cooling cycles were calculated via the onset from baseline for peak integration. The heat flow, which was calculated from the peak area via integration was not of interested for this investigation (DTA mode).

4.5 Heat treatment

After the DTA and 3D-DSC measurements the Ta-crucibles were again sealed in quartz glass, homogenized and quenched as mentioned before (see section “4.1 Weighing and sealing of the samples & 4.2 Alloy preparation (alloying)”). Quenching of the liquid phase led to smaller crystals with high surface to volume ratio, facilitating solid-state diffusion on annealing.

The sealed samples were annealed for about 1 to 2 months at 140, 220, 245, 327, 360, 380 and 550 °C depending on the composition. The aim of annealing was to establish the respective phase equilibria at the chosen temperatures and compositions via solid-state reaction. After annealing the ampules were quenched in water to room temperature to freeze the obtained equilibrium-phase(s) at the respective temperatures (see Fig. 63). The quartz glass ampules were opened by crushing to get the Ta-crucibles out.

Figure 63 Annealed and quenched sample In-Li 3 (upper crucible) and In-Li 4 (lower crucible) in quartz glass ampule.

4.6 XRD measurement

For the measurement of the air and moisture sensitive In-Li samples flat zero-background sample holders with domes were used. They consist of a Si single crystal with a certain non-diffracting orientation covered by a dome of amorphous polycarbonate PC to ensure airtightness. These sample holders were cleaned with ethanol and if necessary, by sonication in ethanol for a couple of minutes to remove any contaminating residue.

Next were the crucibles opened inside the glovebox with a side-cutter and combination pliers. Brittle samples were powdered by a WC-mortar. The powder was carefully distributed onto the sample holder covered in a thin layer of dry petroleum jelly to fix the powder on the surface. Some samples were too ductile for powdering, but too soft for filing by a diamond file. Hence, these samples were cut and flattened before they were placed on the sample holder.

The sample holder was closed airtight with the mentioned dome, shuttled out of the glovebox and placed at the autosampler of the XRD. An older and a newer version of the Bruker D8 Advance Diffractometer with Bragg-Brentano pseudo-focusing geometry was used. Both were equipped with an X-ray tube powered with 40 kV and 40 mA for CuK_α radiation with average wavelength of 1.5418 Å. The older XRD had a fixed incident slit with a Ni-filter for filtering CuK_β radiation and a 1D Lynx-Eye 1 Si-strip detector applied with 665 V (see Fig. 64), while the newer XRD had a variable incident slit for fixed sample illumination (which was

used) and a 1D Lynx-Eye 2 Si-strip detector with a Ni-filter. Measured was in Θ/2Θ-goniometer-mode in the range of 2θ = 10 to 100° within 3 h (old XRD) and in Θ/Θ-goniometer-mode from 2θ = 10 to 120° within 2 h with a step size of 0.01° (new XRD).

Figure 64 “Old” Bruker D8 Advance Diffractometer. Left: X-Ray tube. Middle: Autosampler loaded with 3 sample holders with dome, containing powdered In-Li samples under dry Ar. Right: 1D-detector.

For the phase identification and quantification by Rietveld refinement the software TOPAS-64 7.13 of Bruker was used. The necessary information of the known crystal structures was gained from the ICSD and Springer Materials data base and the correct crystallographic setting was checked. First refinement step included the implementation of the emission profile, the instrumental parameters and background as well as geometric correction. The chosen emission profile for the CuK_α radiation was the empirical Berger model with 5 individual peaks (see Fig. 65).

	Area	WL (Å)	Lortz. HW (r	Gauss HW (r
1	0.0159	1.534753	3.6854	0
2	0.5691	1.540596	0.437	0
3	0.0762	1.541058	0.6	0
4	0.2517	1.544410	0.52	0
5	0.0871	1.544721	0.62	0

Figure 65 Used Berger model for CuKα radiation of TOPAS-64 7.13 of Bruker.

An instrument parameter file of the with LaB_6 standard reference material calibrated XRD device was loaded for refinement (fundamental parameter approach, see Fig. 666).

	Use	Value
Goniometer radii		
Primary radius (mm)		217.5
Secondary radius (mm)		217.5
Equatorial Convolutions		
Point detector	☐	
Capillary	☐	
Linear PSD	☑	
2Th angular range of LPSD (°)		4
FDS angle (°)		0.68
Beam spill, sample length (mm)	☑	20
Correct Intensity	☑	
Tube Tails	☑	
Source Width (mm)		0.07
Z1 (mm)		-1
Z2 (mm)		1.3
Fraction		0.00187159
Axial Convolutions		
Full Axial Model	☐	
Finger_et_al	☐	
Simple Axial Model (mm)	☐	12

	Use	Value
Goniometer radii		
Primary radius (mm)		250
Secondary radius (mm)		250
Equatorial Convolutions		
Point detector	☑	
Receiving Slit Width (mm)	☐	0.1
FDS Shape, angle(°)	☐	1
VDS irradiated length (mm)	☑	10
VDS Scale Intensity	☑	
Capillary	☐	
Linear PSD	☐	
Tube Tails	☑	
Source Width (mm)		0.2
Z1 (mm)		-0.026
Z2 (mm)		0.27
Fraction		0.082
Axial Convolutions		
Full Axial Model	☑	
Source length (mm)		12
Sample length (mm)		20
RS length (mm)		16
Prim. Soller (°)	☑	2.5
Sec. Soller (°)	☑	2.5
N Beta		30
Finger_et_al	☐	
Simple Axial Model (mm)	☐	12

Figure 66 Instrument parameter files for the divergent beam of TOPAS-64 7.13 of Bruker. Left: “Old” Bruker D8 Advance Diffractometer file. Right: “New” Bruker D8 Advance Diffractometer file.

The background correction was described empirically by a Chebyshev polynomial of 7th order with a 1/x term. Geometric correction like the sample displacement correction was applied to counter the peak shift, while the Lorentz-Polarization factor was fixed at 0. One should mention that the background was also improved by inserting peaks at 2Θ = ~20° (old XRD) and at ~20 and ~45° (new XRD). At these angles appeared a “bulge” (very broad reflection) of the amorphous PC-dome. However, this led to less accurate Rwp values. Next step was the testing and refinement of suitable crystal structures. This was done by refining the lattice parameters and the scaling factor as well as the average crystalline domain size (Scherrer equation) using the fundamental parameter approach. Sometimes it was necessary to refine the strain parameter with a Lorentzian function. This was for example necessary when ductile (In) phase was deformed during sample preparation, because no stress annealing was applied.
Last step was the refinement of the sites of all used phases. If required, then was the isotropic thermal displacement parameter (temperature factor) of every site simultaneously refined. If a non-physically value like ≤ 0 Å^2 or a value like ≥ 1.5 Å^2 appeared, then one common factor was used for every site. Eventually was the occupation factor of the sites refined, when the mechanism of the constitutional defect formation was known. At last was if applicable the refinement of free atomic positions accomplished.

4.7 SCXRD measurement

For the depiction of single crystals, the sample was finely powdered with a WC-mortar inside the glovebox and placed between two microscope slides covered with dry petroleum jelly. Next step was to choose a suitable single crystal with an approximate size of 0.1 to 0.5 mm in diameter. This was accomplished outside the glovebox by assistance of a reflected light microscope with zoom function (Leica M165 C). The chosen single crystal remained coated with petroleum jelly as protection layer against the atmosphere as well as for adhesion. It was mounted on top of a glass fiber sample holder with the help of an acupuncture steel needle. Next was the sample holder placed on the goniometer head of the 4-circle κ-goniometer of the SCXRD (Enraf Nonius FR590, see Fig. 67) to align the crystal with the X-ray beam by adjusting its position with the aid of a microscope camera. The SCXRD was equipped with a Mo X-ray tube applied with

50 kV and 30 mA for a wavelength of 0.7107 Å (MoK_α), a graphite monochromator and a 300 µm-capillary collimator. As 2D-detector was a CCD, combined with a scintillator and fiber optics (Nonius Kappa CCD) in use, which was cooled to -60 °C.

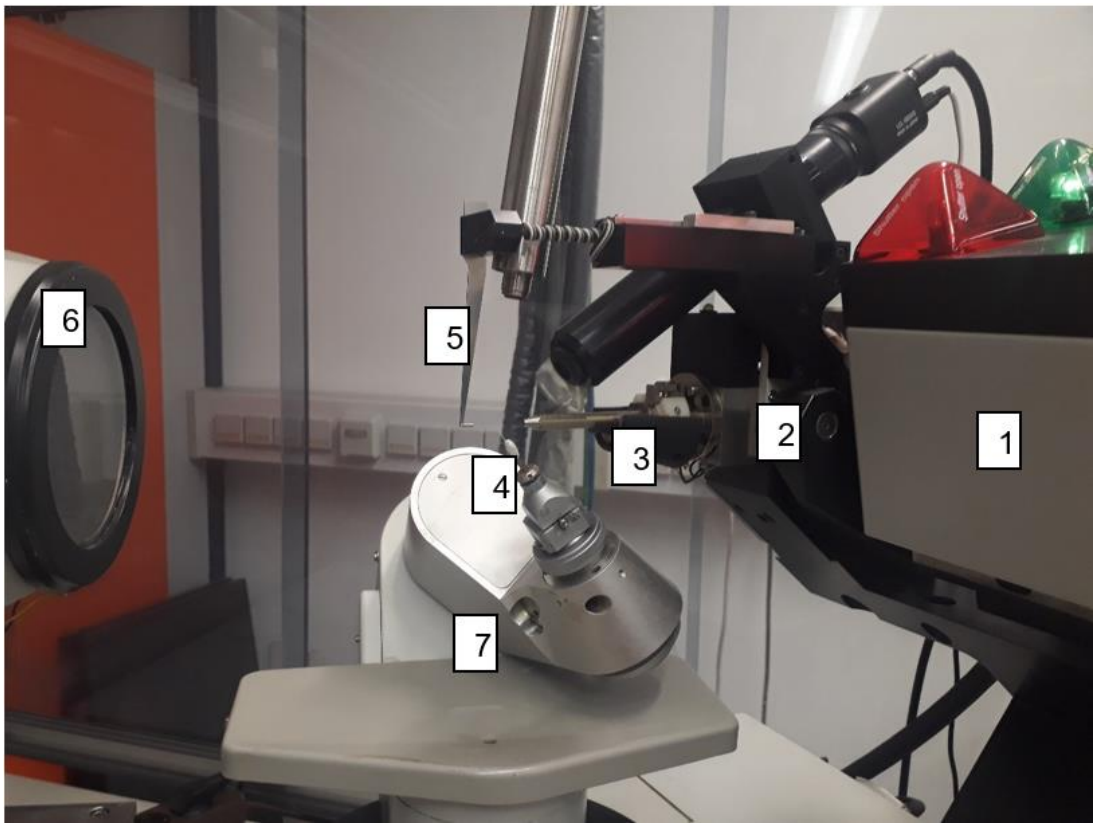

Figure 67 Used Enraf Nonius FR590 4-circle SCXRD with goniometer. 1…X-Ray tube, 2…monochromator, 3…collimator, 4…sample holder with mounted single crystal, 5…beam stopper, 6…2D-detector, 7…4-circle κ-goniometer.

Eventually was the quality of the chosen crystal investigated by measuring a couple of reflections by a detector distance of dx = 32 cm and θ = κ = ω = 0°, while rotating the ϕ-axis for the scan. If no suitable phase pure single crystal with the mandatory size was found, then the growth of bigger single crystals was tried to accomplish. This was done by sealing an aliquot of the powdered sample in a Ta-crucible inside a quartz glass tube as described before, followed by appropriate heat treatment according to the known phase diagrams from the literature [50][51][52][70][74] (see section “5. Results and discussion”).
Further ϕ-scanning and least-square refinement of some reflections was accomplished for cell refinement (preliminary indexing). The next step was choosing a

measurement program for data collection with suitable parameters (angles, detector distance, step size, scan rate, number of reruns, etc.). For additional protection of the sample against the atmosphere during longer measurement was a dry $N_{2(g)}$-stream with a temperature of 293 K in use. Then data integration was accomplished for indexing and intensity evaluation, so background correction was applied. Afterwards was the data idealized by data scaling through Lorentz, polarization and absorption correction. Latter was carried out by the multi-scan method (semiempirical absorption correction with equivalent reflections). Data collection, integration and scaling were done via the software COLLECT.
Phasing was done with a combination of the direct methods and Patterson summation via the software SHELXS-97. At last was the crystal structure refined by full-matrix least square techniques applied on the intensity data and by difference Fourier synthesis through the software SHELXL-97.

4.8 F-AAS and TXRF measurement

For the F-AAS and TXRF investigations aliquots of ~10 mg of each selected sample was weighed directly into a separate 50 ml Erlenmeyer flask or beaker using the analytical balance inside the glovebox. Next step was the digestion of the samples. So, half concentrated $HNO_{3(aq.)}$ was made from 69 wt.% HNO_3 p.a., (63.01 g/mol, 1.41 g/ml (20 °C)) from Merck via 1:1 dilution with Millipore water. A small amount of the half concentrated $HNO_{3(aq.)}$ was added slowly to the samples, leading to a highly exothermic reaction. The vessels were slowly heated under stirring through a magnetic stirrer, while closed by watch glasses for reflux. Eventually were the resulting solutions cooled down to room temperature, transferred into clean 100 ml volumetric flasks and filled-up to the mark with Millipore water. For better handling were ~50 ml aliquots taken and transferred to 50 ml Falcon tubes.
The measuring range of the F-AAS was about 0.3 to 5 mg/l for Li and about 6 to 100 mg/l for In. Latter range for In was also used for the TXRF investigations. As a result, dilution of certain samples, based on the weighed element content, in the ratio 1:10 for Li and 1:1 for In was necessary.
For external calibration via non-linear fit were 5 standard solutions for each element mandatory (see Fig. 68 and 69). Hence, stock solutions of 10 mg/l Li and 100 mg/l In were prepared by 1:100 dilution of a 1 g/l Li and 1:10 dilution of a

1 g/l In TraceCert© standard solution from Sigma Aldrich. The resulting stock solutions were again diluted in the ratio 1:1 followed by further dilution to produce standards with 5, 2.5, 1.25, 0.625 and 0.3125 mg/l Li and standards with 100, 50, 25, 12.5 and 6.25 mg/l In. This was accomplished through 100 to 1000 µl and 1 to 10 ml piston pipettes, 100 ml volumetric flasks and 50 ml Falcon tubes. All standards and samples were diluted with a solution of 2 %HNO_3.

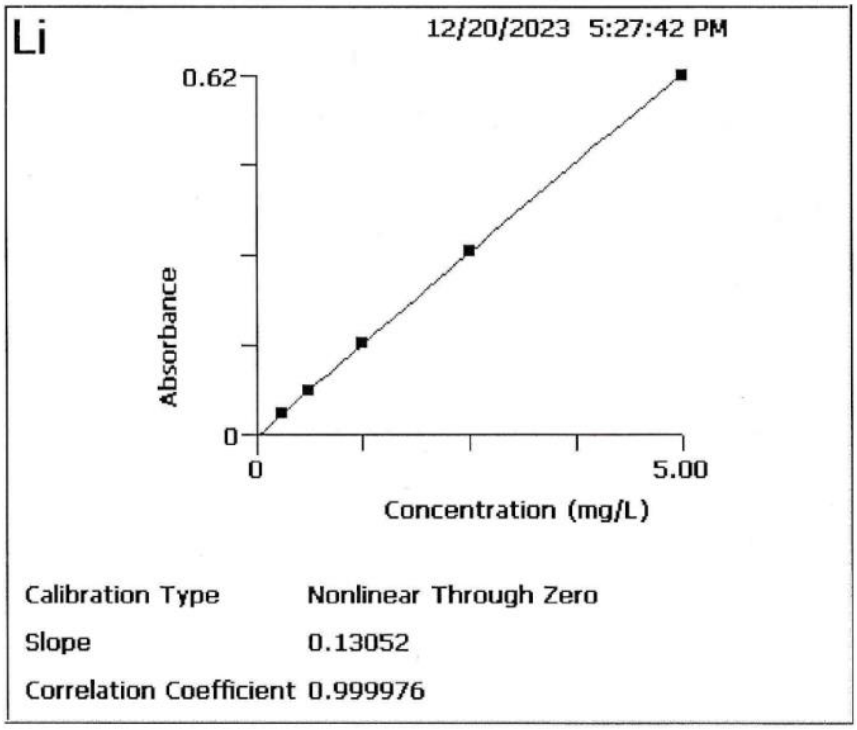

Figure 68 Calibration curve (Absorbance vs. Concentration (mg/l)) for Li, measured by F-AAS (Perkin Elmer AAnalyst 200).

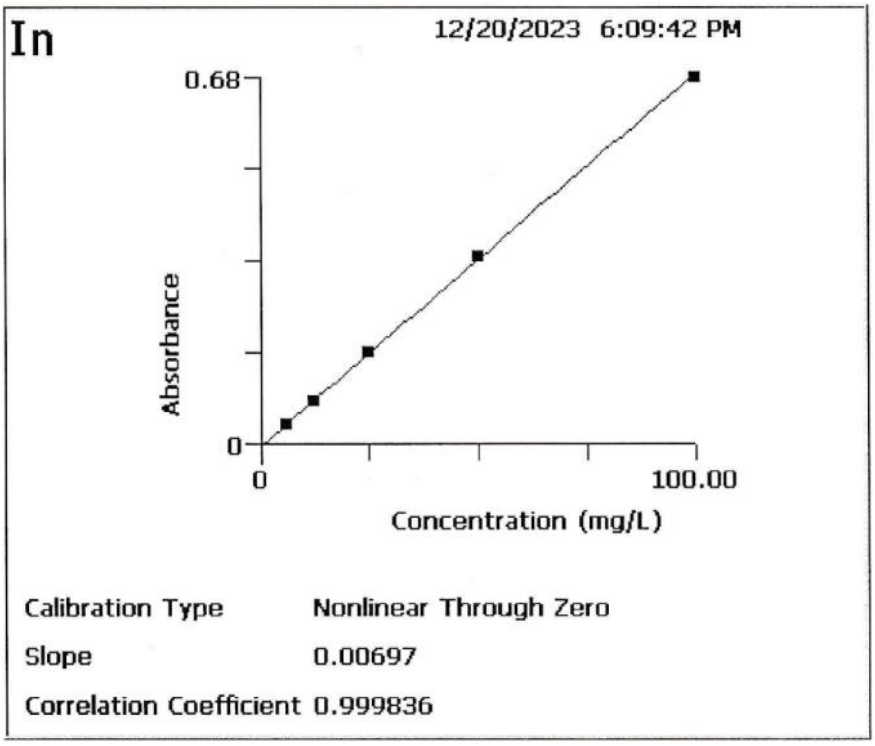

Figure 69 Calibration curve (Absorbance vs. Concentration (mg/l)) for In, measured by F-AAS (Perkin Elmer AAnalyst 200).

For the F-AAS measurement a Perkin Elmer AAnalyst 200 Atomic Absorption Spectrometer was used equipped with a HCL for In and another for Li, placed in a 4-lamp turret with automatic lamp alignment, slit and current selection. A 10 cm single-slot burner with an acetylene-air flame was used. The F-AAS had a double-beam echelle optical system with deuterium background correction and an echelle monochromator with a segmented solid-state detector.[99]

At first a solution of 2 %HNO_3 was measured as blank sample to determine the background followed by the standards with increasing concentration and finally were the diluted samples measured.

For the TXRF measurements 500 µl of a 5 mg/l Pt standard were placed into 1.5 ml Eppendorf tube for internal calibration. Then 500 µl of the diluted sample and 100 µl of a 0.3 g/l Polyvinyl alcohol PVA solution was added. Latter improved the homogeneity. The resulting solution was homogenized thoroughly by a vortexer. Then 5 µl of the solution were transferred onto the center of a cleaned 30 mm diameter quartz disc sample holder. This procedure was done for every sample. The loaded sample holders were dried in a vacuum through an IR-lamp and a water jet pump for about 30 min (see Fig. 70). Next were all discs put into

a sample cassette for auto-sampling and placed in the TXRF instrument for measurement. An TXRF (Bruker S2 PICOFOX) equipped with an X-ray tube for MoKα radiation powered by 50 kV and 1 mA, a multilayer monochromator and a Pelletier-cooled Si-detector was used [100]. The spectrum was evaluated by a profil bayes optimized fit.

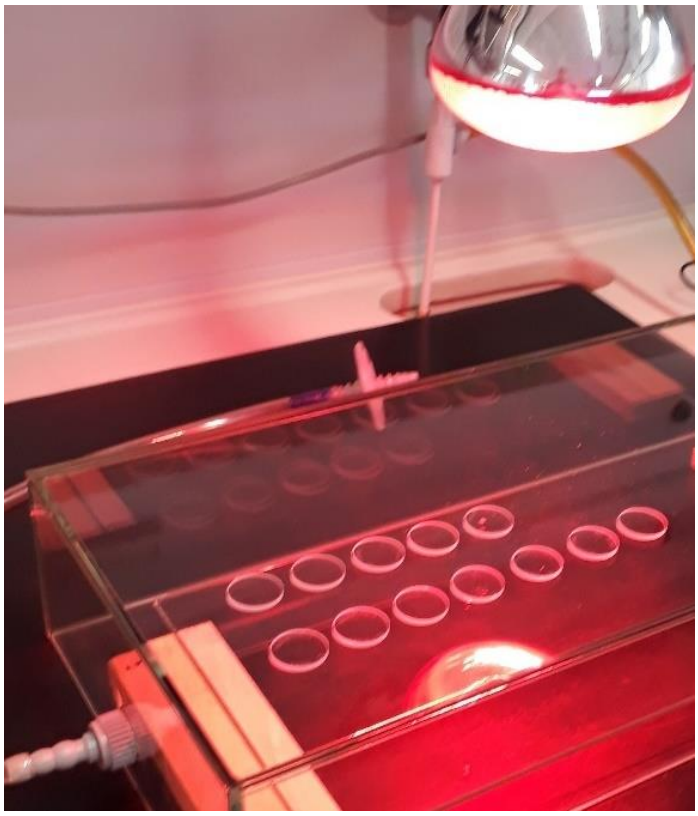

Figure 70 Prepared samples on TXRF discs drying under an IR-lamp in a vacuum.

5. Results and discussion

5.1 General remarks

In this diploma thesis the nominal stochiometric composition of the samples were chosen in a way to check the published experimental and calculated descriptions of the In-Li system as well as to explore into regions of concentration and temperature where no data is available yet. Accordingly, samples were prepared in a range of 5 to 95 at.% Li, annealed at 140, 220, 245, 327, 360, 380 and 550 °C (see Fig. 71 and Table 21) and investigated by DTA, Calvet-type 3D-DSC, XRD, SCXRD, TXRF and F-AAS whereby not all experimental methods were applied to each sample.

Metallographic techniques for microstructure analysis e.g. optical microscopy or scanning electron microscopy SEM with backscattering electrons, combined with electron probe microanalysis, EPMA, could not be accomplished because the high reactivity of the In-Li alloys with water and air prevented embedding, grinding and polishing of samples with the equipment available. Furthermore, a direct measurement of the Li-concentration with EPMA is not possible. The calculation of the Li content from remaining mass percent after the determination of the In-concentration is very inaccurate because of the high atomic mass relation $\frac{M_{In}}{M_{Li}} = 16.5$. Thus, all the valuable information from metallography like the number and composition of phases present within an alloy as well as the shape, size and distribution of the crystallites in the texture leading to the crystallization sequence, the presences of a miscibility gap in the liquid and the type of invariant reactions was not accessible. This lack of information on the In-Li investigations made the research much more challenging.

The samples In-Li 4, 6, 9, 10, 10-1, 14, 17, 21, and 32 were chosen to verify the existence of the binary compounds $InLi_9$, In_2Li_3, $InLi_{19}$, $In_{4+x}Li_{11-x}$ (x=1.05), In_4Li_5, $InLi_3$ and $In_{2+x}Li_{10-x}$ (x=1.59) as well as $In_{8+x}Li_{22-x}$ (x=0.1).

In-Li 25 and 26 were mainly used to identify the liquidus, thus they were not annealed. An attempt was also made to shed some light on the range of ~70 to 85 at.% Li at a temperature regime of ~300 to 390 °C. This was done with the samples In-Li 5, 11, 11-1, 12, 19, 23 and 24 as well as 38.

The rest of the prepared samples were used to estimate the homogeneity range of certain compounds or the extension of 2-phases regions. Other samples were

prepared to explore the InLi homogeneity range and to develop a suitable homogenization technique. Sample In-Li 19-1 which was prepared to grow larger single crystals for structure determination.

In the following phase diagrams (see Fig. 71) only samples used to construct a new In-Li phase diagram version were plotted.

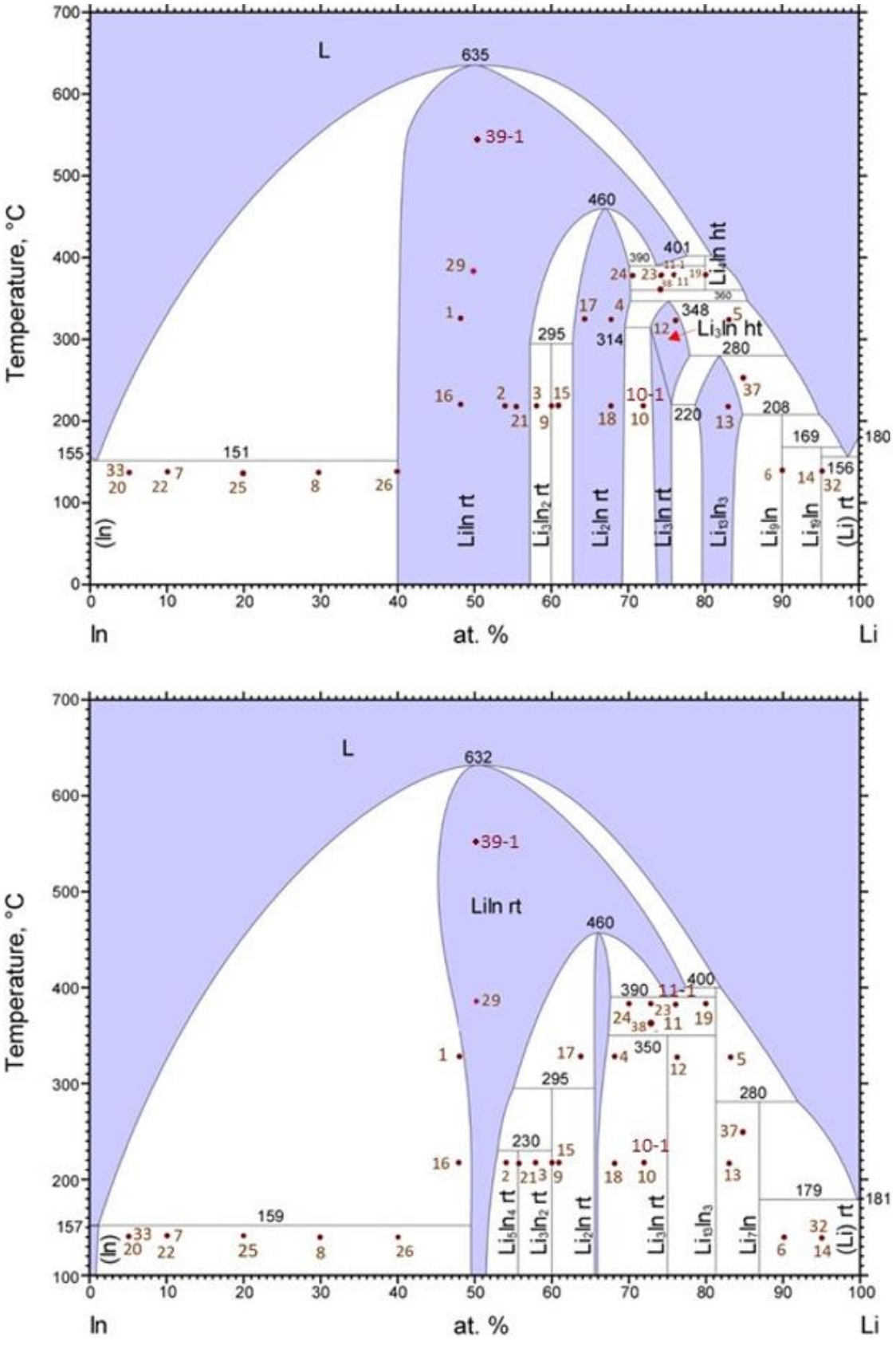

Figure 71 Prepared samples plotted on the In-Li phase diagram of Thümmel et al. (top) and of Sangster et al. (bottom).[50][52][101][102]

The following Table 21 shows all prepared samples with their planned, weighed and measured Li-content, the alloy preparation/homogenization method and the annealing temperature and time.

Table 21 All In-Li alloy samples prepared

Samples relevant for In-Li phase diagram construction:						
Sample ID	**Planned content (at% Li)**	**Weighed content (at% Li)**	**Measured content (at% Li)[f]**	**Alloying method[g]**	**Annealing temperature (°C)**	**Annealing time (d)**
In-Li1	48.0	48.1	-	1	327	57
In-Li2	54.0	53.9	-	3	220	90
In-Li3	58.0	58.0	-	3	220	90
In-Li4	68.0	67.8	-	1	327	57
In-Li5	83.0	83.1	-	3	327	37
In-Li6	90.0	89.8	-	3	140	54
In-Li7	10.0	10.0	13.3	3	140	82
In-Li8	30.0	29.9	-	3	140	82
In-Li9	60.0	60.2	58.0	3	220	90
In-Li10	72.0	71.9	-	3	220	83
In-Li10-1	72.0	72.0	-	9	220	28
In-Li11	76.0	75.8	74.2	1	380	44
In-Li11-1	76.0	76.0	-	9	380	27
In-Li12	76.0	75.9	-	3	327	54
In-Li13	83.0	82.7	-	3	220	83
In-Li14	95.0	94.7	-	1	140	73
In-Li15	-	61.3	-	1	220	86
In-Li16	48.0	48.0	-	1	220	86
In-Li17	64.0	63.9	-	1	327	85
In-Li18	68.0	67.9	-	1	220	86
In-Li19	80.0	79.8	77.0	1	380	47
In-Li20	5.0	5.0	5.3	1	140	101
In-Li21	55.6	55.7	-	1	220	86
In-Li22	10.0	10.0	-	1	140	76
In-Li23	72.9	72.9	-	1	380	47
In-Li24	70.1	70.0	74.8	1	380	47
In-Li25	20.0	20.0	-	5	-	-
In-Li26	40.0	40.0	-	5	-	-
In-Li29	50.0	50.0	51.0	5	380	76
In-Li32	95.0	94.9	-	5	140	68
In-Li33	5.0	5.0	-	5	140	68
In-Li37	85.0	84.8	-	1	245	42

[f] Results calculated from Li-concentration in respect to weighed sample mass.

[g] See section “4.2 Alloy preparation (alloying)”.

In-Li38	72.9	73.0	-	1	360	42
In-Li39-1	50.0	50.0	-	9	550	29
In-Li14-1	95.0	94.9	-	-	-	-
In-Li20-1	5.0	4.3	-	-	-	-
Samples to test homogenization techniques and investigation of the InLi homogeneity range:						
Sample ID	**Planned content (at% Li)**	**Weighed content (at% Li)**	**Measured content (at% Li)**	**Alloying method**	**Annealing temperature (°C)**	**Annealing time (d)**
In-Li1-1	48.0	48.0	-	1	-	-
In-Li23-1	72.9	72.8	-	9	220	28
In-Li23-2	72.9	71.5	-	9	220	28
In-Li27	50.0	49.9	-	3	550	29
In-Li28	50.0	50.0	-	4	550	28
In-Li30	50.0	50.0	-	2	550	28
In-Li31	50.0	50.0	-	5	-	-
In-Li34	50.0	50.0	-	6	610	1
In-Li35	50.0	50.0	-	7	550	3
In-Li36	50.0	49.9	-	8	550	1
In-Li39	50.0	50.0	-	9	-	-
In-Li40	50.0	49.9	-	9	-	-
Sample to grow larger single crystals:						
Sample ID	**Planned content (at% Li)**	**Weighed content (at% Li)**	**Measured content (at% Li)**	**Alloying method**	**Annealing temperature (°C)**	**Annealing time (d)**
In-Li19-1	80.0	80.0	-	-	390	7

In some cases after annealing a brown to silver-black coloring of the quartz glass ampule apeared either near the Ta-curcible walls or in the total ampule (see Fig. 72). This happened most likley due to the reduction of SiO_2 (quartz glass) by Li vapor, $Li_{(g)}$ forming SiO and Si. There was no indication of an untight welding joint of the crucible what leads to the conclusion that Li can diffuse through the crucible walls. The darker the quartz glass the more Li was probably released. The conditions enhancing the Li-diffusion in Ta supposedto be the annealing time and temperature as well as the Li-activity a_{Li} of the sample. However, no clear trend of discoloration of the quartz glass according to sample composition and annealing conditions could be observed.

Figure 72 Left- and right-side: Brown to silver-black colored quartz glass ampules with the samples In- Li 2, 3, 5, 9, 10, 13 and 12. In the middle: Clear quartz glass ampules with the samples In- Li 6, 7 and 8 for comparison.

In addition, sometimes a red coloration of the plasma during arc welding was noticed, caused by the evaporation and excitement of small amounts of Li.
However, there was no change of sample mass recognized, which did exceed the statistical weighing error of the balances used. Nevertheless, TXRF and F-AAS measurements were accomplished to verify the nominal stoichiometric composition of the critical samples In-Li 7, 9, 11, 19, 20, 24 and 29. The F-AAS results (see Table 22) showed no evidence of a significant loss of Li and the weighed content of Li and In could be confirmed, even so the relative error in samples with low Li-content is quite high. The mole fraction of Li, x_{Li} was calculated in respect to the weighed sample mass used for F-AAS measurement, while the mole fraction of In x_{In} was calculated by the difference of x_{Li} to 100 %.at.%. On the other hand, was x_{Li} and x_{In} calculated independent of each other in respect to the measured amount of Li or In respectively. Significant differences between the with F-AAS measured Li and In content and the weighed content are obvious, but the differences are not systematic and within an acceptable range of error.
The TXRF spectra showed besides the lines of In only Si from the quartz discs, Ar from air and Mo from the target of the X-ray tube as well as Pt of the internal standard. Hence, no other detectable impurities were in the samples. Unfortunately, the results of the TXRF measurements could only be used qualitatively due to the absence of the right correction term S_S/S_A (internal standard element

sensitivity/analyte sensitivity), crucial for quantification of In with an internal Pt standard.

Table 22 F-AAS results.

Results calculated from Li-concentration in respect to weighed sample mass:			**Weighed content x_{Li} (at.%)**
Samples ID	**x_{Li} (at.%)**	**x_{In} (at.%)** [h]	
In-Li7	13.3	86.7	10.0
In-Li9	58.0	42.0	60.2
In-Li11	74.2	25.8	75.8
In-Li19	77.0	23.0	79.8
In-Li20	5.3	94.7	5.0
In-Li24	74.8	25.2	70.0
In-Li29	51.0	49.0	50.0
Results calculated in respect to measured concentrations of both elements:			
Samples ID	**x_{Li} (at.%)**	**x_{In} (at.%)**	
In-Li7	13.6	86.4	
In-Li9	58.6	41.4	
In-Li11	73.8	26.2	
In-Li19	78.0	22.0	
In-Li20	4.7	95.3	
In-Li24	67.0	33.0	
In-Li29	48.7	51.3	

After 57 days of annealing at 327 °C a XRD measurement of In-Li 4 with 68 at.% Li was accomplished. The expected equilibrium phases were according to the phase diagram of ref. [50] $InLi_2$ or $InLi_2$ and $InLi_3$ according to ref. [52]. However, turned out that the sample was not in phase equilibrium because it contained four phases, $InLi_{(Li\text{-}rich)}$, (In), $InLi_2$ and LiOH. The latter is a hydrolyzation product of In-Li compounds or (Li), caused by humidity of the air which can penetrated the sealed XRD sample holder or by moisture contained in the petroleum jelly used for fixing the powder. As a consequence, the petroleum jelly dried in a rotavapor. It is to mention that (In) could also be a product of hydrolyzation of In-Li compounds, in combination with LiOH. However, (In) could have been also

[h] In-content calculated from difference of Li-content to 100 %.at.%.

present before hydrolyzation. None the less, whether $InLi_{(Li\text{-}rich)}$ nor (In) or (Li) should be stable according to literature. [50][52][101][102]

This leads to the conclusion, that the sample was not yet in equilibrium and the In-Li system must exhibits a quit slow solid-state interdiffusion.

Many other samples were not in phase equilibrium (see table beneath). (In) was found in some samples up to 75 at.% Li nominal composition. Similar difficulties were described by Debski et al. [103], they also found unwanted remains of (In) and/or (Li) after alloying.

All samples were of metallic grey color, but only samples with a Li-content of 48 to 85 at.% were of brittle nature. In contrary to samples with < 48 or > 85 at.% Li, which were ductile and soft. It was noticed that samples with > 85 at.% Li had a low surface tension and strong adhesion leading to the total coverage of the Ta-crucible walls, while samples with < 48 at.% Li had a higher surface tension resulting in the spherical shape of the sample (see Fig. 73).

Figure 73 Typical appearance of In-Li alloys in relation to an increasing amount of Li from left to right. In-Li 33 (left), In-Li 9 (middle) and In-Li 14 (right).

These results led to the conclusion that a combination of the slow solid-state interdiffusion, the creeping of $Li_{(l)}$ as well as its low density in respect to $In_{(l)}$ caused the severe liquid mixing and phase equilibration difficulties.
Different alloy preparation methods (see section “4.2 Alloy preparation (alloying)”) were tested on samples within the InLi region to counter the phase equilibration difficulties. Finally, alloying method 9 was the most promising method according to sample In-Li 40. However, it was not possible to prepare all samples again via method 9, due to time schedule reasons.

Only the samples In-Li 10, 11 and 23 were again prepared by method 9, labeled as In-Li 10-1, 11-1, 23-1 and 23-2. However, the latter 2 samples were only shaken and turned 3-times instead of 6-times. In addition, In-Li 23-1 and 23-2 were annealed at 220 °C instead of 380 °C due to strong oxidation of the Ta-crucibles. After annealing In-Li 10-1 and 11-1 were in phase equilibrium, but In-Li 23-1 and 23-2 showed, beside the expected phases $InLi_2$ and $In_{8+x}Li_{22-x}$ (x=0.1), also (In) and $In_{2+x}Li_{10-x}$ (x=1.59). This could be explained with the lower number of shaking and turning. Nevertheless, was alloying method 9 with ≥ 6-times of shaking and turning the key to bring most of the samples into phase equilibrium, which is crucial to model a phase diagram.

However, for samples within the InLi phase field also method 9 failed, probably due to the occurrence of metastable miscibility of InLi as well as a large metastable solubility of Li in (In) described below in section “5.4.5 The InLi phase region”.

Interestingly, the homogenization difficulties do not seem much influence DTA and Calvet-type 3D-DSC measurements. The DTA measurements were carried out after alloy preparation followed by Calvet-type 3D-DSC measurements to determine the temperatures of the occurring reactions at certain sample compositions.

Conventionally would a part of the already annealed sample be investigated by DTA or Calvet-type 3D-DSC respectively. However, this would have made an additional sealing step necessary, which was not done to save time and consumption of Ta-crucibles.

XRD measurements were used to identify and quantify the alloy phases and to measure the lattice parameters leading to information on e.g. non-stoichiometry of a phase.

5.2 DTA and Calvet-type 3D-DSC results

The results of the DTA and the Calvet-type 3D-DSC measurements of the heating cycles were listed in the Table 23 and 24. The temperatures (average of both heating cycles) of the reactions (thermal effects) were roughly categorized by the intensities (or areas) of the related peaks. Thus, strong peaks had a high intensity and weak peaks a low intensity relative to each other. The last temperature occurring in the DTA measurements was the liquidus, while the last temperature of

the Calvet-type 3D-DSC measurements was only identified as liquidus after comparison with the DTA results and the literatures.

Table 23 DTA results.

DTA (heating)			
Sample ID	**Liquidus (°C)**	**Strong peak (°C)**	**Weak peak (°C)**
In-Li1	623.4	-	615.0
In-Li2	627.5	-	-
In-Li3	619.8	-	-
In-Li4	571.30	463.0	337.3
		513.3	395.9
			472.5
In-Li5	386.6	265.3	-
In-Li6	305.1	191.1	264.2
		226.9	
In-Li7	-	159.1	-
In-Li8	511.3	158.3	-
In-Li9	603.9	337.1	-
In-Li10	526.0	338.9	363.8
		389.6	460.4
		488.3	
In-Li11	481.3	342.1	342.1
		353.1	370.6
		431.8	400.6
In-Li12	480.5	341.9	370.8
		352.3	406.8
		427.7	
In-Li13	393.6	-	266.2
In-Li14	229.8	190.5	-
In-Li15	613.6	327.0	594.4
		594.4	
In-Li16 (after annealing)	623.0	-	-
In-Li17	594.3	324.6	430.0
		564.6	
In-Li18	571.3	460.4	338.0
		513.7	396.3
In-Li19	423.0	263.1	-
		369.1	
		397.1	
In-Li20	-	156.1	-
In-Li21	624.6	-	-
In-Li22	-	156.0	-
In-Li23	510.6	333.2	-

		345.6	
		367.9	
		466.6	
		490.7	
In-Li24	547.7	337.3	356.7
		396.0	439.4
		494.5	
In-Li25	419.7	156.1	-
In-Li26	591.9	156.7	-
In-Li37	362.4	226.1	207
		258.3	
In-Li38	509.7	351.1	369.3
		468.3	
		493.3	
In-Li14-1	226.8	178.9	-
In-Li20-1	-	157.9	155.8

Table 24 Calvet-type 3D-DSC results.

Calvet-type 3D-DSC (heating)			
Sample ID	**Liquidus (°C)**	**Strong peak (°C)**	**Weak peak (°C)**
In-Li1	-	-	-
In-Li2	-	-	-
In-Li3	-	-	-
In-Li4	-	-	-
In-Li5	-	225.42	-
		262.04	
In-Li6	-	195.42	253.53
		227.09	
		281.03	
In-Li7	-	159.17	-
In-Li8	-	159.15	-
In-Li9	-	-	-
In-Li10	-	-	-
In-Li11	-	-	-
In-Li12	-	-	-
In-Li13	-	-	263.48
In-Li14	237.53	191.07	-
		227.20	
In-Li15	-	-	-
In-Li16 (after annealing)	-	-	-
In-Li17	-	-	-
In-Li18	-	-	-
In-Li19	-	267.34	-
In-Li20	217.26	159.30	-

In-Li21	-	-	-
In-Li22	-	159.11	-
In-Li23	-	-	-
In-Li24	-	-	-
In-Li25	-	158.94	-
In-Li26	-	159.00	-
In-Li37	-	227.02	-
In-Li38	-	-	-

5.3 XRD results

The results of the XRD measurements were listed in Table 25. The quality of the Rietveld refinement was described by the R-factor of the weighted pattern Rwp. Further, the identified phase, its mass fraction w and the lattice parameters were listed as well as the mechanical property and the most likely stable phases of the associated sample.

Table 25 XRD results.

XRD results contributing to the In-Li phase diagram modeling:							
Sample ID	**Rwp**	**Phase**	**w (wt.%)**	**Lattice parameters[i]**			
				a (Å)	**b (Å)**	**c (Å)**	**ß (°)**
In-Li4	3.048	(In) [j]	12.0	3.253(1)	-	4.944(3)	-
		$InLi_{(Li\text{-}rich)}$ [k]	25.0	6.764(3)	-	-	-
		LiOH [l]	21.2	3.55(3)	-	4.39(6)	-
		$InLi_2$	41.8	4.79(2)	10.01(2)	4.79(2)	-
In-Li5	2.23	In_3Li_{13}	100.0	13.392(5)	-	-	-
In-Li5-1	2.005	In_3Li_{13}	89.4	13.394(4)	-	-	-
		$InLi_4$ ht	10.6	5.8(7)	-	-	-
In-Li6	2.148	In_3Li_{13}	100.0	13.396(8)	-	-	-
In-Li7	2.718	(In)	100.0	3.256(1)	-	4.9390(2)	-
In-Li8	3.574	(In)	79.9	3.2562(7)	-	4.938(2)	-
		$InLi_{(Li\text{-}deficient)}$ [m]	20.1	6.77(8)	-	-	-
In-Li9	3.253	(In)	9.1	3.254(2)	-	4.946(5)	-
		$InLi_{(Li\text{-}rich)}$	41.0	6.778(3)	-	-	-
		In_2Li_3	49.9	4.768(6)	-	14.65(4)	-

[i] Only variable lattice parameters are mentioned e.g. only a for a cubic lattice, not α, β and γ.

[j] (In) or (In)' respectively, was mostly refined with 15 at.% Li-excess ($In_{1.7}Li_{0.3}$).[21]

[k] $InLi_{(Li\text{-}rich)}$ was mostly refined with 3 at.% Li-excess ($In_{0.985}Li_{1.015}$).[45][40]

[l] LiOH in a sample was produced by hydrolysis during XRD measurement.

[m] $InLi_{(Li\text{-}deficient)}$ was mostly refined with 3 at.% Li-deficiency ($InLi_{0.97}$).[45][40]

In-Li10	2.154	$InLi_2$	55.4	4.770(6)	10.04(1)	4.737(6)	-
		$In_{8+x}Li_{22-x}$ (x=0.1)	44.6	14.19(3)	4.737(8)	8.66(2)	105.8(2)
In-Li10-1	2.252	$InLi_2$	62.6	4.77(1)	10.09(3)	4.74(1)	-
		$In_{8+x}Li_{22-x}$ (x=0.1)	37.4	14.18(5)	4.74(1)	8.67(3)	105.8(3)
In-Li11	2.079	$InLi_2$	39.1	4.76(2)	10.08(5)	4.72(2)	-
		$InLi_4$ ht	5.4	5.77(2)	-	-	-
		$In_{2+x}Li_{10-x}$ (x=1.59)	55.5	4.711(4)	-	11.55(2)	-
In-Li11-1	2.261	$InLi_4$ ht	9.8	5.777(8)	-	-	-
		$In_{2+x}Li_{10-x}$ (x=1.59)	90.2	4.716(5)	-	11.55(2)	-
In-Li12	1.98	$InLi_4$ ht	23.5	5.773(7)	-	-	-
		$InLi_2$	26.8	4.78(1)	10.12(2)	4.72(1)	-
		$In_{2+x}Li_{10-x}$ (x=1.59)	43.5	4.712(6)	-	11.55(2)	-
		LiOH	6.2	3.46(0)	-	4.40(2)	-
In-Li13	2.155	In_3Li_{13}	91.9	13.393(3)	-	-	-
		$InLi_4$ ht	8.1	5.802(8)	-	-	--
In-Li14	2.104	In_3Li_{13}	54.6	13.394(5)	-	-	-
		LiOH	45.4	3.55(2)	-	4.34(4)	-
In-Li15	2.870	(In)	25.0	3.2543(9)	-	4.945(2)	-
		$InLi_{(Li\text{-}rich)}$	50.7	6.778(2)	-	-	-
		In_4Li_5	24.3	4.765(7)	-	8.81(3)	-
In-Li17	2.704	(In)	3.9	3.256(3)	-	4.944(7)	-
		$InLi_{(Li\text{-}deficient)}$	33.1	6.774(4)	-	-	-
		$InLi_2$	38.2	4.77(2)	10.07(3)	4.77(2)	-
		In_2Li_3	24.8	4.777(7)	-	14.68(4)	-
In-Li18	2.562	$InLi_{(Li\text{-}rich)}$	18.8	6.754(6)	-	-	-
		$InLi_2$	78.9	4.765(6)	10.04(1)	4.741(5)	-
		(In)	2.3	3.248(7)	-	4.9452)	-
In-Li19	2.449	$InLi_{(Li\text{-}rich)}$ [n]	74.1	6.691(5)	-	-	-
		$InLi_4$ ht	25.9	5.805(5)	-	-	-
In-Li19-1	3.737	In_3Li_{13}	73.2	13.38(1)	-	-	-
		$InLi_4$ ht	26.8	5.798(6)	-	-	-
In-Li20	2.187	(In)	100.0	3.256(1)	-	4.933(2)	-
In-Li22	2.472	(In)	100.0	3.254(3)	-	4.937(7)	-
In-Li23	2.133	(In)	6.1	3.254(2)	-	4.95(6)	-
		$InLi_2$	50.7	4.78(2)	10.08(4)	4.75(2)	-
		$InLi_{(Li\text{-}rich)}$	19.4	6.770(6)	-	-	-
		LiOH	23.8	3.54(3)	-	4.39(7)	-
In-Li23-1	2.123	(In)	2.2	3.253(4)	-	4.94(1)	-
		$InLi_2$	37.8	4.773(7)	10.05(2)	4.740(7)	-

[n] $InLi_{(Li\text{-}rich)}$ of sample In-Li 19 was refined with 25 at.% Li-excess, due to its exceptionally low lattice parameter a ($In_{0.5}Li_{1.5}$).

		$In_{2+x}Li_{10-x}$ (x=1.59)	21.7	4.78(2)	-	11.69(8)	-
		$In_{8+x}Li_{22-x}$ (x=0.1)	38.3	14.19(3)	4.74(1)	8.66(2)	105.8(2)
In-Li23-2	2.198	(In)	3.0	3.25(1)	-	4.94(0)	-
		$InLi_2$	42.4	4.78(1)	10.07(2)	4.75(1)	-
		$In_{2+x}Li_{10-x}$ (x=1.59)	17.7	4.79(1)	-	11.67(5)	-
		$In_{8+x}Li_{22-x}$ (x=0.1)	36.9	14.20(3)	4.74(1)	8.66(2)	105.8(2)
In-Li24	1.969	(In)	8.8	3.255(1)	-	4.945(3)	-
		$In_{2+x}Li_{10-x}$ (x=1.59)	40.4	4.789(8)	-	11.69(4)	-
		$InLi_2$	35.2	4.77(2)	10.10(5)	4.75(2)	-
		LiOH	15.6	3.55(4)	-	4.38(8)	-
In-Li25	2.328	(In)	84.2	3.255(2)	-	4.939(4)	-
		$InLi_{(Li\text{-}deficient)}$	15.8	6.776(6)	-	-	-
In-Li26	2.108	(In)	58.0	3.252(7)	-	4.93(2)	-
		$InLi_{(Li\text{-}deficient)}$	42.0	6.772(8)	-	-	-
In-Li32	2.209	In_3Li_{13}	47.5	13.392(7)	-	-	-
		LiOH	52.5	3.54(2)	-	4.35(4)	-
In-Li33	2.343	(In)	100.0	3.252(4)	-	4.94(1)	-
In-Li37	2.048	In_3Li_{13}	68.2	13.396(8)	-	-	-
		$InLi_4$ ht	31.8	5.83(3)	-	-	-
In-Li38	2.043	$InLi_2$	46.3	4.771(5)	10.05(1)	4.736(5)	-
		$In_{8+x}Li_{22-x}$ (x=0.1)	53.0	14.19(2)	4.733(7)	8.66(1)	105.8(1)
		(In)	0.7	3.25(1)	-	4.95(3)	-

Sample ID	Mechanical property	Most likely stable phase(s)
In-Li4	brittle	$InLi_2$
In-Li5	brittle	$InLi_4$ ht
In-Li5-1	brittle	L + $InLi_4$ ht
In-Li6	ductile, soft	(Li) + In_3Li_{13}
In-Li7	ductile, soft	(In) + InLi
In-Li8	ductile, soft	(In) + InLi
In-Li9	brittle	In_2Li_3
In-Li10	brittle	$InLi_2$ + $In_{8+x}Li_{22-x}$ (x=0.1)
In-Li10-1	brittle	
In-Li11	brittle	$InLi_4$ ht + $In_{2+x}Li_{10-x}$ (x=1.59)
In-Li11-1	brittle	
In-Li12	brittle	$InLi_4$ ht + $In_{8+x}Li_{22-x}$ (x=0.1)
In-Li13	brittle	In_3Li_{13}
In-Li14	ductile, soft	(Li) + In_3Li_{13}
In-Li15	brittle	In_2Li_3 + $InLi_2$
In-Li17	brittle	$InLi_2$ + InLi ⇄ In_2Li_3
In-Li18	brittle	$InLi_2$ + $In_{8+x}Li_{22-x}$ (x=0.1)
In-Li19	brittle	$InLi_4$ ht

In-Li19-1	brittle	
In-Li20	ductile, soft	(In) + InLi
In-Li22	ductile, soft	(In) + InLi
In-Li23	brittle	$InLi_4$ ht + $In_{2+x}Li_{10-x}$ (x=1.59)
In-Li23-1	brittle	$InLi_2$ + $In_{8+x}Li_{22-x}$ (x=0.1)
In-Li23-2	brittle	
In-Li24	brittle	$InLi_2$ + $In_{2+x}Li_{10-x}$ (x=1.59)
In-Li25	ductile, soft	(In) + InLi
In-Li26	ductile, soft	(In) + InLi
In-Li32	ductile, soft	In_3Li_{13} + (Li)
In-Li33	ductile, soft	(In) + InLi
In-Li37	ductile, soft	In_3Li_{13} + $InLi_4$ ht
In-Li38	brittle	$In_{8+x}Li_{22-x}$ (x=0.1) + $In_{2+x}Li_{10-x}$ (x=1.59)

XRD results of samples within the InLi phase region:

Sample ID	Mechanical behavior	Rwp	Phase	w (wt.%)	Lattice parameters		Likely stable phase
					a (Å)	c (Å)	
In-Li1-1	brittle	3.907	(In)'	6.2	3.253(4)	4.94(1)	L
			$InLi_{(Li\text{-}rich)}$	63.8	6.7841(5)	-	
			$InLi_{(Li\text{-}deficient)}$	30.0	6.7744(8)	-	
In-Li1	brittle	3.592	(In)'	15.8	3.254(1)	4.937(4)	InLi
			$InLi_{(Li\text{-}rich)}$	60.4	6.7745(7)	-	
			$InLi_{(Li\text{-}deficient)}$	23.8	6.785(1)	-	
In-Li2	brittle	3.049	(In)'	7.1	3.253(3)	4.940(8)	InLi
			$InLi_{(Li\text{-}rich)}$	73.7	6.7893(5)	-	
			$InLi_{(Li\text{-}deficient)}$	19.2	6.778(3)	-	
In-Li3	brittle	3.441	(In)'	6.7	3.252(5)	4.94(2)	InLi
			$InLi_{(Li\text{-}rich)}$	93.3	6.78(1)	-	
In-Li16	brittle	3.279	(In)'	67.9	3.2535(6)	4.943(1)	InLi
			$InLi_{(Li\text{-}deficient)}$	32.1	6.7727(7)	-	
In-Li16 (after DTA)	brittle	3.727	(In)'	18.6	3.253(1)	4.940(3)	InLi
			$InLi_{(Li\text{-}rich)}$	53.8	6.7724(6)	-	
			$InLi_{(Li\text{-}deficient)}$	27.6	6.780(1)	-	
In-Li21	brittle	2.725	(In)'	2.4	3.255(7)	4.94(2)	InLi
			$InLi_{(Li\text{-}rich)}$	97.6	6.7790(9)	-	
In-Li27	brittle	4.308	(In)'	17.0	3.255(2)	4.942(5)	InLi
			$InLi_{(Li\text{-}rich)}$	55.1	6.7893(9)	-	
			$InLi_{(Li\text{-}deficient)}$	27.9	6.778(1)	-	
In-Li28	brittle	4.131	(In)'	36.2	3.2545(8)	4.940(2)	InLi
			$InLi_{(Li\text{-}rich)}$	46.7	6.7747(9)	-	
			$InLi_{(Li\text{-}deficient)}$	17.1	6.787(1)	-	
In-Li29	brittle	2.699	(In)'	66.1	3.2525(7)	4.942(2)	InLi
			$InLi_{(Li\text{-}rich)}$	31.2	6.7720(8)	-	
			$InLi_{(Li\text{-}deficient)}$	2.7	6.788(7)	-	
In-Li30	brittle	5.667	(In)'	50.2	3.2594(9)	4.943(2)	InLi
			$InLi_{(Li\text{-}rich)}$	41.4	6.775(1)	-	
			$InLi_{(Li\text{-}deficient)}$	8.4	6.786(3)	-	
In-Li31	brittle	4.765	(In)'	34.1	3.2544(8)	4.942(2)	InLi

			$InLi_{(Li\text{-}rich)}$	36.5	6.7747(8)	-	
			$InLi_{(Li\text{-}deficient)}$	29.4	6.789(1)	-	
In-Li34	brittle	2896	(In)'	22.6	3.254(1)	4.942(3)	InLi
			$InLi_{(Li\text{-}rich)}$	42.9	6.7868(7)	-	
			$InLi_{(Li\text{-}deficient)}$	34.5	6.7750(6)	-	
In-Li35	brittle	2.580	(In)'	49.3	3.2539(6)	4.942(1)	InLi
			$InLi_{(Li\text{-}rich)}$	32.3	6.7734(6)	-	
			$InLi_{(Li\text{-}deficient)}$	18.4	6.786(2)	-	
In-Li35-1	brittle	5.275	(In)'	18.1	3.255(4)	4.95(1)	InLi
			$InLi_{(Li\text{-}rich)}$	56.9	6.788(1)	-	
			$InLi_{(Li\text{-}deficient)}$	25.0	6.778(2)	-	
In-Li36	brittle	2.507	(In)'	43.1	3.2535(7)	4.942(2)	InLi
			$InLi_{(Li\text{-}rich)}$	48.1	6.7737(7)	-	
			$InLi_{(Li\text{-}deficient)}$	8.8	6.787(2)	-	
In-Li39	brittle	2.604	(In)'	3.7	3.254(3)	4.940(9)	InLi
			$InLi_{(Li\text{-}rich)}$	81.5	6.7887(4)	-	
			$InLi_{(Li\text{-}deficient)}$	14.8	6.776(1)	-	
In-Li39-1	brittle	2.698	(In)'	33.6	3.2536(5)	4.944(1)	InLi
			$InLi_{(Li\text{-}rich)}$	39.7	6.7890(7)	-	
			$InLi_{(Li\text{-}deficient)}$	26.7	6.7735(5)	-	
In-Li40	brittle	2.952	(In)'	1.6	3.25(2)	4.94(4)	InLi
			InLi	98.4	6.7895(3)	-	

The invariant reactions of the In-Li system based on the measurements, their type and the temperature of their appearance were listed in Table 26.

Table 26 Invariant reactions occurring in the constructed In-Li phase diagram, based on the measured results. T…temperature.

Invariant reaction	**Type of reaction**	**T (°C)**
$L + InLi \rightleftarrows (In)$	peritectic	~158
$L \rightleftarrows InLi$	congruent melting	~628
$InLi \rightleftarrows InLi_2 + InLi_4$ ht	eutectoid	~397
$L \rightleftarrows (In)' + InLi_{(Li\text{-}deficient)}/InLi_{(Li\text{-}rich)}$	2^{nd} ord. phase transition	~580
$InLi + InLi_2 \rightleftarrows In_2Li_3$	peritectoid	~326
$InLi \rightleftarrows InLi_2$	congruent transformation	~473
$InLi_2 + InLi_4$ ht $\rightleftarrows In_{2+x}Li_{10-x}$ (x=1.59)	peritectoid	~390

$In_{2+x}Li_{10-x}$ (x=1.59) ⇄ $InLi_2$ + $In_{8+x}Li_{22-x}$ (x=0.1)	eutectoid	~338
$In_{2+x}Li_{10-x}$ (x=1.59) + $InLi_4$ ht ⇄ $In_{8+x}Li_{22-x}$ (x=0.1)	peritectoid	~370
L + InLi ⇄ $InLi_4$ ht	peritectic	~400
$InLi_4$ ht ⇄ In_3Li_{13} + L	metatectic	~227
$In_{8+x}Li_{22-x}$ (x=0.1) + $InLi_4$ ht ⇄ In_3Li_{13}	peritectoid	~265
L+ In_3Li_{13} ⇄ (Li)	peritectic	~191

5.4 Discussion of the results of representative samples

The results of the samples In-Li 20, 25, 17, 10 and 10-1, 1, 19, 11 and 11-1 as well as 14 are representative examples, mandatory to establish the new In-Li phase diagram version. They are discussed in detail in the following part.

5.4.1 In-Li 20

The DTA measurement of In-Li 20 (5.0 at.% Li), see Fig. 74 showed a strong peak on heating with an average temperature of 156.1 °C from an endothermic reaction. This signal was confirmed during cooling by the exothermic reaction with a strong peak at an average temperature of 156.9 °C. The associated peritectic reaction is L + InLi ⇄ (In). The average temperature during cooling should be lower than during heating due to supercooling. This is not the case, but the 0.8 °C difference is within the standard deviation. For verification of the peritectic kind of the invariant reaction, another sample In-Li 20-1 (4.3 at.% Li) was prepared by heating with a muffle furnace to 300 °C within 2 h followed by multiple shaking/turning of the sample at 300 °C and slow cooling to room temperature. This sample was investigated by DTA (see 4.3 DTA measurement) but instead of a α-Al_2O_3 pure In was used as reference. The result showed a weak, exothermic peak at 155.8 °C followed by a strong endothermic peak at 157.9 °C. Thus, the reference melted before the invariant reaction took place (exothermic peak), meaning the reaction should be of peritectic kind.

Interestingly, a liquidus signal is only visible on cooling as weak peak at an average temperature of 193.1 °C. Thus, the liquidus reaction L⇄ L + InLi must appear

at a temperature > 193.1 °C, considering possible supercooling of the L. The missing liquidus peak on heating is most likely caused by the steep slope of the liquidus line making it difficult to detect by DTA.

The same was observed for the liquidus in samples In-Li 7 and In-Li 22, both at 10 at.% Li but annealed at 220 and 140 °C, respectively. Thus, only the liquidus signals from cooling of these samples were used to correctly estimate the liquidus line in the new constructed In-Li phase diagram.

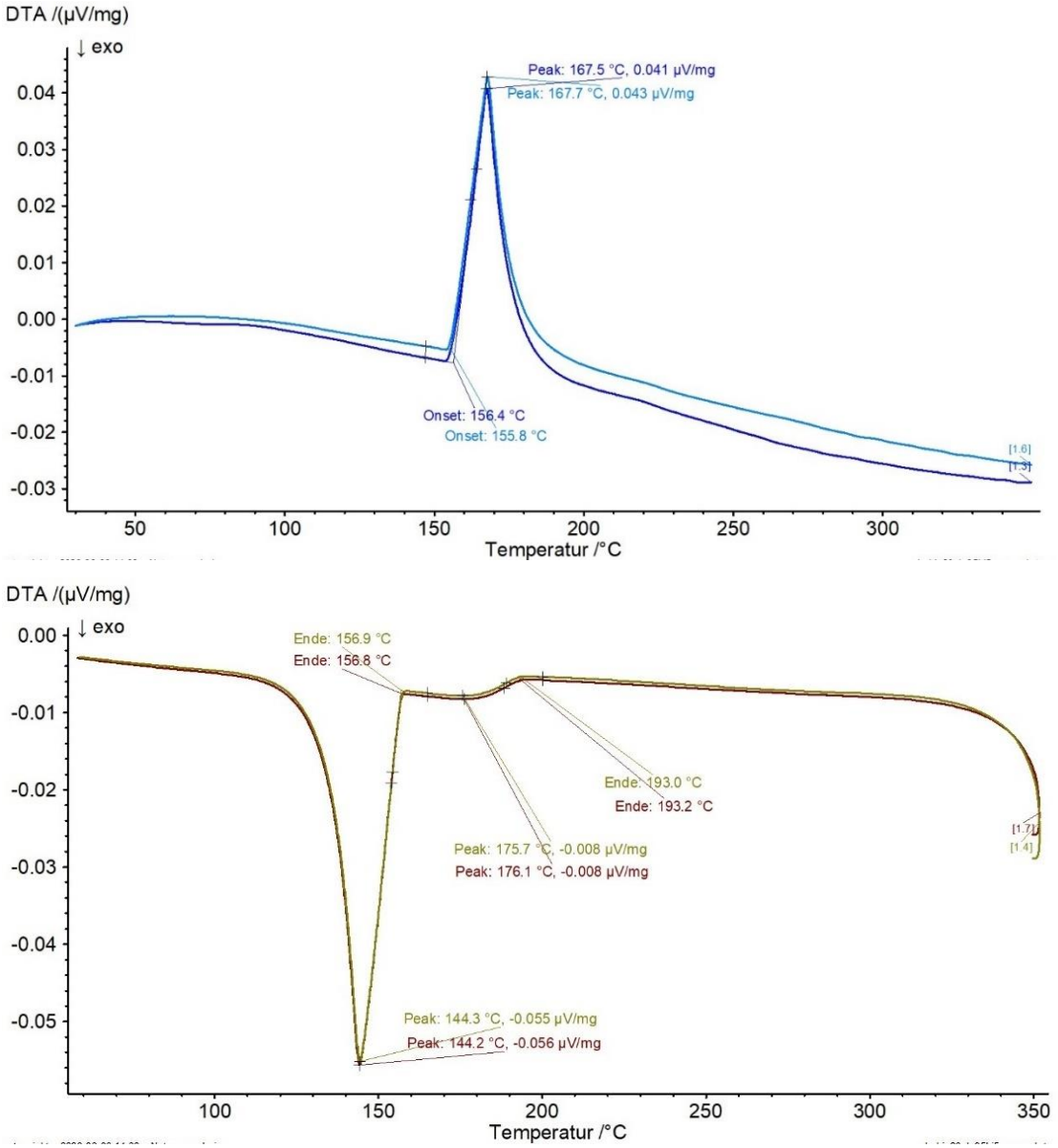

Figure 74 DTA plot (of Netzsch: Proteus® 6.1.0.) (thermoelectric voltage (µV/mg) vs. Temperature (°C)) of sample In-Li 20. Top: Result of 1st (dark blue) and 2nd heating cycle (bright blue), with endothermic reactions. Bottom: Result of 1st (green) and 2nd cooling cycle (red), with exothermic reactions. “Peak” marks the maximum/minimum temperature of the occurring reaction, “Onset/Ende” marks the temperature of the occurring reaction calculated by double-tangent method.

The Calvet-type 3D-DSC measurement of In-Li 20 (see Fig. 75) was complementary to the DTA results. The endothermic strong peaks during heating appeared at a slightly higher average temperature of 159.30 °C, compared to the DTA signal and the associated exothermic strong peaks during cooling appeared at 153.29 °C. Both are affiliated to the peritectic reaction L + InLi ⇄ (In). This result underlines the peritectic character of the reaction since the corresponding transition temperature is significantly above the melting point of pure In (156,6 °C).

Contrary to the DTA measurement occurred an endothermic, weak liquidus peak on heating at 217.26 °C, confirming the established liquidus line in the In-Li phase diagram. The samples In-Li 7 and 22 even did not show this liquidus peak in the Calvet-type 3D-DSC.

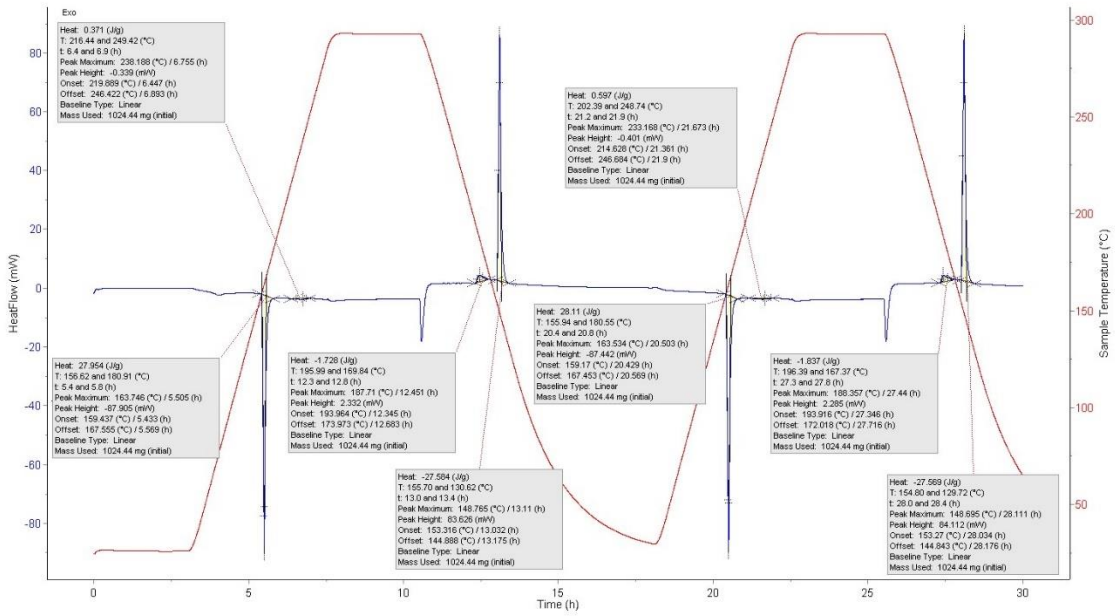

Figure 75 Calvet-type 3D-DSC plot (of SETSYS Evaluation). Left: Heat flow (mW) (blue curve), right: Sample Temperature (°C) (red curve) vs. Time (h), with 2 measured heating/cooling cycles of sample In-Li 20. The yellow part (integrated area) during heating/cooling marks the peak with its starting temperature (Onset within gray box) resulting from endothermic (peak points down)/exothermic (peak points up) reactions.

For XRD In-Li 20 (5.0 at.% Li, annealed at 140 °C) was too ductile and soft to be powdered. Such samples were cut and flattened (see Fig. 76), leading to strain and a high sample displacement factor, which is caused by the sample height.

Figure 76 Soft and ductile sample, flattened for XRD investigation.

The XRD measurement (see Fig. 77) only showed reflections of the phase (In) (tetragonal, *I4/mmm*). After refinement with Rwp = 2.187 the lattice paramters were determined as a = 3.256 (1) Å and c = 4.933 (2) Å.

(In) appeared to dissolve major amounts of Li indicated by the sole presence of (In) and the deviation of the lattice parameters from pure In, a = 3.252(1) Å and c = 4.941 (4) Å.

Based on published phase diagrams with a small solubility of Li in (In), it was assumed that the sample In-Li 20 should be in the 2-phase region (In) + InLi, but only the presence of (In) could be confirmed. The reason for this XRD result could be an overlapping of the high background noise with the InLi reflections, creeping of $Li_{(l)}$, hindering a proper homogenization because some $Li_{(l)}$ would stick most likely as thin layer to the crucible wall. Similar explanations were already discussed by Graham et al. [21] and Alexander et al. [51] for samples in the same 2-phase region (> 6.5 at.% Li). However, the small but significant change of the lattice parameters of (In), see above, indicates at least a small solubility of Li in (In).

The samples In-Li 7, 22 and 33 showed the same results, only (In) was identified in the XRD patterns. According to Alexander et al. [51] (In) exhibits a solubility of 1.5 at.% Li and thus we assumed that samples with 5 or 10 at.% Li would be in the 2-phase field (In) + InLi. However, it is to mention that (In) was also described with a solubility of 15 at.% Li according to Graham et al. [21]. There is no evidence

for the Li-content of (In) from the XRD peak intensities because of the extremely weak interaction of X-rays with Li compared to In.

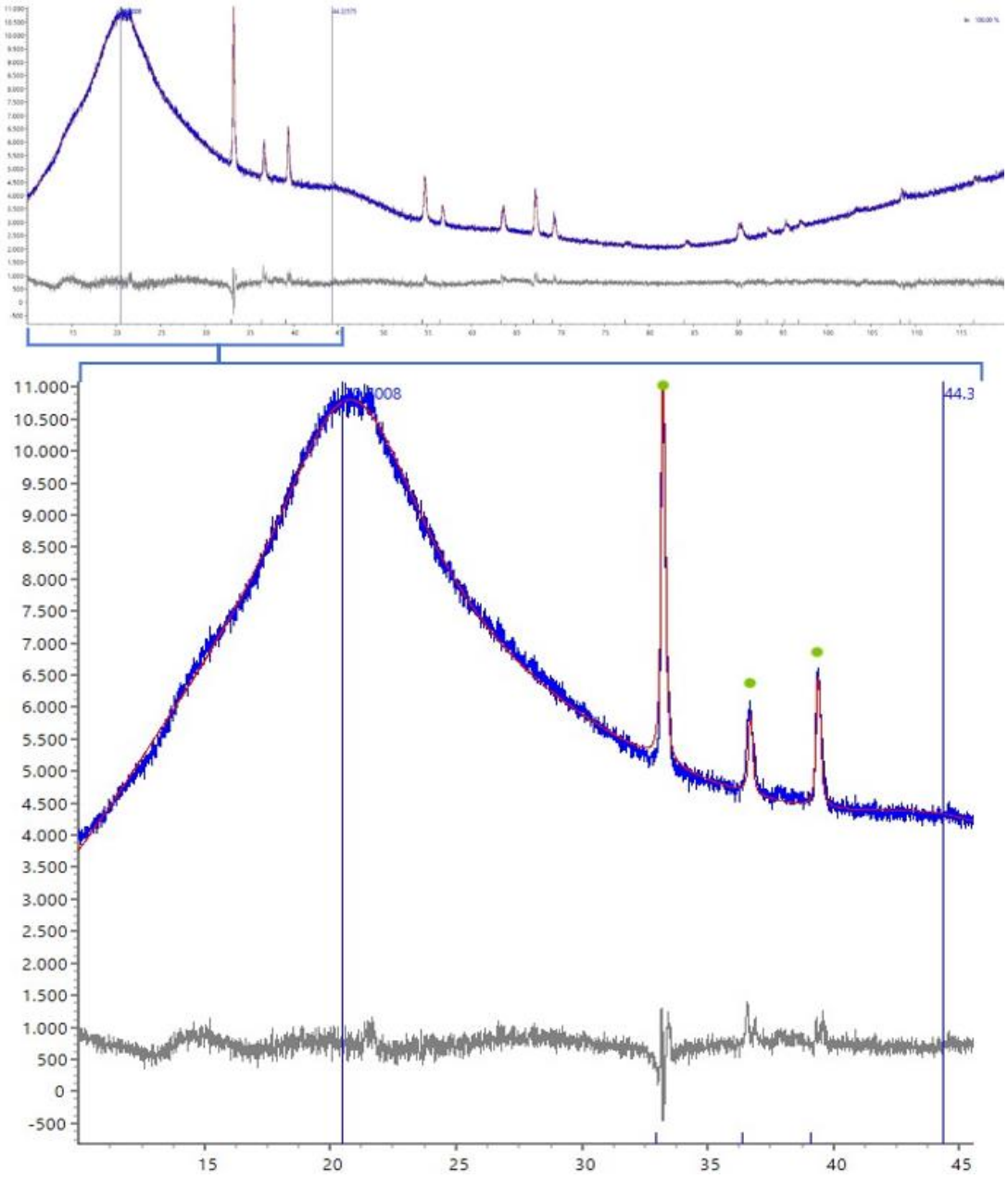

Figure 77 XRD pattern (of TOPAS-64 7.13 of Bruker) (counts vs. 2θ) of sample In-Li 20. Magnified part (2θ=10 to 45°) with significant reflections of: (In)…●. The “bulge” at 20 and 45° (θ/θ-goniometer mode) originates from the amorphous PC dome of the sample holder. Blue curve: Measured pattern. Red curve: Refined pattern. Grey curve: Difference between measured and refined pattern.

5.4.2 In-Li 25

The DTA measurement of In-Li 25 (20.0 at.% Li) showed on heating a strong endothermic peaks at an average temperature of 156.1 °C (see Fig. 78) again resulting from the peritectic reaction L + InLi ⇄ (In), taking the range of error into account. This reaction was confirmed by strong, supercooled exothermic peaks on cooling with an average temperature of 155.8 °C. The liquidus was detected on heating as weak endothermic peak with relatively large deviation of the 1st cycle (407.5 °C) from the 2nd cycle (419.7 °C). Only the 2nd liquidus temperature was used for the In-Li phase diagram since the temperature was probably more precise due to better thermal contact of the sample to the bottom after first melting.

Two supercooled exothermic “liquidus” peaks at 394.6 °C (weak peaks) and at 380.1 °C (strong peaks) were visible on both cooling cycles. An explanation could be the appearance of kinetic effects on crystallization or metastable reaction but a final answer to this question is still missing. A similar liquidus result during cooling was noticed in sample In-Li 8, at 30 at.% Li, but not at sample In-Li 26, at 40 at.% Li.

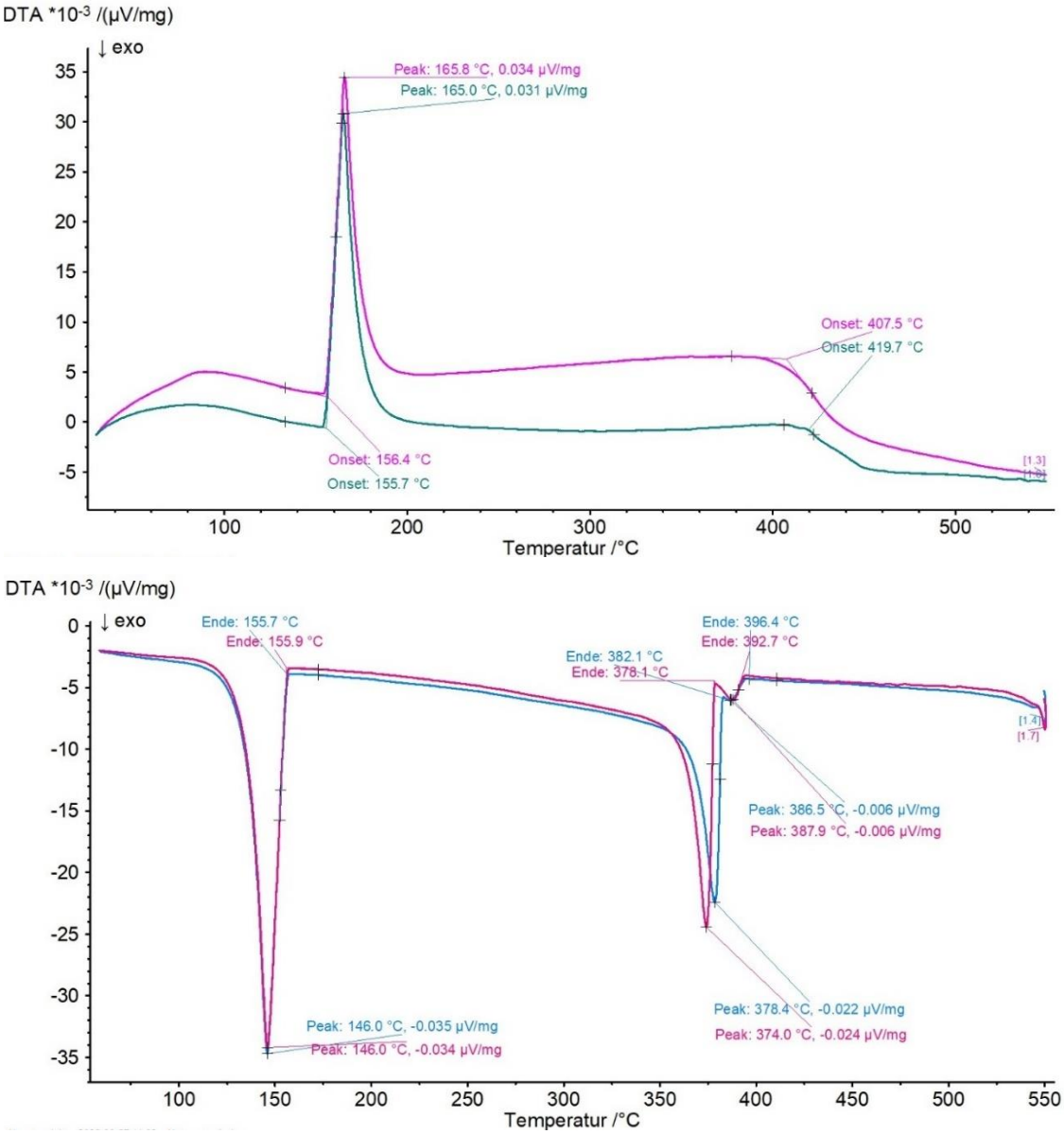

Figure 78 DTA plot (of Netzsch: Proteus® 6.1.0.) (thermoelectric voltage (µV/mg) vs. Temperature (°C)) of sample In-Li 25. Top: Result of 1st (pink) and 2nd heating cycle (green), with endothermic reactions. Bottom: Result of 1st (green) and 2nd cooling cycle (red), with exothermic reactions. “Peak” marks the maximum/minimum temperature of the occurring reaction, “Onset/Ende” marks the temperature of the occurring reaction calculated by double-tangent method.

The Calvet-type 3D-DSC measurement of In-Li 25 (see Fig. 79) was complementary to the DTA results. Thus, the endothermic, strong peaks of the reaction already mentioned above, during heating appeared at a slightly higher average temperature of 158.94 °C, compared to the DTA signal and the associated exothermic, strong peaks during cooling appeared at 153.26 °C. At this point it has

to be noted that the heating peaks of DTA for the reaction L + InLi ⇄ (In) are at temperatures slightly below the melting of pure In what contradicts the peritectic nature of this reaction. However, it is within the error of approx. 3 K and the more accurate Calvet-type 3D-DSC analysis shows characteristic temperatures clearly above the melting of pure In. Therefore, we assume the reaction to be peritectic as it is described in most of literature data.

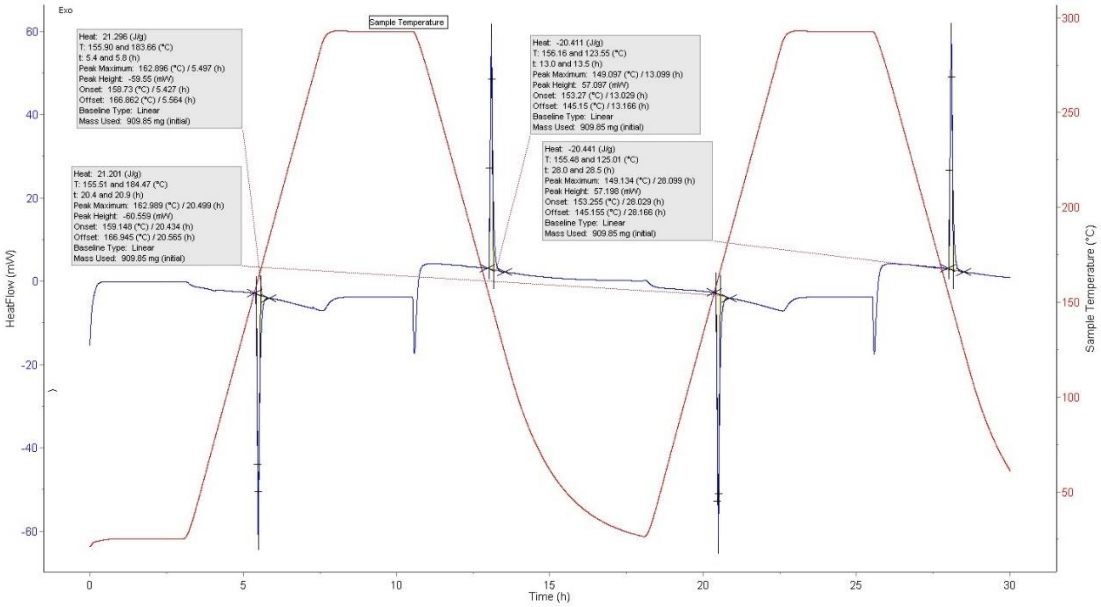

Figure 79 Calvet-type 3D-DSC plot (of SETSYS Evaluation). Left: Heat flow (mW) (blue curve), right: Sample Temperature (°C) (red curve) vs. Time (h) with 2 measured heating/cooling cycles of sample In-Li 25. The yellow part (integrated area) during heating/cooling marks the peak with its starting temperature (Onset within gray box) resulting from endothermic (peak points down)/exothermic (peak points up) reactions.

In-Li 25 (20.0 at.% Li, as cast) was too ductile and soft for powdering for XRD, hence the samples was cut and flattened leading to strains and a high sample displacement factor because of the sample height. The XRD measurement (see Fig. 80) showed reflections of the phases InLi (cubic, $Fd\bar{3}m$ with Li-deficiency and (In) (tetragonal, *I4/mmm*). After refinement resulting with R_{wp} = 2.328, 15.8 wt.% InLi with the lattice paramter a = 6.776 (6) Å as well as 84.2 wt.% (In) with the lattice paramters a = 3.255 (2) Å and c = 4.939 (4) Å were determined.

Thus $InLi_{(Li\text{-deficient})}$ and (In) showed solid solubility indicated by the deviation of their lattice parameters from literature[23][46] with a = 6.799(0) Å as well as with a = 3.252(1) Å and c = 4.941(4) Å.

Also sample In-Li 25 was not annealed, the experimental data confirm the phase diagram information given in literature.

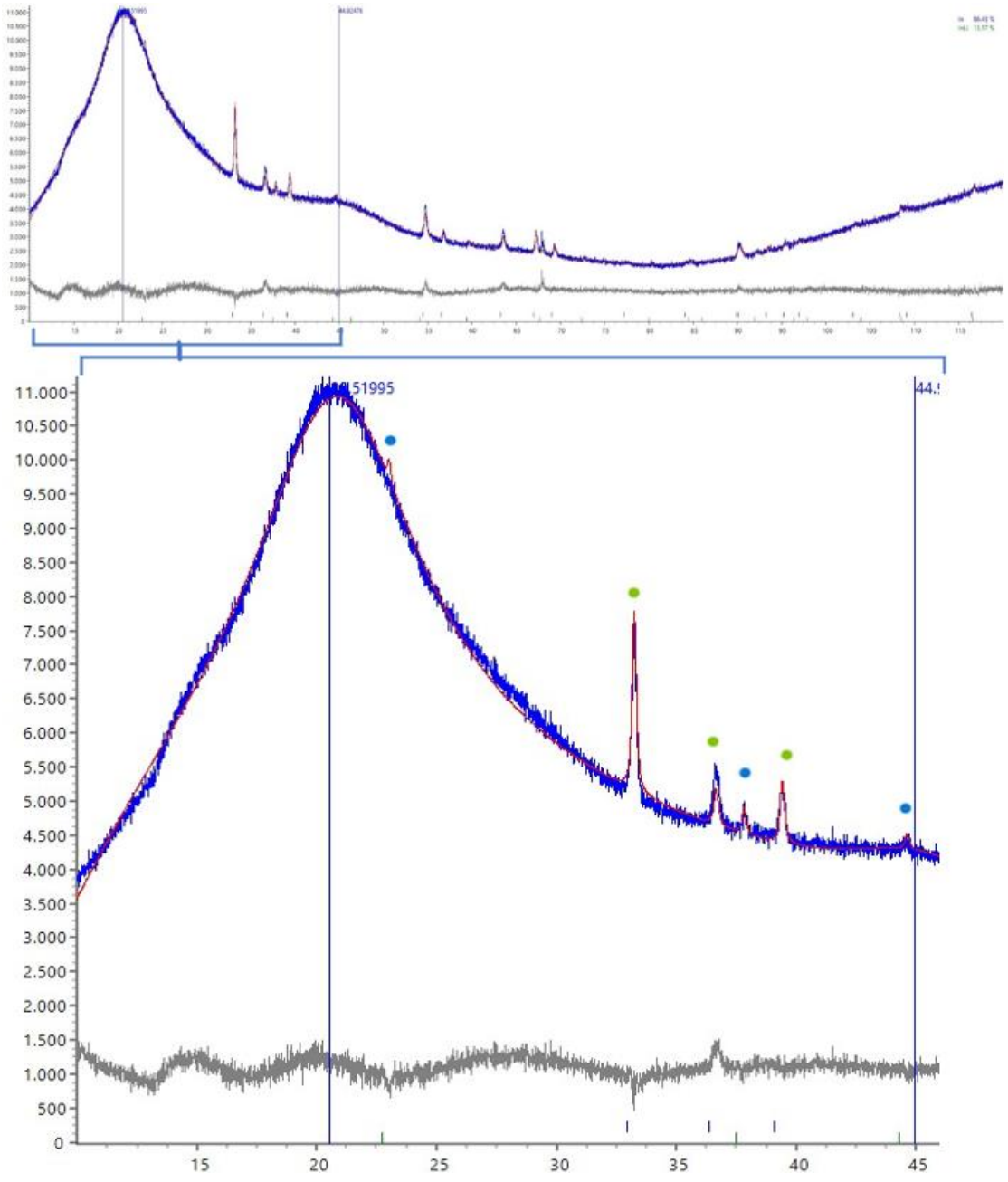

Figure 80 XRD pattern (of TOPAS-64 7.13 of Bruker) (counts vs. 2θ) of sample In-Li 25. Magnified part (2θ=10 to 45°) with significant reflections of: $InLi_{(Li\text{-deficient})}$… ● and (In)… ●. The "bulge" at 20 and 45° (θ/θ-goniometer mode) originates from the amorphous PC dome of the sample holder. Blue curve: Measured pattern. Red curve: Refined pattern. Grey curve: Difference between measured and refined pattern.

5.4.3 In-Li 17

The DTA measurement of In-Li 17 (63.9 at.% Li) showed a strong peak with mean temperature of 324.6 °C, a weak peaks at 430.5 °C and again strong peaks at 564.6 °C and 594.3 °C from endothermic reactions on heating (see Fig. 81). These signals were confirmed during cooling by the exothermic reactions with the strong peaks at an average temperature of 598.2 °C, the weak peaks at 405.4 °C and the strong peaks at 292.0 °C. The associated reactions are the liquidus reaction $L \rightleftarrows L + InLi$ (at 594.3 °C), the solidus reaction $L + InLi \rightleftarrows InLi$ (at 564.6 °C), the reaction at the solvus $InLi \rightleftarrows InLi + InLi_2$ (at 430.5 °C) near the congruent transformation $InLi \rightleftarrows InLi_2$ and $InLi + InLi_2 \rightleftarrows In_2Li_3 + InLi_2$ (at 324.6 °C), which occurred at the tie line of the peritectoid reaction $InLi + InLi_2 \rightleftarrows In_2Li_3$. During cooling overlapped the liquidus reaction with the solidus reaction due to supercooling.

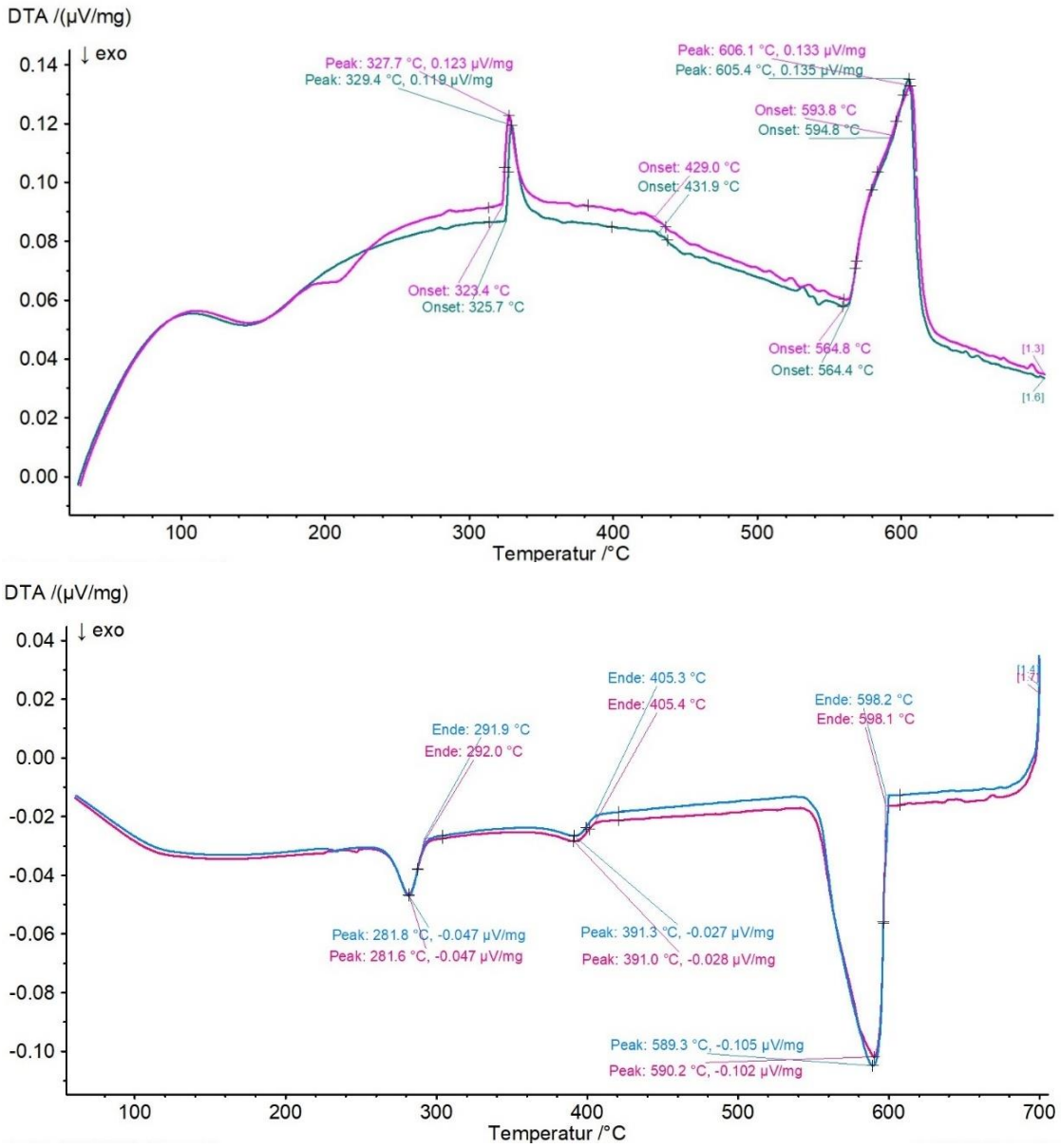

Figure 81 DTA plot (of Netzsch: Proteus® 6.1.0.) (thermoelectric voltage (µV/mg) vs. Temperature (°C)) of sample In-Li 17. Top: Result of 1st (pink) and 2nd heating cycle (green), with endothermic reactions. Bottom: Result of 1st (green) and 2nd cooling cycle (red), with exothermic reactions. “Peak” marks the maximum/minimum temperature of the occurring reaction, “Onset/Ende” marks the temperature of the occurring reaction calculated by double-tangent method.

The Calvet-type 3D-DSC measurement of In-Li 17 showed no reaction beneath 300 °C (see Fig. 82).

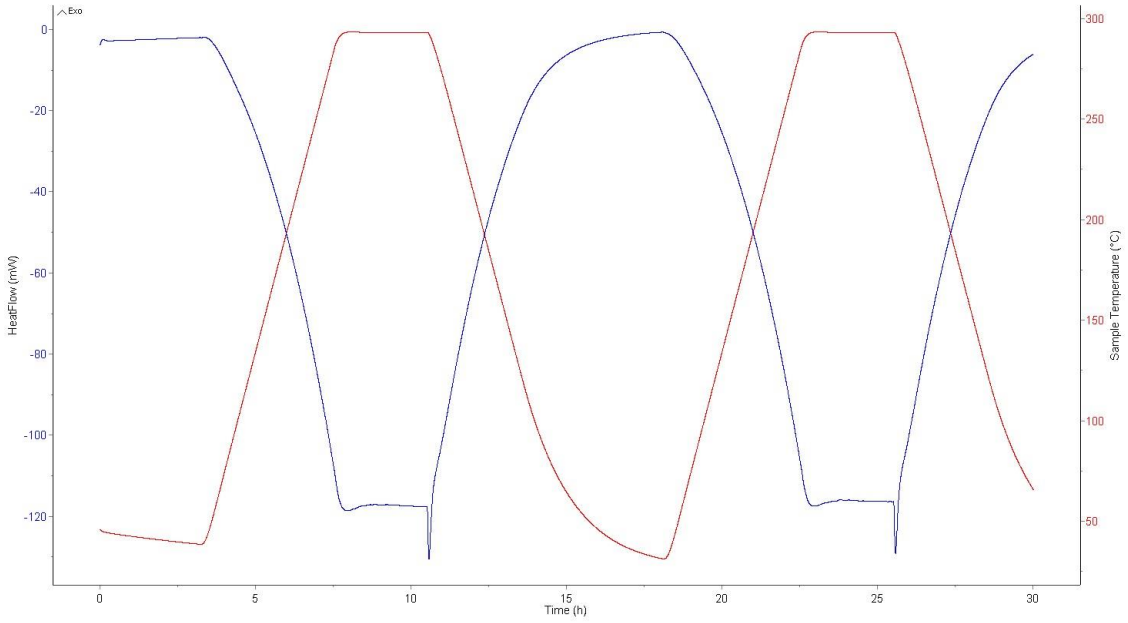

Figure 82 Calvet-type 3D-DSC plot (of SETSYS Evaluation). Left: Heat flow (mW) (blue curve), right: Sample Temperature (°C) (red curve) vs. Time (h) with 2 measured heating/cooling cycles of sample In- Li 17.

In-Li 17 (63.9 at.% Li, annealed at 327 °C) was brittle enough to powder it for the XRD measurement, which showed reflections of the phases $InLi_{(Li\text{-}rich)}$ (cubic, *Fd*$\bar{3}$*m*), (In) (tetragonal, *I4/mmm*), $InLi_2$ (orthorombic, *Cmcm*), and In_2Li_3 (hexagonal, *R*$\bar{3}\bar{3}$*m*), (see Fig. 83). After refinement with a quality of Rwp = 2.704, were 33.1 wt.% $InLi_{(Li\text{-}rich)}$ with the lattice paramter a = 6.774(4) Å, 3.9 wt.% (In) with the lattice paramters a = 3.256 (3) Å and c = 4.944 (7) Å, 38.2 wt.% $InLi_2$ with a = 4.77 (2) Å, b = 10.07 (3) Å and c = 4.77 (2) Å as well as 24.8 wt.% In_2Li_3 with a = 4.777 (7) Å and c = 14.68 (4) Å found.

All four phases appeared to have a homogenity range due to the deviation of their lattice parameters from the literature values a = 6.79(0) Å for $InLi_{(Li\text{-}rich)}$, a = 3.252 (1) Å and c = 4.941 (4) Å for(In), a = 4.763 (0) Å, b = 10.017 (0) Å and c = 4.735 (0) Å for $InLi_2$ and a = 4.74 (8) Å and c = 14.7 (4) Å for In_2Li_3.

The sample In-Li 17 was annealed at 327 °C, slightly above the peritectoid reaction $InLi + InLi_2 \rightleftarrows In_2Li_3$ at 324.6 °C. The presence of In_2Li_3 shows that the $InLi + InLi_2$ two-phase equilibrium could not be fully quenched. Traces of (In)

indicate a poor homogenization before annealing. This assumption is supported due to the fact that In-Li 17 was not homogenized by better alloying method 9. Nevertheless, the sampe confirms the peritectoid reaction and its characteristic temperature.

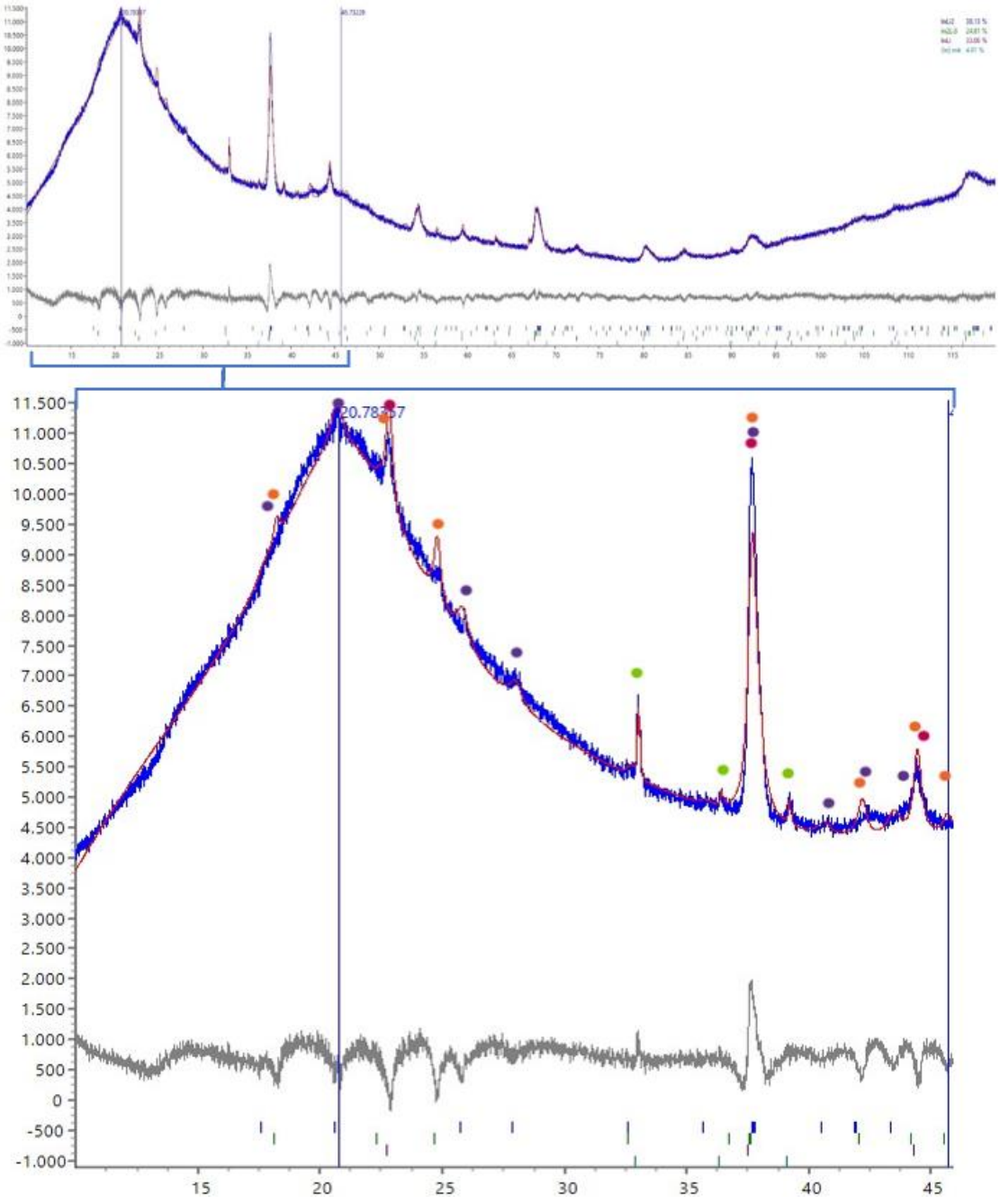

Figure 83 XRD pattern (of TOPAS-64 7.13 of Bruker) (counts vs. 2θ) of sample In-Li 17. Magnified part (2θ=10 to 45°) with significant reflections of: $InLi_{(Li\text{-}rich)}$… ● and (In)… ●, $InLi_2$… ● and In_2Li_3… ●. The “bulge” at 20 and 45° (θ/θ-goniometer mode) originates from the amorphous PC dome of the sample holder. Blue curve: Measured pattern. Red curve: Refined pattern. Grey curve: Difference between measured and refined pattern.

5.4.4 In-Li 10 and 10-1

The DTA measurement of In-Li 10 (71.9 at.% Li), see Fig. 84 showed strong peaks during heating with an average temperature of 338.9 °C, weak peaks at 363.8 °C and again strong peaks at 389.6 °C, weak peaks at 460.4 °C as well as strong peaks at 488.3 °C and 526.0 °C from endothermic reactions. Except this at 460.4 °C the heating signals were confirmed on cooling by the exothermic reactions with strong peaks at average temperatures of 522.2, 488.1, 394.3 and 319.8 °C. It is to mention that it was not possible to determine the real Onset of overlapping peaks via the used software of Netzsch Proteus® 6.1.0.

The associated reactions are the liquidus reaction L ⇄ L + InLi (at 526.0 °C), the solidus reaction L + InLi ⇄ InLi (at 488.3 °C) and the reaction InLi ⇄ InLi + InLi2 (at 460.4 °C) at the solvus starting from the congruent transformation InLi ⇄ InLi2.

Further the following reactions occur: InLi ⇄ $InLi_4$ ht + $InLi_2$ (eutectoic, at ≥ 394.3, unresolved in DTA), $InLi_4$ ht + $InLi_2$ ⇄ $In_{2+x}Li_{10-x}$ (x=1.59) (peritectoic, at 389.6 °C), $In_{2+x}Li_{10-x}$ (x=1.59) + $InLi_4$ ⇄ $In_{8+x}Li_{22-x}$ (x=0.1) (peritectoic at 363.8 °C) and $In_{2+x}Li_{10-x}$ (x=1.59) ⇄ $In_{8+x}Li_{22-x}$ (x=0.1) + $InLi_2$ (eutectoic at 338.9 °C).
The strong peaks of the cooling cycle at 394.3 °C appeared at a higher temperature than respective strong peak of the heating cycle at 389.6 °C, in contradiction to supercooling. Accordingly, there must occur two reactions with quite small temperature difference, resulting in one overlapping strong peak, third peak on heating shown in Fig. 84. Thus, the two invariant reactions InLi ⇄ $InLi_2$ + $InLi_4$ ht, and $InLi_2$ + $InLi_4$ ht ⇄ $In_{2+x}Li_{10-x}$ (x=1.59) occur in a narrow temperature regime.

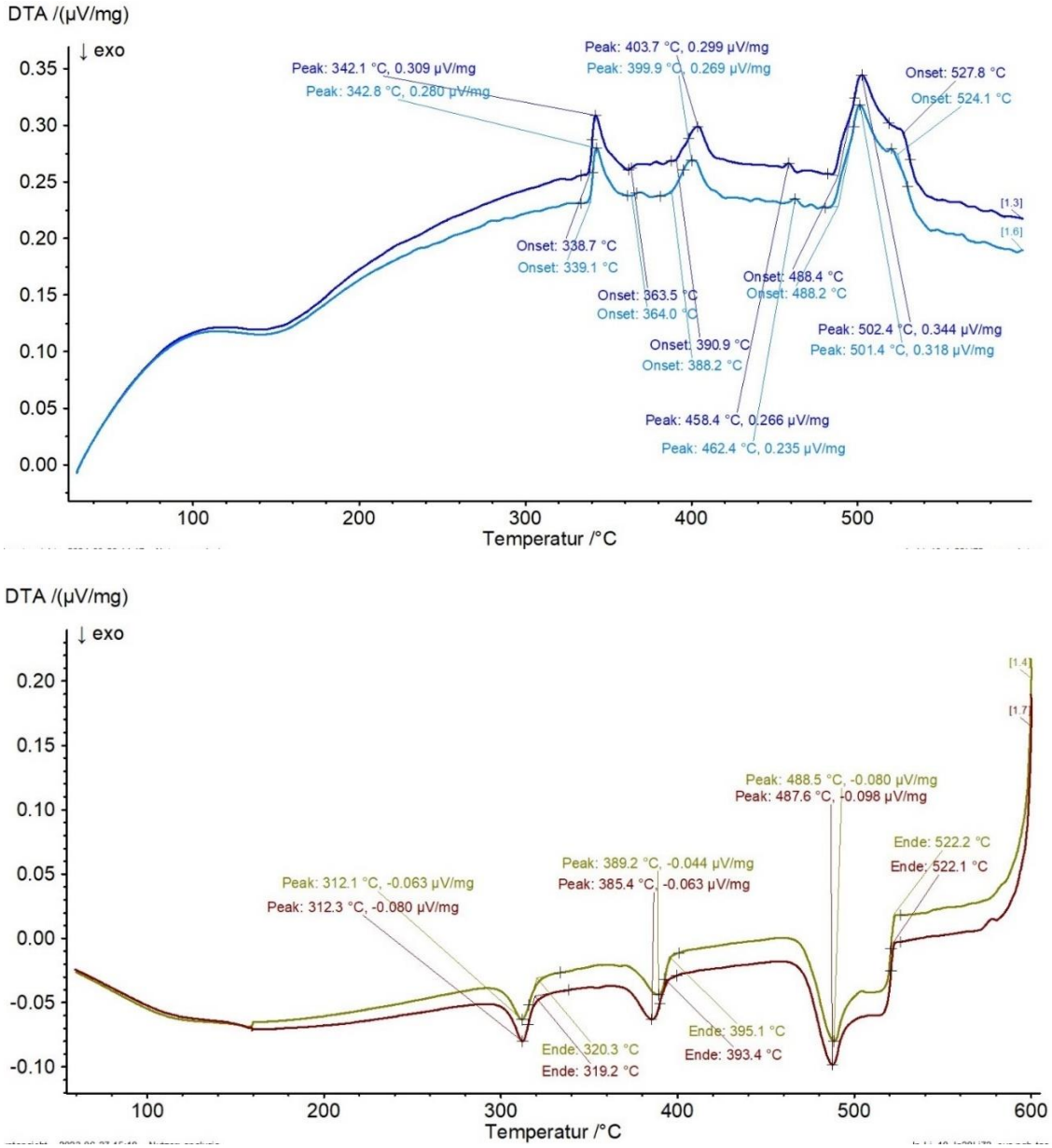

Figure 84 DTA plot (of Netzsch: Proteus® 6.1.0.) (thermoelectric voltage (µV/mg) vs. Temperature (°C)) of sample In- Li 10. Top: Result of 1st (dark blue) and 2nd heating cycle (bright blue), with endothermic reactions. Bottom: Result of 1st (green) and 2nd cooling cycle (red), with exothermic reactions. “Peak” marks the maximum/minimum temperature of the occurring reaction, “Onset/Ende” marks the temperature of the occurring reaction calculated by double-tangent method.

The Calvet-type 3D-DSC measurement of In-Li 10 showed no reactions beneath 300 °C (see Fig. 85).

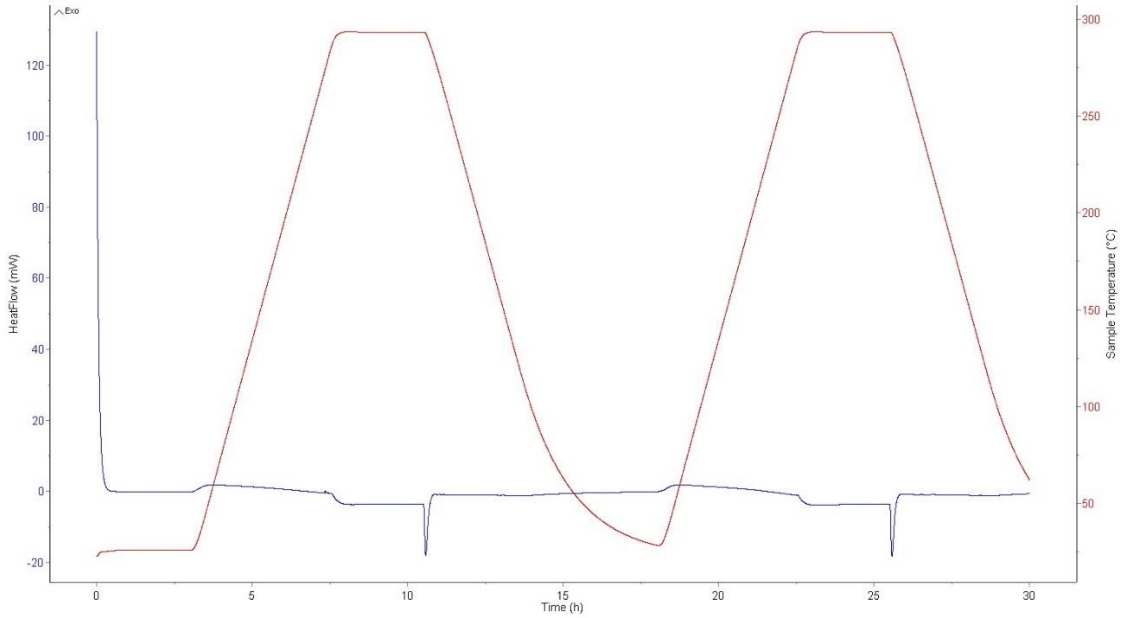

Figure 85 Calvet-type 3D-DSC plot (of SETSYS Evaluation). Left: Heat flow (mW) (blue curve), right: Sample Temperature (°C) (red curve) vs. Time (h) with 2 measured heating/cooling cycles of sample In-Li 10.

In-Li 10-1 (72.0 at.% Li, annealed at 220 °C) has almost the same composition and annealing temperature as In-Li 10 but was homogenized by alloying method 9. In-Li 10-1 was brittle enough to powder it for the XRD measurement, which showed reflections of the phases $InLi_2$ (orthorombic, *Cmcm*) and $In_{2+x}Li_{22-x}$ (x=0.1) (monoclinic, *C2/m*), (see Fig. 86). After refinement of a quality of Rwp = 2.252, were 62.6 wt.% $InLi_2$ with the lattice paramter a = 4.77(1) Å, b = 10.09 (3) Å and c = 4.74 (1) Å as well as 37.4 wt.% $In_{2+x}Li_{22-x}$ (x=0.1) with the lattice parameters a = 14.18 (5) Å, b = 4.74 (1) Å, c = 8.67 (3) Å and β = 105.8 (3)° found.

$InLi_2$ and $In_{2+x}Li_{22-x}$ (x=0.1) appeared to have a homogenity range due to the deviation from their lattice parameters of the literature a = 4.763 (0) Å, b = 10.017 (0) Å and c = 4.735 (0) Å as well as a = 14.15 (6) Å, b = 4.72 (9) Å, c = 8.61 (7) Å and β = 105.8 (9)°, indicating a certain solubility for Li.

The sample In-Li 10-1 was in a 2-phase field were $InLi_2$ was in phase equilibrium with $In_{2+x}Li_{22-x}$ (x=0.1).

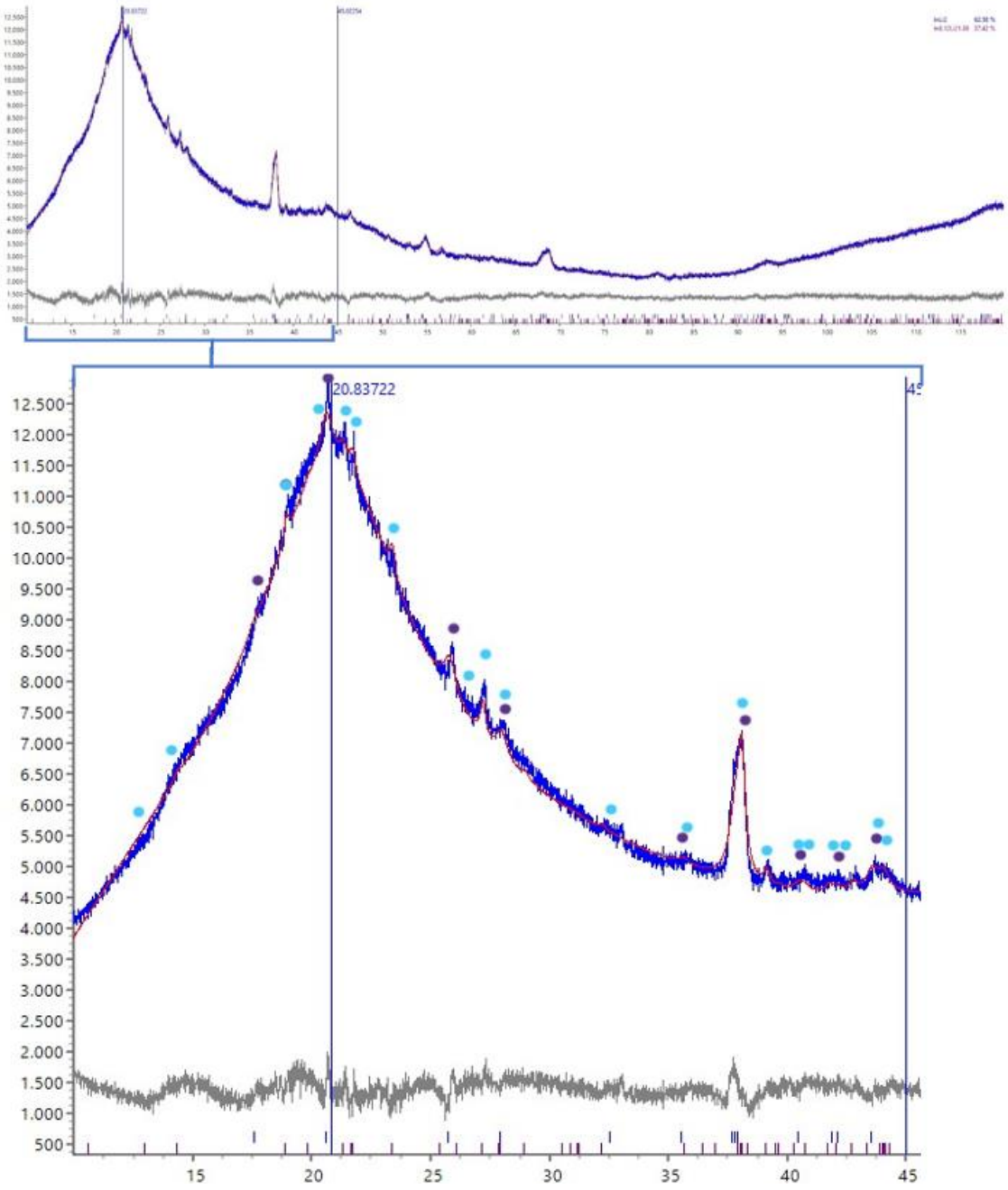

Figure 86 XRD pattern (of TOPAS-64 7.13 of Bruker) (counts vs. 2θ) of sample In-Li 10-1. Magnified part (2θ=10 to 45°) with significant reflections of: $InLi_2$… ● and $In_{2+x}Li_{22-x}$ (x = 0.1)… ●. The "bulge" at 20 and 45° (θ/θ-goniometer mode) originates from the amorphous PC dome of the sample holder. Blue curve: Measured pattern. Red curve: Refined pattern. Grey curve: Difference between measured and refined pattern.

5.4.5 The InLi phase region

It is worth mentioning that the XRD patterns of certain samples showed two cubic InLi phases with slightly different lattice parameters, hence broadened (low 2θ regime) or split reflections, see below. This effect was already observed by Alexander et al. [51], who suggested the occurrence of a second (metastable) InLi phase. Also Debski et al. [103] observed a dynamic instability of InLi by phonon dispersion analysis. They came also to the conclusion that InLi could undergo another polymorphic transformation at elevated temperatures beneath the liquidus.

However, these assumptions could not be proven by DTA or 3D-DSC measurements of samples within the InLi phase region, there was no peak observed besides the solid/liquid transformation (see discussion of sample In-Li 1).

At the first glance reflection splitting was thought to indicate the occurrence of the tetragonal crystal structure InLi lt. However, according to Ehrenberg et al. [45] InLi lt should only appear below 170 (10) K. In addition, we observed splitting of all reflections, while InLi lt would show only splitting of certain reflections, characteristic for a tetragonal distortion of a cubic lattice.

Another concept, supported by the severe homogenization difficulties during alloying and on the XRD data of sample In-Li 1-1 (see Fig. 87), was the appearance of a (metastable) miscibility gap in the liquid (forming L1 + L2), which would lead to the formation of two InLi phases with different lattice parameters on cooling, resulting from the different Li-concentration of L1 and L2.

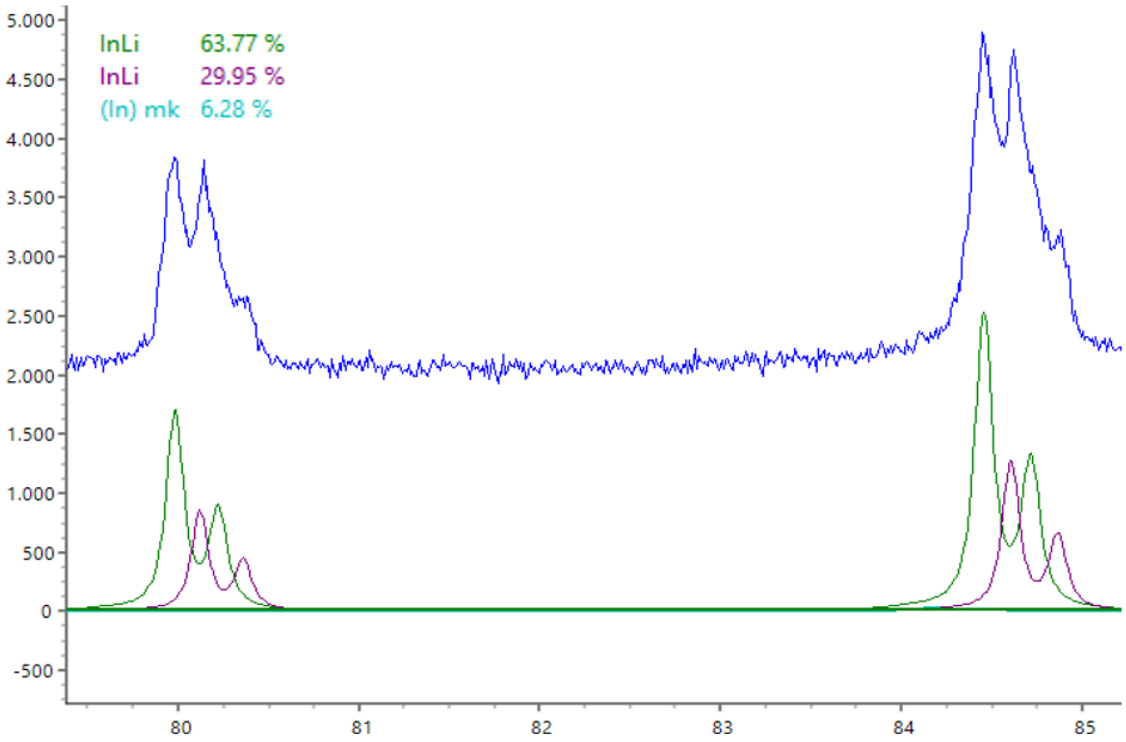

Figure 87 Representative part of the XRD pattern (of TOPAS-64 7.13 of Bruker) (counts vs. 2θ) from the range 2θ ≈ 80 to 85° showing the reflection splitting of InLi of the sample In-Li 1-1, quenched from melt. Hence, 3 (deconvoluted 4) peaks per reflection occurred instead of 2 from $CuK_{\alpha 1}$ and $CuK_{\alpha 2}$ radiation.

For the verification of this concept, the sample In-Li 39 was prepared by method 9 (shaken and turned 3-times). XRD investigation revealed a low In-phase content of ~3 wt.%, but still two InLi phases with different lattice parameter a. This sample was sealed again and annealed at 500 °C for 29 days to bring the phases in equilibrium. Annealing should have dissolved the left ~3 wt.% of In-phase, while combining the two InLi phases with different lattice parameter a to a single InLi phase.

However, XRD results on this sample showed an increased content of the In-phase with ~27 wt.% and still two InLi phases with different lattice parameter a, but with changed mass fraction. Alexander et al. [51] described also difficulties homogenizing the InLi phases through annealing.

A similar phenomenon occurred in the binary Ni-Al system within the single-phase region of the non-stoichiometric compound NiAl of CsCl-type. The non-stoichiometry was described via Ni-vacancies v_{Ni} in the Ni-deficient region and Ni-antisites Ni_{Al} in the Ni-rich region, leading to the appearance of a triple defect. Also,

NiAl showed evidence for the simultaneous presence of two NiAl “phases” with the same crystal structure, but different lattice parameters in respect to the Ni-content. These “phases” are spatially separated by a split line causing a concentration gradient even within single grains. It is suggested, that the splitting phenomenon is caused without nucleation at grain boundaries, similar to spinodal decomposition, but rather by decomposition due to a slow diffusion rate near the equimolar concentration. [104][105][106]

This leads to the, in this diploma thesis called “InLi-split hypothesis”, where InLi splits into a Li-rich and a Li-deficient InLi region with the same NaTl-type crystal structure, but with different lattice parameter a, similar to NiAl. However, in contrast to NiAl, where long-time annealing at 750 °C should result eventually in a stable, single NiAl phase, such annealing led only in some cases e.g. sample In-Li 16, to a stable, single InLi phase, but always in combination with an In-solid solution (see Fig. 88 and table 25).

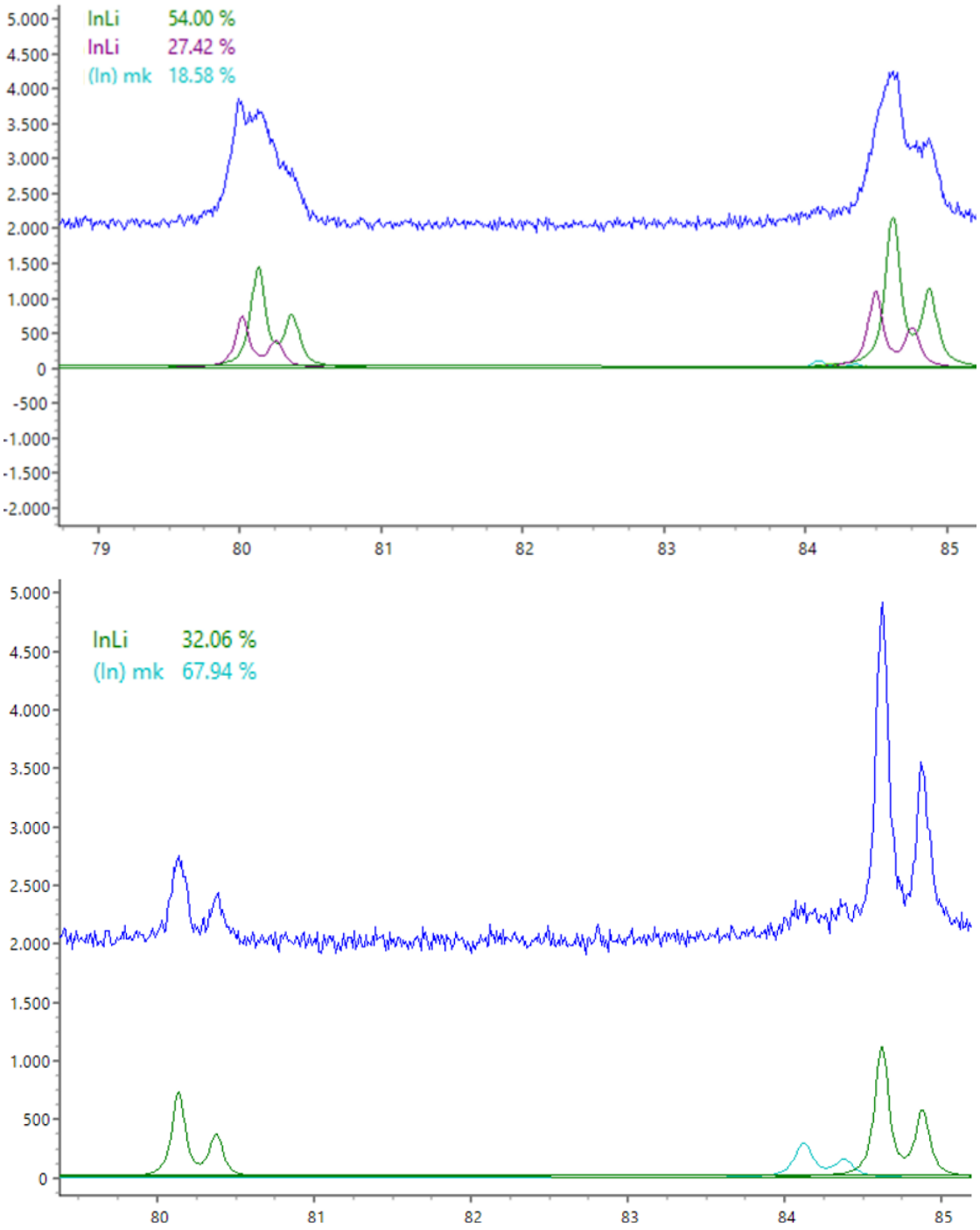

Figure 88 Representative part of the XRD pattern (of TOPAS-64 7.13 of Bruker) (counts vs. 2θ) from the range 2θ ≈ 80 to 85° showing reflections of sample In-Li 16 after DTA measurement, before annealing with the reflection splitting of InLi (3 peaks per reflection) (top) and reflections of In-Li 16 annealed at 220 °C for 86 days with no splitting (bottom). Hence, only 2 peaks per reflection occurred from $CuK_{\alpha 1}$ and $CuK_{\alpha 2}$ radiation. Blue curves: Detected pattern. Green, purple and turquoise curves: Refined pattern with phase composition in the upper, left corner.

It is assumed that this In-phase, here called (In)', results from a phase transition of 2nd order and contains much more Li compared to (In). This could probably be verified via DTA measurements, because a 2nd order phase transition should lead to a change of the baseline of the (1st) heating curve. However, the used DTA sample holder was not appropriate for such investigations. An alternative for future investigations could be a sample holder for heat capacity measurements, compatible for the used Ta-crucibles.

The activation energy of the 2nd order transition product (In)' must also be quite high, because annealing did not remove this metastable phase within the InLi phase region.

Such an 2nd order phase transition was already well described in the binary Al-Li system, the metastable phase in this case is Al_3Li. There is a single phase field of the Zintl-phase AlLi (NaTl-type structure) and a 2-phase field AlLi + (Al) with a 2nd order phase transition boundary containing the stable (Al) and the metastable Al_3Li [107].

A similar situation could take place in the In-Li system. The existence of a metastable (In)' phase is also supported by the determination of the lattice parameters via XRD and the brittleness of the (In)' solid solution phase in some samples with $x_{Li} > 0.40$. A larger lattice parameter c was observed in samples with brittle character (see Table 27). Pure In or (In) with only a few atomic percent Li is highly ductile, what can be recognized on powdering and also results in much wider XRD peaks. Contrary, the brittle (In)' with higher Li-contents of 15 to 25 at.% shows comparably smaller peaks and respective alloy samples can be easily powdered, even if they contained up to ~68 wt.% (In)'. These results led to the assumption that there is some ordering of atoms in (In)' where Li-atoms could, e.g. preferably occupy the atomic position (½ ½ ½), (see Fig. 89 and ref. [21]). Li-atoms do not have d-electrons in opposite to In-atoms, which leads to weaker bonds to the coordinating 8 In-atoms. This could result in the discovered elongation of the c lattice parameter. However, XRD, is not suitable to determine preferred occupation of Li at a certain atomic position, especially when combined with a quite heavy element like In, since it has only 3 electrons whereas In has 49. Relative intensity of peaks is hardly affected by the way of Li-distribution of the atomic sites. Neutron diffractometry would be suitable to verify this structural

question, because the atomic scattering factor of Li is much higher, due to stronger interaction of neutrons with Li in comparison to X-rays.

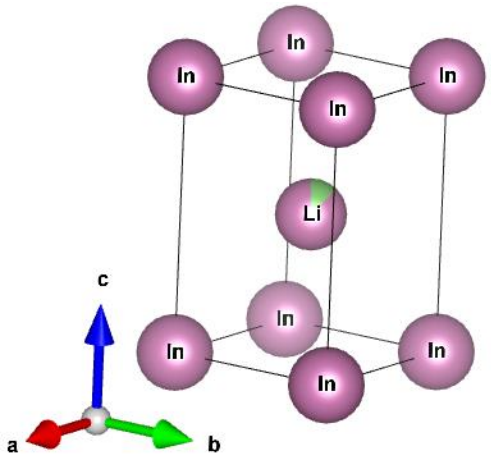

Phase name	(In)´
R-Bragg	1.318
Spacegroup	P4/mmm
Scale	2.46252e-03
Cell Mass	215.359
Cell Volume (Å^3)	52.27624
Wt% - Rietveld	0.000
Double-Voigt|Approach	
Cry size Lorentzian	142.2
k: 1 LVol-IB (nm)	90.506
k: 0.89 LVol-FWHM (nm)	126.528
Crystal Linear Absorption Coeff. (1/cm)	1604.081
Crystal Density (g/cm^3)	6.841
Lattice parameters	
a (Å)	3.2531281
c (Å)	4.9397164

Site	Np	x	y	z	Atom	Occ	Beq
In	1	0.00000	0.00000	0.00000	In	1	1
Li	1	0.50000	0.50000	0.50000	Li	0.1323	1
					In	0.8677	1

Figure 89 Crystal structure with crystallographic data of the postulated brittle (In)‘ phase (of TOPAS-64 7.13 of Bruker).

Table 27 Comparison of the lattice parameters of ductile (In) and brittle (In)' of some samples.

Sample ID	a (Å)	Average a (Å)	c (Å)	Average c (Å)	Annealing temperature (°C)	Mechanical behavior	
In-Li 7	3.256 (1)		4.939 (2)				
In-Li 8	3.2562 (7)		4.938 (2)				
In-Li 20	3.256 (1)		4.933 (2)				
In-Li 22	3.254 (3)	**3.254(2)**	4.937 (7)	**4.937(4)**	140	**ductile**	**(In)**
In-Li 25	3.255 (2)		4.940 (4)				
In-Li 26	3.252 (7)		4.93 (2)				
In-Li 33	3.252 (4)		4.94 (1)				
In-Li 1	3.254 (1)		4.937 (4)				
In-Li 1-1 (quenched L)	3.253 (4)		4.94 (1)				
In-Li 2	3.253 (3)		4.940 (8)				
In-Li 3	3.252 (5)	**3.253(1)**	4.94 (2)	**4.940(2)**	220, 327, 380	**brittle**	**(In)'**
In-Li 16	3.2535 (6)		4.943 (1)				
In-Li 16 (after DTA)	3.253 (1)		4.940 (3)				
In-Li 21	3.255 (7)		4.94 (2)				
In-Li 29	3.2525 (7)		4.942 (2)				

Concluding these results for the "InLi-split hypothesis" following reaction is suggested:

$$L \xrightarrow{\text{cooling}} (In)' + InLi_{(Li\text{-deficient})}/InLi_{(Li\text{-rich})} \xrightarrow{\text{annealing}} (In)' + InLi$$

The associated reaction is supposed to be a further delithiation $InLi_{(Li\text{-deficient})}$ leading to the formation of (In)' and $InLi_{(Li\text{-rich})}$. This reaction would explain the risen content of (In)' from ~3 to ~27 mass fraction, and the lowered content of $InLi_{(Li\text{-deficient})}$ but a verification would need kinetic investigations.

It is also to mention that no splitting of InLi was observed only in samples from x_{Li} = 0.48 to 0.58 which are inside the InLi homogeneity range. In samples In-Li 8 and In-Li 9 at 30 and 60 at.% Li, respectively, InLi is formed as an equilibrium phase but not split (see Fig. 90). This also supports the "InLi-split hypothesis", assuming a slow diffusion based reaction of (In)' + $InLi_{(Li\text{-deficient})}/InLi_{(Li\text{-rich})}$ to InLi and eventually to In_2Li_3 during annealing. In-Li 8 also supports the assumption

that the occurrence of brittle (In)' is always combined with InLi splitting since in this sample only the ductile (In) with smaller lattice parameter c is present.

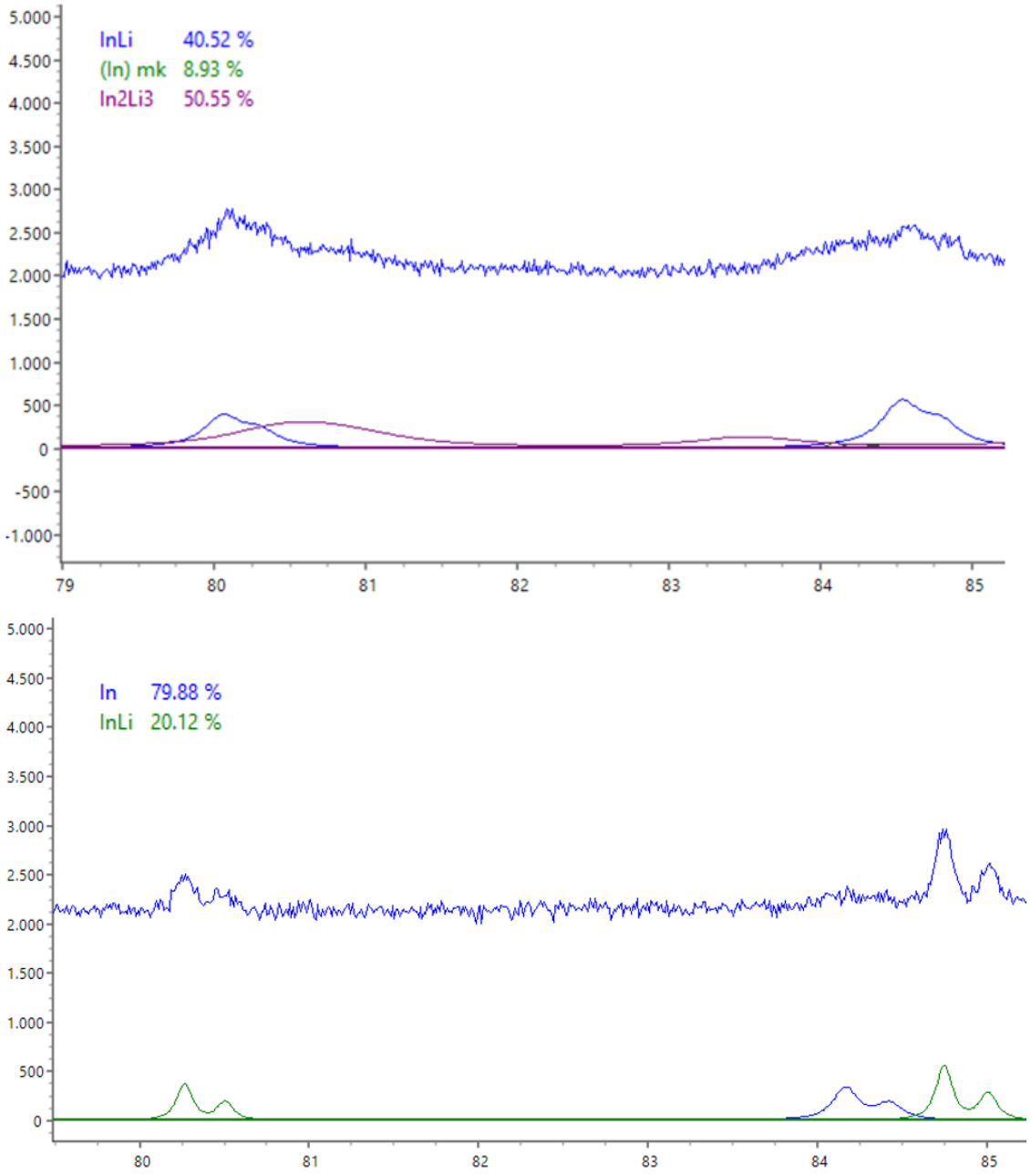

Figure 90 Representative part of the XRD pattern (of TOPAS-64 7.13 of Bruker) (counts vs. 2θ) from the range 2θ ≈ 80 to 85° showing reflections of sample In-Li 9 annealed at 220 °C (top) and reflections of In-Li 8 annealed at 140 °C (bottom) with no splitting. Hence, only 2 peaks per reflection occurred from $CuK_{\alpha 1}$ and $CuK_{\alpha 2}$ radiation. Blue curves: Detected pattern. Blue, green and purple curves beneath: Refined pattern with phase composition in the upper, left corner.

5.4.6 In-Li 1

The DTA measurement of In-Li 1 (48.1 at.% Li), see Fig. 91 showed only a strong endothermic peak during heating at an extrapolated onset temperature of 614.9 °C and 623.4 °C at the peak maximum. This was confirmed on cooling by a strong exothermic peak at an average onset temperature of 594.3 °C. The associated reaction is InLi + (In) ⇄ L (at 623.4 °C) followed by the reaction at the solvus InLi ⇄ InLi + (In) (at 614.9 °C), near the congruent melting L ⇄ InLi at slightly higher Li-content.

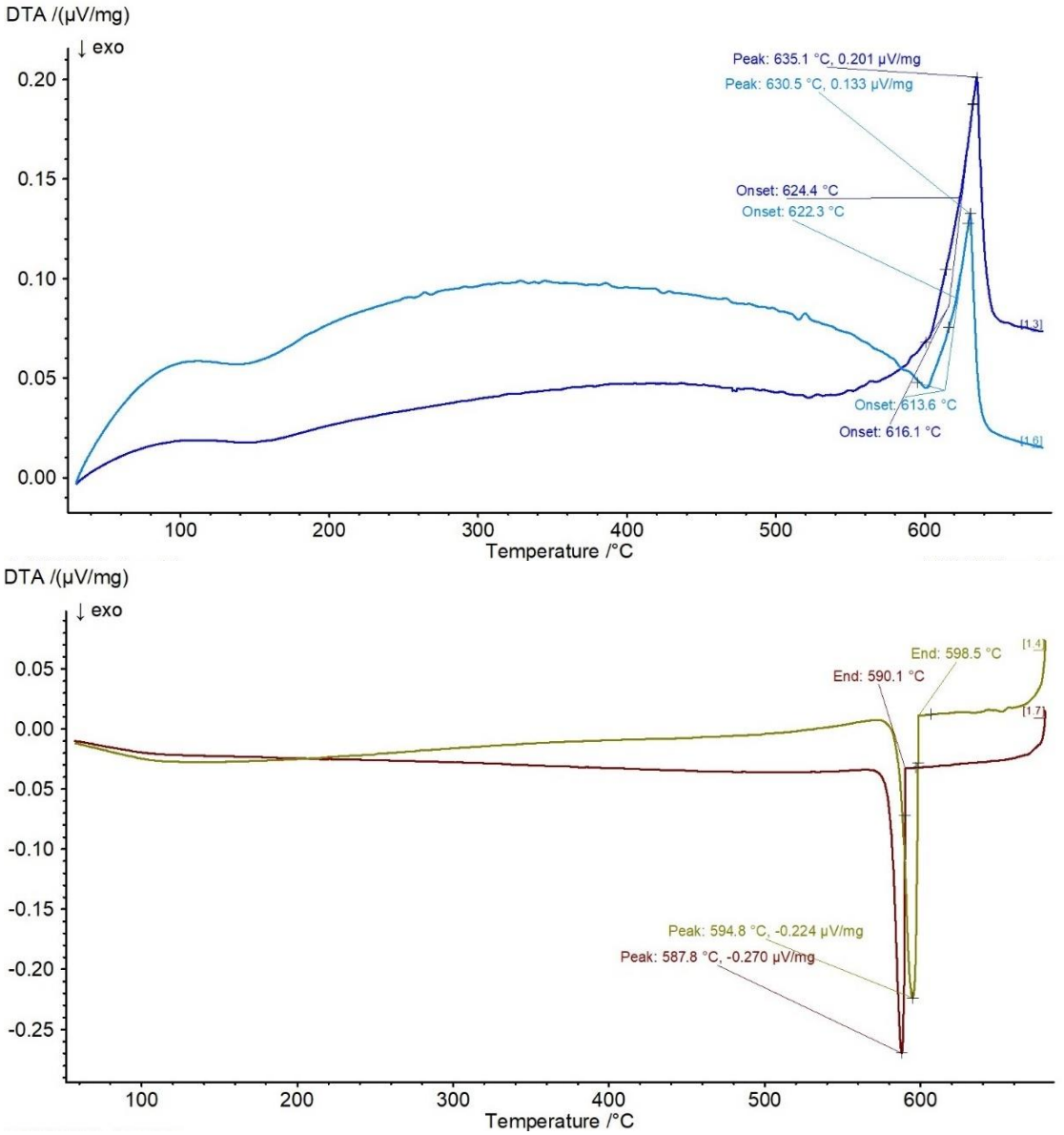

Figure 91 DTA plot (of Netzsch: Proteus® 6.1.0.) (Thermoelectric voltage (µV/mg) vs. Temperature (°C)) of sample In-Li 1. Top Result of 1st (dark blue) and 2nd heating cycle (bright blue), with endothermic reactions. Bottom: Result of 1st (green) and 2nd cooling cycle (red), with exothermic reactions. “Peak” marks the maximum/minimum temperature of the occurring reaction, “Onset/Ende” marks the temperature of the occurring reaction calculated by double-tangent method.

The Calvet-type 3D-DSC measurement of In-Li 1 showed no reaction beneath 300 °C (see Fig. 92).

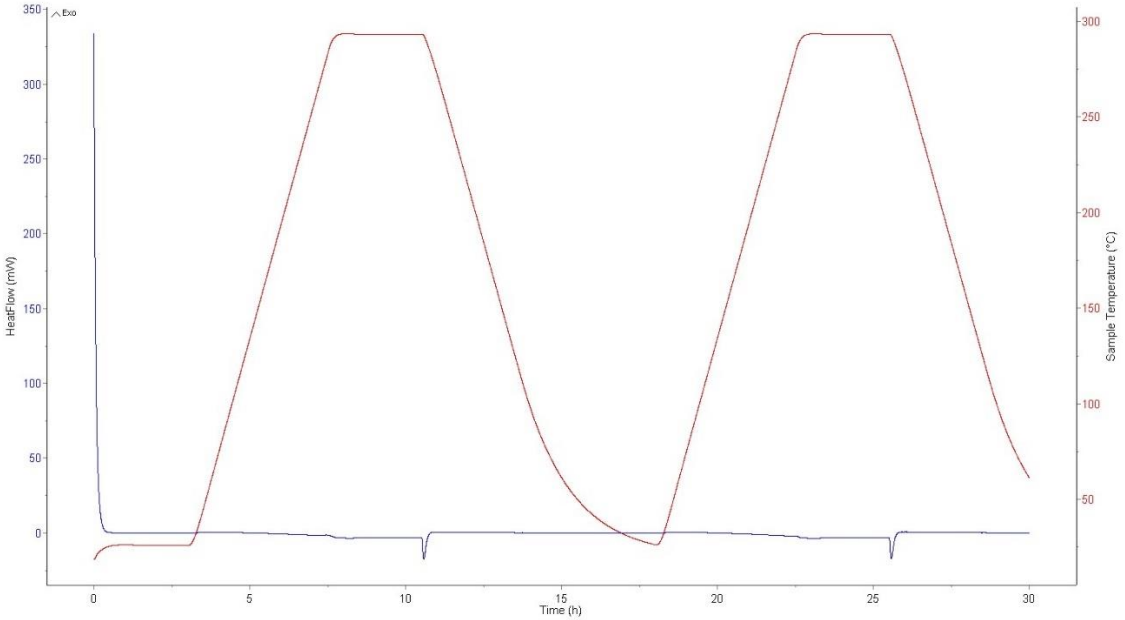

Figure 92 Calvet-type 3D-DSC plot (of SETSYS Evaluation). Left: Heat flow (mW) (blue curve), right: Sample Temperature (°C) (red curve) vs. Time (h) with 2 measured heating/cooling cycles of sample In-Li 1.

In-Li 1 (48.1 at.% Li, annealed at 327 °C) was brittle enough to powder it for the XRD measurement, which showed reflections of the phases $InLi_{(Li\text{-}deficient)}$/$InLi_{(Li\text{-}rich)}$ (cubic, $Fd\bar{3}m$) and (In)' (tetragonal, $I4/mmm$), (see Fig. 93). After refinement for phase anaylsis with a quality of Rwp = 3.592, 60.4 wt.% $InLi_{(Li\text{-}rich)}$ with the lattice paramter a = 6.7745 (7) Å and 23.8 wt.% $InLi_{(Li\text{- }deficient)}$ with a = 6.785 (1) Å as well as 15.8 at.% (In)' with a = 3.254 (1) Å and c = 4.937 (4) Å were found. $InLi_{(Li\text{-}deficient)}$/$InLi_{(Li\text{-}rich)}$ showed the already discussed "splitting".
According to the DTA and Calvet-type 3D-DSC results the sample In-Li 1 was in the InLi phase region, however, as already discussed even after annealing at 327 °C for 57 days phase equilibrium was still not established.

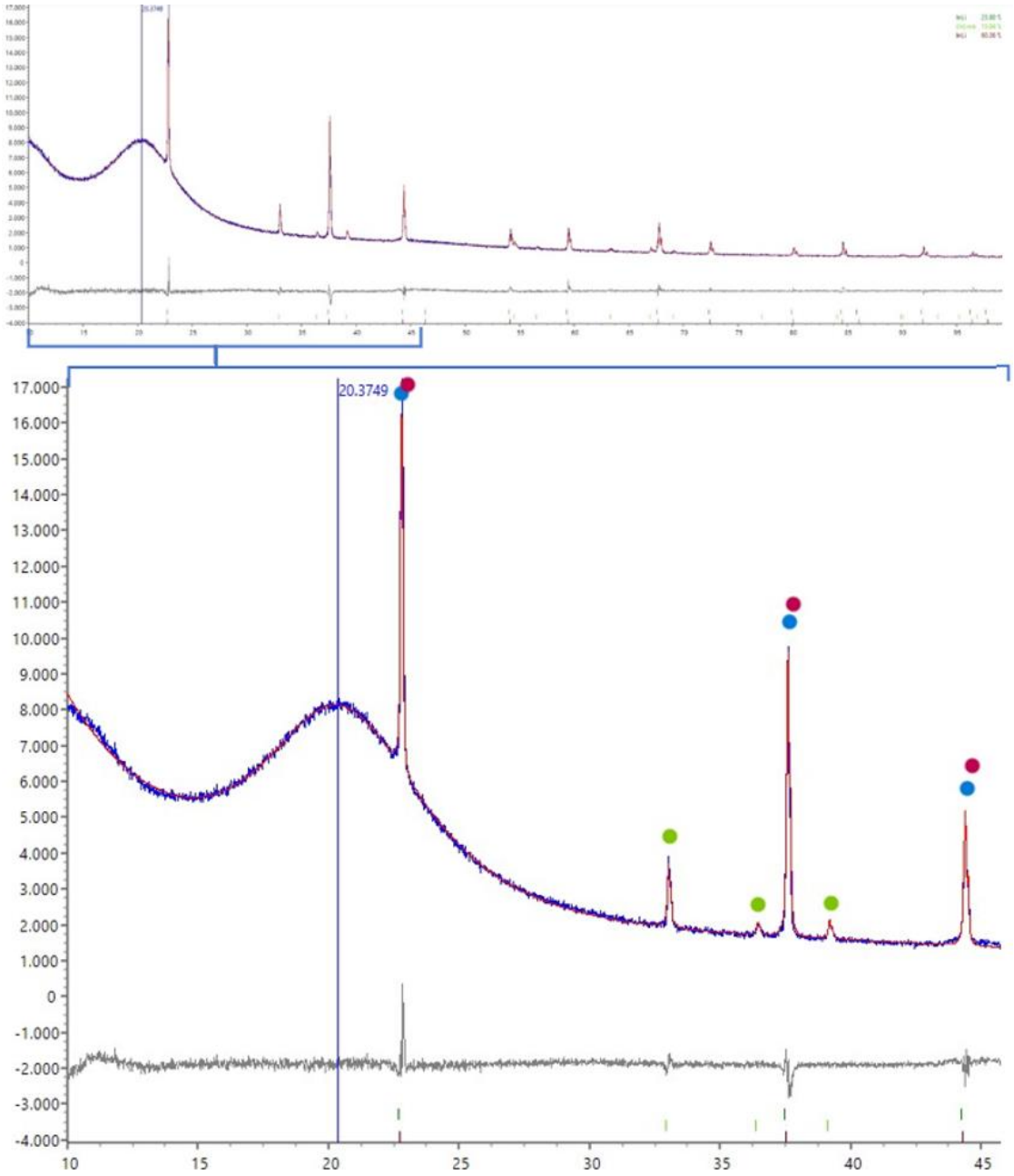

Figure 93 XRD pattern (of TOPAS-64 7.13 of Bruker) (counts vs. 2θ) of sample In-Li 1. Magnified part (2θ=10 to 45°) with significant reflections of: $InLi_{(Li\text{-deficient})}$…●, $InLi_{(Li\text{- rich})}$…● and (In)'…●. The "bulge" at 10 and 20° (θ/2θ-goniometer mode) originates from the amorphous PC dome of the sample holder. Blue curve: Measured pattern. Red curve: Refined pattern. Grey curve: Difference between measured and refined pattern.

5.4.7 The new phase $InLi_4$ ht

The samples In-Li 11, 11-1, 12, 19 and 37, all in the range of 76 to 85 at.% Li, did not reveal an unkown phase in XRD phase analysis. As already mentioned, Thümmel et al. [50] suggested the existence of the high temperature phase $InLi_4$ ht at its nominal stoichiometric composition, based on thermal analysis and powder XRD data. However, they could not do indexing, due to the appearance of too many reflections. Alexander et al. [51] did confirm a reversible transformation of a high and a low temperature phase with the most likely composition of $InLi_4$. They recognized the similarity of the phase's XRD pattern to the one of the fcc phase Pb_5Li_{22}. However, 3 reflections did not fit with the indexing of the new phase for the description as crystal structure of Pb_5Li_{22}-type and the calculated lattice parameter a was also not suitable. These 3 reflections would rather be indexed on a primitive cubic cell. Stöhr et al. [54] were eventually the first who identified the low temperature phase "$InLi_4$" as In_3Li_{13} by SCXRD.

Based on this data and on the structural relation to the trial structures InLi and In_3Li_{13} was indexing of reflections related to the unknown phase accomplished. The XRD pattern seemed to have characteristic reflections of a bcc lattice, thus the best suitable space group was $Im\bar{3}m$. Then was the lattice parameter a = 5.805 (5) Å for a bcc lattice calculated (see Fig. 94 and section "3.2.2 X-ray diffraction", Bragg-law). The value of a was identified as the half of the space diagonal of the cubic trial structure InLi. Subsequently were the atomic coordinates approximated based on the stoichiometry of $InLi_4$ and on the structural relation to the trial structures. Finally, was the occupation factor refined describing a possible non-stoichiometry via substitution mechanism. The result was a $InLi_4$ ht (≈In_3Li_{13} ht) phase of $MnGa_4$- or $PtHg_4$-type respectively with a bcc In-sublattice and a primitive cubic Li-sublattice (see Fig. 95).

h	k	l	m	d	th2
1	1	0	12	4.10487	21.63190
2	0	0	6	2.90258	30.77954
2	1	1	24	2.36995	37.93450
2	2	0	12	2.05243	44.08689
2	2	2	8	1.67580	54.73014
3	1	0	24	1.83575	49.61979
3	2	1	48	1.55149	59.53583
3	3	0	12	1.36829	68.52211
3	3	2	24	1.23766	76.98037
4	0	0	6	1.45129	64.11471
4	1	1	24	1.36829	68.52211
4	2	0	24	1.29807	72.79967
4	2	2	24	1.18497	81.09154
4	3	1	48	1.13849	85.15689
4	3	3	24	0.99558	101.37835
4	4	0	12	1.02622	97.28808
4	4	2	24	0.96753	105.52837
5	1	0	24	1.13849	85.15689
5	2	1	48	1.05987	93.23489
5	3	0	24	0.99558	101.37835
5	3	2	48	0.94172	109.76385
5	4	1	48	0.89576	118.62021
6	0	0	6	0.96753	105.52837
6	1	1	24	0.94172	109.76385
6	2	0	24	0.91788	114.11521

Figure 94 hkl…Miller Indices, m…multiplicity, d…lattice plane spacing and th2… 2θ of $InLi_4$ ht of sample In-Li 19 (of TOPAS-64 7.13 of Bruker).

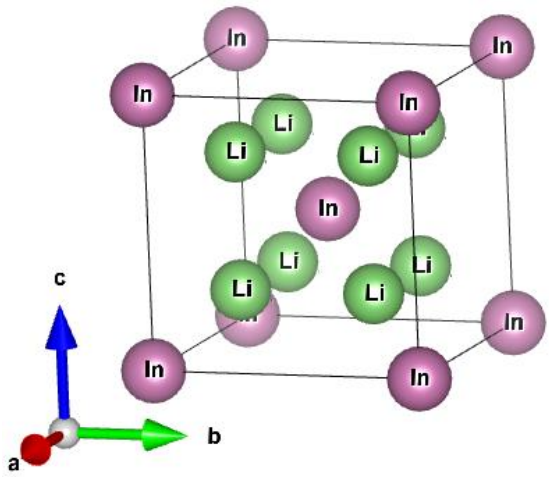

Phase name	InLi4
R-Bragg	2.411
Spacegroup	Im-3m
Scale	0.000685(16)
Cell Mass	288.0(3)
Cell Volume (Å^3)	195.63(5)
Wt% - Rietveld	25.9(6)
Double-Voigt|Approach	
Cry size Lorentzian	42.0(16)
k: 1 LVol-IB (nm)	26.7(10)
k: 0.89 LVol-FWHM (nm)	37.4(15)
Crystal Linear Absorption Coeff. (1/cm)	465.25(11)
Crystal Density (g/cm^3)	2.444(2)
Lattice parameters	
a (Å)	5.805 (5)

Site	Np	x	y	z	Atom	Occ	Beq
In	2	0.00000	0.00000	0.00000	In	1	1.5
					Li	0	1.5
Li	8	0.25000	0.25000	0.25000	Li	0.997(5)	1.5
					In	0.003(5)	1.5

Figure 95 Crystal structure with crystallographic data of the postulated $InLi_4$ ht (≈In_3Li_{13} ht) phase (of TOPAS-64 7.13 of Bruker).

The verification of the $InLi_4$ ht crystal structure model described by powder-XRD was tried to do with SCXRD. It turned out that almost all choosen “single crystals” of the samples In-Li 11, 11-1 and 12, which seemed to be suitable for SCXRD measurement in terms of shape and size, were polycrystalline particles. Eventually one suitable phase pure single crystal was found in sample In-Li 19. However, this one was identified as InLi crystal by SCXRD indexing. Nonetheless was a crystal structure determination performed (see Fig. 96) to verify the powder XRD result, which showed that In-Li 19 contained $InLi_4$ ht and InLi and/or $In_{2+x}Li_{10-x}$ (x=1.59) (discussed in detail in section “5.4.8 In-Li 19”). The latter two phases show a very similar pattern and cannot be clearly distinguished. In any

case, the sample contained $InLi_4$ ht and InLi, so In-Li 19 was not in phase equilibrium. It is suggested that fast cooling led to coring, typical for peritectic reactions resulting in a InLi residue, while the already discussed slow solid-state diffusion inhibited phase equilibration.

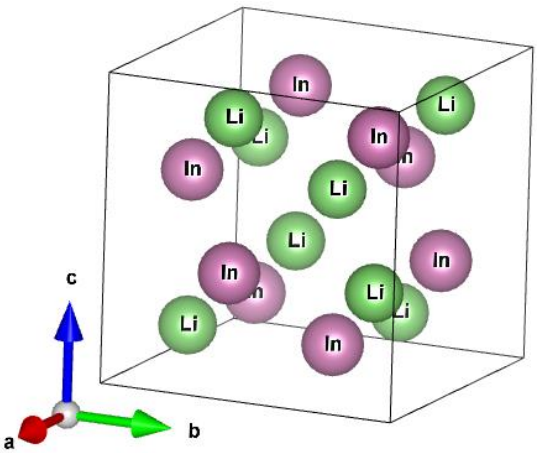

Lattice type F
Space group name F d -3 m
Space group number 227
Setting number 2

Lattice parameters

a	b	c	alpha	beta	gamma
6.79000	6.79000	6.79000	90.0000	90.0000	90.0000

Unit-cell volume = 313.046834 Å^3

Structure parameters

		x	y	z	Occ.	U	Site	Sym.
1 In	In	0.12500	0.12500	0.12500	1.000	0.019	8a	-43m
2 Li	Li	0.37500	0.37500	0.37500	1.000	0.046	8b	-43m

Figure 96 Crystal structure with crystallographic data of the phase InLi of sample In-Li 19, identified by SCXRD (via the software COLLECT, SHELXS-97 and SHELXL-97).

It was tried to grow bigger $InLi_4$ ht single crystals from the sample In-Li 19 and from a new bigger batch with the composition of in-Li 19 labeled as In-Li 19-1. In addition, was also In-Li 5 used for crystal growth efforts, due to its partially liquid state at ~380 °C.

Following heat treatment for crystal growth was used: The molten samples were fast cooled from 500 °C with ~10 °C/min to 390 °C and held there for 5 to 7 days. In the case of In-Li 5 and 19 was an additional cooling step carried out to get 380 °C within 48 h. After 6 days at 380 °C (or 7 days at 390 °C in the case of In-Li 19-1) were the sample quenched with water to room temperature.

In the case of In-Li 5 a suitable single crystal could not be found, most likely due to the soft and ductile solidified melt Li-rich melt covering the single crystals. The crystals of In-Li 19-1 were in the sub-micrometer range, thus only polycrystalline particles had the crucial size for SCXRD investigations. In summary, the postulated $InLi_4$ ht crystal structure could not be confirmed by SCXRD yet.

5.4.8 In-Li 19

The DTA measurement of In-Li 19 (79.8 at.% Li), see Fig. 97 showed a strong peak on heating with an average temperature of 263.1 °C and then three overlapping, strong peaks at onset temperatures of 369.1 °C and 397.1 °C, the maximum of the third peak is at 423.0 °C (“Onset”) respectively from endothermic reactions. These reactions were partly confirmed on cooling by strong exothermic reactions with Onsets at an average temperature of 424.4, 401.1 and 232.0 °C. It is to mention that it was not possible to determine the real onset of overlapping peaks via the used software of Netzsch Proteus® 6.1.0.

The associated reactions are the liquidus reaction L ⇄ L + InLi (at 423.0 °C), the peritectic reaction L + InLi ⇄ $InLi_4$ ht at 397.1 °C, as well as the peritectoid reaction $InLi_4$ ht + $In_{2+x}Li_{10-x}$ ⇄ $In_{8+x}Li_{22-x}$ (x=0.1) at 369.1 °C and the peritectoid reaction $InLi_4$ ht + $In_{8+x}Li_{22-x}$ (x=0.1) ⇄ In_3Li_{13} (x=0.1) at 263.1 °C.

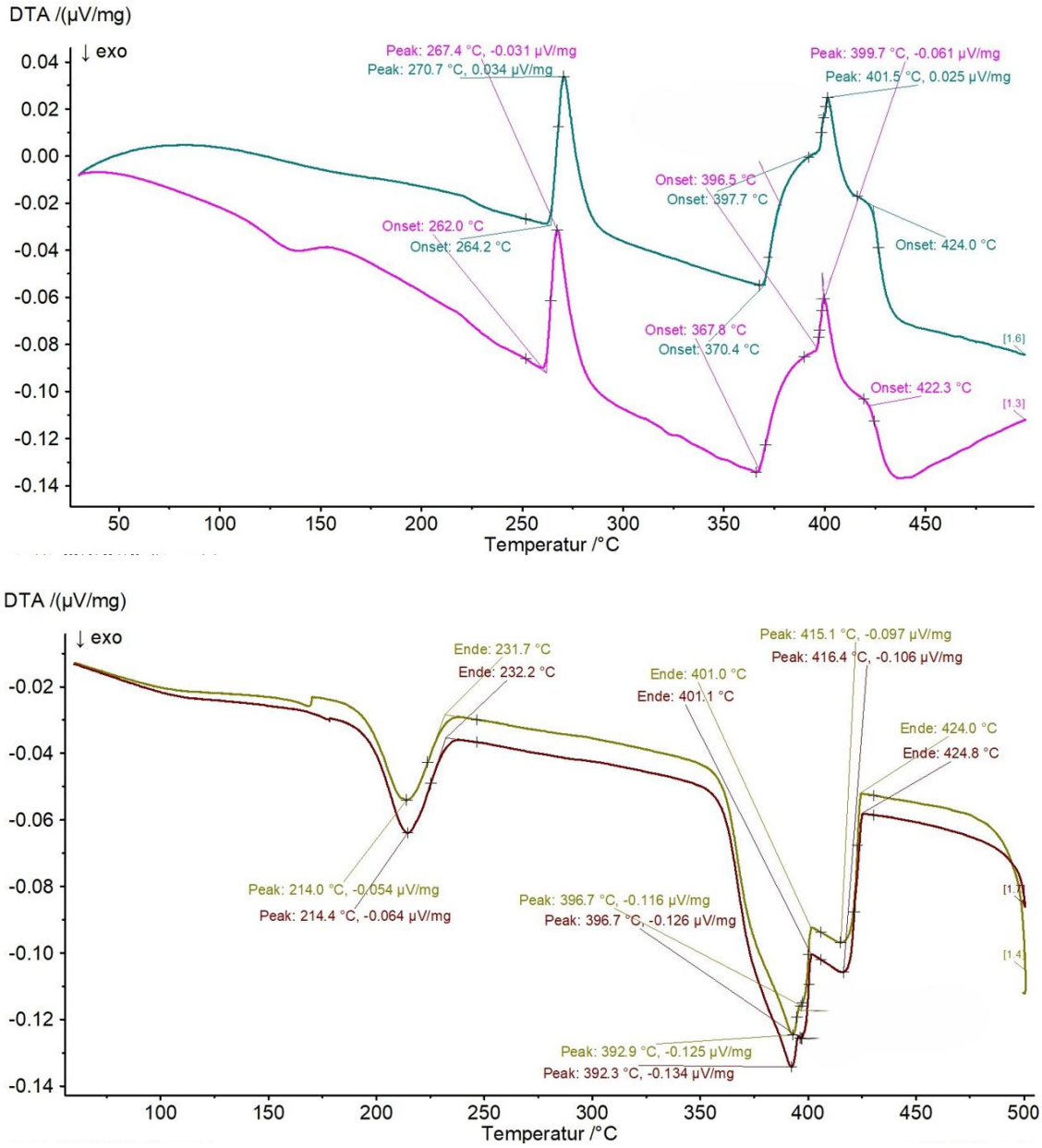

Figure 97 DTA plot (of Netzsch: Proteus® 6.1.0.) (thermoelectric voltage (µV/mg) vs. Temperature (°C)) of sample In-Li 19. Top: Result of 1st (pink) heating cycle (green), with endothermic reactions. Bottom: Result of 2nd (green) cooling cycle (red), with exothermic reactions. “Peak” marks the maximum/minimum temperature of the occurring reaction, “Onset/Ende” marks the temperature of the occurring reaction calculated by double-tangent method.

The results of the Calvet-type 3D-DSC measurement of In-Li 19 (see Fig. 98) were complementary to the DTA results. Thus, the endothermic, strong peaks during heating appeared at a slightly higher average temperature of 267.34 °C,

compared to the first DTA signals and the associated exothermic, strong peaks during cooling appeared at 245.93 °C.

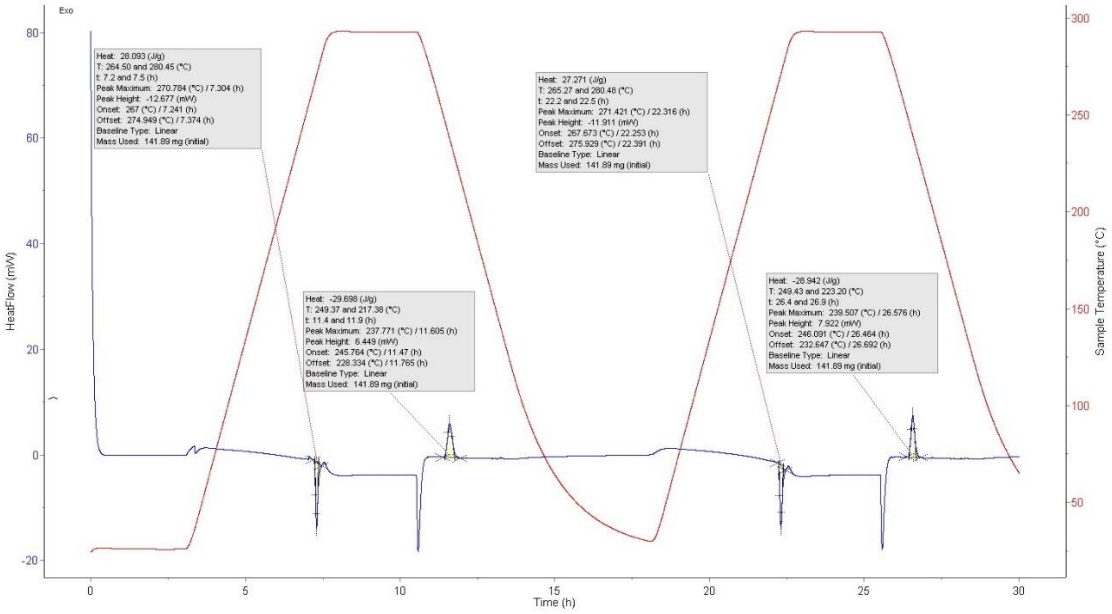

Figure 98 Calvet-type 3D-DSC plot (of SETSYS Evaluation). Left: Heat flow (mW) (blue curve), right: Sample Temperature (°C) (red curve) vs. Time (h) with 2 measured heating/cooling cycles of sample In- Li 19. The yellow part (integrated area) during heating/cooling marks the peak with its starting temperature (Onset within gray box) resulting from endothermic (peak points down)/exothermic (peak points up) reactions.

In-Li 19 (79.8 at.% Li, annealed at 380 °C) was brittle enough to be powdered for the XRD measurement, which showed peaks allocated to the phases InLi (cubic, *Fd*$\bar{3}$*m*) and $InLi_4$ ht (cubic, *Im*$\bar{3}$*m*), (see Fig. 99). After refinement of a quality of Rwp = 2.449 for phase analysis, 74.1 wt.% InLi with the lattice paramter a = 6.691 (5) Å and 25.9 wt.% $InLi_4$ ht with the lattice parameters a = 5.805 (5) Å were found. Alternatevely, the pattern can be refinded with $In_{2+x}Li_{10-x}$ as an additional phase.

The lattice parameter a of InLi is significantly smaller than this of stoichiometric InLi (a = 6.79 (0) Å) and can thus be consdiered as $InLi_{(Li\text{-}rich)}$. That verifies the broad homogenity range at elevated temperatures (~400 °C, up to ~75 at.% Li) postulated in the literature.

Phase equilibrium was not fully established in sample In-Li 19 due to slow solid-state diffusion on annealing.

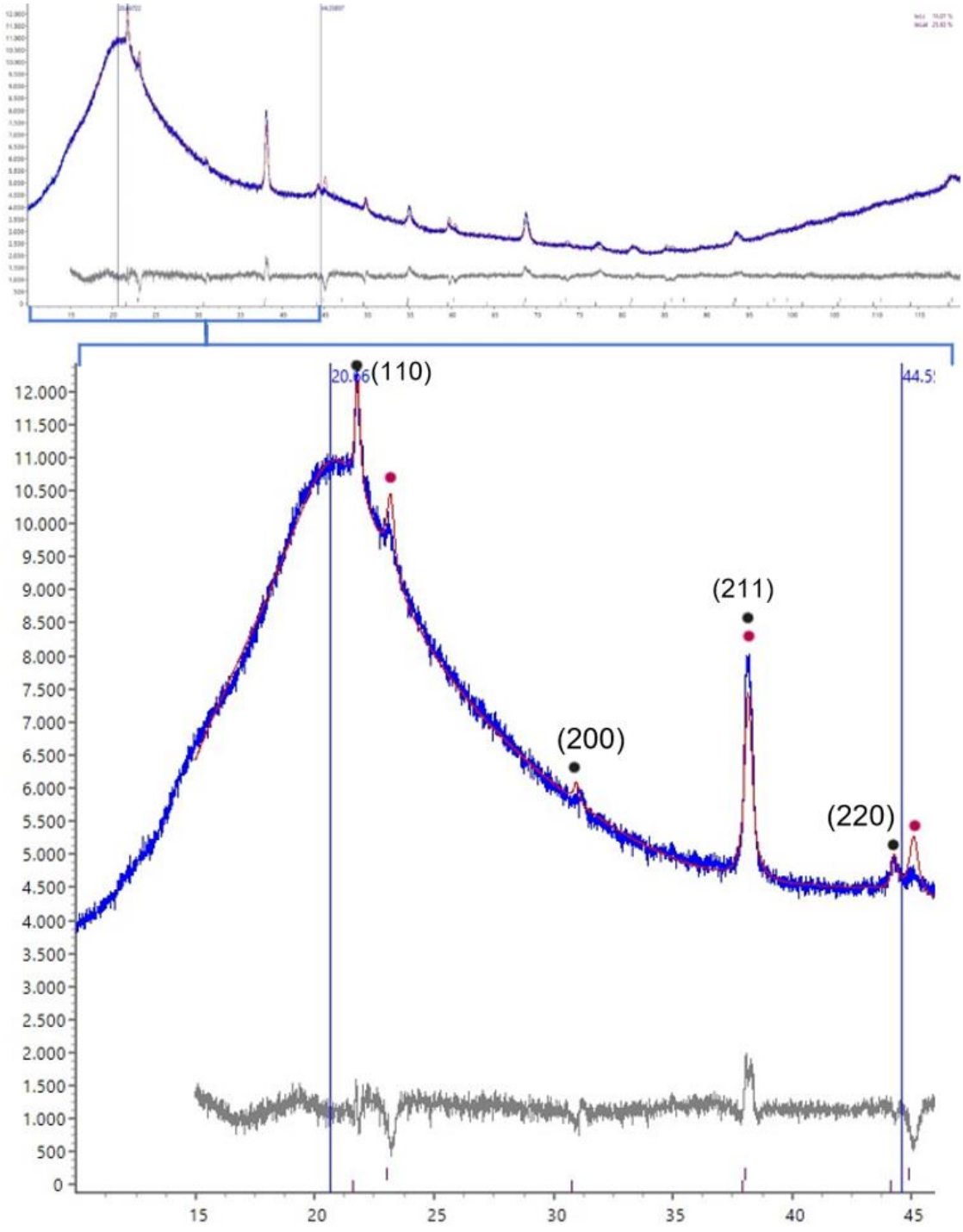

Figure 99 XRD pattern (of TOPAS-64 7.13 of Bruker) (counts vs. 2θ) of sample In-Li 19. Magnified part (2θ=10 to 45°) with significant reflections of: $InLi_{(Li\text{-}rich)}$… ● and $InLi_4$ ht… ● with Miller indices. The "bulge" at 20 and 45° (θ/θ-goniometer mode) originates from the amorphous PC dome of the sample holder. Blue curve: Measured pattern. Red curve: Refined pattern. Grey curve: Difference between measured and refined pattern.

5.4.9 In-Li 11 and In-Li 11-1

The DTA measurement of In-Li 11 (75.8 at.% Li), see Fig. 100 showed slightly overlapping, strong peaks with an average temperature of 342.1 °C and 353.1 °C as well as weak peaks at 367.2 °C and at 400.6 °C from endothermic reactions on heating. Overlapping, strong peaks from endothermic reactions appeared also at 431.8 °C and at 481.3 °C (maximum). The strong peaks were partly confirmed during cooling by the exothermic reactions at average temperatures of 475.3, 428.8, 346.6 and 330.7 °C. It is to mention that it was not possible to determine the real Onset of overlapping peaks via the used software of Netzsch Proteus® 6.1.0.

The associated reactions are first solidification $L \rightleftarrows L + InLi$ (at 481.3 °C), the solidus reaction $L + InLi \rightleftarrows InLi$ (at 431.8 °C) as well as the peritectic reaction $L + InLi \rightleftarrows InLi_4$ ht at 400.6 °C. The eutectoid reaction $InLi \rightleftarrows InLi_2 + InLi_4$ ht should also be present but the corresponding DTA-peak certainly overlaps with that of the peritectic reaction. The same is the case for the peritectoid reaction $InLi_2 + InLi_4$ ht $\rightleftarrows In_{2+x}Li_{10-x}$ (x=1.59). Further the reaction $In_{2+x}Li_{10-x}$ (x=1.59) + $InLi_4$ ht $\rightleftarrows In_{8+x}Li_{22-x}$ (x=0.1) at 367.2 °C occurred. Here it is to mention that the weak peak at 367.2 °C occurred only on second heating cycle, most likely due to enhanced thermal contact of the sample to the crucible bottom. The two effects at 342.1 and 353.1 °C would fit to $InLi + InLi_2 \rightleftarrows In_2Li_3$ and $In_{2+x}Li_{10-x}$ (x=1.59) $\rightleftarrows InLi_2 + In_{8+x}Li_{22-x}$ (x=0.1), but should, however, not appear in this sample.

During cooling only three strong peaks were visible, probably due to overlapping caused by supercooling.

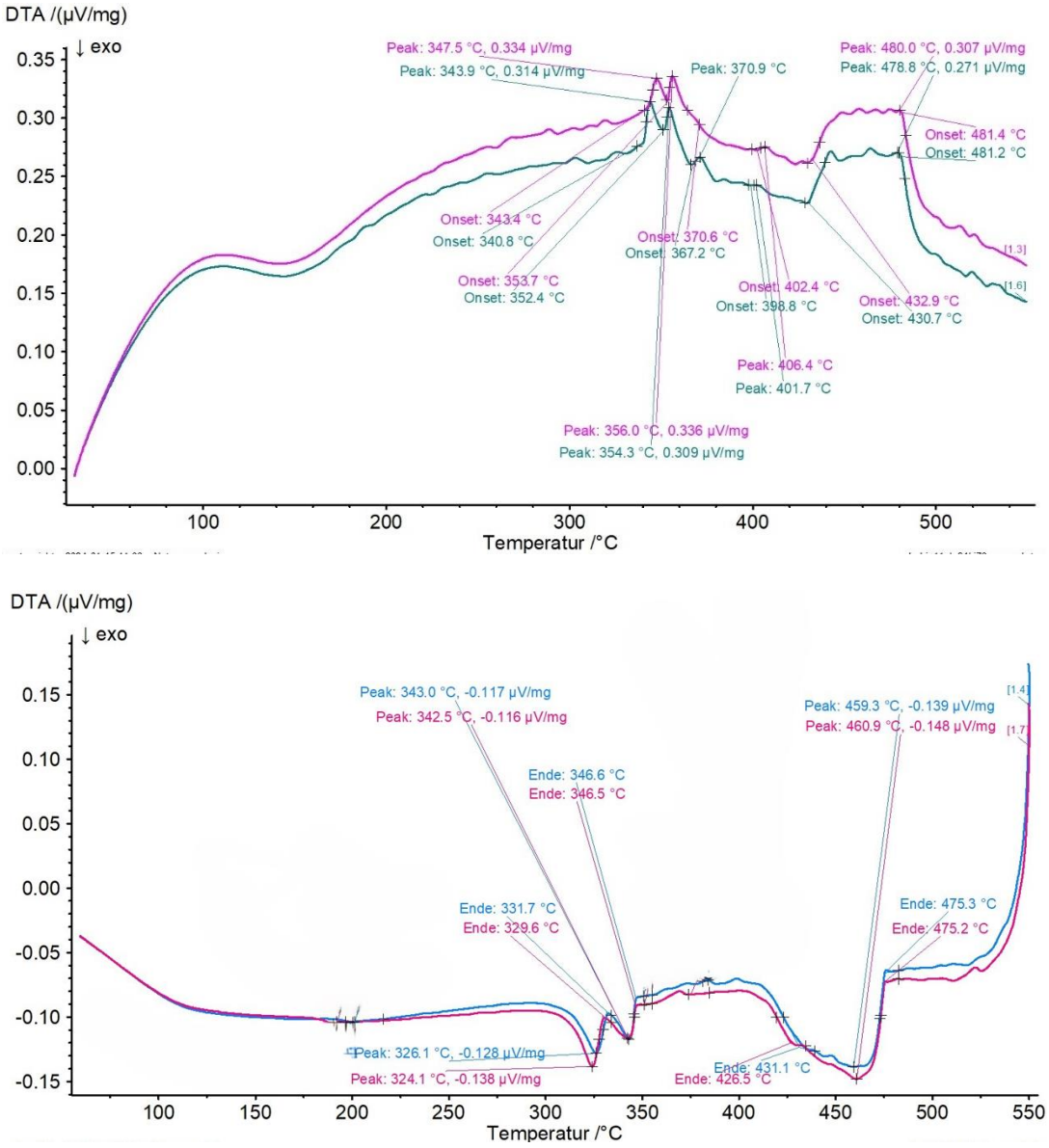

Figure 100 DTA plot (of Netzsch: Proteus® 6.1.0.) (thermoelectric voltage (µV/mg) vs. Temperature (°C)) of sample In-Li 11. Top: Result of 1st (pink) and 2nd heating cycle (green), with endothermic reactions. Bottom: Result of 1st (blue) and 2nd cooling cycle (red), with exothermic reactions. “Peak” marks the maximum/minimum temperature of the occurring reaction, “Onset/Ende” marks the temperature of the occurring reaction calculated by double-tangent method.

The Calvet-type 3D-DSC measurement of In-Li 11 also showed no reaction beneath 300 °C (see Fig. 101).

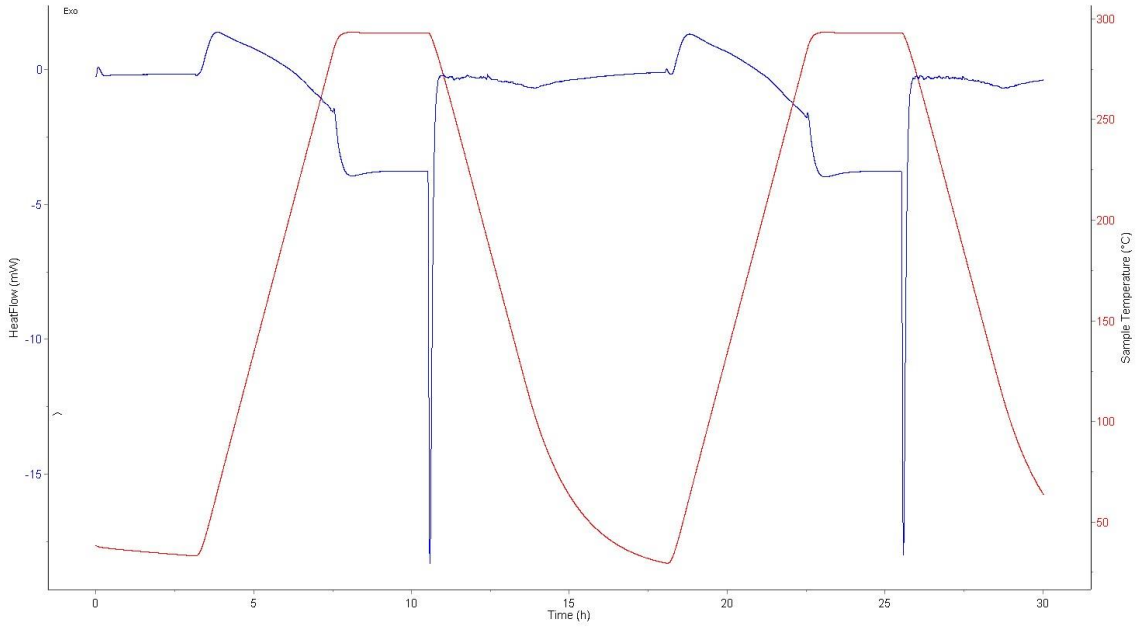

Figure 101 Calvet-type 3D-DSC plot (of SETSYS Evaluation). Left: Heat flow (mW) (blue curve), right: Sample Temperature (°C) (red curve) vs. Time (h) with 2 measured heating/cooling cycles of sample In-Li 11.

In-Li 11-1 (76.0 at.% Li, annealed at 380 °C) differs from In-Li 11 only by application of alloying method 9. In-Li 11-1 was brittle enough to powder it for the XRD measurement, which showed reflections of the phases $In_{2+x}Li_{10-x}$ (x=1.59) (hexagonal, *P6/mmm*) and $InLi_4$ ht (cubic, $Im\bar{3}m$), (see Fig. 102). After refinement for phase analysis with a quality of Rwp = 2.261, 90.2 wt.% $In_{2+x}Li_{10-x}$ (x=1.59) with the lattice paramters a = 4.716 (5) Å and c = 11.55 (2) Å as well as 9.8 wt.% $InLi_4$ ht with the lattice parameter a = 5.777 (8) Å were found.

$In_{2+x}Li_{10-x}$ (x=1.59) and $InLi_4$ ht were proved to have a homogenity range, due to the deviation from their lattice parameters of the literature a = 4.697 (5) Å and c = 11.52 (6) Å or a = 5.805 (5) Å respectively.

This the sample In-Li 11-1 represents a two-phase field were $In_{2+x}Li_{10-x}$ (x=1.59) is in equilibrium with $InLi_4$ ht.

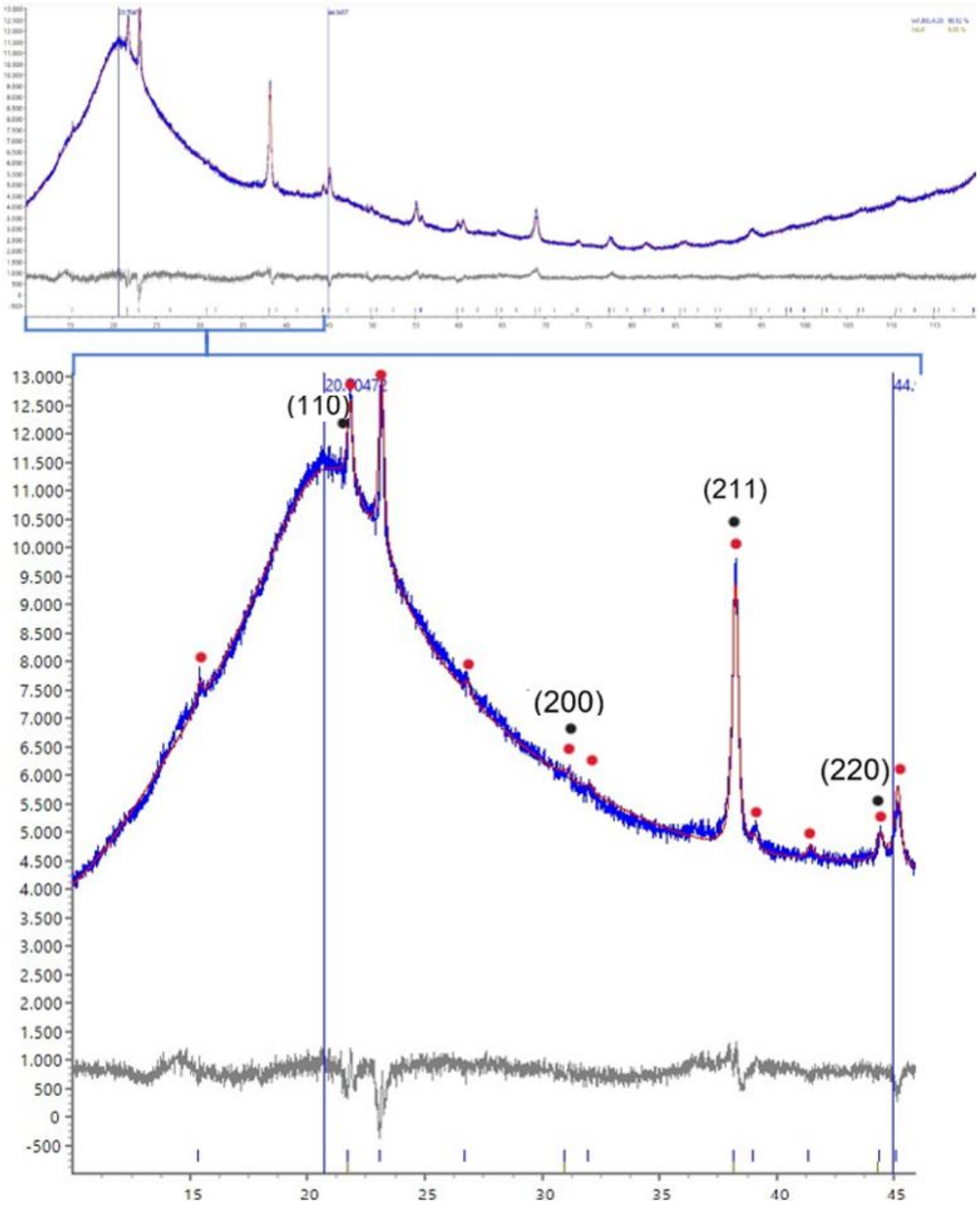

Figure 102 XRD pattern (of TOPAS-64 7.13 of Bruker) (counts vs. 2θ) of sample In-Li 11-1. Magnified part (2θ=10 to 45°) with significant reflections of: $In_{2+x}Li_{10-x}$ (x=1.59)… ● and $InLi_4$ ht… ● with Miller indices. The "bulge" at 20 and 45° (θ/θ-goniometer mode) originates from the amorphous PC dome of the sample holder. Blue curve: Measured pattern. Red curve: Refined pattern. Grey curve: Difference between measured and refined pattern.

5.4.10 In-Li 14

The DTA measurement of In-Li 14 (94.7 at.% Li), see Fig. 103 showed overlapping, strong peaks during heating with an average temperature of 190.5 °C and of 229.8 °C from endothermic reactions. These signals appeared on cooling by strong exothermic, overlapping peaks at an average temperature of 236.6 °C and 192.1 °C. It is to mention that it was not possible to determine the real Onset of overlapping peaks via the used software of Netzsch Proteus® 6.1.0.

One associated reaction on heating is the metatectic reaction $InLi_4$ ht ⇄ In_3Li_{13} + L at ~229.8 °C. It is noteworthy at this point that in two of our samples, In-Li 14 and In-Li 6, the onset temperatures of signal for the invariant reaction involving L + In_3Li_{13} + (Li) (DTA: 190.5 and 191.1 °C; Calvet-type 3D-DSC: 191.07 and 195.42 °C) were significantly higher than the melting point of (Li) (180.54 °C) and the temperatures given by Grube et al. [47] (179, 178, 177 and 178 °C). Also, Lamprecht et al. [49], Thümmel et al. [50] and Alexander et al. [51] described this reaction as eutectic and not peritectic type.

Hence, to verify the eutectic kind of the invariant reaction at 190.5 °C, another sample In-Li 14-1 (94.9 at.% Li) was prepared by heating with a muffle furnace to 300 °C within 2 h followed by multiple shaking/turning of the sample at 300 °C and slow cooling to room temperature. This sample was investigated by DTA (see 4.3 DTA measurement) but instead of a α-Al_2O_3 pure Li was used as reference. The result showed a strong exothermic peak at 178.9 °C overlapping the endothermic peak of the invariant reaction. Thus, the reference melted (exothermic peak) before the invariant reaction took place, meaning the reaction should be of a peritectic kind and not of eutectic kind as described in the literature. So, at 190.5 °C the peritectic reaction L + In_3Li_{13} ⇄ (Li) could be established.

On cooling only strong peaks were visible, probable due to overlapping caused by supercooling. The first onset at 236.6 °C represents the, may be supercooled, solidification followed by the metatectic reaction, which cannot be resolved because of the quite small temperature difference, leading to overlapping. In addition, the reaction temperatures of 190.5 °C on heating was lower than the reaction temperatures of the cooling cycle. This can be explained with inaccurate evaluations caused by the overlapping of the peaks.

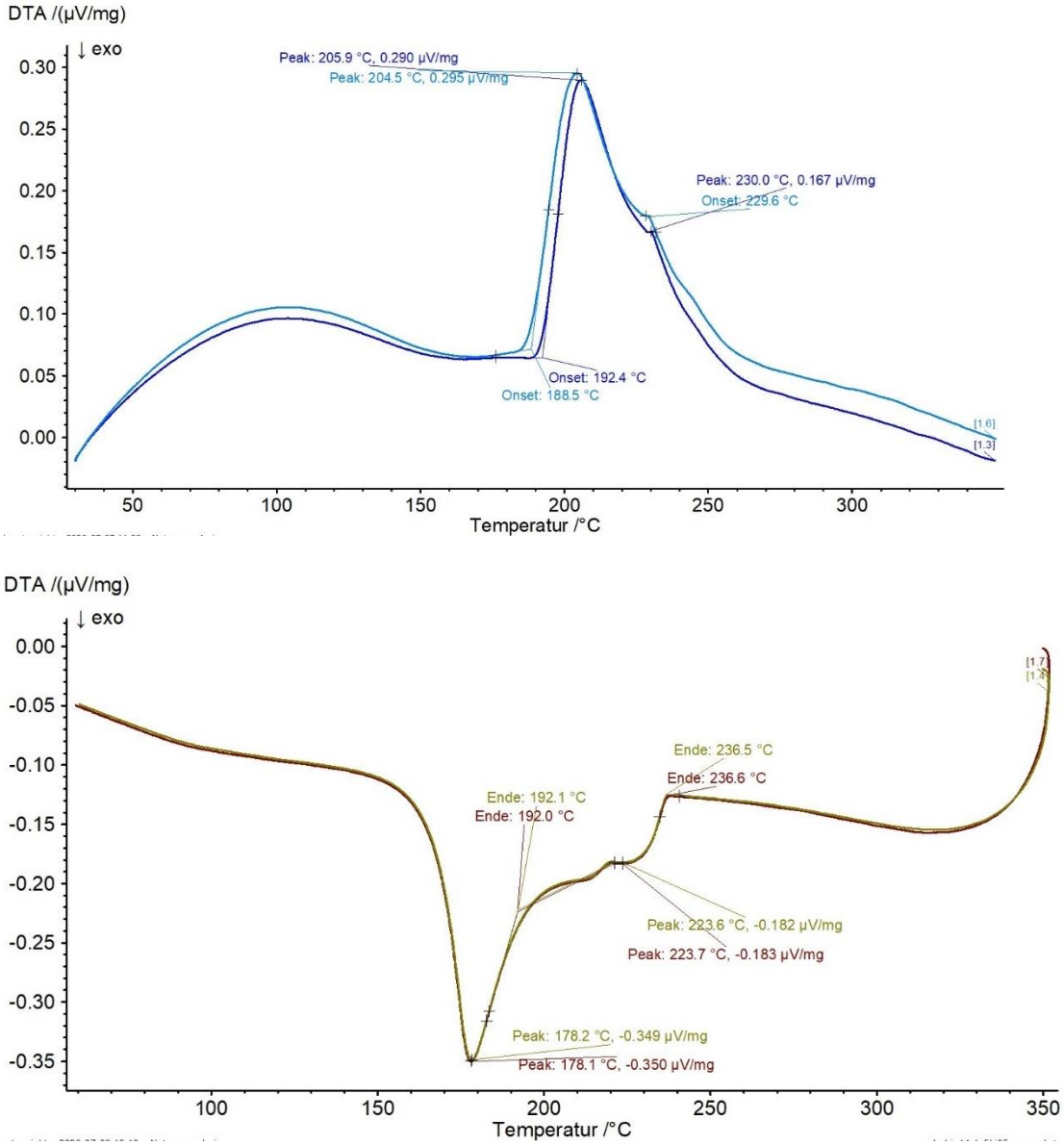

Figure 103 DTA plot (of Netzsch: Proteus® 6.1.0.) (thermoelectric voltage (µV/mg) vs. Temperature (°C)) of sample In- Li 14. Top: Result of 1st (dark blue) and 2nd heating cycle (bright blue), with endothermic reactions. Bottom: Result of 1st (green) and 2nd cooling cycle (red), with exothermic reactions. “Peak” marks the maximum/minimum temperature of the occurring reaction, “Onset/Ende” marks the temperature of the occurring reaction calculated by double-tangent method.

The Calvet-type 3D-DSC measurement of In-Li 14 was complementary to the DTA results. The endothermic, strong peaks during heating appeared at a slightly higher average temperature of 191.07 °C compared to the DTA signal. In addition, it was it possible to resolve the temperature of the metatectic reaction at 227.20 °C from the liquidus temperature at 237.53 °C (see weak peaks in Fig.

104). The associated weak peaks of the exothermic reactions during cooling appeared at 234.73 °C and 217.53 °C, while the strong peaks appeared at an average temperature of 196.97 °C. The last temperature on cooling is most likely too high due to inaccurate evaluation. According to our findings the invariant reaction should be of peritectic type, L + In_3Li_{13} ⇄ (Li). Thus, the measured results of DTA and 3D-DSC were weighted higher for the In-Li phase diagram construction of this diploma thesis than the contradicting results from literature.

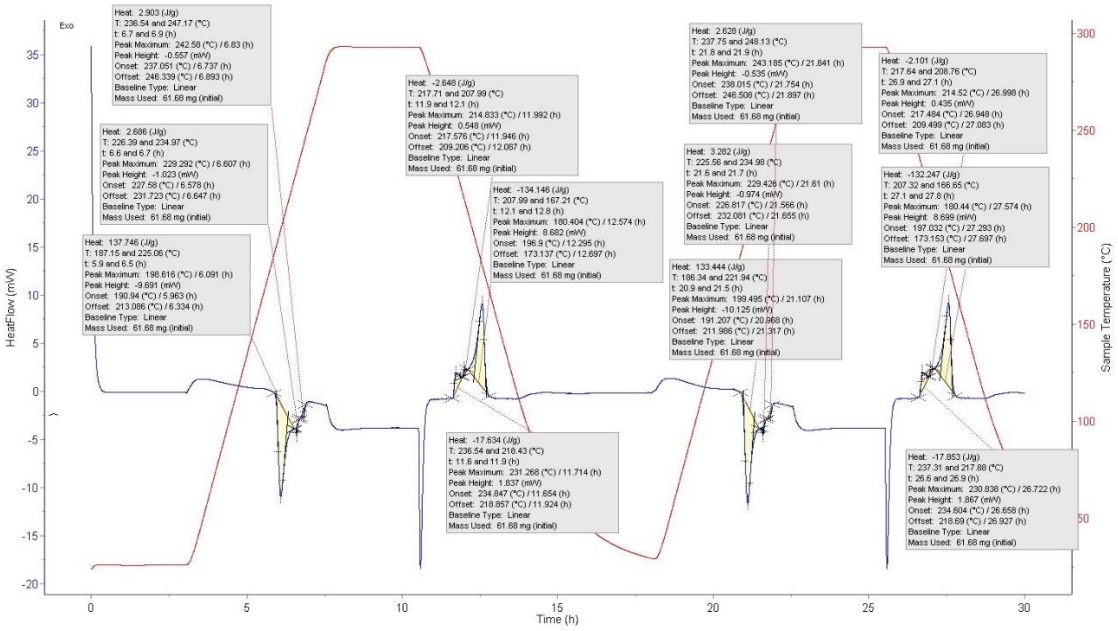

Figure 104 Calvet-type 3D-DSC plot (of SETSYS Evaluation). Left: Heat flow (mW) (blue curve), right: Sample Temperature (°C) (blue curve) vs. Time (h) with 2 measured heating/cooling cycles of sample In-Li 14. The yellow part (integrated area) during heating/cooling marks the peak with its starting temperature (Onset within gray box) resulting from endothermic (peak points down)/exothermic (peak points up) reactions.

As expected In-Li 14 (94.7 at.% Li, annealed at 140 °C) was too ductile and soft for powdering, hence the sample was cut and flattened leading to strains and a high sample displacement factor, because of the large sample height. Nevertheless, the XRD measurement clearly showed reflections of the phases In_3Li_{13} (cubic, *Fd*$\bar{3}$*m*) and LiOH (tetragonal, *P4/nmm*), (see Fig. 105). After refinement for phase analysis with a quality of Rwp = 2.104, 54.6 wt.% In_3Li_{13} with

the lattice paramter a = 13.394 (5) Å and 45.4 wt.% LiOH with the lattice parameters a = 3.55 (2) Å and c = 4.34 (4) Å were found.

In_3Li_{13} appeared to be a non-stoichiometric compound due to the deviation from its lattice parameter of the literature at stoichiometric composition a = 13.556 (0) Å.

Obviously, (Li) present as a pristine equilibrium phase, was hydrolysed giving LiOH. The hydrolization was caused by humidity penetrating the seald sample holder during XRD measurement or still presnt in the dryed petrol jelly for fixing the sample. Powder XRD of the samples In-Li 6 and 32 showed similar results.

Thus, the sample In-Li 14 represents a two-phase field were In_3Li_{13} was in equilibrium with (Li).

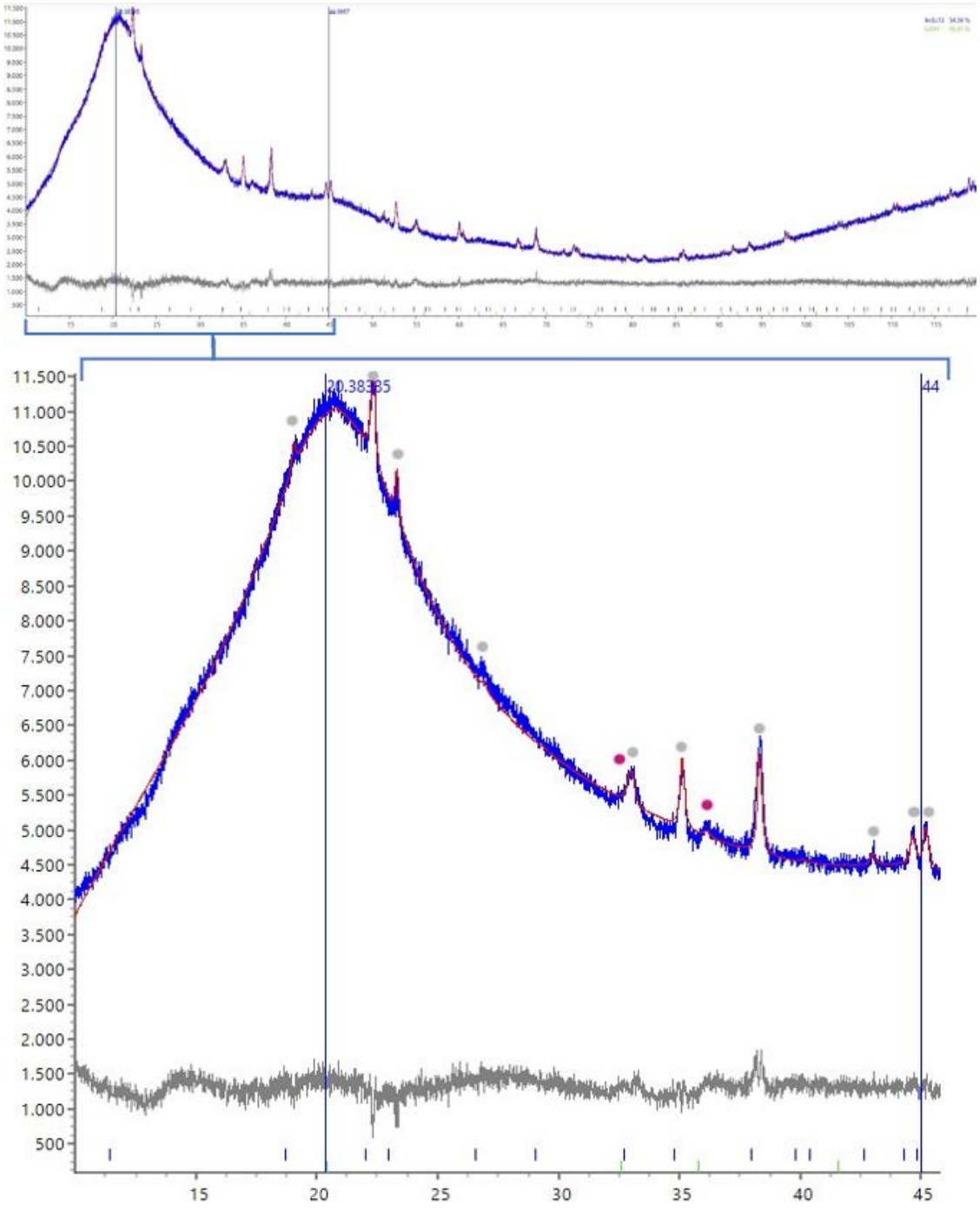

Figure 105 XRD pattern (of TOPAS-64 7.13 of Bruker) (counts vs. 2θ) of sample In-Li 14. Magnified part (2θ=10 to 45°) with significant reflections of: In_3Li_{13}… ● and LiOH… ● . The “bulge” at 20 and 45° (θ/θ-goniometer mode) originates from the amorphous PC dome of the sample holder. Blue curve: Measured pattern. Red curve: Refined pattern. Grey curve: Difference between measured and refined pattern.

5.5 The constructed In-Li phase diagram

In the following In-Li phase diagram shown in Fig. 106 the metastable miscibility gap $InLi_{(Li\text{-}deficient)}$/$InLi_{(Li\text{-}rich)}$ within the stable InLi homogeneity range was indicated as dashed line. LiOH from hydrolyzation, found in XRD was considered to be (Li) and (In)' was not indicated as stable phases. According to Alexander et al. [51] the (In) phase field was described with a solubility of 1.5 at.% Li. The peritectic reaction of L + InLi ⇄ (In) mostly described in the literature was confirmed by specially designed measurements. Since In-Li 20 and 22 did not show a liquidus signal on heating by DTA the liquidus from the cooling cycle was used for phase diagram construction. Other utilized data were taken from Grube et al. [47] and drop calorimetry data of Fischer et al. [108] which were not yet published.

From the new 3 intermetallic compounds $In_{4+x}Li_{11-x}$ (x=1.05), $In_{2+x}Li_{10-x}$ (x=1.59) and $In_{8+x}Li_{22-x}$ (x=0.1) discovered by Chumak et al. [75], could only $In_{2+x}Li_{10-x}$ (x=1.59) and $In_{8+x}Li_{22-x}$ (x=0.1) be verified. The reaction involving L + In_3Li_{13} + (Li) was described as peritectic reaction L + In_3Li_{13} ⇄ (Li), contradicting to the literature but based on specially designed measurements.

The In-Li phase diagram in Fig. 106 is a new version which includes new data from literature like phases of Chumak et al. [75] and our own experimental results. However, there are still some open questions, mandatory to describe the postulated metastable equilibria, discussed as the "split hypothesis" in this work. It is also necessary to prepare samples again, which were not in phase equilibrium (In-Li 4, 5, 9, 12, 15, 17, 18, 19, 23, 24 and 38) via the alloying method 9, which was first developed quite at the end of my experimental work. Furthermore, the crystal structure of $InLi_4$ ht must also be verified by SCXRD.

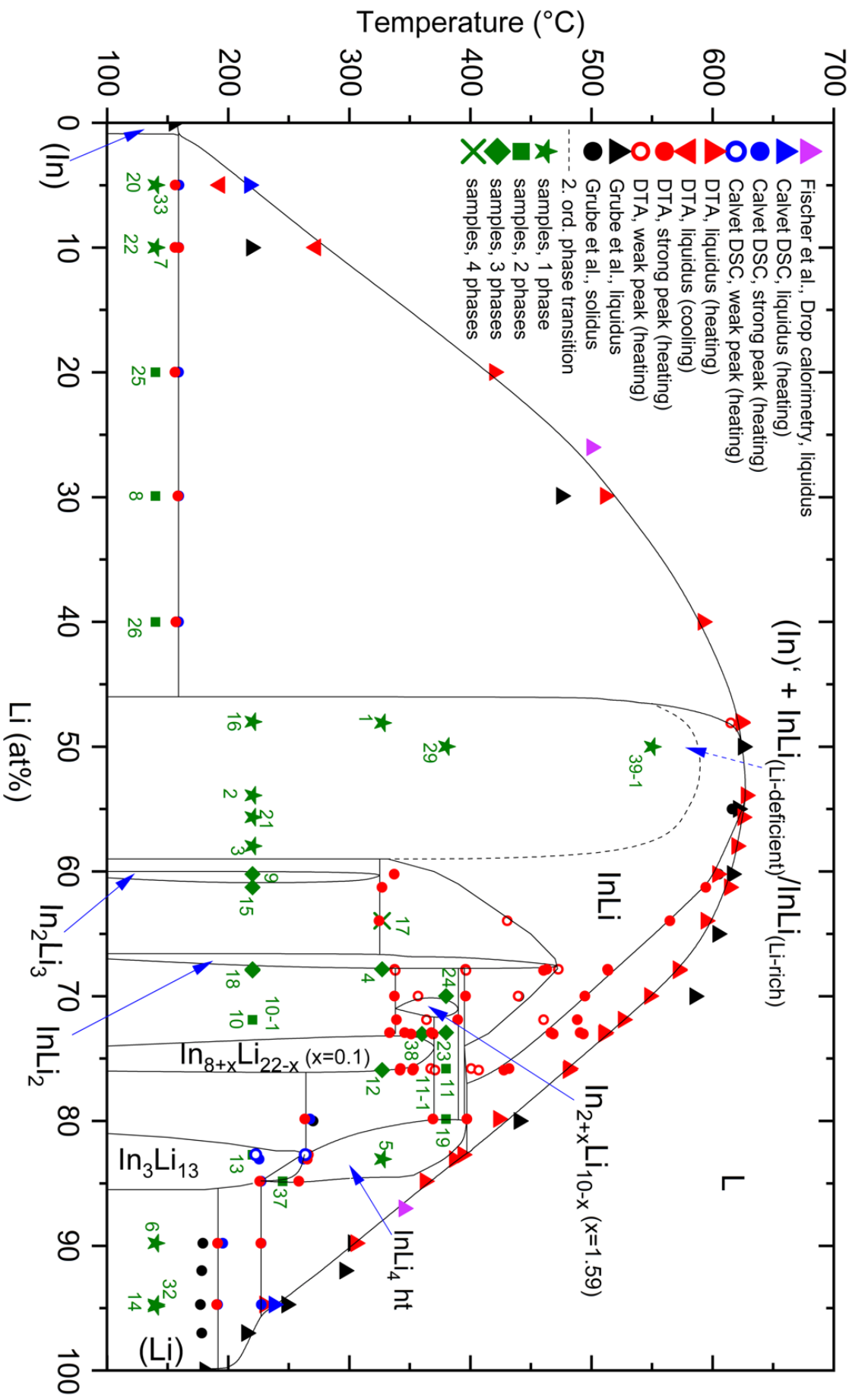

Figure 106 In-Li phase diagram constructed with Origin 2022.

6. Abstract

The goal of this diploma thesis was to investigate the phase relations in the intermetallic system In-Li, which is among other applications interesting for metal alloying anodes. These anodes are promising candidates for applications in Li-ion batteries of the latest generation, due to their abilities of self-healing and Li dendrite growth suppression.

The In-Li system was already investigated by several authors, nevertheless there are significant differences between the resulting phase diagrams. They concern the kind and number of phases and their stability ranges, both in terms of concentration and temperature. Thus, further investigations by powder XRD and SCXRD, DTA and Calvet-type 3D-DSC as well as F-AAS and TXRF to verify the elemental composition of the samples were accomplished. 48 samples with different Li-content in the range of 5 to 95 at.% had to be prepared and annealed at 140, 220, 245, 327, 360, 380 and 550 °C.

It was quickly noticed that samples were difficult to homogenize on preparation and bring them into phase equilibrium through annealing. Those severe problems were probably caused by the relatively slow solid-state diffusion combined with the relatively low surface tension of $Li_{(l)}$ and by the strong density differences of $Li_{(l)}$ and $In_{(l)}$. 9 different alloying methods had to be developed and tested until a successful homogenization was achieved.

It is to mention that samples within the InLi homogeneity region contained always an In-phase besides InLi. In addition, some samples showed the presence of two InLi phases simultaneously, with different lattice parameter a. However, no related phase transition was found by thermal analysis, leading to the conclusion that InLi should be described having a metastable miscibility gap $InLi_{(Li\text{-}deficient)}$/$InLi_{(Li\text{-}rich)}$ within its homogeneity range, similar to the phase NiAl, where this behavior is caused by distinct diffusion kinetics. In addition, the present In-phase showed brittleness and a larger lattice parameter c compared to (In). Hence, in this case the In-phase was described as metastable solid solution (In)' with a partially ordered substitution of In with Li at the atomic position (½ ½ ½). It was suggested that (In)' results from a 2nd order phase transition, related to the occurrence of the $InLi_{(Li\text{-}deficient)}$/$InLi_{(Li\text{-}rich)}$ miscibility gap. For the verification of these results, other techniques like neutron diffraction and kinetic investigations are mandatory.

A high temperature phase with the nominal stoichiometric composition of $InLi_4$ or In_3Li_{13}, respectively was already postulated in literature, but not doubtless crystallographically described yet. This was done in this diploma thesis. The cubic crystal structure of $InLi_4$ ht was found, preliminary based on powder XRD results and crystal chemical relations to InLi and In_3Li_{13}. However, a final verification by SCXRD was not successful yet, due to failed efforts to grow phase pure $InLi_4$ ht single crystals with a suitable size.

Nevertheless, finally all measured results and the assessed data from the literature were combined to construct a new In-Li phase diagram version.

7. Zusammenfassung

Das Ziel dieser Diplomarbeit war es die Phasenbeziehungen des intermetallischen Systems In-Li zu untersuchen, was neben anderen Anwendungen für die Nutzung von legierungsbildenden Anoden von Interesse ist. Diese Anoden sind vielversprechende Kandidaten für Anwendungen in Li-Ionen-Akkumulatoren der neusten Generation. Bedingt durch deren selbstheilende Eigenschaften und der Unterdrückung des Wachstums von Li-Dendriten.

Das In-Li-System wurde bereits von mehreren Autoren untersucht, dennoch sind signifikante Unterschiede zwischen den beschriebenen Phasendiagrammen ersichtlich in Bezug auf Art und Anzahl der Phasen und ihre Stabilitätsbereiche, sowohl in Hinblick auf die Konzentration als auch auf die Temperatur. Weswegen weitere Untersuchungen mittels Pulver-XRD und SCXRD, DTA und Calvet-Typ 3D-DSC, sowie zur Bestimmung der elementaren Zusammensetzung der Proben per F-AAS und TXRF, durchgeführt wurden. 48 Proben mit unterschiedlichen Li-Gehalt im Bereich von 5 bis 95 at.% wurden hergestellt und geglüht bei 140, 220, 245, 327, 360, 380 und 550 °C.

Schnell fiel auf, dass die Proben während der Präparation schwierig zu homogenisieren und durch Glühen ins Phasengleichgewicht zu bringen waren. Dieses erhebliche Problem wurde wahrscheinlich durch die relativ langsame Festkörperdiffusion, kombiniert mit der relativ niedrigen Oberflächenspannung von $Li_{(l)}$ und den durch die deutlichen Dichteunterschiede von $Li_{(l)}$ und $In_{(l)}$, verursacht. 9 verschiedene Legierungsmethoden wurden entwickelt und getestet, bis eine erfolgreiche Homogenisierung erreicht wurde.

Weiters ist zu erwähnen, dass Proben innerhalb des InLi-Homogenitätsbereichs immer eine In-Phase neben InLi enthielten. Zusätzlich zeigten manche Proben die simultane Anwesenheit von zwei InLi Phasen, mit unterschiedlichem Gitterparameter a. Da per thermischer Analyse kein zugehöriger Phasenübergang gefunden werden konnte, wurde geschlussfolgert, dass InLi mit metastabiler Mischungslücke $InLi_{(Li\text{-}deficient)}$/$InLi_{(Li\text{-}rich)}$ innerhalb ihres Homogenitätsbereich zu beschreiben war. Ähnlich der Phase NiAl, bei welcher dieses Verhalten durch eine bestimmt Diffusionskinetik verursacht wird. Zusätzlich zeigte die weiters vorhandene In-Phase Sprödigkeit und einen, im Vergleich zu (In) größeren Gitterparameter c. Somit wurde in diesem Fall die In-Phase als metastabiler Mischkristall

(In)‘, mit teils geordneter Substitution von In mit Li an der Atomposition (½ ½ ½), beschrieben. Es wurde vorgeschlagen, dass (In)‘ durch einen Phasenübergang 2. Ordnung entsteht, welcher in Beziehung mit dem Auftreten der $InLi_{(Li\text{-}deficient)}$/$InLi_{(Li\text{-}rich)}$ Mischungslücke liegt. Zur Verifizierung dieser Ergebnisse sind jedoch andere Techniken wie Neutronenbeugung und kinetische Untersuchungen unabdingbar.

Eine Hochtemperaturphase mit der nominalen, stöchiometrischen Zusammensetzung $InLi_4$ bzw. In_3Li_{13} wurde bereits in der Literatur postuliert, jedoch noch nicht kristallographisch, zweifelsfrei beschrieben. Dies wurde in dieser Diplomarbeit versucht. Die kubische Kristallstruktur von $InLi_4$ ht wurde, vorläufig auf Pulver-XRD-Ergebnissen und kristallchemischen Zusammenhängen mit InLi und In_3Li_{13} basierend, bestimmt. Jedoch war eine endgültige Verifizierung mittels SCXRD noch nicht erfolgreich, bedingt durch die misslungenen Bemühungen phasenreine $InLi_4$ ht-Einkristalle, mit passender Größe zu züchten.

Dennoch wurden zu guter Letzt alle gemessenen Ergebnisse mit bewerteten Literaturdaten kombiniert, um eine neue Version eines In-Li-Phasendiagramms zu konstruieren.

8. References

[1] H. J. Schellnhuber, S. Rahmstorf, and R. Winkelmann, “Why the right climate target was agreed in Paris,” *Nat. Clim. Chang.*, vol. 6, no. 7, pp. 649–653, 2016, doi: 10.1038/nclimate3013.

[2] E. R. Ezeigwe, L. Dong, R. Manjunatha, M. Tan, W. Yan, and J. Zhang, “A review of self-healing electrode and electrolyte materials and their mitigating degradation of Lithium batteries,” *Nano Energy*, vol. 84, no. November 2020. Elsevier Ltd, p. 105907, 2021. doi: 10.1016/j.nanoen.2021.105907.

[3] B. Dunn, H. Kamath, and J. M. Tarascon, “Electrical energy storage for the grid: A battery of choices,” *Science (80-.).*, vol. 334, no. 6058, pp. 928–935, 2011, doi: 10.1126/science.1212741.

[4] C. Wei *et al.* , “Review of room-temperature liquid metals for advanced metal anodes in rechargeable batteries,” *Energy Storage Mater.*, vol. 50, no. May, pp. 473–494, 2022, doi: 10.1016/j.ensm.2022.05.024.

[5] J. Qu, J. Xiao, T. Wang, D. Legut, and Q. Zhang, “High Rate Transfer Mechanism of Lithium Ions in Lithium–Tin and Lithium–Indium Alloys for Lithium Batteries,” *J. Phys. Chem. C*, vol. 124, no. 45, pp. 24644–24652, 2020, doi: 10.1021/acs.jpcc.0c07880.

[6] A. Eftekhari, *Future Lithium-ion Batteries*. London: Royal Society of Chemistry, 2019. [Online]. Available: https://search.ebscohost.com/login.aspx?direct=true&db=nlebk&AN=2090515&site=ehost-live

[7] X. Guo *et al.* , “A Self-Healing Room-Temperature Liquid-Metal Anode for Alkali-Ion Batteries,” *Adv. Funct. Mater.*, vol. 28, no. 46, pp. 1–8, 2018, doi: 10.1002/adfm.201804649.

[8] B. Han *et al.* , “Spontaneous repairing liquid metal/Si nanocomposite as a smart conductive-additive-free anode for lithium-ion battery,” *Nano Energy*, vol. 50, no. May, pp. 359–366, 2018, doi: 10.1016/j.nanoen.2018.05.044.

[9] A. M. Alfantazi and R. R. Moskalyk, “Processing of indium: A review,” *Miner. Eng.*, vol. 16, no. 8, pp. 687–694, 2003, doi: 10.1016/S0892-

6875(03)00168-7.

[10] W. Jing *et al.* , “Li-Indium alloy anode for high-performance Li-metal batteries,” *J. Alloys Compd.*, vol. 924, pp. 1–9, 2022, doi: 10.1016/j.jallcom.2022.166517.

[11] M. Nagao, A. Hayashi, and M. Tatsumisago, “Bulk-type lithium metal secondary battery with indium thin layer at interface between Li electrode and Li2S-P2S5 solid electrolyte,” *Electrochemistry*, vol. 80, no. 10, pp. 734–736, 2012, doi: 10.5796/electrochemistry.80.734.

[12] C. Wei, H. Fei, Y. An, Y. Tao, J. Feng, and Y. Qian, “Uniform Li deposition by regulating the initial nucleation barrier: Via a simple liquid-metal coating for a dendrite-free Li-metal anode,” *J. Mater. Chem. A*, vol. 7, no. 32, pp. 18861–18870, 2019, doi: 10.1039/c9ta06663b.

[13] J. Park and S. Ahn, “Electrochemical characteristics of Li-In/Cu anode for dendrite-free Lithium-ion batteries,” *Mater. Lett.*, vol. 297, p. 129994, 2021, doi: 10.1016/j.matlet.2021.129994.

[14] S. Luo *et al.* , “Growth of lithium-indium dendrites in all-solid-state lithium-based batteries with sulfide electrolytes,” *Nat. Commun.*, vol. 12, no. 1, pp. 1–9, 2021, doi: 10.1038/s41467-021-27311-7.

[15] J. Wang, I. D. Raistrick, and R. A. Huggins, “Behavior of Some Binary Lithium Alloys As Negative Electrodes in Organic Solvent Based Electrolytes.,” *Electrochem. Soc. Ext. Abstr.*, vol. 84–2, pp. 184–185, 1984, doi: 10.1149/1.2108601.

[16] A. L. Santhosha, L. Medenbach, J. R. Buchheim, and P. Adelhelm, “The Indium−Lithium Electrode in Solid-State Lithium-Ion Batteries: Phase Formation, Redox Potentials, and Interface Stability,” *Batter. \& Supercaps*, vol. 2, no. 6, pp. 524–529, 2019, doi: https://doi.org/10.1002/batt.202100237.

[17] “Indium - An Illuminating Element,” *AmericanChemical Society*, 2020.

[18] P. Enghag, “Gallium, Indium and Thallium,” in *Encyclopedia of the Elements*, John Wiley & Sons, Ltd, 2004, pp. 845–867. doi: https://doi.org/10.1002/9783527612338.ch38.

[19] N. Felix, “Indium and Indium Compounds,” in *Ullmann’s Encyclopedia of Industrial Chemistry*, Wiley-VCH Verlag GmbH & Co. KGaA, 2000, pp. 65–74. doi: 10.1002/14356007.a14_157.

[20] A. W. Hull and W. P. Davey, “Graphical determination of hexagonal and tetragonal crystal structures from x-ray data,” *Phys. Rev.*, vol. 17, no. 5, pp. 549–570, 1921, doi: 10.1103/PhysRev.17.549.

[21] J. Graham and G. V Raynor, “Indium-rich indium-magnesium and indium-lithium alloys,” *Philos. Mag.*, vol. 2, no. 23, pp. 1354–1363, 1957, doi: 10.1080/14786435708243212.

[22] K. Takemura and H. Fujihisa, “High-pressure structural phase transition in indium,” *Phys. Rev. B*, vol. 47, no. 14, pp. 8465–8470, Apr. 1993, doi: 10.1103/PhysRevB.47.8465.

[23] P. Villars and K. Cenzual, Eds., “indium (In) Crystal Structure: Datasheet from ‘PAULING FILE Multinaries Edition – 2022’ in SpringerMaterials.” https://materials.springer.com/isp/crystallographic/docs/sd_1251842

[24] P. Villars and K. Cenzual, Eds., “In(II) (In hp, p = 93(5) GPa) Crystal Structure: Datasheet from ‘PAULING FILE Multinaries Edition – 2022’ in SpringerMaterials.” https://materials.springer.com/isp/crystallographic/docs/sd_1251906

[25] P. Enghag, “Lithium,” in *Encyclopedia of the Elements*, John Wiley & Sons, Ltd, 2004, pp. 287–300. doi: https://doi.org/10.1002/9783527612338.ch12.

[26] F. Meng, J. McNeice, S. S. Zadeh, and A. Ghahreman, “Review of Lithium Production and Recovery from Minerals, Brines, and Lithium-Ion Batteries,” *Miner. Process. Extr. Metall. Rev.*, vol. 42, no. 2, pp. 123–141, 2021, doi: 10.1080/08827508.2019.1668387.

[27] A. W. Hull, “A New Method of X-Ray Crystal Analysis,” *Powder Diffr.*, vol. 7, no. 1, pp. 13–27, 1917, doi: 10.1017/S0885715600016018.

[28] D. W. Levinson, “Lithium_On the lattice parameter of Mg-Li β alloys.pdf,” *Acta Metall.*, vol. 3, no. 3, pp. 294–295, 1955.

[29] R. Berliner, O. Fajen, H. G. Smith, and R. L. Hitterman, “Neutron powder-diffraction studies of lithium, sodium, and potassium metal,” *Phys. Rev. B*,

vol. 40, no. 18, pp. 86–97, 1989.

[30] H. G. Smith, R. Berliner, J. D. Jorgensen, and J. Trivisonno, “Pressure effects on the martensitic transformation in metallic sodium,” *Phys. Rev. B*, vol. 43, no. 5, pp. 4524–4526, 1991, doi: 10.1103/PhysRevB.43.4524.

[31] M. Hanfland, K. Syassen, N. E. Christensen, and D. L. Novikov, “New high-pressure phases of lithium,” *Nature*, vol. 408, no. 6809, pp. 174–178, 2000, doi: 10.1038/35041515.

[32] P. Villars and K. Cenzual, Eds., “Li Crystal Structure: Datasheet from ‘PAULING FILE Multinaries Edition – 2022’ in SpringerMaterials.” https://materials.springer.com/isp/crystallographic/docs/sd_0557551

[33] P. Villars and K. Cenzual, Eds., “Li (T = 140 K, p = 0.65 GPa) Crystal Structure: Datasheet from ‘PAULING FILE Multinaries Edition – 2022’ in SpringerMaterials.” https://materials.springer.com/isp/crystallographic/docs/sd_0557622

[34] P. Villars and K. Cenzual, Eds., “Li hR1 (Li hp2) Crystal Structure: Datasheet from ‘PAULING FILE Multinaries Edition – 2022’ in SpringerMaterials.” https://materials.springer.com/isp/crystallographic/docs/sd_1254020

[35] P. Villars and K. Cenzual, Eds., “Li cI16 (Li hp3, T = 180 K, p = 44.5 GPa) Crystal Structure: Datasheet from ‘PAULING FILE Multinaries Edition – 2022’ in SpringerMaterials.” https://materials.springer.com/isp/crystallographic/docs/sd_1254021

[36] M. Bertau, A. Müller, P. Fröhlich, and M. Katzberg, “Metalle und ihre Verbindungen,” in *Industrielle Anorganische Chemie*, 2013, pp. 197–394. doi: 10.1002/9783527649563.ch3.

[37] P. Villars, “Cl-K-Li Vertical Section of Ternary Phase Diagram: Datasheet from ``PAULING FILE Multinaries Edition -- 2022'' in SpringerMaterials.” https://materials.springer.com/isp/phase-diagram/docs/c_0207620

[38] E. Zintl and G. Brauer, “Über die Valenzelektronenregel und die Atomradien unedler Metalle in Legierungen,” *Zeitschrift für Phys. Chemie*, vol. 20B, no. 1, pp. 245–271, 1933, doi: 10.1515/zpch-1933-2023.

[39] K. Kuriyama, “Bridgman growth of lithium indium alloy single crystals,” *J. Cryst. Growth*, vol. 23, no. 2, pp. 160–162, 1974, doi: 10.1016/0022-0248(74)90120-1.

[40] T. S. Huang and J. O. Brittain, “Defect structure and mechanical behavior of B LiIn,” *Mater. Sci. Eng.*, vol. 93, no. C, pp. 83–92, 1987, doi: 10.1016/0025-5416(87)90414-9.

[41] E. Zintl, “Intermetallische Verbindungen,” *Angew. chemie*, vol. 52, no. 1, pp. 1–6, 1939.

[42] P. Villars and K. Cenzual, Eds., “Li0.97In (LiIn rt, T = 300 K) Crystal Structure: Datasheet from ‘PAULING FILE Multinaries Edition – 2022’ in SpringerMaterials.” https://materials.springer.com/isp/crystallographic/docs/sd_1925699

[43] G. Dmytriv, H. Pauly, H. Ehrenberg, V. Pavlyuk, and E. Vollmar, “Homogeneity range of the NaTl-type Zintl phase in the ternary system Li-In-Ag,” *J. Solid State Chem.*, vol. 178, no. 9, pp. 2825–2831, 2005, doi: 10.1016/j.jssc.2005.06.033.

[44] P. Villars and K. Cenzual, Eds., “Li1.03In (LiIn rt, T = 300 K) Crystal Structure: Datasheet from ‘PAULING FILE Multinaries Edition – 2022’ in SpringerMaterials.” https://materials.springer.com/isp/crystallographic/docs/sd_1925701

[45] H. Ehrenberg, H. Pauly, T. Hansen, J. C. Jaud, and H. Fuess, “Phase transition from the cubic Zintl phase LiIn into a tetragonal structure at low temperature,” *J. Solid State Chem.*, vol. 167, no. 1, pp. 1–6, 2002, doi: 10.1006/jssc.2002.9590.

[46] P. Villars and K. Cenzual, Eds., “LiIn Crystal Structure: Datasheet from ‘PAULING FILE Multinaries Edition – 2022’ in SpringerMaterials.” https://materials.springer.com/isp/crystallographic/docs/sd_0458271

[47] G. Grube and W. Wolfe, “Die legierungen des lithiums mit quecksilber und indium.,” *Ztschr. Elektrochem.*, vol. 41, no. 9, pp. 675–681, 1935.

[48] W. Klemm and H. Fricke, “Über das magnetische Verhalten der Intermetallischen Phasen vom NaTl-Typ,” *ZAAC - J. Inorg. Gen. Chem.*, vol. 282, no. 1–6, pp. 162–168, 1955, doi: 10.1002/zaac.19552820119.

[49] G. J. Lamprecht and P. Crowther, “The systems Na-In and Li-In,” *J. Inorg. Nucl. Chem.*, vol. 31, pp. 925–931, 1969.

[50] R. Thümmel and W. Klemm, “Das Verhalten der Alkalimetalle zu den Metallen der Gruppe III B,” *Zeitschrift für Anorg. und Allg. Chemie*, vol. 376, no. 1, pp. 44–63, 1970, doi: https://doi.org/10.1002/zaac.19703760107.

[51] W. A. Alexander, L. D. Calvert, R. H. Gamble, and K. Schinzel, “The lithium–indium system,” *Can. J. Chem.*, vol. 54, no. 7, pp. 1052–1060, 1976, doi: 10.1139/v76-150.

[52] J. Sangster and A. D. Pelton, “The In-Li (Indium-Lithium) System,” *J. Phase Equilibria*, vol. 12, no. 1, pp. 37–41, 1991.

[53] J. Stöhr and H. Schäfer, “Die Kristallstrukturen von Li3In2, Li5Tl2 und Li3Tl,” *Zeitschrift für Naturforsch. B*, vol. 34, no. 5, pp. 653–656, 1979, doi: doi:10.1515/znb-1979-0501.

[54] J. Stöhr, W. Müller, and H. Schäfer, “ Darstellung und Kristallstruktur von Li 2 In und Li 13 In 3 / Preparation and Crystal Structure of Li 2 In and Li 13 In 3 ,” *Zeitschrift für Naturforsch. B*, vol. 33, no. 12, pp. 1434–1437, 1978, doi: 10.1515/znb-1978-1212.

[55] J. Stöhr, W. Müller, and H. Schäffer, “Structural Principles of Lithium-Group III-Compounds,” *Acta Crystallogr. A*, vol. 37, pp. C–185, 1981.

[56] P. Villars and K. Cenzual, Eds., “Li2In Crystal Structure: Datasheet from ‘PAULING FILE Multinaries Edition – 2022’ in SpringerMaterials.” https://materials.springer.com/isp/crystallographic/docs/sd_0300011

[57] P. Villars and K. Cenzual, Eds., “Li3In2 Crystal Structure: Datasheet from ‘PAULING FILE Multinaries Edition – 2022’ in SpringerMaterials.” https://materials.springer.com/isp/crystallographic/docs/sd_0300014

[58] P. Villars and K. Cenzual, Eds., “Li5In4 Crystal Structure: Datasheet from ‘PAULING FILE Multinaries Edition – 2022’ in SpringerMaterials.” https://materials.springer.com/isp/crystallographic/docs/sd_0527595

[59] F. Sommer, B. Fischer, and B. Predel, “Determination of The Formation Enthalpies of Sodium Alloys of Lithium with In, Tl, Sn, Pb and Bi,” *Mater. Behav. Phys. Chem. Liq. Met. Syst.*, no. 2, pp. 395–400, 1982, doi:

10.1007/978-1-4684-8366-6_40.

[60] V. D. Bushmanov and S. P. Yatsenko, “Thermodynamic properties of binary systems of lithium, sodium, potassium with aluminium, gallium, indium, thallium,” *Zh. Fiz. Khim.*, vol. 55, no. 11, pp. 2951–2952, 1981.

[61] A. Schneider and O. Hilmer, “Wärmeinhalte und Schmelzentropien von NaTl-Phasen,” *Zeitschrift für Anorg. und Allg. Chemie*, vol. 286, no. 3–4, pp. 97–117, 1956, doi: https://doi.org/10.1002/zaac.19562860302.

[62] C. J. Wen and R. A. Huggins, “Thermodynamic and mass transport properties of ‘LiIn,’” *Mater. Res. Bull.*, vol. 15, no. 9, pp. 1225–1234, 1980, doi: 10.1016/0025-5408(80)90024-0.

[63] S. P. Yatsenko and E. A. Saltykova, “Thermodynamic properties of Li-In liquid alloys system,” *Ehlektrokhimiya*, vol. 11, no. 4, pp. 580–581, 1975, Accessed: Oct. 10, 2023. [Online]. Available: https://inis.iaea.org/search/search.aspx?orig_q=RN:6203912

[64] A. G. Morachevskii, A. I. Demidov, and M. N. Ivantsova, “Thermodynamic Properties of Molten Alloys in the Li-In System,” *Elektrokhimiya*, vol. 10, no. 5, pp. 845–846, 1974.

[65] C. Van Der Marel, E. P. Brandenburg, and W. Van Der Lugt, “Knight shift and electrical resistivity of liquid Li-In alloys,” *J. Phys. F Met. Phys.*, vol. 8, no. 11, pp. 273–275, 1978, doi: 10.1088/0305-4608/8/11/006.

[66] B. Predel and G. Dehme, “Kalorimetrische Untersuchung flüssiger Lithium-Thallıum-, Lithium-Indium- und Lithium-Wismut-Legierungen,” *Int. J. Mater. Res.*, vol. 70, no. 9, pp. 618–623, 1979, doi: doi:10.1515/ijmr-1979-700913.

[67] N. E. Christensen, “Structural phase stability of B2 and B32 intermetallic compounds,” *Phys. Rev. B*, vol. 32, no. 1, pp. 207–228, 1985, doi: 10.1103/PhysRevB.32.207.

[68] P. Villars and K. Cenzual, Eds., “LiIn, hp (LiIn hp) Crystal Structure: Datasheet from ‘PAULING FILE Multinaries Edition – 2022’ in SpringerMaterials.” https://materials.springer.com/isp/crystallographic/docs/sd_1925845

[69] U. Schwarz, S. Bräuninger, K. Syassen, and R. Kniep, “Pressure-Induced

Phase Transformation of LiIn and LiCd: From NaTl-Type Phases toβ-Brass-Type Alloys,” *J. Solid State Chem.*, vol. 137, no. 1, pp. 104–111, 1998, doi: 10.1006/jssc.1997.7724.

[70] X. Zhou, F. Zhang, S. Liu, Y. Du, and B. Jin, “Phase equilibria and thermodynamic investigation of the In–Li system,” *Calphad Comput. Coupling Phase Diagrams Thermochem.*, vol. 70, no. April, p. 101779, 2020, doi: 10.1016/j.calphad.2020.101779.

[71] G. GASIOR W; SCHWITZGEBEL, “Thermodynamic properties of Li-In liquid and solid solutions,” *Arch. Metall.*, vol. 37, no. 1, pp. 25–36, 1992.

[72] A. Dębski, M. Zabrocki, and W. Gąsior, “Calorimetric study and thermodynamic description of liquid In-Li alloys,” *J. Mol. Liq.*, vol. 243, pp. 72–77, 2017, doi: 10.1016/j.molliq.2017.08.022.

[73] B. Lab, “https://next-gen.materialsproject.org/materials?chemsys=In-Li,” *Materials Project*, 2024.

[74] W. Gierlotka, W. Gąsior, A. Dębski, and M. Zabrocki, “Thermodynamic Modeling of the Binary Indium-Lithium System, A Promising Li-Ion Battery Material,” *J. Min. Metall. Sect. B Metall.*, vol. 58, no. 1, pp. 75–84, 2022, doi: 10.2298/JMMB210205041G.

[75] I. Chumak, V. Pavlyuk, and H. Ehrenberg, “Binary lithium indides Li22-xIn8+x (x = 0.1), Li 11-xIn4+x (x = 1.05), and Li10-xIn 2+x (x = 1.59) with clusters,” *Eur. J. Inorg. Chem.*, no. 12, pp. 2053–2064, 2014, doi: 10.1002/ejic.201301444.

[76] P. Villars and K. Cenzual, Eds., “LiIn (T = 2 K) Crystal Structure: Datasheet from ‘PAULING FILE Multinaries Edition – 2022’ in SpringerMaterials.” https://materials.springer.com/isp/crystallographic/docs/sd_1925697

[77] P. Villars and K. Cenzual, Eds., “LiIn3 Crystal Structure: Datasheet from ‘PAULING FILE Multinaries Edition – 2022’ in SpringerMaterials.” https://materials.springer.com/isp/crystallographic/docs/sd_1925844

[78] K. Richter, “Lecture VO Phasendiagramme - Binary systems.” pp. 1–38, 2020. chrome-extension://efaidnbmnnnibpcajpcglclefindmkaj/https://moodle.univie.ac.at/pluginfile.php/11779809/mod_resource/content/5/C_Binary%20Systems.p

df

[79] S. M. Sarge, W. H. H, and W. Hemminger, *Calorimetry in Food Processing Analytical Methods in Supramolecular Chemistry*. 1899.

[80] NETZSCH-Gerätebau GmbH, “Brochure: Netzsch - Differentials Scanning Calorimetry - DSC 404 F1/F3 Pegasus.” pp. 1–24, 2023.

[81] P. Haines, “Chapter 3 - Differential Thermal Analysis and Differential Scanning Calorimetry,” in *Principles of Thermal Analysis and Calorimetry*, 2002, pp. 55–93. doi: 10.1039/9781847551764-00055.

[82] H. Flandorfer, “Lecture VO Synthese und Thermodynamische Charakterisierung - Thermochemische Messmethoden (Teil 3).” pp. 1–76, 2019. chrome-extension://efaidnbmnnnibpcajpcglclefindmkaj/https://moodle.univie.ac.at/pluginfile.php/8721608/mod_resource/content/3/MC-1_Thermochemie_Methoden.pdf

[83] KEP Technologies group, “Brochure: C80 Calvet Calorimeter - From ambient to 300°C by Setaram.” pp. 1–8.

[84] G. F. Harrington and J. Santiso, “Back - to - Basics tutorial : X - ray diffraction of thin films,” *J. Electroceramics*, no. 47, pp. 141–163, 2021.

[85] L. Spieß, G. Teichert, R. Schwarzer, H. Behnken, and C. Genzel, *Moderne Röntgenbeugung*. 2009.

[86] W. Massa, *Kristallstrukturbestimmung*. 2011.

[87] K. Richter, “Lecture VO Rietveld refinement.” pp. 1–106, 2023. https://moodle.univie.ac.at/course/view.php?id=377737

[88] T. Grüne, “Lecture Chemical Crystallography and Structural Chemistry.” pp. 1–480, 2021.

[89] B. D. Cullity and S. R. Stock, *Elements of X-Ray Diffraction*, vol. 3. 2014. doi: 10.1016/0014-5793(79)80596-7.

[90] R. E. Dinnebier, A. Leineweber, and J. S. O. Evans, *Rietveld refinement: Practical powder diffraction pattern analysis using TOPAS*. 2018. doi: 10.1515/9783110461381.

[91] G. Taylor, “The phase problem,” *Acta Crystallogr. - Sect. D Biol.*

Crystallogr., vol. 59, no. 11, pp. 1881–1890, 2003, doi: 10.1107/S0907444903017815.

[92] E. Margui and R. van Grieken, “Chapter 6 - Total Reflectio X-Ray Spectrometry (TXRF),” in *X-ray fluorescence spectrometry and related techniques: An introduction*, 2013, pp. 1–20. doi: 10.1002/9783527678679.dg13365.

[93] M. Brunda *et al.* , *Arbeitsbuch für Analytische Chemie und das Analytisch-Chemische Laboratorium - Band 3 Instrumentelle Methoden - Schulbuchnummer 7794*. 2009.

[94] M. Farrukh Akhyar, *Atomic absorption spectroscopy*. 2012. doi: 10.1007/BF02631956.

[95] Carl Zeiss AG - Mikroskopie, “Stemi 1000/2000/2000-C Stereo Microscopes Operating Manual.” pp. 1–68, 1998. [Online]. Available: http://www.zeiss.de

[96] S. A. Krat *et al.* , “Wetting properties of liquid lithium on lithium compounds,” *Fusion Eng. Des.*, vol. 117, pp. 199–203, 2017, doi: 10.1016/j.fusengdes.2016.06.038.

[97] Merck KGaA, “Merck PSE.”

[98] T. Hahn, *INTERNATIONAL TABLES FOR CRYSTALLOGRAPHY - Vol. A, Space-group symmetry - 5th edition*. 2005.

[99] PerkinElmer, “AAnalyst 200 AA Spectrometer Specifications.” pp. 1–2, 2011.

[100] Bruker, “S2 PICOFOX - Benchtop TXRF Spectrometer.” pp. 1–9, 2019. [Online]. Available: https://www.bruker.com/fileadmin/user_upload/8-PDF-Docs/X-rayDiffraction_ElementalAnalysis/TXRF/Brochures/bro_s2_picofox_en_rev_4_4_komplett_lores.pdf

[101] P. Villars and H. Okamoto, Eds., “In-Li Binary Phase Diagram 0-100 at.% Li: Datasheet from ‘PAULING FILE Multinaries Edition – 2022’ in SpringerMaterials https://materials.springer.com/isp/phase-diagram/docs/c_0901388

[102] P. Villars and H. Okamoto, Eds., “In-Li Binary Phase Diagram 0-100 at.% Li: Datasheet from ‘PAULING FILE Multinaries Edition – 2022’ in SpringerMaterials https://materials.springer.com/isp/phase-diagram/docs/c_0906650

[103] A. Dębski, W. Gierlotka, M. Zabrocki, A. Góral, and W. Gąsior, “Thermodynamic measurements and ab initio calculations of the indium-lithium system,” *J. Min. Metall. Sect. B Metall.*, vol. 59, no. 3, pp. 407–420, 2023, doi: 10.2298/jmmb230706035d.

[104] M. Poliserpi, R. Buzolin, R. Boeri, C. Poletti, and S. Sommadossi, “Analysis of Splitting and Martensitic Transformation of AlNi Intermetallic Obtained by Transient Liquid Phase Bonding,” *Metall. Mater. Trans. B Process Metall. Mater. Process. Sci.*, vol. 51, no. 3, pp. 916–924, 2020, doi: 10.1007/s11663-020-01832-w.

[105] F. M. d’Heurle and R. Ghez, “Reactive diffusion in a prototype system: nickel-aluminum I: Non-constant diffusion coefficient,” *Thin Solid Films*, vol. 215, no. 1, pp. 19–25, 1992, doi: 10.1016/0040-6090(92)90695-8.

[106] I. Kwiecien, P. Bobrowski, A. Wierzbicka-Miernik, L. Litynska-Dobrzynska, and J. Wojewoda-Budka, “Growth kinetics of the selected intermetallic phases in Ni/Al/Ni system with various nickel substrate microstructure,” *Nanomaterials*, vol. 9, no. 2, pp. 1–18, 2019, doi: 10.3390/nano9020134.

[107] A. J. Ardell, “The Equilibrium α (Al-Li Solid Solution) and Metastable δ′ (Al3Li) Phase Boundaries in Aluminum–Lithium Alloys,” *J. Phase Equilibria Diffus.*, vol. 44, no. 2, pp. 255–268, 2023, doi: 10.1007/s11669-023-01039-x.

[108] L. Fischer and H. Flandorfer, “Manuscript in preparation.” 2024.

9. Appendix

List of Figures

List of Tables